Precision Cosmology Using Voids

by

Alex Woodfinden

A thesis
presented to the University of Waterloo
in fulfilment of the
thesis requirement for the degree of
Doctor of Philosophy
in
Physics

Waterloo, Ontario, Canada, 2023

Examining Committee Membership

The following served on the Examining Committee for this thesis. The decision of the Examining Committee is by majority vote.

External Examiner:	Nelson Padilla Professor, Instituto de Astronomía Teórica y Experimental, CONICET - Universidad Nacional de Cordoba (UNC)
Supervisor:	Will Percival Professor, Dept. of Physics and Astronomy, University of Waterloo
Internal Member:	Michael Balogh Professor, Dept. of Physics and Astronomy, University of Waterloo
Internal Member:	Dustin Lang Adjunct Associate Professor, Dept. of Physics and Astronomy, University of Waterloo
Internal-External Member:	Ghazal Geshnizjani Research Associate Professor, Dept. of Applied Mathematics, University of Waterloo

Author's Declaration

This thesis consists of material all of which I authored or co-authored: see Statement of Contributions included in the thesis. This is a true copy of the thesis, including any required final revisions, as accepted by my examiners.

I understand that my thesis may be made electronically available to the public.

Statement of Contributions

I am the sole author of Chapters 1 & 6 which were written under the supervision of Prof. Will Percival and were not written for publication.

This thesis consists in part of two manuscripts written for publication. Exceptions to sole authorship of material are broken down by chapter below. In several sections, I summarise results from manuscripts of which I am an author but not the first author. These sections are all in my own words; I do not use any text from the manuscripts.

Chapter 2:

Various paragraphs of Sections 2.1, 2.5, 2.6, 2.7, and 2.8 are adapted from publication Woodfinden et al. (2022). I was the primary investigator for this work along with co-authors Seshadri Nadathur, Will Percival, Slađana Radinović, Elena Massara, and Hans Winther. As part of this work I conducted all analyses shown, made all figures, and wrote the large majority of the text. My co-authors contributed guidance and some of the text as well as contributed to the interpretation of the results. Section 2.9 summarises work published in manuscript Massara et al. (2022). This summary is not taken from the manuscript and is presented in my own words. As a co-author of this work, I produced several void catalogues and collaborated with the principal investigator regarding results and interpretation.

Chapter 3:

This chapter is adapted from publication Woodfinden et al. (2022). I was the primary investigator for this work along with coauthors Seshadri Nadathur, Will Percival, Slađana Radinović, Elena Massara, and Hans Winther. As part of this work, I conducted all analyses shown, made all figures, and wrote the large majority of the text. My coauthors contributed guidance and some of the text as well as contributed to the interpretation of the results. Also included in this chapter (and publication Woodfinden et al. 2022) are results from publication Nadathur et al. (2020b) on which I was the second author. In this work I was involved in the production of template functions used, void finding, and correlation function measurements, as well as contributed to the interpretation of results.

Chapter 4:

This chapter is adapted from publication Woodfinden et al. (2022). I was the primary investigator for this work along with coauthors Seshadri Nadathur, Will Percival, Slađana Radinović, Elena Massara, and Hans Winther. As part of this work, I conducted all analyses shown, made all figures, and wrote the large majority of the text. My coauthors contributed guidance and some of the text as well as contributed to the interpretation of the results.

Chapter 5:

This chapter is adapted from publication Woodfinden et al. (2023). I was the primary investigator for this work along with coauthors Will J. Percival, Seshadri Nadathur, Hans A. Winther, T. S. Fraser, Elena Massara, Enrique Paillas, and Slađana Radinović. As part of this work, I conducted all analyses shown, made all figures, and wrote the large majority of the text. My coauthors contributed guidance and some of the text as well as contributed to the interpretation of the results.

Chapter 6:

Sections of this chapter summarise results and reproduce figures from publication Radinović et al. (2023). All words written are my own and are not taken from this manuscript. I was a co-author of this publication and provided guidance on the work and contributed to the interpretation of the results.

Abstract

In the late 1990s, the discovery that the expansion rate of the Universe was accelerating was a decisive moment for cosmology (Perlmutter et al., 1999; Riess et al., 1998). The last 25 years have seen the consolidation of this component, called dark energy, which dominates the total energy of the Universe at the present day. Cosmologists have developed many techniques to measure the properties of dark energy and attempt to reveal insights into the physics behind this mysterious component (Huterer and Turner, 2001; Weinberg et al., 2013). Many explanations for dark energy exist, the simplest being that it is a form of energy permeating all of space (a cosmological constant), and alternatives include modifications to theories of general relativity and scalar fields (Peebles, 1993). The modern era of precision cosmology has been dedicated to the measurement of cosmological parameters that describe and distinguish different models. Despite decades of work in this area, little insight has been found into the nature of dark energy. More accurate measurements from next-generation cosmological surveys are needed to uncover the underlying physics behind this fundamental component of the Universe (Padmanabhan, 2019).

Cosmic voids are patches of the Universe that are less dense than the cosmic average. These large-scale underdensities are a natural consequence of structure growth. Voids are special places in the Universe where the physics of their growth can be easily modelled (Hamaus et al., 2014). Although the density is non-linear (the density in the centre of voids is close to zero), the motions of galaxies still track their primordial form (Nadathur et al., 2019a) making it possible to extract cosmological information (Pisani et al., 2019). This information primarily comes from two physical processes - the Alcock-Paczynski (AP) effect and Redshift-Space Distortions (RSDs). The AP effect is a geometrical consequence where an object's shape becomes distorted if measured using a wrong cosmological model. Stacking voids will produce a spherical averaged shape only if the AP parameter, $D_{\rm M}/D_{\rm H}$, is correct (where $D_{\rm M}$ is the transverse comoving distance that is a measure perpendicular to the line of sight and $D_{\rm H}$ is the Hubble distance which is a measure parallel to the line of sight) (Alcock and Paczynski, 1979; Lavaux and Wandelt, 2012; Nadathur et al., 2019b). RSDs are the distortions of measured distances due to the Doppler effect of a galaxy's peculiar velocity. On large scales, the growth rate of cosmological structure is the dominant source of RSDs (Kaiser, 1987; Chuang et al., 2017). Using the linear motions of galaxies around voids, RSDs are used to measure the growth rate of structure parameterised by $f(z)\sigma_8(z)$ (where $f(z)$ relates to the growth rate of structure and σ_8 relates to the redshift space galaxy power spectrum) (Percival and White, 2009; Percival et al., 2011).

Measurements of voids within the large-scale structure of the Universe can be made using galaxy spectroscopic surveys. These surveys use the positions of galaxies as tracers

of the underlying matter distribution. Information in these surveys has primarily been extracted using two techniques: Baryonic Acoustic Oscillations (BAO) and RSD. BAO provide a standard ruler through which the expansion rate of the Universe can be measured (Eisenstein et al., 2005), while RSD allows for a measurement of the growth rate of structure. The use of voids has emerged as another technique to extract even more information from these surveys. This thesis presents the background and modelling that can be used to extract and analyze this information.

After all necessary background is summarised, measurements of the anisotropic cross-correlation of galaxies and cosmic voids in data from the Sloan Digital Sky Survey Main Galaxy Sample (MGS), Baryon Oscillation Spectroscopic Survey (BOSS) and extended BOSS (eBOSS) luminous red galaxy catalogues from SDSS Data Releases 7, 12 and 16, covering the redshift range $0.07 < z < 1.0$ are presented (Woodfinden et al., 2022). This uses the clustering of galaxies around voids to extract information and is the first time that a consistent analysis method has been applied to extract information from voids in this full redshift range. A reconstruction method is applied to the galaxy data before void-finding to remove selection biases when constructing the void samples. Results of a joint fit to the multipole moments of the measured cross-correlation for the growth rate of structure and the ratio $D_{\rm M}(z)/D_{\rm H}(z)$ are reported in six redshift bins. For $D_{\rm M}/D_{\rm H}$, voids are able to achieve significantly higher precision than that obtained from analyses of BAO and RSD in the same datasets. Our growth rate measurements are of lower precision but still comparable with galaxy clustering results. For both quantities, the results agree well with the expectations for a ΛCDM model. The degeneracy directions obtained for the study of voids in galaxy spectroscopic surveys are consistent with and complementary to those from other cosmological probes and result in a significant gain of information. These results consolidate void-galaxy cross-correlation measurements as a pillar of modern observational cosmology.

Also presented are cosmological models fits to voids and the combination of voids with other probes (Woodfinden et al., 2023). A standard ΛCDM cosmological model is fit to measurements from voids as well as various extensions including a constant dark energy equation of state not equal to -1, a time-varying dark energy equation of state, and these same models allowing for spatial curvature. Results on key parameters of these models are reported for void-galaxy and galaxy-galaxy clustering alone, both of these combined, and all these combined with measurements from the cosmic microwave background (CMB) and supernovae (SN). The results show a remarkable agreement with a flat ΛCDM cosmology for all cosmological models tested. The gain of information from void measurements made at multiple redshifts, compared to compressing all information into one measurement at a single effective redshift, is also demonstrated.

Finally, a forward look to the future of voids as cosmological probes is presented. This thesis uses the best public galaxy redshift survey data available to date; however, this will soon be surpassed once DESI (DESI Collaboration et al., 2016a,b) and Euclid (Laureijs et al., 2011) results are released within the next few years. Forecast constraints from applying a consistent analysis method to that presented in this thesis on a mock catalogue expected to match data from Euclid are shown (Radinović et al., 2023).

Cosmic voids provide another analysis method that can extract independent cosmological constraints with complementary parameter degeneracies that, combined with information from BAO/RSD, increase the precision of information extracted from galaxy spectroscopic surveys. Future surveys will need to continue to build on the current modelling of voids to reduce systematic errors and provide valuable hints towards the fundamental nature of our Universe.

Acknowledgements

Cheers everyone.

Dedication

This thesis is dedicated to all those who have supported me throughout my education, in particular my amazing wife and family. Thank you all.

Table of Contents

List of Figures

List of Tables

List of Abbreviations

2dFGRS Two-degree-Field Galaxy Redshift Survey

6dFGS Two-degree-Field Galaxy Survey

AP Alcock-Paczynski

BAO Baryonic Acoustic Oscillations

BBN Big Bang Nucleosynthesis

BOSS Baryon Oscillation Spectroscopic Survey

CAMB Code for Anisotropies in the Microwave Background

CDM Cold Dark Matter

CfA Centre for Astrophysics

CLASS Cosmic Linear Anisotropy Solving System

CMASS Constant Mass

CMB Cosmic Microwave Background

Cobaya COde for BAYesian Analysis

DESI Dark Energy Spectroscopic Instrument

DIVE Delaunay trIangulation Void findEr

DR Data Release

eBOSS Extended Baryon Oscillation Spectroscopic Survey

ELG Emission Line Galaxy

EZmocks Effective Zel'dovich approximation mocks

FFT Fast Fourier Transform

FLRW Friedmann-Lemaître-Robertson-Walker

GAMA Galaxy And Mass Assembly

GR General Relativity

GSM Gaussian Streaming Model

HOD Halo Occupation Distribution

IFFT Inverse Fast Fourier Transform

LOS Line of Sight

LOWZ Low Redshift

LRG Luminous Red Galaxy

LSS Large Scale Structure

MGS Main Galaxy Survey

MCMC Markov Chain Monte Carlo

NGS North Galactic Cap

PDF Posterior Distribution Function

POS Perpendicular to the Line of Sight

QSO Quasar Stellar Object

Revolver REal-space VOid Locations from surVEy Reconstruction

RSD Redshift Space Distortions

SDSS Sloan Digital Sky Survey

SGC South Galactic Cap

SN Supernovae

SVF Spherical Void Finder

tRGB Tip of the Red Giant Branch

VIDE Void IDentification and Examination toolkit

VIMOS VIsible Multi-Object Spectrograph

VIPERS VIMOS Public Extragalactic Redshift Survey

WVF Watershed Void Finder

ZOBOV ZOnes Bordering On Voidness

Chapter 1

Introduction

1.1 Cosmology

The theory of General Relativity, published in 1916 (Einstein, 1916), set the framework for modern cosmology and allowed, for the first time, the construction of a self-consistent model for the Universe as a whole. The century following this publication has led to the discovery of various components that make up our modern-day picture of cosmology. In 1929 Edwin Hubble measured the recessional velocity of galaxies and found that this was linearly related to their distance, showing that the Universe is expanding (Hubble, 1929). It wasn't until the late 1990s that it was shown that this expansion was accelerating, driven by a component of the Universe called dark energy (Riess et al., 1998; Perlmutter et al., 1999). The 20th century also led to the discovery of another component of the Universe, dark matter. Fritz Zwicky, when studying the velocities of galaxies in the Coma cluster in 1933, concluded that there must be 400 times the amount of visible matter to hold the cluster together (Zwicky, 1933). This was not widely accepted until the 1970s when various other observations including the motion of satellites around the Milky Way and other nearby galaxies (Ostriker et al., 1974; Einasto et al., 1974) and the measurement of the rotation curves of spiral galaxies (Roberts and Rots, 1973; Rubin et al., 1978, 1980) provided strong evidence for its existence. The remainder of this section will explore the chronology of the Universe through these components (along with baryonic matter and radiation) and introduce the main topics of this thesis. This chronology is intentionally brief aiming to set up the background information needed for the remainder of this chapter.

The history of the Universe is the story of how it changed during various periods of expansion, happening at differing rates. The very early Universe was an infinitely dense

form of energy. At around 10^{-36} seconds into the life of the Universe a process known as inflation caused the incredibly rapid expansion of space filled with this energy. The inflationary period ended at approximately 10^{-33} and 10^{-32} seconds once this primordial energy was transformed into matter and energy as we know it (Guth, 1981). At 10^{-6} seconds into the life of the Universe expansion was still continuing but at a much lower rate than during the inflationary period. As the Universe cooled, the first fundamental particles decoupled by the first second, such as quarks, electrons, photons, and neutrinos, along with their antimatter counterparts. These combined at high energies and formed protons and neutrons. During this time, a process called baryogenesis occurred, resulting in an imbalance of baryons and antibaryons that is observed today (Barrow and Turner, 1981).

As expansion continued into the first few seconds to minutes into the life of the Universe, protons and neutrons formed hydrogen, helium, and lithium in a process known as Big Bang Nucleosynthesis (BBN) (Peebles, 1966). Most protons remained uncombined as hydrogen nuclei comprising approximately 75% of all mass, 25% of the mass is in helium nuclei and just trace amounts of heavier elements. The Universe continued to expand and cool and at around 300,000 years electrons and nuclei could combine to form neutral atoms. This period is known as the time of recombination. The resulting drop in the number density of free electrons caused the Universe to become transparent to photons; this is known as decoupling. A relic of this is visible today as the cosmic microwave background, photons that have been travelling uninhibited since recombination (Sunyaev, 1974).

This time from the beginning of the Universe onward was the radiation-dominated era. Most of the energy in the Universe was in the form of radiation which gradually diluted as the Universe expanded. This era lasted until approximately 50,000 years when the energy in matter and energy in radiation were equal and the matter-dominated era began; however, photons outnumbered baryons by a factor of approximately 10^9. As the expansion continued, light waves were diluted to lower and lower energies while matter travelled onward largely unaffected. During this time the clouds of mostly primordial hydrogen and helium gas, along with dark matter, started to collapse due to small anisotropies in their density. These formed dark matter halos, and the gas collapsed to form the first stars and galaxies (Mo and White, 1996; Mo et al., 2010). Matter in the Universe (dark and baryonic) has evolved in the present day to form a massive network known as the cosmic web. The cosmic web is comprised of massive clusters of galaxies, connected by long filaments of matter and cosmic voids filling in the low-density regions.

The matter-domination era ended approximately 9.8 billion years into the life of the Universe when the dark energy-dominated era began. Dark energy in this time drives an accelerated expansion of the Universe that is measured in the present day.

Many different observations can be made in the present day to help confirm and precisely measure this cosmological model; see Section 1.6 for a summary of these. This thesis uses information primarily from galaxy-spectroscopic surveys that aim to map the large-scale structure of the Universe. This large-scale structure contains information on dark energy, dark matter, baryons, and fluctuations in the early Universe. Much of the work to understand the large-scale structure of the Universe focuses on over-dense regions. Recently the study of under-dense regions known as cosmic voids has gained popularity. Modern (and upcoming) surveys have allowed for high-quality measurements of the large-scale structure of the Universe and have sampled galaxies in sparse environments in much more detail. The work of this thesis will explore cosmic voids as cosmological probes, make new measurements using these, and explain the implications of these results. The remainder of this chapter will first provide the cosmological background needed to make and interpret these observations, summarise alternative cosmological probes, and motivate the need for precise cosmological measurements.

1.2 The Homogeneous and Isotropic Universe

There are two fundamental components to the standard model of cosmology

- The Cosmological Principal - on large enough scales the Universe is i) homogeneous and ii) isotropic. Forces are uniform throughout space so large-scale structure should have no irregularities.
- General Relativity - Gravitation interactions can be entirely described by GR (Einstein, 1916).

The theory of General relativity proposes that the Universe consists of a spacetime framework with four dimensions (one time dimension and three spatial dimensions). Matter distributed in the Universe will perturb this spacetime, resulting in an effective gravitational force. The relationship between the geometry of spacetime and the matter within can be described by the Einstein field equations

$$G_{\mu\nu} + \Lambda g_{\mu\nu} = \frac{8\pi G}{c^4} T_{\mu\nu}. \tag{1.1}$$

$G_{\mu\nu}$ is the Einstein tensor which expresses the curvature of spacetime, Λ is the cosmological constant, G is the gravitational constant, c is the speed of light, and $T_{\mu\nu}$ is the stress-energy tensor which expresses the density and flux of energy and momentum in spacetime. The

metric tensor, $g_{\mu\nu}$, is used to describe the infinitesimal line element, ds, between two points in spacetime (x^μ and x^ν)

$$ds^2 = g_{\mu\nu} dx^\mu dx^\nu. \tag{1.2}$$

Using these components, a general metric, known as the Friedmann-Lemaître-Robertson-Walker (FLRW) metric (Friedmann, 1922; Lemaître, 1931; Robertson, 1935; Walker, 1937), can be written as

$$ds^2 = (cdt)^2 - a^2(t) \left[\frac{dr^2}{1 - kr^2} + S_k^2(d\theta^2 + \sin^2\theta d\phi^2) \right], \tag{1.3}$$

where

$$S_k(r) = \begin{cases} \frac{1}{\sqrt{k}} \sin \sqrt{k} r, & k > 0 \\ r, & k = 0 \\ \frac{1}{\sqrt{-k}} \sinh \sqrt{-k} r, & k < 0. \end{cases} \tag{1.4}$$

Here $a(t)$ is a time-varying scale factor describing the expansion of coordinates normalised to $a(0) = 1$ at the present day and k is a constant representing the global curvature of the Universe. When $k = 0$ represents flat curvature, $k > 0$ represents a closed curvature (i.e. spherical geometry), and $k < 0$ represents open curvature (i.e. hyperbolic geometry). The scale factor $a(t)$ is related to redshift z by

$$a(t) = \frac{1}{1 + z}. \tag{1.5}$$

The redshift of an object is a consequence of the expansion of the Universe. The wavelength of light (λ) emitted will stretch out with this expansion. This process is proportional to the scale factor and this stretching factor can be defined as

$$1 + z = \frac{\lambda_{\text{observed}}}{\lambda_{\text{emitted}}} = \frac{a_{\text{observed}}}{a_{\text{emitted}}}. \tag{1.6}$$

Using this metric the Einstein field equations can be solved, resulting in three main equations that can describe the evolution of the Universe: the acceleration equation, the fluid equation, and the Friedmann equation.

The acceleration equation describes the expansion of the Universe

$$\left(\frac{\ddot{a}}{a} \right)^2 = \frac{-4\pi}{3} G(\rho + 3p), \tag{1.7}$$

where G is the gravitational constant and ρ is the volumetric mass density, and p is pressure. Note that the acceleration of the Universe decreases with increasing pressure or energy density.

The fluid equation describes density conservation in an expanding (or contracting) Universe

$$\dot{\rho} + 3\frac{\dot{a}}{a}(\rho + p) = 0. \tag{1.8}$$

Solutions to this equation require an equation of state relating ρ and p. This equation of state will be unique to each component of the Universe. The known components are matter (dark matter and baryons), radiation, and the cosmological constant (which describes the energy density of the vacuum and its associated negative pressure). We can treat each of these components as a perfect fluid and write down an equation of state

$$p = w\rho, \tag{1.9}$$

where

$$\begin{cases} w = 0, & \text{for relativistic matter} \\ w = 1/3, & \text{for radiation} \\ w = -1, & \text{for example, a cosmological constant.} \end{cases} \tag{1.10}$$

w is known as the equation of state parameter. For a cosmological constant, the pressure is negatively proportional to density which acts to cause the expansion of the Universe. Each of these components can be substituted into the fluid equation (equation 1.8) to derive how each of these components evolves with the scale factor, giving

$$\begin{aligned} \rho_{\mathrm{m}} &\propto a^{-3}, \\ \rho_{\mathrm{r}} &\propto a^{-4}, \\ \rho_{\Lambda} &\propto a^{0}, \end{aligned} \tag{1.11}$$

for each of the known components. The subscript m is used for matter (sometimes b is used just to represent just baryonic matter), r is used for radiation, and Λ is used to represent a cosmological constant. The density evolution with the scale factor can also be written as

$$\rho_i \propto a^{-3(w_i+1)}, \tag{1.12}$$

where the subscript i refers to each component. The scale factor a will be 1 at the beginning of the Universe, move through a radiation-dominated era, to a matter-dominated era, and finally the present dark-energy-dominated era. A value of $a = 0$ denotes the present day.

The Friedmann equation describes how the expansion rate of the Universe is related to the energy density and curvature

$$\left(\frac{\dot{a}}{a}\right)^2 = \frac{8\pi}{3}G\rho - \frac{k}{a^2}. \tag{1.13}$$

To define the critical density, the density needed for a Universe with flat curvature, we set $k = 0$ (this assumes a flat Universe) and define the Hubble parameter $H \equiv \frac{\dot{a}}{a}$ to find

$$\rho_{\text{crit}} = \frac{3H(a)^2}{8\pi G}. \tag{1.14}$$

This critical density can be used to normalise each component of the density of the Universe as $\Omega_i = \rho_i/\rho_{\text{crit}}$. Similarly, an expression for the curvature of the Universe can be found as

$$\Omega_k = -\frac{k}{H_0^2}. \tag{1.15}$$

Substituting these back into equation 1.13 one finds

$$H^2(a) = H_0^2 \sum_i \Omega_{i,0}(a/a_0)^{-3(w_i+1)} + H_0^2\Omega_k(a/a_0)^{-2}, \tag{1.16}$$

which can be filled in as

$$H^2(a) = H_0^2(\Omega_{r,0}(a/a_0)^{-4} + \Omega_{m,0}(a/a_0)^{-3} + \Omega_{k,0}(a/a_0)^{-2} + \Omega_{\Lambda,0}), \tag{1.17}$$

where the subscript 0 denotes the values at the present day.

1.2.1 ΛCDM

The current best cosmological model is known as ΛCDM. This model has a spatially flat Universe (i.e. $\Omega_k = 0$) and a constant dark energy equation of state with $w = -1$ resulting in the expansion of the Universe and a majority of matter in the Universe to be in the form of dark matter. Current experiments aim to measure these parameters allowing the Universe to be described under an FLRW metric and test the ΛCDM cosmological model. Popular extensions to a ΛCDM cosmological model include non-spatial flatness ($\Omega_k \neq 0$), a dark energy equation of state with an equation of state parameter that differs from -1 ($w \neq -1$), as well as a time-varying dark energy equation of state ($w \equiv w(a)$). These popular models are explored in Chapter 5.

1.3 Geometry

Distances in cosmology can be defined in terms of the Friedmann equation shown in equation 1.17. We start with the Hubble distance $D_{\rm H}$, which is defined as

$$D_{\rm H}(z) \equiv \frac{c}{H(z)}, \tag{1.18}$$

this is the distance to an object along the line of sight. From this, we can define the comoving distance $D_{\rm C}$ which is the proper distance between two objects divided by the ratio of the scale factors of those objects

$$D_{\rm C}(z) \equiv \int_0^z D_{\rm H}(z')dz' = \int_0^z c/H(z')dz'. \tag{1.19}$$

This is a measure of the distance between two objects that is decoupled from the Hubble flow.

The comoving distance $D_{\rm C}$ can be used to calculate the transverse comoving distance $D_{\rm M}$. This distance will have a dependence on spatial curvature brought in through the S_k term of equation 1.3 and can be written as

$$D_{\rm M}(z) = S_k(r) = \begin{cases} D_{\rm H}(0)\frac{1}{\sqrt{|\Omega_{\rm k}|}}\sin\left(\sqrt{|\Omega_{\rm k}|}\frac{D_{\rm C}}{D_{\rm H}(0)}\right), & \Omega_{\rm k} < 0 \\ D_{\rm C}, & \Omega_{\rm k} = 0 \\ D_{\rm H}(0)\frac{1}{\sqrt{\Omega_{\rm k}}}\sinh\left(\sqrt{\Omega_{\rm k}}\frac{D_{\rm C}}{D_{\rm H}(0)}\right), & \Omega_{\rm k} > 0. \end{cases} \tag{1.20}$$

This is the distance between two objects across the line of sight. Note the n the spatial curvature of the Universe.

The angular diameter distance $D_{\rm A}$ is the ratio between an object's physical transverse size and the angular size of an object on the sky

$$D_{\rm A} = \frac{D_{\rm M}}{1+z}. \tag{1.21}$$

This is used to convert the angular separation between two objects as is measured to the actual separation.

Finally, the luminosity distance is defined as the ratio between the observed bolometric flux that is measured to the actual luminosity

$$D_{\rm L} = (1+z)D_{\rm M}, \tag{1.22}$$

and is used to measure the distance to objects of known luminosity. This is of particularly interesting1.6 where we detail standard candles such as Type Ia supernovae that are used to measure the distance to galaxies in the nearby Universe. Figure 1.1 describes how these distances evolve with redshift for one chosen cosmological model.

The expansion of the Universe can be used as a proxy for the distance to an object. As space expands objects are receding away from us, and the recessional velocity will increase as the distance increases. This is known as the Hubble flow and can be described by Hubble's law as

$$v = H_0 d, \tag{1.23}$$

where v is a galaxy's recessional velocity and d is the distance to said galaxy. A galaxy's redshift can be defined in terms of its recessional velocity as $zc = v$ which gives the distance redshift relation

$$d = \frac{zc}{H_0}. \tag{1.24}$$

1.4 Density Perturbations in the Universe

Previously in Section 1.2 a general framework for a homogeneous and isotropic Universe was introduced. We now introduce density perturbations in this framework. Density fields are used in cosmology to map the distribution of matter in space onto a continuous function. These fields come from observational data of discrete tracers, such as the location of galaxies mapped by spectroscopic surveys. A statistical analysis of these density fields allows for information to be found on the nature of dark matter, the behaviour of dark energy, and the evolution of the Universe. These fields form the basis of the field of large-scale structure.

Galaxy surveys observe a patch of the Universe that will have an angular mask on the sky along with a radial distribution. To correct for the sampling of galaxies in this patch varying with position studies of the density field rely on the density contrast $\delta(\mathbf{x})$

$$\delta(\vec{x}) \equiv \frac{\rho(\vec{x}) - \bar{\rho}}{\bar{\rho}}, \tag{1.25}$$

where $\rho(\vec{x})$ is the density at position $\vec{x}$ and $\bar{\rho}$ is the mean density. Galaxy surveys trace out the density field of galaxies $\delta_{\mathrm{g}}(\vec{x})$ which is used to approximate the density field of all matter $\delta_{\mathrm{m}}(\vec{x})$.

The galaxy distribution sampled will not match that of a Poisson sampling of the matter distribution (Bardeen et al., 1986). This can be seen by observing the clustering of galaxies

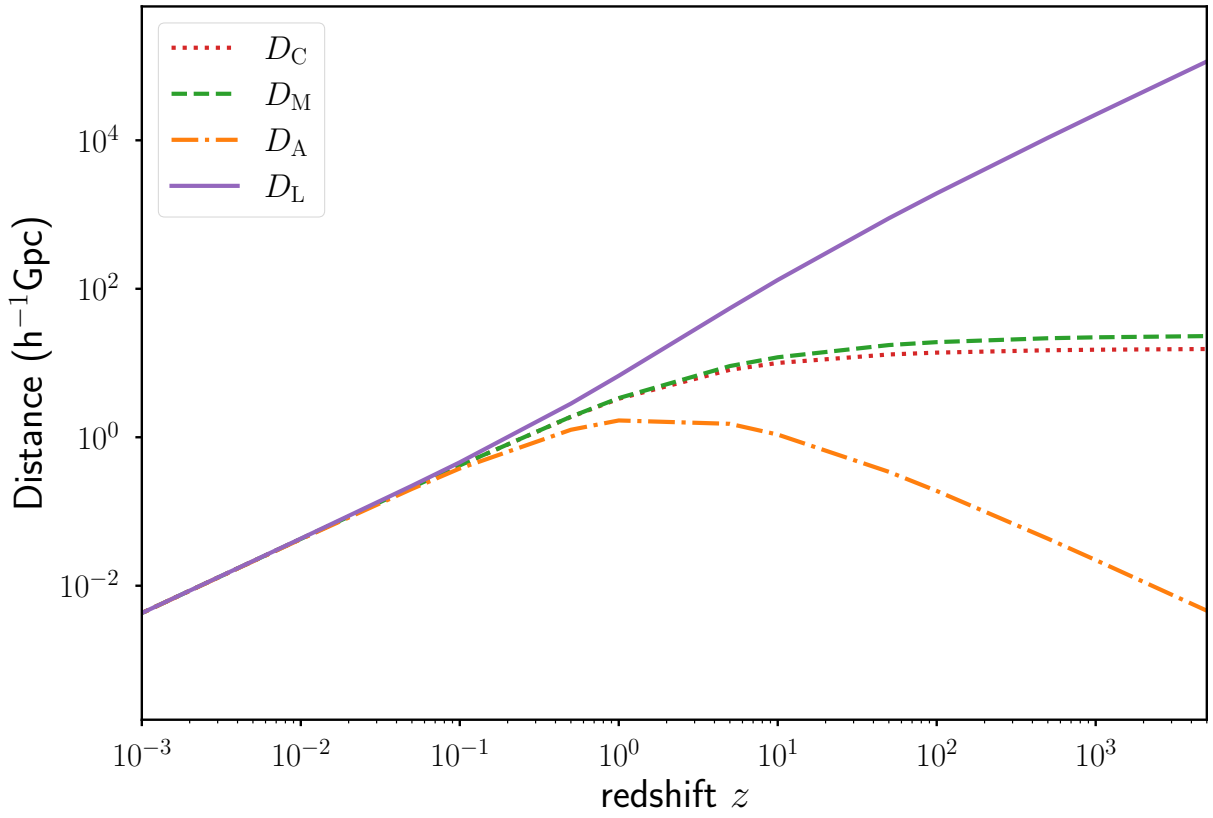

Figure 1.1: Various distances versus redshift including the co-moving distance $D_{\rm C}$, transverse comoving distance $D_{\rm M}$, angular diameter distance $D_{\rm A}$, and luminosity distance $D_{\rm L}$. Distances are calculated at the fiducial cosmology $\Omega_{\rm m} = 0.2$, $\Omega_\Lambda = 0.6$, $\Omega_{\rm r} = 0$, $w = -1$, and $H_0 = 70$. A non-flat cosmology ($\Omega_{\rm k} = 1 - \Omega_{\rm m} - \Omega_\Lambda - \Omega_{\rm r} = 0.1 > 0$, i.e. an open Universe) is used to highlight the differences between $D_{\rm m}$ and $D_{\rm c}$.

using different cuts made to sample the galaxy population (ex. luminosity, colour, mass). The clustering of these samples will differ, so they cannot all be a Poisson sampling of the matter distribution. Instead, it is assumed that the galaxy density field is a function of the matter density field and can be written in an expanded basis for a local, non-deterministic model as

$$\delta_g(\vec{x}) = \sum_{i=1}^{\infty} \frac{b_i}{i!} \delta_m^i(\vec{x}), \tag{1.26}$$

where b_i are the galaxy bias parameters. If the matter density is small ($\delta_{\rm m} \ll 1$) then this can be approximated as

$$\delta_g(\vec{x}) = b\delta_m(\vec{x}), \tag{1.27}$$

where the bias parameter is now just one constant b. This is known as the linear bias parameter.

1.4.1 Two-point Correlation Function and Power Spectrum

The density contrast $\delta(\vec{x})$ has a distribution close to that of Gaussian, adiabatic perturbations both in early times and on large scales at the present day (Planck Collaboration et al., 2020). It is well approximated as a Gaussian random field. This is due to inflation where quantum fluctuations in the very early Universe became magnified to cosmic size (Guth, 1981). A Gaussian random field can be assumed to be the sum of a large number of spherical waves with a uniformly distributed random phase. The central limit theorem dictates that at any point the sum of wave contributions will exhibit a Gaussian distribution. This Gaussian random field can be entirely described through its power spectrum and, therefore, by its two-point autocorrelation function (i.e. the distribution can be entirely described by 2-point statistics) (Abrahamsen, 1997).

The two-point correlation function, ξ, is commonly used to measure the clustering in a galaxy density field. This function measured the probability of finding two galaxies that are separated by distance $\vec{r}_{12} = \vec{r}_1 - \vec{r}_2$. It is defined by

$$\delta P = \bar{n}^2 \delta V_1 \delta V_2 (1 + \xi(\vec{r}_{12})), \tag{1.28}$$

where δP is the probability of finding two such galaxies, $\bar{n}$ is the average density, and δV_i is the infinitesimally small volume represented by position $\vec{r}_i$. The two-point correlation function can also be written as

$$\xi(\vec{r}') = \langle \delta(\vec{r} + \vec{r}')\delta(\vec{r}) \rangle, \tag{1.29}$$

where $\vec{r}'$ denotes the separation between two galaxies. When $\xi(\vec{r}') = 0$ there is no clustering (i.e. a random distribution), when $\xi(\vec{r}') > 0$ there is clustering (ie. an overdensity), and when $\xi(\vec{r}') < 0$ there is anti-clustering (i.e. an underdensity). Under the assumption of isotropy and statistical homogeneity, the correlation function depends only on the separation between points, i.e. $\xi(\vec{r}') = \xi(r)$.

The power spectrum, $P(k)$, is the Fourier transform of the two-point correlation function defined as

$$P(k) = \int \xi(r) e^{i\vec{k}\vec{r}} d^3r, \tag{1.30}$$

where k is a wave number that describes the number of oscillations of the matter density field within a given length scale in units of inverse length. A high k represents small scales and a low k represents large scales. The power spectrum can be interpreted as the variance in the amplitude distribution of functions on the given scale k. A small value of the power spectrum means that there are few over/under densities on this scale (i.e. the distribution is smooth) and a large value means that there are many prominent over/under dense regions. The correlation function and power spectrum are a Fourier pair where the correlation function can be found from the power spectrum as

$$\xi(r) = \frac{1}{(2\pi)^3} \int P(k) e^{i\vec{k}\vec{r}} d^3k. \tag{1.31}$$

In principle, both the power spectrum and the correlation function provide the same information making the choice on which to use somewhat arbitrary (Hamilton, 2005). In practice, the information contained in the power spectrum/correlation function is moved to different scales that may be easier to extract using one method over the other.

In addition to two-point clustering, higher orders can be measured (ex. three-point, four-point, etc.). These n-point clustering measures represent the excess probability of finding n points at a given separation compared to that from a random distribution. Higher order clustering provides information on the non-Gaussianity of the matter distribution, which happens when the distribution of points is not purely Gaussian and instead has a preferred direction or shape.

1.4.2 Multipole Decomposition

While the Universe is expected to be statistically isotropic and homogeneous, anisotropies can be introduced via observational effects discussed later in Section 1.5. These anisotropies are expected to be symmetric about the line of sight and can be written, to first order, as

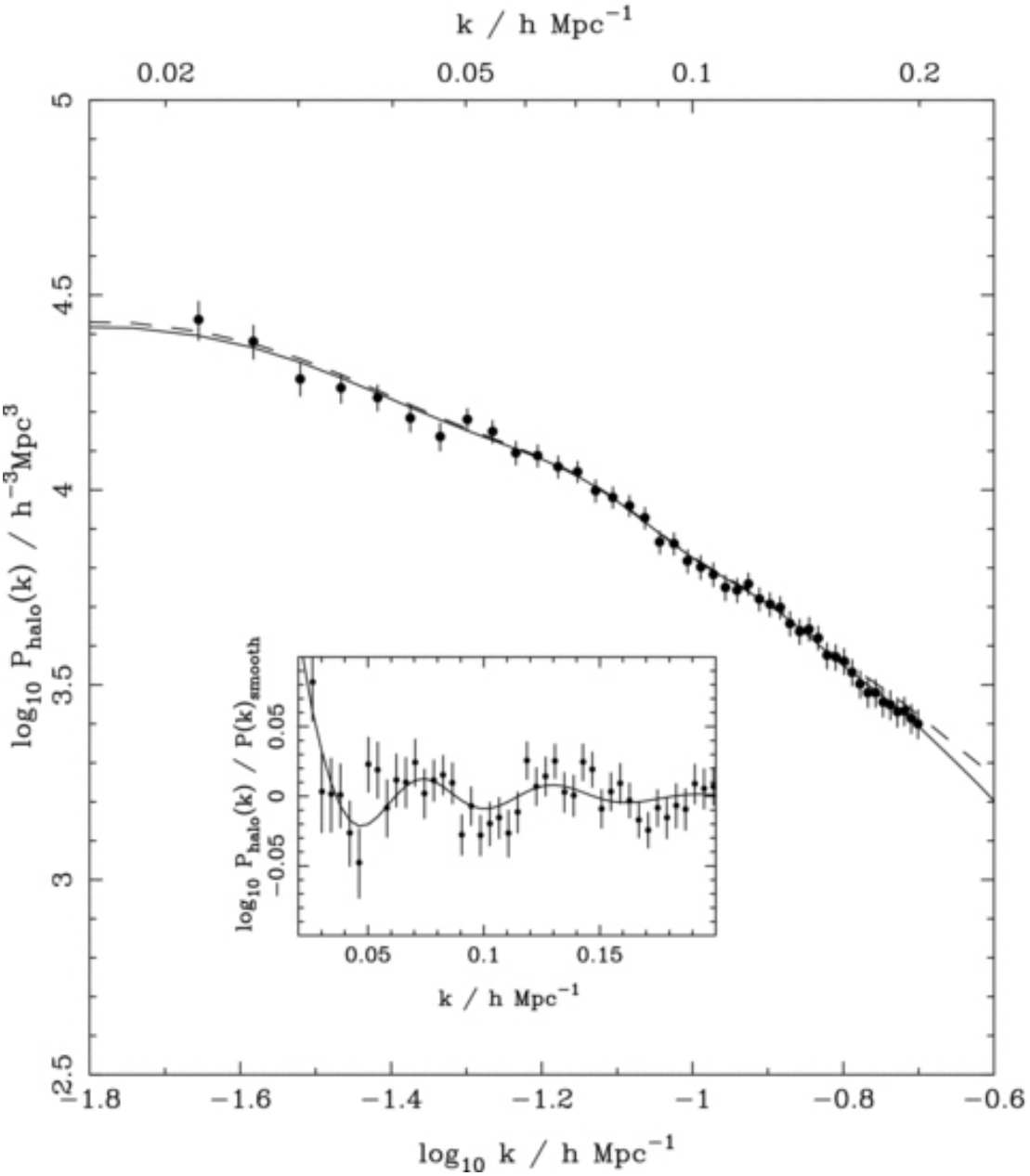

Figure 1.2: The galaxy power spectrum from SDSS DR7 data (see Chapter 3). The points with associated error bars show the measured power in the data while the models are shown as the solid and dashed lines. The inset shows the same data and model divided by a spline fit to a smooth component without wiggles. Image Credit: (Reid et al., 2010)

functions of the square of the cosine of the angle to the line of sight μ^2. Because of this the correlation function and power spectrum are typically written as $\xi(r,\mu)$ and $P(k,\mu)$ and are decomposed into Legendre polynomials to give multipole moments

$$\xi_\ell(r) = (2\ell+1)\int_0^1 \xi(r,\mu)\mathcal{L}_\ell(\mu)d\mu, \tag{1.32}$$

$$P_\ell(k) = (2\ell+1)\int_0^1 P(k,\mu)\mathcal{L}_\ell(\mu)d\mu, \tag{1.33}$$

along with their inverses

$$\xi(r,mu) = \sum_\ell \xi_\ell(r)\mathcal{L}_\ell(\mu), \tag{1.34}$$

$$P(k,\mu) = \sum_\ell P_\ell(k)\mathcal{L}_\ell(\mu). \tag{1.35}$$

$\mathcal{L}_\ell$ are the Legendre polynomials where the first three even polynomials are

$$\mathcal{L}_0(\mu) = 1, \tag{1.36}$$

$$\mathcal{L}_2(\mu) = \frac{1}{2}(3\mu^2-1), \tag{1.37}$$

$$\mathcal{L}_4(\mu) = \frac{1}{8}(35\mu^4-30\mu^2+4). \tag{1.38}$$

1.5 Observational Effects Breaking Statistical Isotrophy

For a galaxy survey, we measure the positions using angles and redshifts and the resultant measurements are known as being in redshift space. The conversion of these redshifts to distances assumes a Universe that is homogeneous and statistically isotropic so that the velocity of galaxies is solely due to their recessional velocity and not from any other peculiar velocity. Redshift space will become distorted from real space by two main processes that lead to a dilation of clustering caused by the distance-redshift relationship applied to convert redshifts into comoving distances: redshift space distortions (RSDs) and the Alcock-Paczynski (AP) effect.

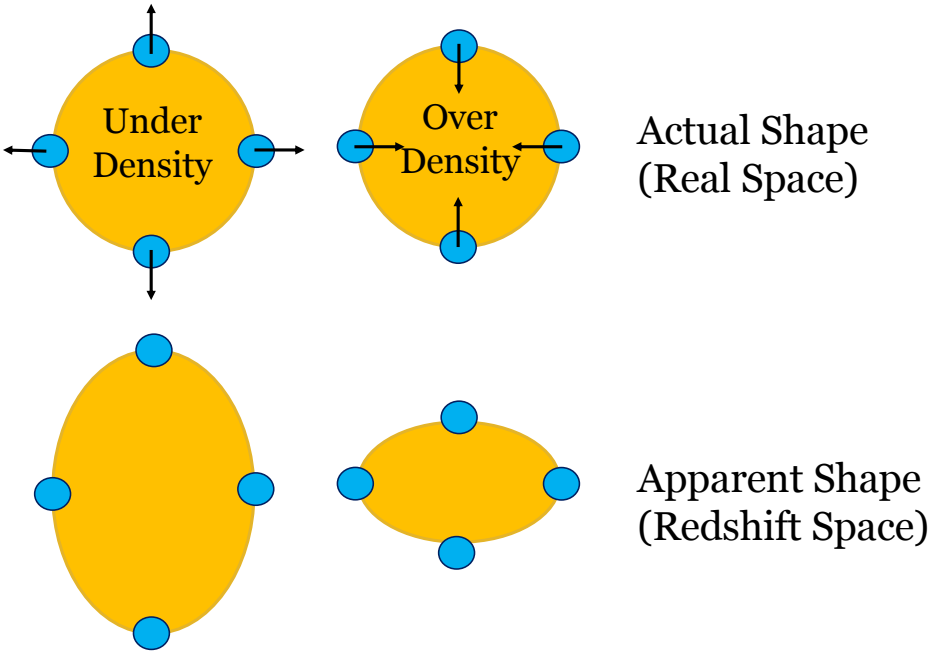

Figure 1.3: The effect of redshift space distortions on overdensities (right) and underdensities (left). The top row shows the actual shape of the structure in real space, where arrows indicate the velocity of each object. The bottom row shows the apparent shape in redshift space.

1.5.1 Redshift Space Distortions

The local environment around galaxies causes additional velocity, not from the Hubble flow, due to the gravitational effect from these surroundings. These are called peculiar velocities. Any component of this velocity along the line of sight will be added onto the recessional velocity due to the expansion of the Universe when redshifts are converted to distances using equation 1.24, Figure 1.3 shows a simplified illustration of this. This causes a distortion of the measured distance to an object. This is a scale-dependent effect on the measured density distribution of objects. This peculiar velocity is linked to the growth rate of structure, the rate at which the density fluctuations in the cosmic matter distribution grow over time due to gravitational attraction between matter. Redshift space distortions can therefore be used as a measure of this growth rate.

The position of an object in redshift space $\vec{s}$ is related to its real space position $\vec{r}$ by the peculiar velocity along the line of sight $\vec{v}$ by

$$\vec{s} = \vec{r} + (\vec{v} \cdot \hat{\vec{r}})\hat{\vec{r}}. \tag{1.39}$$

The real space position is typically decomposed into components parallel to the line of sight, $r_\parallel$, and perpendicular to the line of sight, $r_\perp$. The redshift space equivalents to these are σ that is equivalent to $r_\parallel$ and π is the redshift space equivalent to $r_\perp$. Combining equation 1.39 with the expected recessional velocity from the Hubble flow one finds

$$\sigma = r_\perp, \tag{1.40}$$

and

$$\pi = r_\parallel + \frac{1+z}{H(z)} v_\parallel, \tag{1.41}$$

where only the line of sight component π has changed. In this case, σ and π are in comoving coordinates and $\mu \equiv \pi/\sqrt{\sigma^2 + \pi^2}$.

The relationship between real and redshift space coordinates can be expressed as

$$d^3s = \left(1 + \frac{du}{dr}\right) d^3r, \tag{1.42}$$

where $u = \vec{v} \cdot \vec{r}$ and the Jacobian $J = (1 + du/dr)$, which can be written as

$$J = \left(1 + \frac{du}{dr}\right) = \left(1 + \frac{1}{H(z)} \frac{dv_\parallel}{dr_\parallel}\right)^{-1} \approx \left(1 - \frac{1}{H(z)} \frac{dv_\parallel}{dr_\parallel}\right). \tag{1.43}$$

The total amount of matter in a given volume element is conserved in the mapping from real to redshift space

$$(1 + \delta_m(\vec{s}))d^3s = (1 + \delta_m(\vec{r}))d^3r, \tag{1.44}$$

where δ_m is the mass density contrast. Applying the Jacobian from equation 1.43

$$(1 + \delta_m(\vec{s})) = (1 + \delta_m(\vec{r}))\left(1 - \frac{1}{H(z)}\frac{dv_\parallel}{dr_\parallel}\right). \tag{1.45}$$

Expanding this and keeping the linear terms one finds

$$\delta_m(\vec{s}) = \delta_m(\vec{r}) - \frac{1}{H(z)}\frac{dv_\parallel}{dr_\parallel}, \tag{1.46}$$

to which a Fourier transform can be applied to find

$$\delta_m(\vec{s}) = \delta_m(r)(1 + f(z)\mu_k^2), \tag{1.47}$$

where $\mu_k = k_\parallel/k$ is the cosine of the angle between the line of sight and $\vec{k}$ and $f(z)$ is known as the growth rate factor.

The growth rate factor describes the growth of linear perturbations; it is defined as

$$f \equiv \frac{d\ln\delta}{d\ln a}. \tag{1.48}$$

Within an FLRW metric the growth can be approximated by the equation

$$f(z) = \Omega_{\rm m}^{\gamma}, \tag{1.49}$$

where γ is usually treated as a constant $\gamma = 0.55$; however, in reality has a weak dependence on other parameters such as the equation of state of dark energy. Many cosmological measurements, including those made later in this thesis, describe the growth rate of structure in the Universe as $f(z)\sigma_8(z)$ where $\sigma_8(z)$ is the amplitude of density fluctuations normalised using the standard deviation of density fluctuations in a sphere of $8h^{-1}$Mpc.

We can use equation 1.27 that relates the matter and galaxy density field and insert this into equation 1.47

$$\delta_m(\vec{s}) = \delta_m(r)(1 + \beta(z)\mu_k^2), \tag{1.50}$$

where $\beta = f/b$. From Section 1.4.1 the power spectrum is known to be related to overdensities by $P(k) \propto \langle\delta^2\rangle$ which gives the anisotropic galaxy power spectrum $P_{gg}(k,\mu)$ as

$$P^s_{gg}(k,\mu) = (1 + \beta(z)\mu_k^2)^2 P_{gg}(k), \tag{1.51}$$

where $P^s_{gg}(k,\mu)$ is in redshift space and $P_{gg}(k)$ is in real space.

1.5.2 Alcock-Paczynski Effect

In galaxy surveys the position of each object is observed in redshift space (and angular coordinates right ascension and declination). In subsequent analyses of the data these are converted to comoving cartesian coordinates, however, this transformation requires an assumption of the fiducial cosmology (as was shown in Section 1.3). Geometrical constraints are provided by the dilation of clustering caused by the distance-redshift relationship applied to convert redshifts into comoving distances. Along the line of sight, provided that the clustering is measured on scales that are small compared to those over which cosmological evolution occurs, the clustering is sensitive to $D_{\rm H}$ shown in equation 1.18. Across the line-of-sight, we are sensitive to the comoving angular diameter distance $D_{\rm M}(z)$ shown in equation 1.20.

Knowing that clustering in galaxy surveys is isotropic, we will only recover this in our comoving maps if the correct cosmology is used in converting redshifts to distances. Alcock and Paczynski (1979) devised a test in which adjusting the cosmological model can be used to constrain the parameter combination

$$F_{AP} = \frac{(1+z)}{c} D_{\rm A}(z) H(z). \tag{1.52}$$

Equivalently many analyses constrain the parameter combination $D_{\rm M}(z)/D_{\rm H}(z)$. Separate measurements of $D_{\rm H}(z)$ and $D_{\rm M}(z)$ can be made if we have a standard ruler whose intrinsic length we know or that depends on other cosmological parameters, such as the BAO scale. Whereas to measure the dimensionless ratio $D_{\rm M}(z)/D_{\rm H}(z)$ we only need an object - such as a stack of voids - that we can use as a standard shape, knowing that it is expected to be spherical but not knowing its intrinsic size (called the AP effect).

1.6 Observational Cosmology

The last few decades of cosmology have seen the rise of a variety of independent probes of the Universe. These observations each give unique constraints on various parameters and parameter combinations that are powerful tests of the current best cosmological models. Recent years have seen the rise of concordance cosmology combining information from different cosmological processes to provide tighter constraints and break degeneracies. In this section we will summarise the major types of observations in cosmology: the cosmic microwave background, baryonic acoustic oscillations, galaxy peculiar velocities, distance ladder measurements (ex. type Ia supernovae), gravitational lensing, and Big Bang nucleosynthesis.

1.6.1 Cosmic Microwave Background

The cosmic microwave background (CMB) is the remnant of the first light that could freely travel in the universe, dating back to recombination. Prior to recombination photons were tightly coupled to electrons and protons in what is called a baryon-photon fluid (Dodelson, 2003). As the Universe expanded this fluid cooled to the point where protons and electrons could combine to form neutral atoms such as hydrogen. This process caused the emission of additional photons. The neutral particles that formed were transparent to light causing photons to become decoupled from matter, in a process aptly known as decoupling. Photons from decoupling travelled freely through the universe without interacting with matter and are observed today as the cosmic microwave background (CMB) (Peebles, 1968). These photons expanded with the continued expansion of the Universe, becoming stretched to longer and longer wavelengths. The spectrum from CMB photons we observe today closely matches that of a blackbody spectrum with a temperature of 2.725K. At the time of last scattering the Universe was at a temperature of approximately 3000K and CMB photons have been redshifted by a factor of 1100 to the currently observed temperature (Planck Collaboration et al., 2020). Related to this process is the surface of last scattering which is defined as where the CMB photons were scattered for the last time before being observed in present-day detectors. All of recombination, decoupling, and the last scattering surface occur at similar redshifts (around $z = 1100$) however recombination is determined by the ionization fraction of the Universe, decoupling is defined by the rate of photon scatter, and the last scattering surface depends on the optical depth of fluid in the early Universe.

Very small anisotropies exist in this spectrum of the order of just 18μK that encode a wealth of cosmological information (Wright et al., 1994). The structure of these anisotropies is determined by matter and photon interactions that occur up to the point of decoupling. The distribution of anisotropies in the CMB in terms of their angular scale can be shown in the power spectrum of the CMB radiation temperature shown in Figure 1.4. This characteristic bumpy pattern of peaks and troughs of varying heights allows for the extraction of cosmological information (Jones and Lasenby, 1998). Anisotropies are classified into two main groups: primary anisotropies that occur at or before the photon decoupling, and secondary anisotropies that occur from effects between photon decoupling and the light reaching an observer. Primary anisotropies are from acoustic oscillations of the photon baryon fluid and Silk damping (the dissipation of small-scale perturbations that is caused by photons random walking out of overdense regions). Secondary anisotropies can be divided into two broad categories: gravitational effects from metric distortions (ex. early and late Integrated Sachs-Wolfe effects, see White and Hu 1997), and rescattering effects from reionization (ex. the thermal Sunyaev–Zeldovich effect, see Sunyaev 1974).

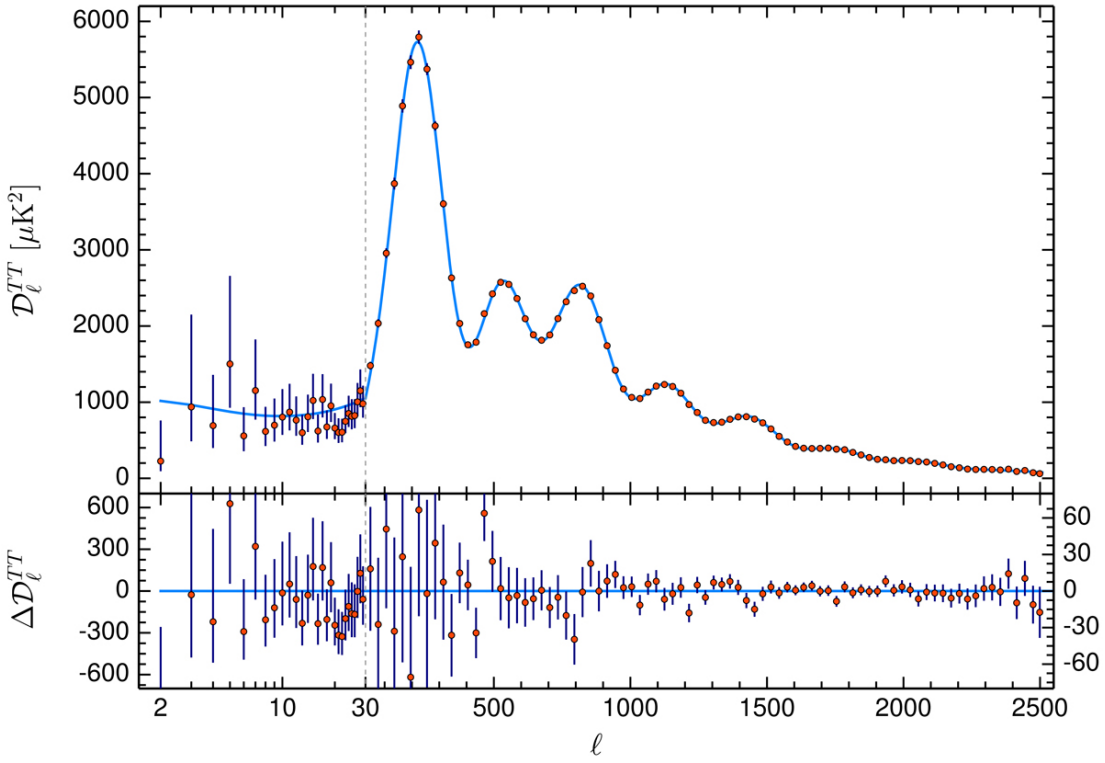

Figure 1.4: The power spectrum of the cosmic microwave background radiation temperature anisotropy in terms of the angular scale from Planck Collaboration et al. (2020) data. The solid line shows the best-fit model assuming a ΛCDM cosmology. Residuals with respect to this model are shown in the bottom panel. Image Credit: (Planck Collaboration et al., 2020).

The best current measurements of the CMB power spectrum come from Planck Collaboration et al. (2020) (as shown in Figure 1.4). Tight constraints of $\Omega_c h^2 = 0.120 \pm 0.001$ and $\Omega_b h^2 = 0.0224 \pm 0.0001$ are found. If a ΛCDM model is assumed then additional constraints of $H_0 = 67.4 \pm 0.5$ km/s/Mpc, $\Omega_m = 0.315 \pm 0.007$, and $\sigma_8 = 0.811 \pm 0.006$ are found.

1.6.2 Large-Scale Stucture

Galaxy spectroscopic surveys have seen a resurgence due to the emergence of multi-object spectrographs on ground-based telescopes (ex. 2dFGRS Colless et al. 2003 and SDSS York et al. 2000). These surveys have traditionally relied on two physical processes in order to extract information, BAO and RSD. This subsection will briefly present how information is extracted from these two techniques. The emergence of voids as a method of extracting additional, complementary information is discussed in more detail in Chapter 2 as well as later in this thesis.

Baryonic Accoustic Oscillations

Baryon acoustic oscillations (BAO) are fluctuations in the density of baryons in the Universe caused by acoustic density waves in the baryon-photon fluid in the early Universe. Overdensities in this fluid attracted matter to it gravitationally while heat from photon-matter interactions produced outward pressure. These opposing forces created oscillations analogous to sound waves in air caused by differences in pressure. These spherical 'sound' waves caused photons and baryons to travel outwards from overdensities until decoupling. The uncoupled photons were then able to freely stream away, as they were no longer interacting with the baryons. This removed the outward pressure from photon-matter interactions. Shells of baryonic matter that had travelled outward from overdensities were left behind. The radius of this shell is called the sound horizon (r_s).

This process occurs at high redshifts but effects from this can be measured in the present day. As structure collapsed and formed later into the life of the Universe these overdense regions formed dark matter halos and galaxies formed at the centre of these halos (Mo and White, 1996). The shells of baryons left behind from BAO caused slightly more overdense regions where galaxies were more likely to form. This can be seen in Figure 1.5, where the clustering of galaxies is measured using the correlation function (see Section 1.4) as a function of the separation distance. The correlation function displays the characteristic bump due to BAO indicating the excess probability of finding galaxies.

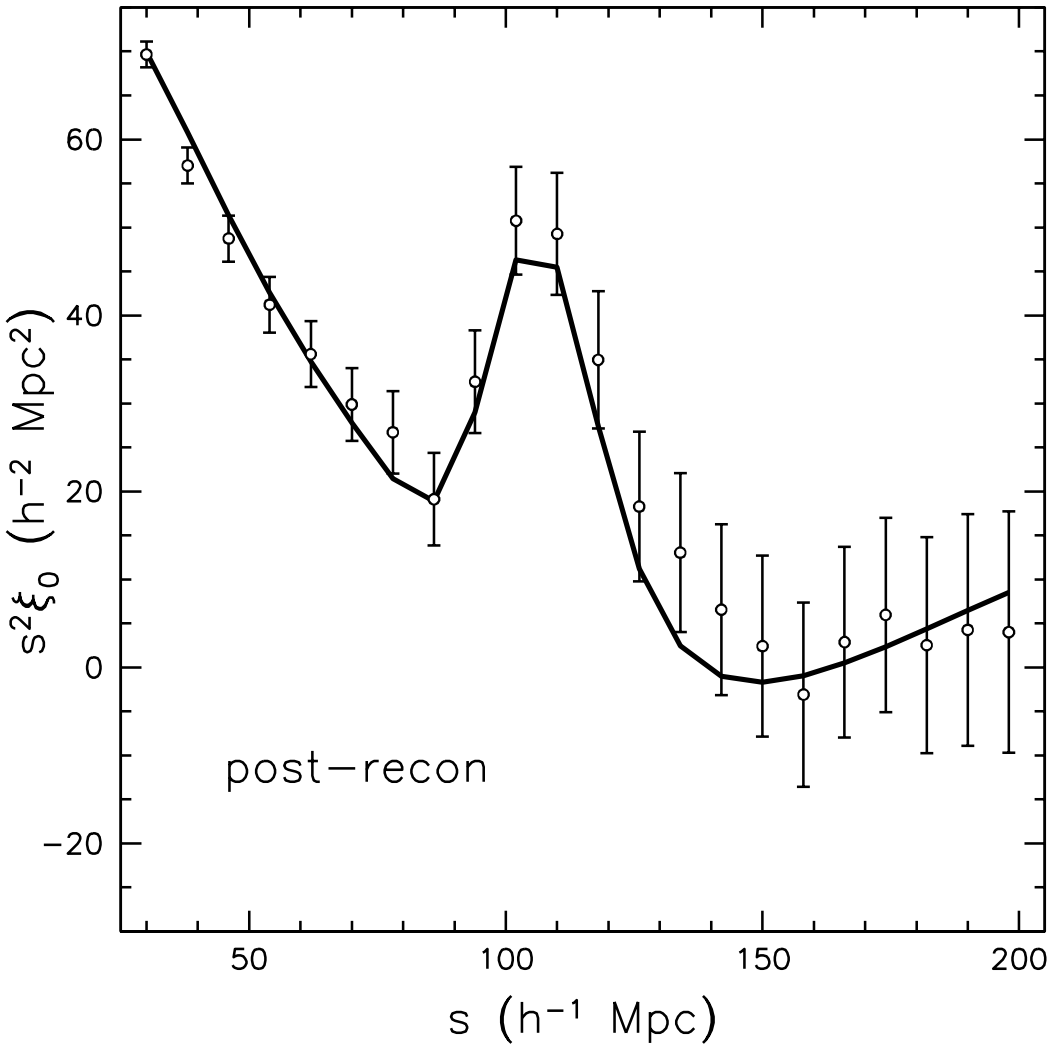

Figure 1.5: The correlation function (i.e. clustering) of galaxies found in the BOSS CMASS DR11 survey. The bump at $\sim$ 110 h^{-}1Mpc shows the BAO feature that is measured in galaxy surveys. The y-axis has been multiplied by s^2 in order to better highlight this feature. Image Credit: (Anderson et al., 2014).

This radius provides a "standard ruler" of known length that allows for cosmological information to be extracted. The sound horizon can be determined as

$$r_s = \int_z^\infty \frac{dt}{H(z)} c_s(t), \tag{1.53}$$

where z is the redshift of decoupling, $c_s(t)$ is the sound speed, and $H(z)$ parameterise the expansion of the Universe. The dependence of parameters on z is small enough that it can be neglected (Knox and Millea, 2020). To determine r_s, $c_s(z)$ and $H(z)$ are needed. The sound speed depends on the baryon density and the radiation density, where the radiation density is determined by the temperature of the CMB (Wright et al., 1994). To determine $H(z)$ (explained in more detail in Section 1.2) the mean densities of matter, radiation, and dark energy are needed, this information is usually either taken from the CMB, or the density of matter can be calculated using the Alcock-Paczynski effect on BAO (explained in Section 1.5.2) as well as with BBN (explained in Section 1.6.5).

Redshift Space Distortions

Galaxy peculiar velocities (and redshift space distortions caused by these) are another method of extracting information from galaxy redshift surveys like with BAO. Peculiar velocities are the motion of galaxies with respect to the comoving background caused by local gravitational interaction with nearby structures. Redshift space distortions are the Doppler effect of a galaxy's peculiar velocity on the measured redshift where the addition of the peculiar velocity will cause a Doppler shift in the measured redshift that is additional to that from cosmic expansion. Useful information can be extracted from these effects. Measurements accounting for these allow for a determination of structure growth (Percival and White, 2009), an important test of non-standard cosmological models, and the behaviour of gravity on large scales (Raccanelli et al., 2013). More detail on peculiar velocities, RSDs, and the constraints that can be calculated using these is explained in Section 1.5.1.

Recent Measurements

The best current measurements of large-scale structure are from the Baryon Oscillation Spectroscopic Survey (BOSS; Dawson et al., 2013) of SDSS-III (Eisenstein et al., 2011), and the extended BOSS (eBOSS; Dawson et al., 2016) of SDSS-IV (Blanton et al., 2017). Final results from these methods will provide constraints on the parameters $f\sigma_8$, $D_\mathrm{M}/r_\mathrm{d}$, and $D_\mathrm{H}/r_\mathrm{d}$ and are summarised in Table 5.1. The parameter r_d is the comoving sound horizon at the baryon drag epoch.

1.6.3 Distance Ladder Measurements

Distance ladder measurements provide useful cosmological information through a direct calibration of the distance-redshift relation (see Section 1.5). To do so they rely on standard candles (objects of known luminosity). If the luminosity of an object is known its brightness on the sky can be measured and used to determine how far away that object is. The most useful standard candles are Type Ia supernovae, which are powerful explosions caused when one star in a binary system is a white dwarf (the end point of a low-mass main sequence star). The white dwarf accretes matter from its partner star until it hits the Chandrasekhar limit (at $\sim 1.4 M_{\odot}$) and the electron degeneracy pressure supporting the star in equilibrium can no longer oppose gravity. At this point, the white dwarf collapses and explodes into a supernova. Due to the narrow mass range of the white dwarf star when this explosion happens, the peak luminosity of this event is well determined. This incredibly bright explosion can be seen at very far distances into the Universe allowing for distances for faraway galaxies to be determined. The redshifts of these galaxies can also be measured allowing the expansion rate of the Universe at the present day, H_0 to be directly measured (see equation 1.24).

In order for this to be determined, the luminosity of supernovae must first be calibrated. This is done using Cepheid stars. Cepheid stars are variable stars that pulse in a predictable way. The period of pulsation is directly related to the luminosity of the star. Distances to nearby Cepheids can be found using stellar parallax measurements and used to calibrate the period-luminosity relation (being careful to determine if this is a Type I or Type II Cepheid as these two populations have different period-luminosity relations). Once this has been calibrated on local Cepheids, the distances to nearby galaxies where these stars have been identified can be determined using the known luminosity of the Cepheids and measuring their flux.

Cepheids can be used as a standard candle in nearby galaxies. To measure distances to further away galaxies Type Ia supernovae are used. Type Ia supernovae are identified in nearby galaxies where Cepheid stars are also present. The distance to these galaxies is determined via the Cepheids and the brightness curves of the Type Ia supernovae can be calibrated so that their luminosity is determined. Figure 1.6 shows Edwin Hubble's first measurement of H_0 using a cosmic distance ladder. While this measurement later showed to be inaccurate, there are more recent measurements that use this same technique to make accurate measurements of the Hubble constant.

It was the use of Type Ia supernovae that led to the discovery of the accelerated expansion of the Universe (i.e. dark energy) in the late 1990s (Perlmutter et al., 1999; Riess et al., 1998). The best current constraints from Type Ia supernovae come from Pantheon

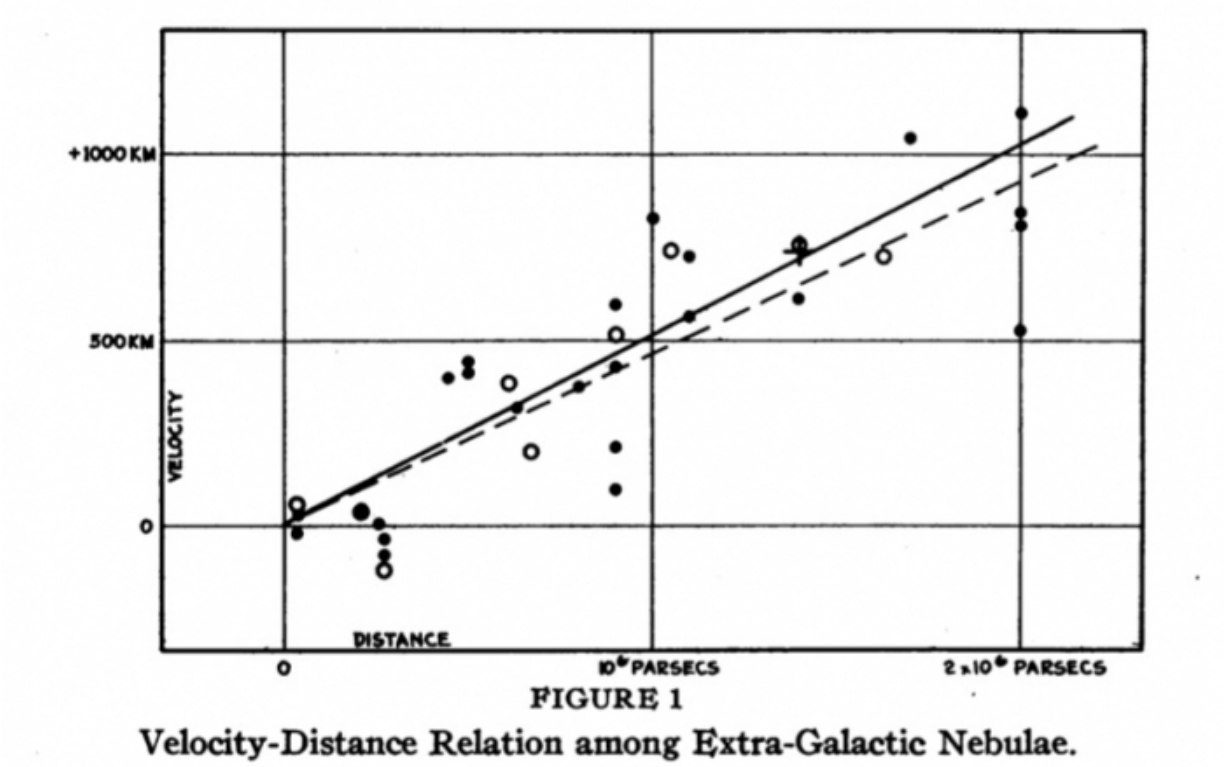

FIGURE 1

Velocity-Distance Relation among Extra-Galactic Nebulae.

Figure 1.6: Edwin Hubble's original plot of the velocity-distance relation for galaxies (Hubble, 1929)

Plus (Scolnic et al., 2022). Measurements are taken from 1550 confirmed supernovae. Assuming a flat ΛCDM cosmology constraints of $\Omega_{\rm m} = 0.334 \pm 0.018$ and $H_0 = 73.6 \pm 1.1$ are found (Brout et al., 2022).

1.6.4 Gravitational Lensing

One of the key predictions of General Relativity is that matter distorts spacetime around its local vicinity. As light passes through this distorted spacetime it too becomes distorted. These effects can be seen in two ways by an observer: strong gravitation lensing and weak gravitational lensing.

In strong gravitational lensing light rays pass in close proximity to a very large lensing mass and the bend angle of the light becomes significant. This magnifies the light, can cause multiple images of the background emitting light source to be seen by an observer, and distorts the background source in an arc shape. As it requires a very high mass in the foreground this is a relatively rare phenomenon.

Weak gravitational lensing is the subtle distortion of background galaxies by the gravitational influence of foreground matter. For weak lensing, this is a much smaller effect requiring large statistical samples to measure. The lensing distortion of background light sources provides an integrated determination of the underlying matter distribution. Weak lensing is typically measured through the shear power spectrum and is used to probe the mass density of the Universe $\Omega_{\rm m}$, the amplitude of matter density fluctuations on scales of $8h^{-1}$ Mpc called σ_8, and the dark energy equation of state parameter w. Due to this being an integrated measurement, there are degeneracies between these parameters and results are usually reported at $S_8 \equiv \sigma_8 \sqrt{\Omega_{\rm m}/0.3}$, $\Omega_{\rm m}$, and w.

The best current weak lensing constraints come from the Dark Energy Survey (DES) year 3 results which find $S_8 = 0.775^{+0.026}_{-0.024}$, $\Omega_{\rm m} = 0.352^{+0.035}_{-0.041}$, and $w = -0.98^{+0.32}_{-0.20}$ for a wCDM cosmological model (Abbott et al., 2022).

1.6.5 BBN

Big Bang nucleosynthesis (BBN) is the production of nuclei other than hydrogen-1 (i.e. a single proton) in the early Universe. At early times, neutrons and protons were interconverting to form deuteron (i.e. a heavy hydrogen nuclei containing a proton and neutron) but the temperature in the Universe is hot enough that the average photon energy is able to photodissociate the deuteron before heavier elements can be built. These conditions

persist until the Universe is a few minutes old and the temperature drops sufficiently (i.e. below 80 keV) so that there are too few photons energetic enough to photodissociate the deuterons (Peebles, 1966).

At this point, protons and neutrons are able to combine to form deuteron, hydrogen-3 (1 proton and 2 neutrons), helium-3 (2 protons and 1 neutron), and helium-4 (2 protons and 2 neutrons). The production of higher-mass elements is limited past these elements due to the lack of stable nuclei of mass-5 (ex. 3 protons and 2 neutrons). In order to form heavier elements helium-4 must collide with either deuteron, hydrogen-3, or helium-3. As all of these nuclei are positively charged the Coulomb repulsion suppresses the reaction rate and severely limits the number of heavy nuclei that form. Mass-8 nuclei are also unstable which ensures the few nuclei that are able to overcome the mass-5 gap are very unlikely to form even heavier elements (Steigman, 2004).

Primordial nucleosynthesis is a short-lived process. Nuclear reactions to form heavier elements required energies that are higher than the Coulomb barriers for these particles. This caused nucleosynthesis to abruptly stop when the temperature drops below approximately 30 keV. This occurs approximately 20 minutes into the life of the Universe. All together BBN lasts just 1000 seconds. BBN predicts that approximately 75% of the mass in the Universe consists of hydrogen, 25% the mass of the Universe consists of Helium, 0.01% is deuterium and even smaller quantities of lithium are made (Malaney and Mathews, 1993).

The prediction of these exact abundances depends on the density of baryons at the time of nucleosynthesis ($\Omega_{\rm b}h^2$). This can be measured using the absorption signal of distant quasars to measure these abundances in the early Universe. The best current measurements of BBN come from Cooke et al. (2016) who measure $\Omega_{\rm b}h^2 = 0.02156 \pm 0.0002$.

1.7 Tensions

Recent advances in the precision of cosmological measurements have greatly increased our understanding of the Universe however, have also revealed tensions between different independent observational probes. There are a number of possible explanations: statistical fluctuations, unaccounted-for systematic errors, or unknown physics not incorporated into the ΛCDM model. Probes of greater precision are needed to verify that these measurements are not due to statistical fluctuations and developing more independent observational probes will allow for unaccounted-for systematic errors to be ruled out. The discovery of new physics beyond ΛCDM will remain a critical area that inspires the next generation of experiments designed to improve our understanding of the Universe.

1.7.1 Hubble Tension

The Hubble tension is the subject of much current work by cosmologists. It refers to the discrepancy by observations of the Hubble constant that describes the expansion rate of the Universe at the present day. Several independent methods exist to measure this fundamental parameter, the two most commonly referred to methods are the indirect measurement of this parameter via the CMB, and the direct measurement via supernovae. The indirect CMB measurement relies on the physics of the early Universe (i.e. high redshift) and measures a lower value of the Hubble constant. Measurements from BAO that use low redshift measurements of early Universe physics support this low measured value (with the caveat that these are not independent measures). The direct supernovae measurement is made in the late Universe (i.e. low redshift) and is supported by other late Universe measurements such as the tip of the red giant branch stars (tRGB) which are an alternative Cepheids in distance ladder measurements (see Section 1.6.3). This tension has only been growing in recent years and current best measurements put it at around a $\gtrsim 4\sigma$ discrepancy (Planck Collaboration et al., 2020; Riess et al., 2021), making it highly unlikely to be due to a statistical fluctuation. Figure 1.7 shows a summary of recent measurements of the Hubble constant, highlighting the difference between direct and indirect measurements.

There have been many theoretical solutions proposed to resolve this tension including early dark energy, primordial magnetic fields, the presence of additional relativistic species, a varying equation of state for dark energy, neutrino interactions, interacting dark energy, modified gravity, and modified cosmologies. Di Valentino et al. (2021) provide a detailed review of feasible proposed solutions as well as what observations constrain them. Despite this wealth of proposed solutions, none have been widely accepted as definitive and many are disfavoured from ΛCDM by current observational probes.

1.7.2 S_8 Tension

The S_8 tension is a discrepancy between the measurements of the $S_8 \equiv \sigma_8 \sqrt{\Omega_m/0.3}$ parameter. This parameter characterises how matter clusters in the Universe on large scales and can be measured using two independent techniques: from CMB observations and from cosmic shear. Cosmic shear is an effect of gravitational lensing where the large-scale structure of the Universe causes light to bend as it travels towards us from distant galaxies resulting in slight coherent distortions of the shapes of these galaxies. These two measurements are in mild tension with each other, with the cosmic shear measurement favouring a slightly

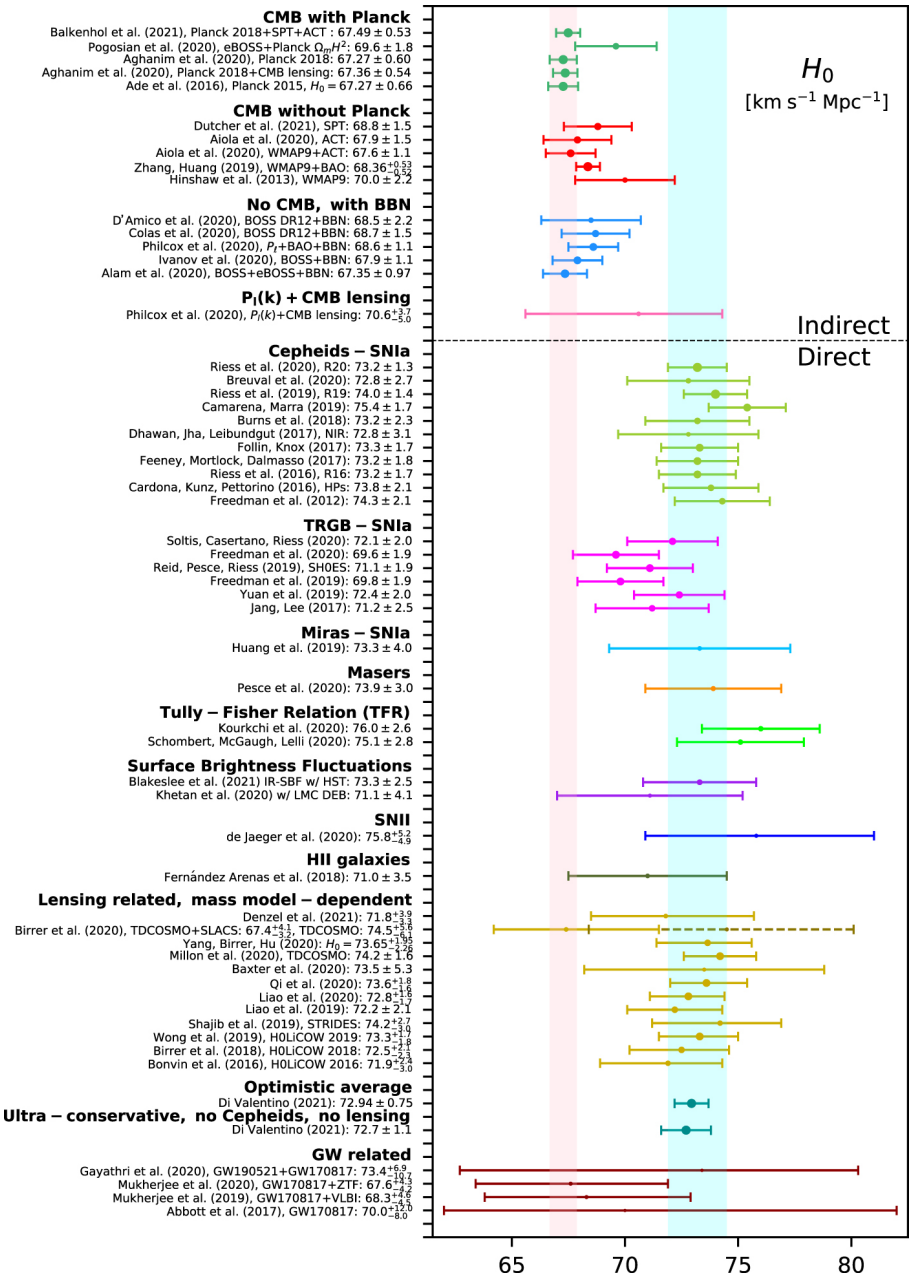

Figure 1.7: Whisker plot showing 1σ constraints of H_0 from direct and indirect measurements. The cyan vertical band corresponds to the measurement by Riess et al. (2021) while the light pink band corresponds to the measurement from Planck Collaboration et al. (2020). Image Credit: (Di Valentino et al., 2021).

lower value of S_8 than the CMB measurement, as shown in Figure 1.8. This tension is currently at a $\sim 3\sigma$ level, albeit with considerable scatter in cosmic shear measurements that may reduce this tension (Planck Collaboration et al., 2020; Hamana et al., 2020; Tröster et al., 2020; Asgari et al., 2021).

As with the Hubble tension, this discrepancy points to unknown systematics in the analyses, a statistical fluctuation, or new physics beyond ΛCDM. A new physics solution to the S8 tension would need to alter the predicted clustering of matter in the Universe in order to reconcile the CMB and cosmic shear results. Possible solutions that would accomplish this include additional neutrino species or dark energy with a different equation of state than that of ΛCDM. There are no solutions that would resolve both the Hubble tension and the S8 tension that are favoured over ΛCDM with currently available data.

1.7.3 CMB Inconsistencies

Another tension is an internal inconsistency in CMB data from Planck Collaboration et al. (2020) with the lensing parameter A_L that characterises the amplitude of the anisotropies in CMB radiation. CMB photons emitted at recombination are deflected due to gravitational lensing from massive cosmic structures. This effect is parameterised by A_L. CMB lensing results are consistent with the expected value of $A_L = 1$, however, measurements of A_L from CMB power spectra alone prefer a higher value of A_L at a $\sim 2.8\sigma$ discrepancy with that expected form ΛCDM, as shown in Figure 1.9. Aside from explanations of unknown systematic uncertainties or statistical fluctuation new physics that could explain these include primordial non-Gaussianity and modifications to general relativity.

1.8 Thesis Plan

The remainder of this thesis will introduce voids as a cosmological probe, explain how information can be extracted, and present results for a variety of cosmological models. Chapter 2 introduces voids as cosmological probes including background on how they can be used to inform the properties of the Universe. Chapter 3 will detail the different observational surveys used in the remainder of the thesis, as well as how data vectors are produced from voids. Chapter 4 details how these data vectors can be used to make cosmological measurements, quantifies systematic errors, and compares results to that from other groups and methodologies. Chapter 5 will show cosmological model fits to information from voids and the combination of information from voids with other probes

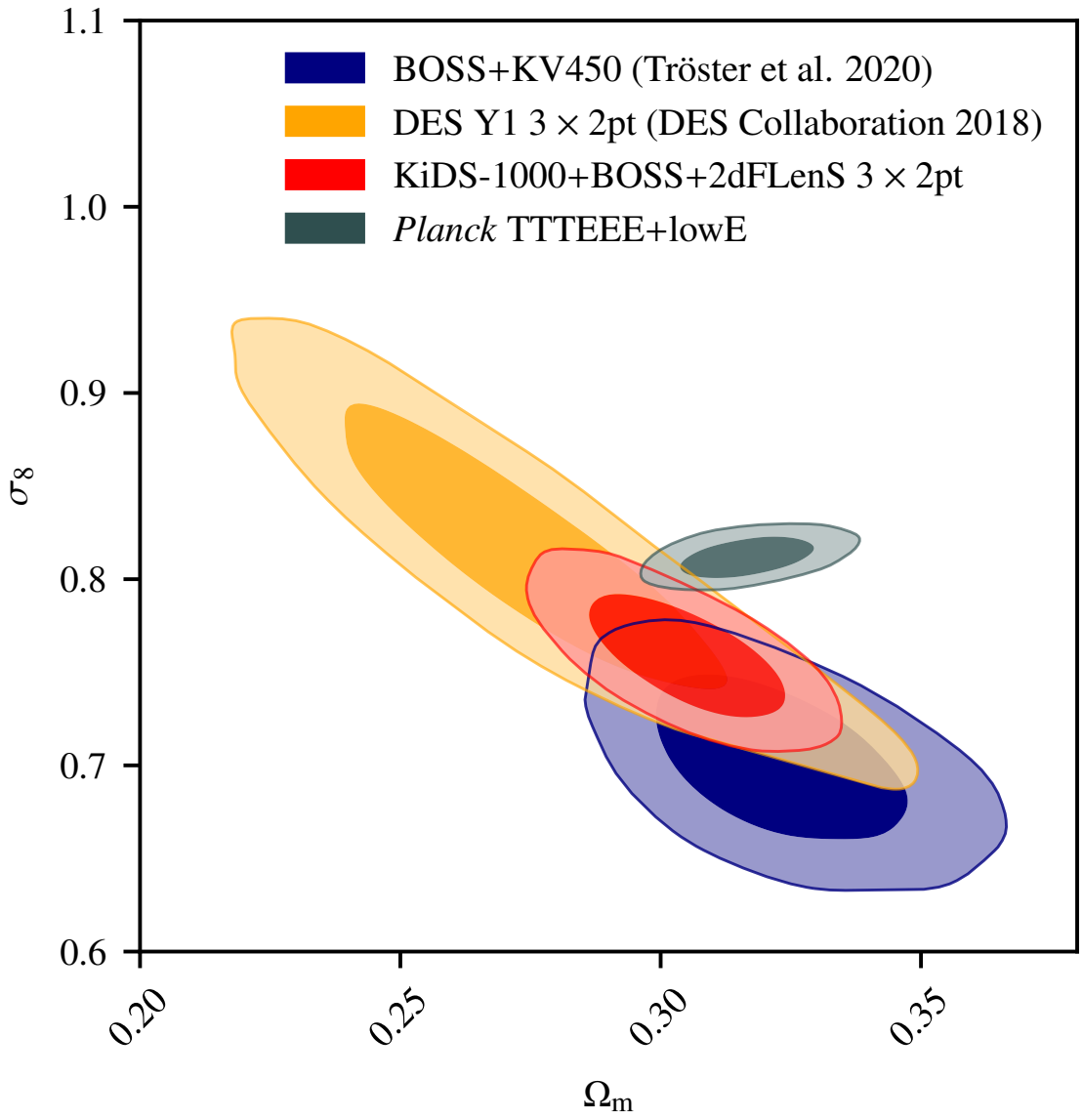

Figure 1.8: Parameter constraints in the $\sigma_8 - \Omega_m$ plane with analyses from KiDS-1000 (3×2 pt) with BOSS and 2dFLenS (Abbott et al., 2020), analysis from DES Y1 (3 x 2 pt) (Heymans et al., 2021), and CMB constraints from Planck Collaboration et al. (2020). Image Credit: (Heymans et al., 2021).

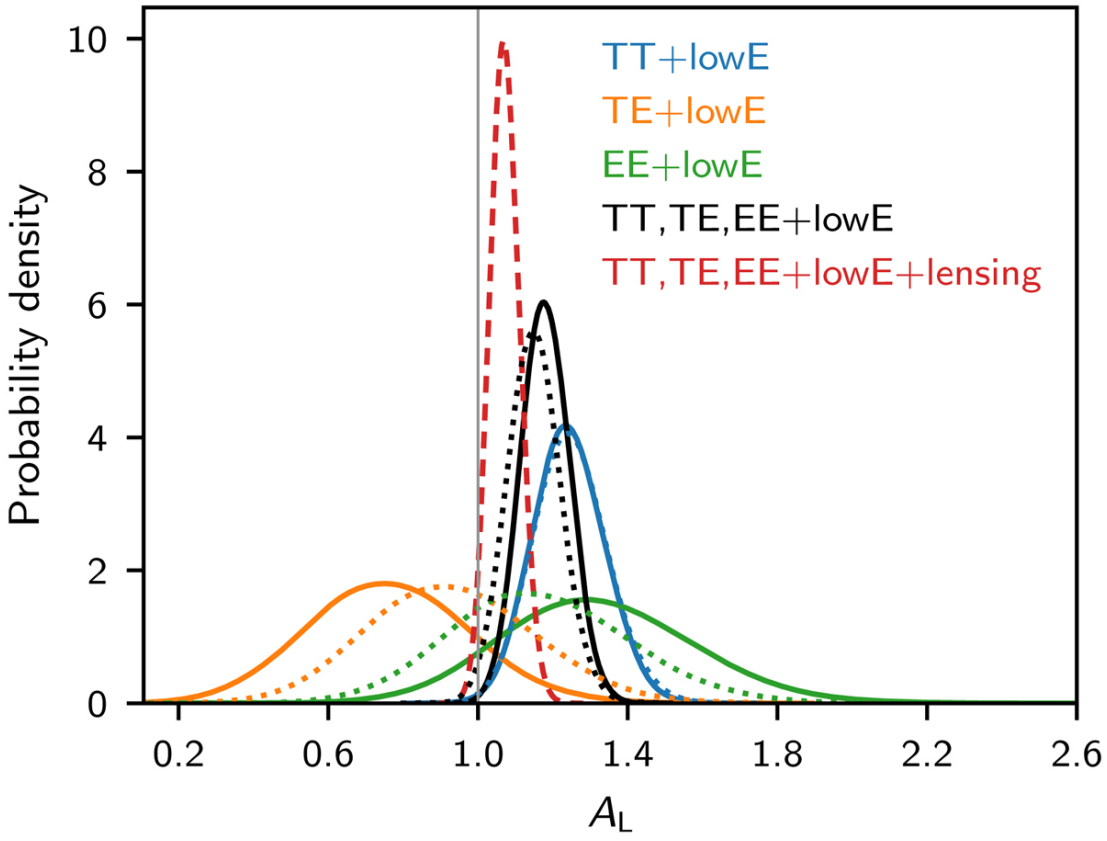

Figure 1.9: Constraints on the value of the consistency parameter $A_{\rm L}$, as a single-parameter extension to the base-ΛCDM model, using various combinations of Planck data. Image Credit: (Planck Collaboration et al., 2020).

such as BAO, RSD, CMB, and BBN. Finally, Chapter 6 will summarise these results and talk about the future of voids as cosmological probes.

Chapter 2

Cosmic Voids as Tracers of Large-Scale Structure

2.1 Introduction

Cosmic voids are a part of the cosmic web corresponding to vast underdense regions. They occupy most of the volume of the Universe and contain information about its expansion history and geometry (Ceccarelli et al., 2013; Cautun et al., 2014). These large-scale under densities are a natural consequence of structure growth. Matter flows towards high-density regions of space due to gravity, forming structures like cosmic clusters and filaments. This matter flows away from underdense regions creating even less dense regions called voids. As explained in greater detail throughout this Chapter, cosmological information is extracted from voids by knowing that a stack of voids will display spherical symmetry in real space, but is distorted in redshift space due to redshift space distortions and the Alcock-Paczynski effect. These observational effects will encode useful information.

Voids are interesting objects to study because the link between the non-linear density and the non-linear peculiar velocity can be accurately mapped using linear theory (Paz et al., 2013; Cai et al., 2016; Nadathur and Percival, 2019). As a consequence, the RSD signal in the distribution of galaxies around voids can be analytically modelled to small scales, and we can obtain information to smaller scales from the RSD and AP measurements than if we had tried to model all galaxy pairs (Lavaux and Wandelt, 2012; Hamaus et al., 2016; Nadathur et al., 2019b). There have consequently been many studies of the AP and RSD effects using the void-galaxy correlation (Paz et al., 2013; Hamaus et al., 2016, 2017; Hawken et al., 2017; Nadathur et al., 2019b; Achitouv, 2019; Hawken et al., 2020;

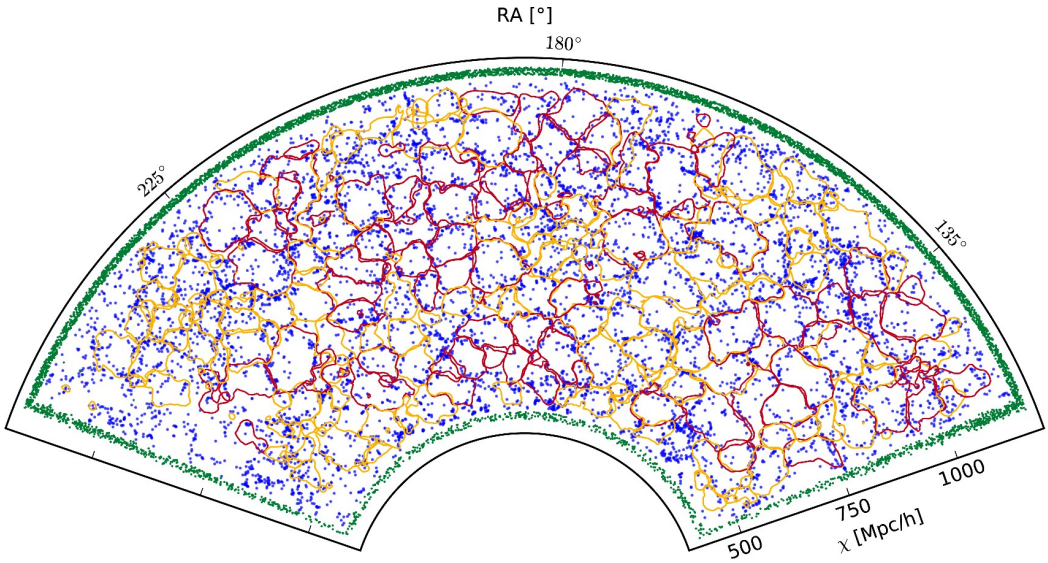

Figure 2.1: A slice of galaxy positions from the SDSS LOWZ survey (see Section 3.2) at dec = 12° with an opening angle of 2°. Shown on top of this in red and yellow are voids found in this sample using a ZOBOV void finding algorithm (see Section 2.3). The colour represents voids found in regions where the galaxy density is higher than the survey average (yellow) or lower (red). Buffer particles needed for a ZOBOV void-finder are seen at the boundaries of the survey volume in green, see Section 2.3 for more detail. Image credit: Nadathur (2016)

Aubert et al., 2022a) and closely related statistics (Paillas et al., 2021). In principle, the statistical precision with which the Alcock-Paczynski effect, introduced in Section 1.5.2 and parameterised by $D_{\rm M}(z)/D_{\rm H}(z)$, can be measured using voids exceeds that obtained from BAO (Hamaus et al., 2016; Nadathur et al., 2019b). However, the potential for systematics is slightly higher given the need to model the RSD signal. The idea behind the Alcock-Paczynski effect is that an object - such as a stack of voids - can be used as a standard shape. For a stack of voids, we know that it is expected to be spherical but do not know its intrinsic size. We will only recover this standard shape in our comoving maps if we use the true value of $D_{\rm M}(z)/D_{\rm H}(z)$ when converting redshifts to distances, in the absence of other effects (Alcock and Paczynski, 1979). Other ways in which voids can be used to test cosmological models include using the void size distribution, void lensing, or void-void clustering (Pisani et al., 2015; Sánchez et al., 2017b; Nadathur, 2016; Raghunathan et al., 2020; Zhao et al., 2022).

In this chapter the theoretical background and modelling relating to using voids as tracers of the large-scale structure of the Universe are introduced. This is applied in later chapters of this thesis to the full luminous red galaxy sample from the Sloan Digital Sky Survey for the first time to build up a picture of the geometry of the Universe, and the growth rate within it, from void-information only. This chapter will delve into the importance of void analysis, void finders, void densities, the void-galaxy correlation function, reconstruction and the necessity prior to void finding, modelling of the void-galaxy correlation function, the expected density of voids in the Universe, velocity field in voids and shot-noise effects on the void-centre definition, and finally previous void analyses.

2.2 Importance of Void Analyses

Cosmic voids are a strong probe of our best cosmological models. They enable us to extract additional information from galaxy surveys that is complementary to information that is extracted using the BAO peak as well as from the peculiar velocities of galaxies (for example, see Figure 5.1). Voids not only provide complementary information to that from galaxy clustering but have advantages. The RSD contribution to anisotropy in voids can be modelled using linear theory with reasonable success and without needing to exclude small scales (Hamaus et al., 2014; Cai et al., 2016; Nadathur and Percival, 2019; Paillas et al., 2021, Section 2.8). This provides our constraints on $f\sigma_8$, however, with the caveat that the potential for systematic bias is higher due to the sparsity of tracers around void centres leading to a mismatch in the velocity profile of dark matter and tracers (Massara et al., 2022, see also Sections 2.8.1 & 2.9). The anisotropies in the void-galaxy cross-correlation

function from RSD can be easily distinguished from those arising from the AP effect, and so measurements of the cross-correlation can be used to measure the AP parameter (Hamaus et al., 2015; Nadathur et al., 2019b, Section 2.8.2). Work in Hamaus et al. (2016); Nadathur et al. (2019b, 2020b) and Woodfinden et al. (2022, see Chapters 3 & 4) applied this method to the BOSS and eBOSS surveys and resulted in a factor of between 1.7 to 3.5 more precise constraints than those from galaxy clustering and BAO in the same data. For a featureless power spectrum (i.e. a power law), there would exist a perfect degeneracy between $f\sigma_8$ and $D_{\rm M}/D_{\rm H}$. This degeneracy is broken by features in the power spectrum such as the BAO feature on large scales. However, the sample variance is significantly reduced if we can work on small scales. Unfortunately for the galaxy-galaxy auto-power, there are few features on small scales, and the degeneracy can only be mildly broken (Ballinger et al., 1996). On the other hand, the small-scale void-galaxy cross-correlation has a number of features due to observational effects, and this degeneracy can be better broken, enhancing measurements.

Modified gravity theories predict that deviations from General Relativity should be more pronounced in voids making them ideal testing environments for different dark energy models to that of ΛCDM (Li et al., 2012; Clampitt et al., 2013; Cai et al., 2015; Achitouv, 2016; Cautun et al., 2018; Paillas et al., 2019; Zivick et al., 2015). Theories predicting a fifth force as responsible for the accelerating expansion of the Universe also predict that this force will be unscreened in low-density environments (e.g. Falck et al., 2017). Chapter 5 takes measurements presented in Chapters 3 & 4 from voids over a wide range in redshift (as well as in combination with complementary probes) and fits these measurements with a ΛCDM model as well as various plausible extensions to ΛCDM (e.g. wCDM, oCDM, $w(z)$CDM) to provide strong constraints on these models and test for deviations from ΛCDM.

Current (BOSS, eBOSS) and next generation (DESI, Euclid) galaxy spectroscopic surveys provide an enormous amount of information at a wide range of redshifts, from as low as redshift 0.07 up to redshift 1.8 and beyond. The application of voids to these surveys allows for a powerful test of the geometry, growth, and expansion history of the Universe and will allow the current best cosmological models to be tested to unprecedented precision. Forecast constraints from these surveys expect a precision of 3% to be achieved for $\Omega_{\rm m}$ and 6% precision is expected for w for a wCDM model (Radinović et al., 2023, see also Chapter 6). These constraints combine forecast values expected in upcoming Euclid data with those presented in this thesis from voids alone and rival the current best precision available from CMB measurements (Planck Collaboration et al., 2020). Section 1.7 shows that tensions exist in a ΛCDM framework, and voids offer a path forward (both on their own and in combination with other probes) to confirm these tensions, constrain plausible

explanations, and hint at possible solutions.

2.3 Void Finders

Various void finders exist to identify underdense regions in galaxy surveys. These void finders differ algorithmically, as well within each void finder, there may be various definitions of void centres. In general, a void finder will give a position for the centre of an underdense region, matching the criteria of that void finder, as well as a scale of the underdensity.

Void-finding techniques can be placed into very broad categories based on the underlying algorithm: watershed-based void finders, spherical-based void finders, and others including Delaunay triangulation-based void finders and weak lensing-based void finders. Of the void finders we describe below both `ZOBOV` and `VOXEL` fall under the watershed category, and as implied by its name the spherical void finder falls under the spherical category.

While the details of their implementation vary, all watershed-based void finders follow the same basic principle. They determine the density field and then voids are found by looking for inflexion points in this density field. Variations include how this void finding algorithm determines the underlying density field (e.g. galaxy counts in cells, Voronoi tesselations), and the criteria for merging neighbouring underdense regions identified by the watershed algorithm (this normally depends on the density contrast of neighbouring cells with the criteria depending on the ratio of neighbouring densities), and void centre definitions (e.g. minima of density field, weighted average of cell positions). Popular watershed-based methods include `VIDE` (Sutter et al., 2015), `ZOBOV` (Neyrinck, 2008), `VOXEL` (Nadathur et al., 2019b), and `WVF` (Platen et al., 2007).

Similarly, spherical-based void finders operate under the same underlying algorithm. They first determine the density field from the tracers used, and then use the lowest density regions in this field and measure the density in spheres of size $R_{\rm v}$ about this region. Variations in spherical void finders are based on the treatment of how this catalogue of spherical regions is turned into a void catalogue. They accept different criteria for the size and density of these regions to be considered voids and how they merge these voids into different regions. For example, some spherical void finders will iterate from the lowest density regions to the highest and remove this void from the catalogue if it overlaps with a more underdense region. Other void finders will merge neighbouring underdense regions based on a specified density criterion. Popular spherical-based void finders include `VOIDFIDNER` (Hoyle and Vogeley, 2002; El-Ad and Piran, 1997), `SVF` (Padilla et al., 2005; Ruiz et al., 2015), and `Popcorn` (Paz et al., 2023).

Other void finders include those based on Delaunay triangulation and weak lensing. Delaunay triangulation void finder identifies all empty spheres that are constrained by four elements of a point set of tracers. They resolve all the largest spheres that are empty of tracers. A popular implementation of this is `DIVE` (Zhao et al., 2016). Weak-lensing-based void-finders use various criteria from weak-lensing maps such as minima, troughs, and tunnels to identify voids, a summary of these void finders can be found in Davies et al. (2021).

This section describes the details of various popular void finders used in analyses involving the void-galaxy correlation function and summarises the void centre definitions available.

2.3.1 ZOBOV

`ZOBOV` (Neyrinck, 2008) is a watershed algorithm that topologically identifies voids in large-scale structures. This algorithm first estimates the local density using a Voronoi tessellation of the discrete galaxy distribution. In Voronoi tessellation, a Voronoi cell is assigned to each tracer and all space is assigned to the cell of the closest tracer. The density of each cell can be calculated as the inverse of its volume and the local minima of the density field are found using these densities. Voronoi cells are then grouped using a watershed procedure where, starting at the deepest minimum, neighbouring cells are combined until a cell of lower density is found. This identifies a saddle point. When a group of cells, called a basin, can no longer grow as it is surrounded by saddle points the next deepest local minima is considered. This continues until all space has been divided into basins. These will then either constitute voids in the final catalogue or, optionally, they may be merged into final voids. This criterion normally depends on the ratio of the density of the Voronoi cell that is at the minimum of the said basin to the density of cells at the boundaries. Prior to tesselation, boundary particles are placed around the edges of the survey volume to prevent arbitrarily large Voronoi volumes. Voids with Voronoi cells that contain boundary particles are removed from final void catalogues as they cannot be properly resolved.

Two main definitions of void centres exist for `ZOBOV` algorithms. The first is a circumcentre approach. In this approach, the void centre is computed as the point of lowest density. To do this the lowest density (highest volume) Voronoi cell is identified and the location of the tracers associated with this cell, as well as the locations of tracers associated with its three next lowest density neighbours, are used to form a tetrahedron. The circumcentre of this tetrahedron is taken as the void centre Nadathur and Hotchkiss (2015). This void centre definition is the sole definition that is used in work presented in Chapters 3, 4, & 5.

The other option is a barycentre definition. The void centre is computed using a volume-weighted approach where the location, $\vec{x}_i$, of the tracer corresponding to each Voronoi cell in the void is found and the weighted average, $\vec{x}_\mathrm{v}$, is computed using the volume of each cell, V_i,

$$\vec{x}_\mathrm{v} = \frac{\sum_i \vec{x}_i V_i}{\sum_i V_i}. \tag{2.1}$$

2.3.2 VOXEL

`VOXEL` is another watershed-based void finding algorithm, similar to `ZOBOV`, that uses a particle mesh method to calculate the density field instead of tesselation. To do this, tracer galaxies are placed onto a mesh grid, where the grid side length a_voxel is determined as

$$a_\mathrm{voxel} = \frac{1}{2}\left(\frac{4\pi\bar{n}}{3}\right)^{-1/3}, \tag{2.2}$$

where $\bar{n}$ is the mean number density of galaxies in the survey. The side length is chosen to match the mean particle separation. This density field is then smoothed using a Gaussian filter of smoothing length $\bar{n}^{-1/3}$ to reduce shot noise fluctuations on small scales. A watershed algorithm is then applied to this density in the same way as for `ZOBOV`: the lowest density point not currently belonging to a basin is found, neighbouring cells are merged into this basin until all neighbouring cells have a lower density, this corresponds to saddle points. This process is repeated until all space corresponds to a basin which are either taken as the final voids output or additional merging into final voids may be applied. Merging is typically based on the density of the centre of a basin compared to its particles at the void edges. Voids found near survey edges are removed from final void catalogues as they cannot be properly resolved.

Within `VOXEL` are two main void centre definitions. The first is the centre of the voxel corresponding to the density minimum in each basin. The second is a barycentre definition that is calculated as the inverse density weighted average of all voxels

$$\vec{x}_\mathrm{v} = \frac{\sum_i \vec{x}_i \rho_i^{-1}}{\sum_i \rho_i^{-1}}. \tag{2.3}$$

where $\vec{x}_i$ is the centre of each voxel in a basin and ρ_i is the density of said voxel.

Figure 2.2 shows the dark matter density profiles of both `ZOBOV` and `VOXEL` voids when applied to the same simulation box using a circumcentre void definition. The simulation box (described in greater detail in Section 3.2.4) is a full N-body simulation of dark matter

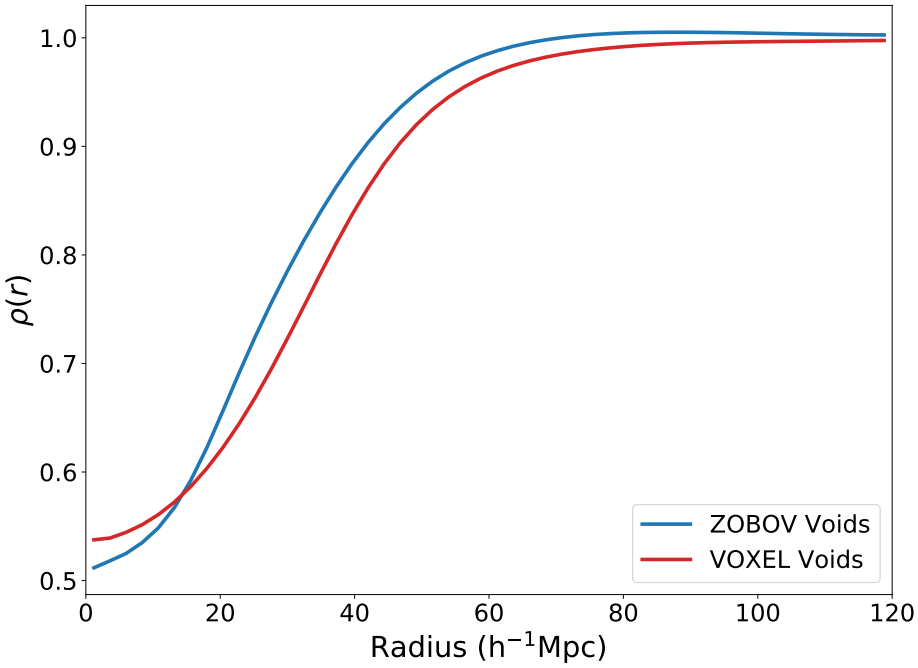

Figure 2.2: The dark matter density of `ZOBOV` and `VOXEL` voids when applied to a BigMD simulation box with a circumcentre void-centre definition, see Section 3.2.4.

particles that can be used to understand the dark matter field around voids. While similar, the two different void finders find different voids and have differing void centres for the same voids that result in different dark matter density profiles.

2.3.3 Spherical

Spherical void finders are non-watershed-based void finders. These void finders require three main choices to be made as inputs: a list of void sizes considered ($R_{\rm V}$), the side length of each voxel ($a_{\rm voxel}$), and a density threshold ($\Delta = \rho/\bar{\rho} - 1$) that is the maximum density of each local minima. Spherical void finders first calculate the density field in the same way as with `VOXEL`, by dividing all space considered into a 3-dimensional grid and counting the number of tracers within each grid cell (voxel), and then smoothing this density field using a top hat filter of smoothing length $R_{\rm V,i}$ where $R_{\rm V,i}$ is the largest

void size input to the algorithm. After filtering out voxels with a density below the input threshold Δ, they are sorted from lowest to highest. This list is then iterated through starting from the lowest density voxel. For each iteration, all voxels within radii $R_{\mathrm{V,i}}$ are grouped into a void. This is then repeated for each subsequent voxel in the sorted list and if no voxels with a void exist in a previously found void, then this void is kept. This process is repeated for all values of $R_{\mathrm{V,i}}$ in the input void size list. Void centres are defined as where the smoothed field is below the input threshold.

2.3.4 Choice of Void Finder

For work concerning the void-galaxy correlation function applied to SDSS data of this thesis, one void finder was chosen and used for all subsequent analyses shown in Chapters 3 & 4, & 5. The void finder `ZOBOV` was chosen for this work. The choice of void finder was restricted to those available in the `Revolver`[1] code due to author's familiarity with this software (including support from coauthors who wrote this code). Available options within `Revolver` are `ZOBOV` and `VOXEL`. While the `VOXEL` void finding algorithm was explored due to better performance in terms of memory usage and computational run time, this implementation had not yet been used in previous analyses at the time of work relating to Woodfinden et al. (2022). This implementation was found to have several bugs that caused larger systematic errors than were acceptable and other unwanted effects such as shifted void centre definition if all tracers were shifted to be located on a different patch of the sky but were otherwise kept the same. These bugs in implementation have since been resolved and `VOXEL` was first used in the analyses of Radinović et al. (2023). Instead, `ZOBOV`, despite the worse computational performance, had been shown to be an effective void finder with minimal systematic biases in previous analyses (Nadathur et al., 2019a, 2020b). This came with the added benefit that the analysis of eBOSS voids used the same void finder as work presented in subsequent chapters of this thesis and so repetition of this analysis with a new void finder was not required, saving both time and computational resources. The choice of a circumcentre definition for the `ZOBOV` void finder was used to match that of the analyses of eBOSS voids in Nadathur et al. (2020b) and was found to have a lower systematic bias than that of a barycentre definition.

[1] https://github.com/seshnadathur/Revolver

2.4 Void Densities

Voids are underdensities in a matter field. They can be characterised by having a low density in their centre, a rising density as the distance from the centre, and approaching the cosmic mean density at large radii. Individual voids do not have a well-defined shape profile. However, in an isotropic Universe, a stack of many similar voids will display a spherical shape (in real space) that can be well described with a radial profile $\delta(r)$. Figure 2.3 shows measured void density profiles for voids found in a simulated box (described in Section 3.2.4). In practice, the integrated density contrast $\Delta(r)$ is used to describe void environments (Ceccarelli et al., 2013). This is written as

$$\Delta(r) = \frac{3}{r^3}\int_0^r \delta(y) y^2 \, \mathrm{d}y \,. \tag{2.4}$$

In general two characteristic types of voids are found: R-type voids and S-type voids (Ceccarelli et al., 2013). R-type voids are characterised by an increasing density that monotonically tends towards the cosmic average density at large radii, see $R_v \geq 51$ voids in Figure 2.3. R-type voids tend to be larger voids. S-type voids are characterised by having a noticeable peak in their density profiles around the typical void radii that then decreases towards the cosmic average, see $15 \leq R_\mathrm{v} \leq 24$ voids in Figure 2.3. S-type voids tend to be smaller voids and tend to be found as voids in higher-density environments.

Several authors have proposed parametric models for void density profiles. Paz et al. (2013) propose two different models for $\Delta(r)$, one each for R-type and S-type voids. For R-type voids they provide the functional form

$$\Delta_\mathrm{R}(r) = \frac{1}{2}\left(\mathrm{erf}(S\log_{10}(r/R)) - 1\right), \tag{2.5}$$

where R is the void radii and S is a steepness coefficient. For S-type voids an additional term is needed to describe the peak seen around the void radii

$$\Delta_\mathrm{R}(r) = \frac{1}{2}\left(\mathrm{erf}(S\log_{10}(r/R)) - 1\right) + P\exp\left\{-\frac{\log_{10}^2(r/R)}{2\Theta^2(r)}\right\}, \tag{2.6}$$

where

$$\Theta(r) \equiv \begin{cases} 1/\sqrt{2S}, & r < R \\ 1/\sqrt{2W}, & r > R. \end{cases} \tag{2.7}$$

This introduces two additional parameters: an amplitude P and a semi-width W. Note that equation 2.5 is the same as equation 2.6 where parameter P has been set to zero. These

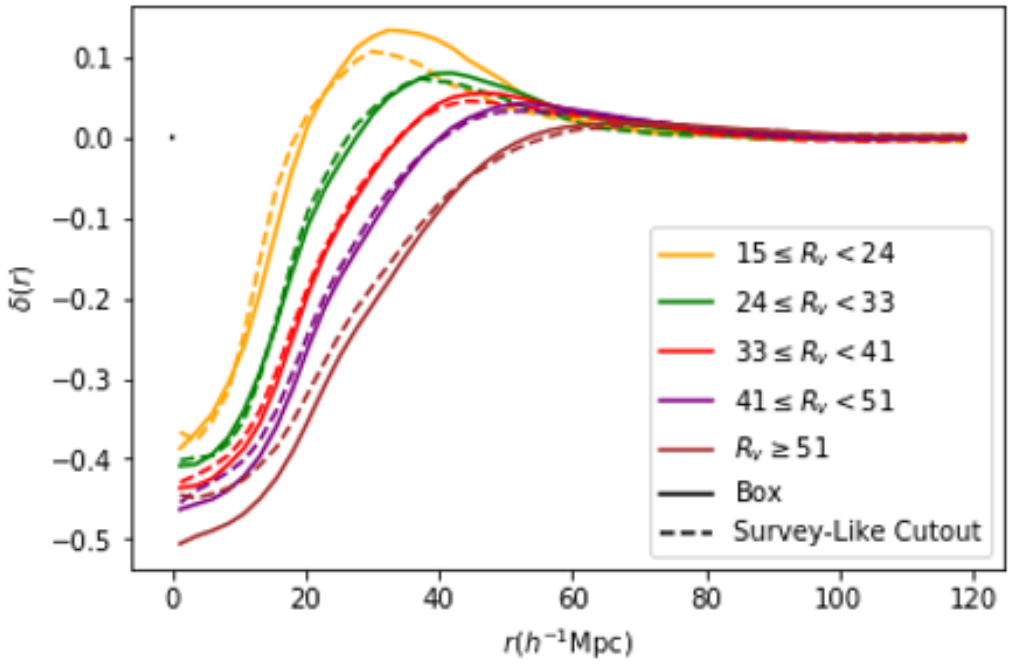

Figure 2.3: Void density profiles for voids found in the BigMD simulation. Voids are grouped into void-radii (R_v) bins to highlight the different density profiles from various-sized voids. Also shown are voids found in a survey-like cutout that closely matches the footprint of CMASS as opposed to a cubic box. Selection effects due to survey boundaries have a significant effect on the density profile of voids found. This Figure highlights the change in void density profiles in a simulation box with and without a realistic survey geometry applied while Figure 2.4 highlights the density changes of voids in the same survey geometry at different redshifts

functional forms are dependent on the void identification method used (see Section 2.3). Paz et al. (2013) tested these forms using a spherical void-finder. Alternatively Hamaus et al. (2014) introduced a functional form for $\delta(r)$

$$\delta(r) = \delta_{\rm c}\frac{1-(r/r_{\rm s})^{\alpha}}{1+(r/r_{\rm v})^{\beta}}, \tag{2.8}$$

which contains five fitting parameters: a central density contract $\delta_{\rm c}$, a scaling radius $r_{\rm s}$, a term describing the inner slope of the peak at void radii α, an effective void radius $r_{\rm v}$, and a term describing the outer slope of the peak at void radii β.

Massara and Sheth (2018) noted that models based on spherical void finders fail to capture that the large-scale bias factor of conserved tracers evolves with redshift. This is directly related to the motion of voids. These void motions are approximately independent of void size, so they are more significant for smaller voids that are typically more numerous but are apparent for all void sizes. To account for this the authors advocate for an improved model. They define their voids through a spherical evolution model as underdense regions that undergo spherically symmetric expansion. In this case, the density profiles have been shown to be well fit by the functional form (Bernardeau, 1994; Sheth, 1998)

$$1+\delta(<R_{\rm E},a) \approx \left(1-\frac{D_{\rm a}\delta_{\rm L}(<R_{\rm L})}{\delta_{\rm c}}\right)^{-\delta_{\rm c}}. \tag{2.9}$$

Here a is the scale factor, $R_{\rm L}$ is some initial scale that evolves to $R_{\rm E}$ at redshift z, $\delta_{\rm L}$ is the initial linear overdensity, $D_{\rm a}$ is the linear growth factor normalise to the present time, and $\delta_{\rm c} = 1.686$. To account for the motion of the void centre with redshift Massara and Sheth (2018) propose an improved model

$$1+\delta_{\rm E}(<R_{\rm E},a) = 1+\delta(<R_{\rm E},a)+D_{\rm a}\delta_2(R_{\rm E},a), \tag{2.10}$$

where $\delta_{\rm E}$ is the initial linear overdensity that has been non-linearly evolved to redshift z. δ is determined in this model by equation 2.9 and δ_2 (described in greater detail in equations 13 through 18 of Massara and Sheth 2018) is a term to account for void centre motions. While this additional term is well-motivated it is not empirically derived.

It should be noted that these functional forms are motivated by the observed shape of void density profiles when found in simulations but are not empirical. They introduce additional nuisance parameters when extracting cosmological information from void shapes that weaken the constraints that can be obtained. An alternative approach is to measure these void density profiles from cosmological simulations that have been designed to match the survey being studied closely. This is called a template-based approach. However, this

introduces potential systematic errors in the analysis if this void density profile measured through simulations does not match the truth. Work in later chapters takes the latter approach and potential systematic errors are quantified through the use of mock catalogues (see Section 4.3).

The density profile of voids is a redshift-dependent quantity. As voids evolve matter continuously flows out of voids toward high-density regions. This causes the central density of voids to decrease at lower redshifts and voids to expand (Sheth and van de Weygaert, 2004). The lower central density can be seen in Figure 2.4 where void density profiles are shown at two different redshifts matching that of the effective redshift LOWZ and CMASS samples (see Chapter 3). Voids at lower redshift are seen to have a lower central density in all void-radii bins shown.

2.5 Correlation function measurement

There are several ways in which voids can be used to test cosmological models including void-galaxy cross-correlations, the void size distribution, void lensing, and void-void clustering (Pisani et al., 2015; Sánchez et al., 2017b; Nadathur, 2016; Raghunathan et al., 2020; Zhao et al., 2022). This thesis focuses on void-galaxy cross-correlations.

To measure the binned void-galaxy correlation function ξ^s (or ξ^r) in redshift space (real space) binning is defined by both the radial direction, i.e. the observed void-galaxy separation distance s (r), and the cosine of the angle μ_s (μ_r) between the separation vector and the line-of-sight direction to the void centre. The correlation function can be defined using a correlation function estimator. Several different estimators exist that use pair counts to provide an approximation of the true correlation function such as the Davis-Peebles estimator (Davis and Peebles, 1983), Hamilton estimator (Hamilton, 1993), Landy-Szalay estimator (Landy and Szalay, 1993)). Kerscher et al. (2000) reviewed several estimators and their application to astrophysical situations concluding that the Landy-Szalay provided the best match to the true correlation function. For work in Chapter 4 the Landy-Szalay estimator is used as it accounts for the differences in populations (e.g. redshift distribution, sky distribution) of both voids and galaxies, see Section 2.7 for a brief discussion on this. The Landy-Szalay estimator for two different populations is defined as

$$\xi^s(s, \mu_s) = \frac{D_1D_2 - D_1R_2 - D_2R_1 + R_1R_2}{R_1R_2}, \tag{2.11}$$

where each term on the right-hand side (e.g. D_1R_2) refers to the number of pairs for the given populations in the bin, normalised by the effective total number of such pairs.

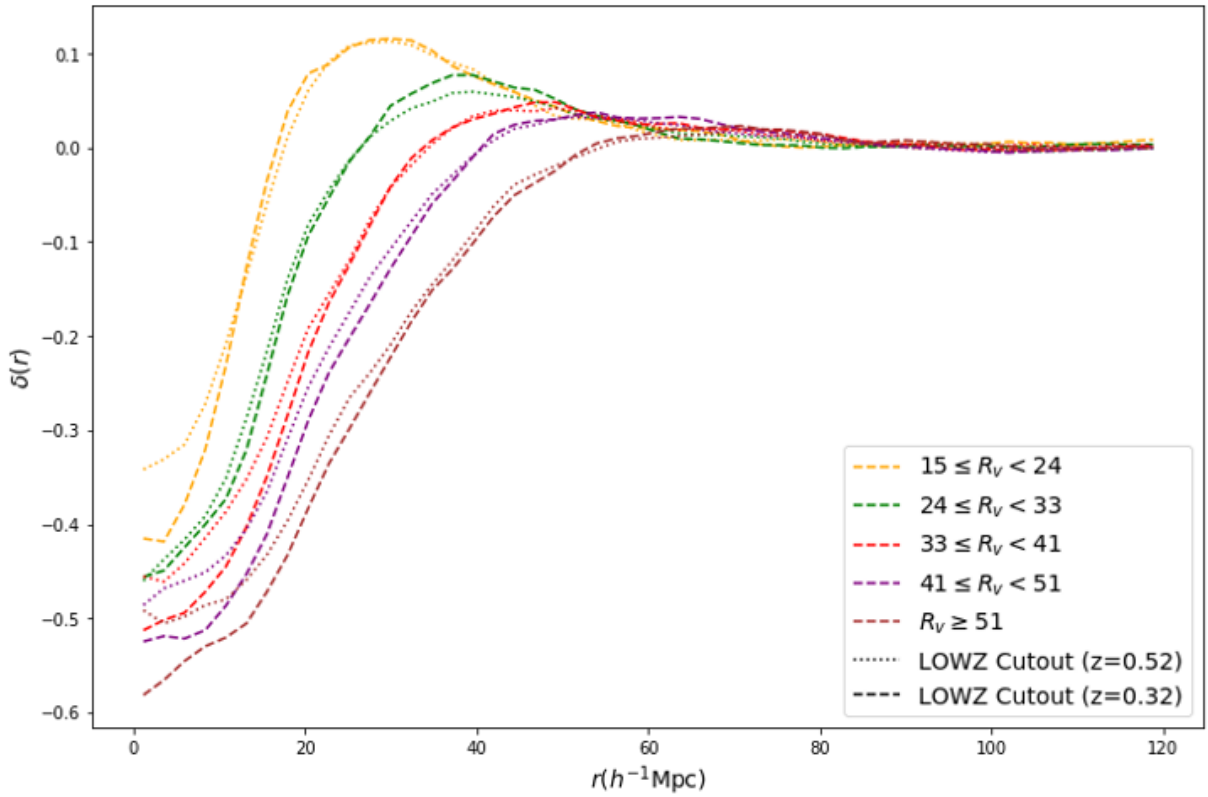

Figure 2.4: Void density profiles for voids found in the BigMD simulation. Voids are grouped into void-radii (R_v) bins to highlight the different density profiles from various-sized voids. Voids are found in a survey-like cutout that closely matches the footprint of LOWZ but at two different effective redshifts, $z = 0.32$ and $z = 0.52$. Voids at lower redshift can be seen to have a lower central density. This Figure highlights the density changes of voids in the same survey geometry at different redshifts while Figure 2.3 highlights the change in void density profiles in a simulation box with and without a realistic survey geometry applied.

Here D_1 refers to the void centre positions, D_2 to the galaxies, and R_1 and R_2 to the corresponding sets of unclustered random points matching the angular and redshift distributions and systematic effects of the void and galaxy catalogues but are several times larger to minimise shot noise. The galaxy randoms R_2 are taken from the publicly provided random catalogues for each sample by SDSS. Void random catalogues R_1 are discussed in Section 2.7.

In computing the pair counts, galaxies and galaxy randoms are weighted by the systematic weights provided in the public data releases. These weights are applied to the galaxy field prior to void-finding to account for various observation effects in the data. Since the locations of the void centres are calculated after these weights have already been accounted for voids and void randoms are all given equal unit weights. Where survey data spans two galactic caps, they can be combined in the correlation estimation by adding pair counts across caps in equation 2.11, having first checked that there are no significant systematic offsets between the estimates in each cap.[2] The measured void-galaxy correlation functions can be decomposed into their Legendre multipole moments (see Section 1.4.2). Of interest in work in Chapter 4 is the monopole, $\xi_0^s(s)$, and quadrupole, $\xi_2^s(s)$, in redshift space, and monopole $\xi_0^r(r)$ in real space. Note that, as later shown in equation 2.18 the only non-zero multipoles of the modelling of the void-galaxy correlation function are the monopole and quadrupole.

2.6 Reconstruction

Previous work on the void-galaxy cross-correlation has shown an excellent match between models (described in more detail in Section 2.8) and simulations on all scales (Nadathur and Percival, 2019). This work however used voids found in real space, information which is unavailable in galaxy surveys. Models for the void-galaxy correlation function are based on a few common assumptions (Nadathur et al., 2019a):

1. The number of voids found is conserved whether voids are found in redshift space or real space
2. Changes in void positions depend only on galaxy velocities when voids are found in redshift and real space
3. The average radial outflow velocity around voids is isotropic

[2] Woodfinden et al. (2022) found that a comparison of results across galactic caps can be useful as a diagnostic of subtle bugs in the reconstruction or void-finding procedure.

4. The real space correlation function is isotropic (see Section 2.5).

While previous studies of RSD around voids have used voids found in redshift space (e.g. Paz et al., 2013; Hamaus et al., 2016; Hawken et al., 2017; Hamaus et al., 2017; Hawken et al., 2017; Achitouv et al., 2017; Hamaus et al., 2020; Hamaus et al., 2022) several authors have noted that the assumptions made for most models as listed above may be violated (Nadathur and Hotchkiss, 2014; Zhao et al., 2016; Correa et al., 2022). Figure 2.5 shows that the void size function is not conserved under the mapping from redshift space to real space. This hints that assumption 1 that the number of voids is conserved is violated for voids found in redshift space as void numbers are not consistent with those found in real space. Correa et al. (2021) argue that this is due to the same voids becoming elongated in redshift space as opposed to real space. They find that outside of shot noise, the number of voids is conserved in the mapping from real space to redshift space for a spherical void finder. This has not been shown to be the case for watershed-based void finders. The validity of these hypotheses has been discussed in more detail in Hamaus et al. (2020). Figure 2.6 shows that assumption 2, void positions depend only on galaxy velocities, is violated for voids found in redshift space as the outflow velocity can be seen to be anisotropic. Figure 2.7 shows that assumption 4, the real space correlation function is isotropic, is violated for voids found in redshift space as the real space correlation function can be seen to be anisotropic for voids found in redshift space cross-correlated with galaxies in real space. A recent thorough study by Correa et al. (2022) characterised this selection effect as an intrinsic ellipticity of samples of redshift space voids. Such an intrinsic ellipticity is currently not modelled in any theoretical description of the void-galaxy correlation.

There are two approaches one can take to account for void finding in redshift space: extend the modelling of the void-galaxy correlation function (e.g. Hamaus et al., 2020; Correa et al., 2022) to account for this or fix the data to approximately recover real space positions prior to void finding. The latter technique is used in Chapter 3 to obtain a suitable population of voids. To do this we first approximately remove the RSD in the galaxy distribution through the use of reconstruction before applying a void-finding algorithm. This procedure was first advocated by Nadathur et al. (2019a), who noted that void-finding performed directly on the redshift space galaxy distribution leads to samples that violate several of the key assumptions necessary to derive theoretical models of the void-galaxy correlation (Nadathur et al., 2019a; Chuang et al., 2017). The reconstruction algorithm used is designed to remove the large-scale velocity flows responsible for void centre motions as described below (Nadathur et al., 2019a).

To apply reconstruction prior to void finding, a Zeldovich reconstruction algorithm described by Nadathur et al. (2019a,b, 2020b) can be used. This has been implemented

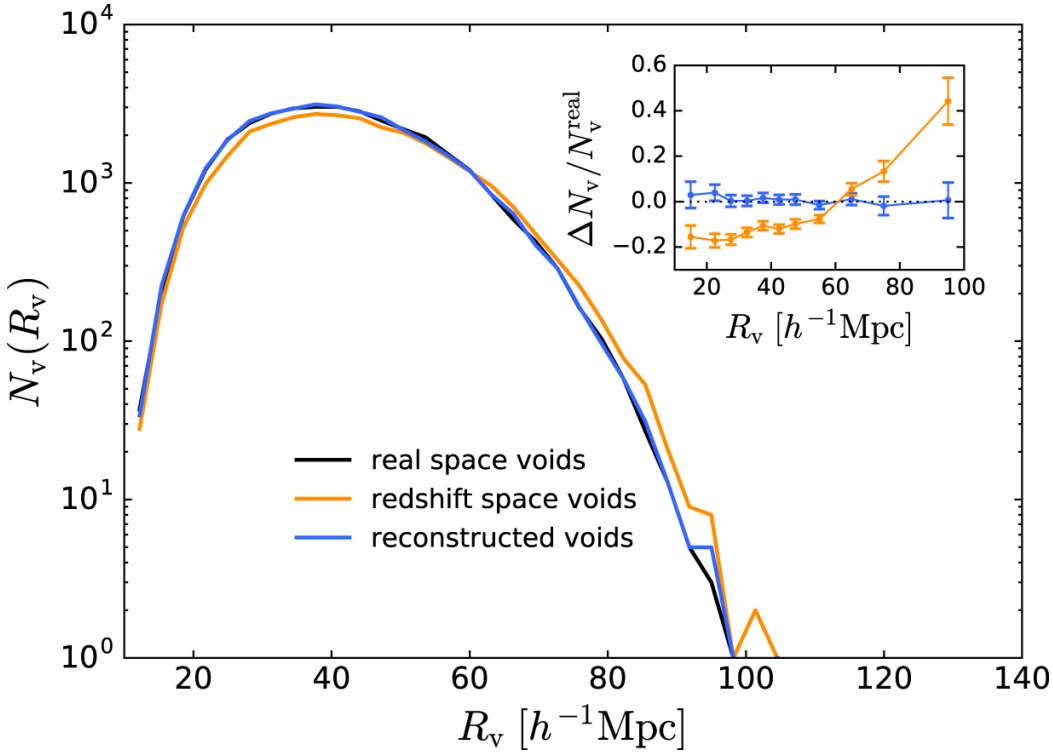

Figure 2.5: The number of voids $N_{\rm v}$ as a function of void radius $R_{\rm v}$ for voids using galaxy positions in real space, redshift space, and after applying a velocity reconstruction method. The inset show the fractional differences in void numbers relative to real space along with Poisson errors. Figure Credit: Nadathur et al. (2019a)

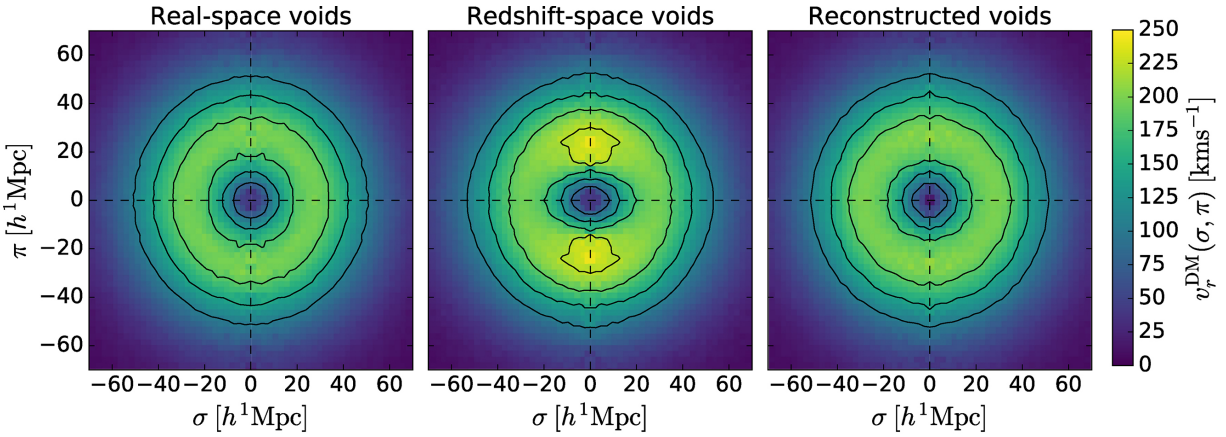

Figure 2.6: Average radial component of dark matter outflow velocity around void centers $v_{\mathrm{r}}^{\mathrm{DM}}(\sigma,\pi)$ as a function of real space distance from the void centre perpendicular (σ) and parallel (π) to the line-of-sight). Voids are found using galaxy positions in real space, redshift space, and after applying a velocity reconstruction method. Figure Credit: Nadathur et al. (2019a)

in the public `Revolver` code[3]. using the iterative fast Fourier transform (FFT) method of Burden et al. (2015) to solve the Zeldovich equation in redshift space (Zel'dovich, 1970; Nusser and Davis, 1994),

$$\nabla \cdot \vec{\Psi} + \frac{f}{b}\nabla \cdot (\vec{\Psi} \cdot \hat{\vec{r}})\hat{\vec{r}} = -\frac{\delta_g}{b}, \tag{2.12}$$

for the Lagrangian displacement field $\vec{\Psi}$, where f is the growth rate, b is the linear galaxy bias, and δ_{g} is the galaxy overdensity in redshift space. For work in Chapter 4, this step is performed on a 512^3 grid, and densities estimated on the grid are first smoothed with a Gaussian kernel of width $R_{\mathrm{s}} = 10\,h^{-1}\mathrm{Mpc}$ before solving for the displacement. Individual galaxies are shifted by $-\vec{\Psi}_{\mathrm{RSD}} = f\left(\vec{\Psi}\cdot\hat{\vec{r}}\right)\hat{\vec{r}}$ to obtain their (approximate) real space positions. The results of the procedure depend only on $\beta \equiv f/b$. This final step differs from the reconstruction algorithms used in BAO analyses where galaxy positions are shifted by $-\Psi$ rather than just the RSD component. BAO analyses aim to remove the effects of all non-linear clustering to sharpen the BAO peak while for voids we are only interested in removing RSD (Eisenstein et al., 2007).

After applying this reconstruction method, Figure 2.5 shows that assumption 1 is valid for voids identified in reconstructed space as the number of voids is consistent with those

[3] https://github.com/seshnadathur/Revolver

found in real space for voids identified in a simulation box. Figure 2.6 shows that assumption 3 is valid for voids identified in reconstructed space in a simulated box as the observed outflow velocity can be seen to be isotropic. Figure 2.7 shows that assumption 4 is valid for voids identified in reconstructed space in a simulated box as the measured quadrupole of the void-galaxy cross-correlation function can be seen to be isotropic (within error).

2.6.1 Alternatives to Reconstruction

As stated above, models for the void-galaxy correlation function rely on four key assumptions that are only valid in real space. While in this work we advocate for the use of reconstruction to approximately recover the real space galaxy field prior to void finding to mitigate these issues, it does come with some disadvantages. These include that it is computationally expensive, assumptions 2 through 4 contain cosmological information which can be extracted (Hamaus et al., 2020; Correa et al., 2022), and if an accurate RSD model can be found then assumptions 2 through 4 can be recovered without the need for additional steps. Several alternatives to reconstruction have been proposed including using projected correlation functions, deprojection techniques, and emulation using simulations.

Projected correlation functions break the void-galaxy correlation function down into components along the line of sight (LOS) and perpendicular to the line of sight (POS). Cosmological information is then extracted from measuring distortions, such as RSD, that will affect the LOS correlation function differently from the POS correlation function. Quantities such as the real space correlation function and the matter density profile around voids are found using either using parametric models or calibrated directly from simulations (Correa et al., 2019, 2022). While promising, this technique needs further development and is not yet able to recover accurate parameter estimates from galaxy spectroscopic surveys (Correa, 2022).

The deprojection technique is similar to projected correlation functions in that it relies on the projected correlation function perpendicular to the line of sight not being subject to RSD effects. The real space correlation function is calculated via deprojection using an inverse Abel transform of the projected correlation function (Pisani et al., 2014; Hamaus et al., 2020; Hamaus et al., 2022). The matter density around voids is found using fitting functions or assuming a linear bias relation between this and the real space correlation function. Additional nuisance parameters are needed to account for potential inaccuracies arising in the deprojection technique, contamination of the void sample by spurious Poisson fluctuations, as well as selection effects when voids are identified in redshift space (Hamaus et al., 2022). This technique has been successfully applied to galaxy spectroscopic surveys

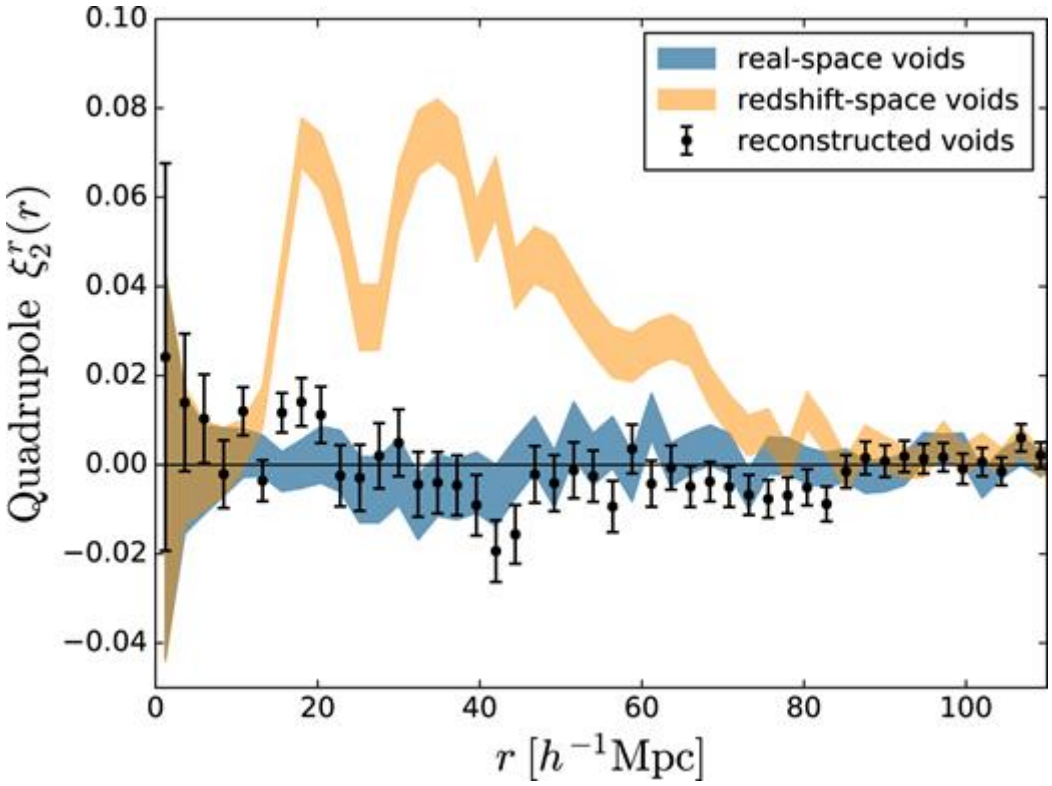

Figure 2.7: Quadrupole $\xi_2^r(r)$ of the void-galaxy cross-correlation for different void populations cross-correlated with real space galaxy positions found in a simulated box. Voids are found using galaxy positions in real space (black data points), redshift space (orange shaded region), and after applying a velocity reconstruction method (blue shaded region). Bandwidths and error bars represent the 1σ error range. Figure Credit: Nadathur et al. (2019a)

and provides competitive cosmological constraints, albeit with worse performance than the reconstruction technique used in this thesis due to the additional nuisance parameters needed (e.g. Hamaus et al., 2022; Radinović et al., 2023).

An alternative to trying to directly model void-related statistics (e.g. the void-galaxy cross-correlation, the void size function) is to instead train an emulator using simulations that encompass a wide range of cosmological models and then use this emulator-based model to infer cosmological parameters. Previous work in this area has used alternate statistics to the void-galaxy correlation function used in this work such as the void size function and void density profile (Kreisch et al., 2022) or the ellipticity, density contrast, and radius of voids (Wang et al., 2022). Neither of these works used these emulator-based models directly on galaxy spectroscopic data. Instead, these authors tested the robustness of their emulator-based approach using simulated data. This application to spectroscopic data has been successful for non-void related statistics (e.g. Chapman et al., 2022; Yuan et al., 2022; Kobayashi et al., 2022). This method has not yet been applied to the void-galaxy correlation function.

2.7 Modelling the Expected Density of Voids

While, on scales much larger than the expected void radius, the expected density of voids in the Universe is statistically isotropic at a given redshift, this is not the case for voids found using galaxy survey data. In galaxy survey data the distribution of galaxies on the sky will be influenced by the survey's sky footprint, radial selection function, and sampling of the survey on the sky. In addition, voids found in this galaxy field will differ from that of the galaxies in terms of density, an exclusion effect where voids near survey boundaries are removed due to the possibility of contamination of the tessellation (Nadathur, 2016) and will have a different redshift distribution than that of galaxies. Figure 2.8 shows a heatmap of the density of galaxies averaged over several mock catalogues designed to closely match the distribution of galaxies in these surveys, as well as of voids found in these mock catalogues. The difference between the distribution of galaxies and voids can be clearly seen between these two diagrams, and the exclusion effect of voids near the galaxy survey boundaries can be seen in the lower density of voids in these regions (compared to galaxies that do not appear to have this same effect). Figure 3.8 shows the redshift distribution of voids compared to galaxies (for the SDSS LRG sample described in Chapter 3) which differs for the same reasons.

To account for these effects, separate unclustered void random catalogues must be constructed to match the spatial distribution of the voids. One method of creating these

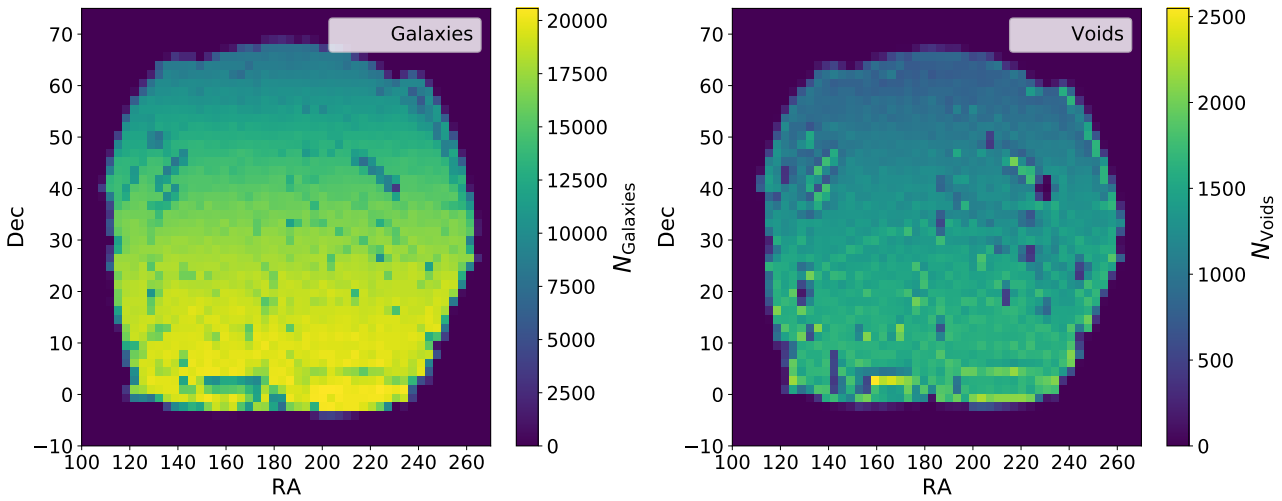

Figure 2.8: Heatmap of the density of galaxies (left) and voids (right) as seen projected onto the sky. Data is taken from SDSS LRGs in the redshift range $0.43 < z < 0.6$ corresponding to BOSS CMASS voids (see Chapter 3). Galaxies are taken from 50 Patchy mock catalogues stacked on top of one another (see Section 3.2.2) and voids are taken from voids found in 1000 of these mock catalogues, reconstruction is run prior to void finding with a fiducial value of $\beta = 0.43$. The density of voids/galaxies decreasing with higher declination is a projection effect arising from projecting a 3D surface onto a 2D map; the density of galaxies/voids is approximately constant with declination. Figure 3.8 shows the redshift distribution of voids compared to galaxies (for the SDSS LRG sample described in Chapter 3).

void random catalogues is to run the reconstruction and void-finding steps described above on mock galaxy catalogues in order to create mock void catalogues. Void positions can be randomly drawn from many mock catalogues stacked together to make a void random catalogue with many more objects than obtained in the survey data. This will result in a catalogue that is very close to being independent of the void randoms due to the large number of mock catalogues used to generate it while matching the spatial distribution of voids, and completely independent when applied to the data. It should be noted that the sky and radial distribution of voids is dependent on the void finding algorithm used, so random catalogues will be unique to each void finder.

2.8 Model

The void-galaxy cross-correlation function encodes the excess probability of finding a galaxy at a given distance from a void centre. In surveys, we measure the redshift space void-galaxy cross-correlation function $\xi^s(s)$ which becomes distorted from these real space void-galaxy cross-correlation $\xi^r(s)$ via two processes: redshift space distortions and the Alcock-Paczynski effect. We first discuss the mapping from real space to redshift space in Section 2.8.1 and then extend this to account for Alcock-Paczynski distortions in Section 2.8.2. In Section 2.8.1 it is shown that the Jacobian method of mapping between redshift and real space (along with a Gaussian dispersion term) described in Nadathur and Percival (2019) is equivalent to that of a Gaussian streaming model used in similar work (e.g. Paz et al., 2013; Cai et al., 2016). Previously these two methods were thought to differ (Nadathur et al., 2020b), however, Woodfinden et al. (2022) demonstrated their equivalence for the first time.

2.8.1 Redshift Space Distortions around Voids

In the absence of Alcock-Paczynski distortions, the redshift space void-galaxy cross-correlation function $\xi^s(\vec{s})$ is related to the real space version $\xi^r(\vec{r})$ by

$$1 + \xi^s(s_\perp, s_{||}) = \int_{-\infty}^{\infty} (1 + \xi^r(\vec{r}))\, P(v_{||}, \vec{r})\, \mathrm{dv}_{||}, \tag{2.13}$$

where $P(v_{||}, \vec{r})$ is the position-dependent PDF of galaxy velocities parallel to the line of sight direction, $v_{||}$, and the real space void-galaxy separation vector $\vec{r}$ and its redshift space

equivalent $\vec{s}$ have components perpendicular to and parallel to the line of sight direction that are related by $s_\perp = r_\perp$ and

$$s_{||} = r_{||} + \frac{v_{||}}{aH}, \tag{2.14}$$

respectively. This expression is general and exact if the number of void-galaxy pairs is conserved. The number of voids is *not* conserved under the application of void-finding separately to real and redshift space galaxy distributions (Chuang et al., 2017; Nadathur et al., 2019a; Correa et al., 2022). The assumption of pair conservation will hold by construction when voids are identified in a reconstructed galaxy field (see Section 2.6). This same sample of voids must be used for evaluation of both $\xi^r(\vec{r})$ and $\xi^s(\vec{s})$.

When considering the distribution of galaxies around a stack of voids, we can further assume spherical symmetry in real space, which means that $\xi^r(\vec{r}) = \xi^r(r)$, and the velocity distribution $P(v_{||}, \vec{r})$ at each r is symmetric around the mean value $v_r(r)\mu_r$, where $\vec{v}(r) = v_r(r)\hat{\vec{r}}$ is the (radially directed) coherent mean galaxy outflow velocity around the void and $\mu_r = r_{||}/r = \cos\theta$ where θ is the angle between the void-galaxy separation vector and the line-of-sight. If we introduce a change of variables $\tilde{v} = v_{||} - v_r(r)\mu_r$, then by using the relations

$$\frac{\mathrm{d}\tilde{v}}{\mathrm{d}v_{||}} = 1 - r_{||}\frac{\mathrm{d}}{\mathrm{d}v_{||}}\left(\frac{v_r}{r}\right) - \left(\frac{v_r}{r}\right)\frac{\mathrm{d}r_{||}}{\mathrm{d}v_{||}}, \tag{2.15}$$

$$\frac{\mathrm{d}r}{\mathrm{d}v_{||}} = \frac{r_{||}}{r}\frac{\mathrm{d}r_{||}}{\mathrm{d}v_{||}}, \tag{2.16}$$

$$\frac{\mathrm{d}r_{||}}{\mathrm{d}v_{||}} = -\frac{1}{aH}, \tag{2.17}$$

we can rewrite equation 2.13 as

$$1 + \xi^s(s, \mu_s) = \int (1 + \xi^r(r)) \left[1 + \frac{v_r}{raH} + \frac{rv_r' - v_r}{raH}\mu_r^2\right]^{-1} P(\tilde{v}, r)\mathrm{d}\tilde{v}\,, \tag{2.18}$$

where $\mu_s = s_{||}/s$, the term in the square brackets is $\frac{\mathrm{d}\tilde{v}}{\mathrm{d}v_{||}}$, and $'$ denotes the derivative with respect to r. The term $P(\tilde{v}, r)$ now represents incoherent dispersion as we have explicitly removed the coherent outflow from the velocity. Equation 2.18 is exactly the model derived by Nadathur and Percival (2019), who derived it using the Jacobian of the mapping between $\vec{s}$ and $\vec{r}$ and then added in a Gaussian dispersion term $P(\tilde{v}, r)$, which was required to fit the simulations. As shown in the derivation above, this term naturally arises in the streaming model as the incoherent component of $P(v_{||}, \vec{r})$ in equation 2.13 as was first demonstrated in Woodfinden et al. (2022).

Note that the key assumption of spherical symmetry in real space requires *both* statistical isotropy of the Universe as a whole *and* that void selection also maintains statistical isotropy – i.e., that the process of identification of voids has no orientation-dependent bias. This cannot in principle be true if void-finding is applied to the redshift space galaxy density field, which already contains line-of-sight anisotropies due to RSD. In this case underdensities with larger outflow velocities along the line-of-sight are preferentially selected as voids, and this selection bias means that neither $\xi^r(\vec{r})$ nor $P(v_{||}, \vec{r})$ are isotropic, and that the PDF is not symmetric about the mean. This leads to a large additional contribution to ξ^s (Nadathur et al., 2019a; Correa et al., 2022) that cannot currently be modelled. To remove this orientation-dependent void selection the additional reconstruction step should be added prior to void finding (see Section 2.6).

When this is done, it has been shown empirically from comparison with simulations that the PDF $P(\tilde{v}, r)$ is close to Gaussian over a range of scales (Nadathur and Percival, 2019; Paillas et al., 2021). Deviations from Gaussianity occur at large r, where the effect of convolution with $P(\tilde{v}, r)$ in equation 2.18 is itself negligible. Therefore $P(\tilde{v}, r)$ can be assumed as a zero-mean Gaussian PDF with standard deviation $\sigma_{v_{||}}$,

$$P(\tilde{v}, r) = \frac{1}{\sqrt{2\pi}\sigma_{v_\parallel}(r)} \exp\left(-\frac{\tilde{v}^2}{2\sigma^2_{v_\parallel}(r)}\right) . \tag{2.19}$$

Evaluation of equation 2.18 then gives very similar results to the Gaussian streaming model (GSM) that has also been used for similar cross-correlation analyses (Paz et al., 2013; Cai et al., 2016; Paillas et al., 2021).[4]

To use equation 2.18, a model needs to be specified for the mean coherent outflow velocity $v_r(r)$. Results from simulations (e.g., Hamaus et al., 2014; Nadathur and Percival, 2019; Nadathur et al., 2019b) show that for voids similar to those used in Chapter 4, the result obtained from linear perturbation theory applied to the continuity equation,

$$v_r(r) = -\frac{1}{3} f a H r \Delta(r) , \tag{2.20}$$

where f is the linear growth rate and $\Delta(r)$ is the average mass density contrast with radius r of the void centre defined in equation 2.4.

The validity of equation 2.20 depends on the choice of void-finding algorithm and the use of alternative algorithms can lead to an agreement that is not as good, requiring

[4]It has previous been erroneously stated (e.g. Nadathur et al., 2020b) that equation 2.18 and the GSM produced numerically significantly different results. This was due to a bug in the implementation of the GSM, though evaluation of equation 2.18 was unaffected.

additional corrections to equation 2.20 (Paillas et al., 2021). Although equation 2.20 is nominally obtained from linear perturbation theory,[5] we do not make further approximations of linearity in our analysis. In particular, equation 2.18 is evaluated directly, without expanding in powers of Δ as is sometimes done.

While equation 2.20 specifies the form of the dependence on the growth rate f, it still refers to the void matter density profile $\Delta(r)$, which is in principle unknown. Some works (e.g. Hamaus et al., 2017; Hawken et al., 2020; Aubert et al., 2022a) model this term using a simple linear bias prescription, $\Delta(r) = \xi^r(r)/b$, where b is the large-scale linear galaxy bias, to relate it to the real space void-galaxy correlation (which can, in turn, be directly measured from the data, where necessary). However other authors have found that this assumption is often a poor approximation and can lead to strongly biased parameter estimates (Nadathur and Percival, 2019; Nadathur et al., 2020b). An alternative method (used in Chapter 4) follows a *template-fitting* approach instead. A fiducial template $\Delta^{\rm fid}(r)$ can be calibrated using galaxy, void and dark matter information in full N-body simulations at snapshot redshift $z_{\rm ref}$. The amplitude of this template profile is allowed to scale freely with the parameter σ_8 describing the amplitude of matter perturbations:

$$\Delta(r; z) = \frac{\sigma_8(z)}{\sigma_8^{\rm BigMD}(z_{\rm ref})} \Delta^{\rm fid}(r; z_{\rm ref}) \,. \tag{2.21}$$

This linear scaling of Δ with σ_8 was verified through comparison with simulations constructed with differing σ_8 by Nadathur et al. (2019b).

In a similar spirit, the dispersion function $\sigma_{v_{||}}(r)$ can be modelled using a template fitting approach following Nadathur et al. (2019b). Templates for the dispersion function are calculated from full N-body simulations, where the amplitude of this template, denoted by σ_v and corresponding to the asymptotic value of $\sigma_{v_{||}}(r)$ at large r, is set to be a free parameter in model fits.

Even once $\Delta(r)$ and $\sigma_{v_{||}}(r)$ have been specified in this way, equation 2.18 only describes the relationship or mapping between the real space and redshift space correlation functions ξ^r and ξ^s. Modelling ξ^r itself from first principles would, at a minimum, require a mathematical model of the action of the void-finding algorithm in addition to cosmological theory. As no such model exists, one approach is to follow Nadathur et al. (2019b) and Nadathur et al. (2020b) by using the estimate $\langle\hat{\xi}^r\rangle$ determined from mocks catalogues instead, where $\hat{\xi}^r$ is the measured void-galaxy correlation obtained using the RSD-removed mock galaxy field after reconstruction, and $\langle\rangle$ denotes the average over all the mocks.

[5]But note that the enclosed mass density profile $\Delta(r)$ here is *not* the linear theory prediction, but rather the fully non-linear density that would be measured in simulations.

An alternative to using this average over the mocks could be to use the estimate $\hat{\xi}^r(r)$ obtained directly from measurement in the SDSS data itself – this would be analogous to the approach taken by Hamaus et al. (2022) to approximate $\xi^r(r)$ from the data, except that they used a deprojection technique instead of reconstruction to accomplish RSD removal. Such an approach has two potential disadvantages however: the estimate of $\xi^r(r)$, being derived from only a single realisation rather than the mean of many mocks, is significantly noisier; and this noise is significantly correlated with measurement noise in $\xi^s(\vec{s})$ since both are measured from the same data. This introduces a significant correlation between the model prediction and the data vector to which it is being compared. This correlation would need to be carefully accounted for in the covariance matrix and propagated through the likelihood. If this is not done, the fit to the data returns an artificially low χ^2 and can lead to a systematic bias in the recovered cosmological parameters. In contrast, for the template fitting procedure described above such accounting is not necessary, since the mean $\langle\hat{\xi}^r\rangle$ over the mocks cannot be correlated with ξ^s measured in the SDSS data.

2.8.2 Alcock-Paczynski Distortions in Voids

While equation 2.18 is only valid in the true cosmology without Alcock-Paczynski (AP) distortions (Alcock and Paczynski, 1979), it is simple to extend this to accommodate differences arising due to the choice of the fiducial model used to convert observed redshifts to distances. To do so the α scaling parameters are defined as

$$\alpha_\perp \equiv \frac{D_\mathrm{M}(z)}{D_\mathrm{M}^\mathrm{fid}(z)} \; ; \; \alpha_\parallel \equiv \frac{D_\mathrm{H}(z)}{D_\mathrm{H}^\mathrm{fid}(z)} \, , \tag{2.22}$$

where $D_\mathrm{M}(z)$ is the comoving angular diameter distance and $D_\mathrm{H}(z) = c/H(z)$ is the Hubble distance at redshift z as discussed in Section 1.5. The correlation function can now be extended as

$$\xi^s(s_\perp, s_\parallel) = \xi^{s,\mathrm{fid}}\left(\alpha_\perp s_\perp^\mathrm{fid}, \alpha_\parallel s_\parallel^\mathrm{fid}\right) \, , \tag{2.23}$$

where the superscript $^\mathrm{fid}$ indicates quantities in the fiducial cosmological model. In calculations using equation 2.18, the input functions $\hat{\xi}^r(r)$, $\Delta(r)$ and $\sigma_{v_\parallel}(r)$ need to be rescaled with the AP α parameters as described by Nadathur et al. (2019b), equivalent to changing the apparent void size by $r \to \alpha_\perp^{2/3}\alpha_\parallel^{1/3} r$ to account for AP dilations. This means the absolute void size is not used as a standard ruler and so the model prediction is sensitive only to the ratio

$$\epsilon \equiv \alpha_\perp/\alpha_\parallel. \tag{2.24}$$

All model calculations shown are made using the public Python package `Victor`.[6] In addition to the model of equation 2.18 described here, `Victor` also implements the GSM and a number of other models that have been used in the literature in order to enable easy comparison of theoretical approaches.

It is also worth noting again that as with the measured data vector, the model prediction for ξ^s inherits an implicit dependence on $\beta = f/b$ through $\xi^r(r)$ which is determined using reconstructed galaxy data. In work in Chapter 4, this is accommodated as described in Section 4.2.

2.9 The Velocity Field in Voids

The velocity profile of galaxies is commonly assumed to match the velocity profile of matter at all scales around voids. This assumption may not be true as the profiles can differ due to selection effects (Massara et al., 2022). One of the ways in which a selection bias can be introduced is through galaxies being biased and sparse tracers of the matter field. This is of particular concern in voids as galaxies are used in their identification. As voids are found using a sparse sample of galaxies as tracers they are very sensitive to the shot noise of the sample. The definition of a void centre can be highly affected by this as it correlated with the particular Poisson noise realization of galaxies used to identify voids. If a void centre is shifted from that of the minimum of the matter density field then the distribution of matter around the void centre may be asymmetric and differ from the galaxy distribution around the void centre. This then causes two main effects: matter and velocity profiles around void centres are different, and the ratio between the galaxy density profile and matter density profiles is different than from just the galaxy bias.

To explore this a toy model can be built to understand the effect of the sparsity of tracers on the properties of a particular void. The first effect explored is whether sparse tracers shift the position of void centres. To test this a simulated matter field is created with a 3D distribution of matter particles that is spherically symmetric about the origin, mimics the density profile found around voids in simulations (see Section 2.4), and has a mean background density matching that of the cold dark matter in the same simulations. The void has radius $R_{\rm v} \sim 30h^{-1}$Mpc. Particles are randomly subsampled (0.3% are used) to mimic the mean number density of halos in simulations. A Voronoi tessellation is applied to the subgroup and the void centre is defined as the centre of the largest Voronoi cell (i.e.

[6] https://github.com/seshnadathur/victor

the cell with the lowest density). Figure 2.9 shows the distribution of shifts from the true void centre which peaks around $15 - 20h^{-1}$Mpc.

To demonstrate the effect of this shift on void density and velocity profiles a 1D toy model is built as follows

$$\delta = \begin{cases} -0.95 & |r| < R_{\rm v}/2 \\ 1.9(|r|/R_{\rm v} - 1) & R_{\rm v}/2 < |r| < R_{\rm v} \\ 0 & |r| > R_{\rm v} \end{cases} \tag{2.25}$$

where r is the distance from the void centre and $R_{\rm v}$ is the void size. Particles are given a radial velocity v that depends on its distance r from the centre as

$$v = \begin{cases} 4/3\, C\, |r|/R_{\rm v} & |r| < 3R_{\rm v}/4 \\ 4/3\, C\, [1 - |r|/(3R_{\rm v})] & |r| > 3R_{\rm v}/4 \end{cases} \tag{2.26}$$

where C is the maximum value of the velocity reached at a distance $r = 3R_{\rm v}/4$. A subgroup of matter particles corresponding to equation 2.25 centred at $x = -15$ is also used, where this shift is taken as the peak of shifts from Figure 2.9. The radial velocity and enclosed density are then calculated for these two different toy models in Figure 2.10. As can be seen in this figure, the velocity and density profiles of the shifted void are different from that of the unshifted void at smaller radii similar to that of the size of the void. This shows that any shift in void centres due to the sparsity of tracers will result in density and velocity profiles that differ from if a void centre was identified correctly.

To quantify these effects a subset of the Quijote simulations is used (Villaescusa-Navarro et al., 2020). The Quijote simulations are a set of 44,100 full N-body simulations spanning more than 7,000 cosmological models where each simulation follows the evolution of 256^3, 512^3, or 1024^3 particles in a box of 1 h^{-1}Gpc length. Three void finders are applied to this subset (spherical, `VOXEL`, and `ZOBOV`, see Section 2.3) along with different void-centre definitions to create five different types of void catalogues.

The sparsity of tracers in the absence of bias is examined. The matter field randomly subsampled to different numbers of dark matter particles is used to do this and voids are identified in this dark matter sample. These results are shown in Figures 2.11 & 2.12. As can be seen, the velocity profiles of the full and subsampled matter field match on all scales for spherical voids. This is not the case for `ZOBOV` and `VOXEL` voids; however, this is mitigated by using a larger number of tracers in the subsampled field.

A similar analysis can be performed for voids found in a halo field. These profiles are found to match at all scales for spherical voids but differ for voids found using `ZOBOV` and

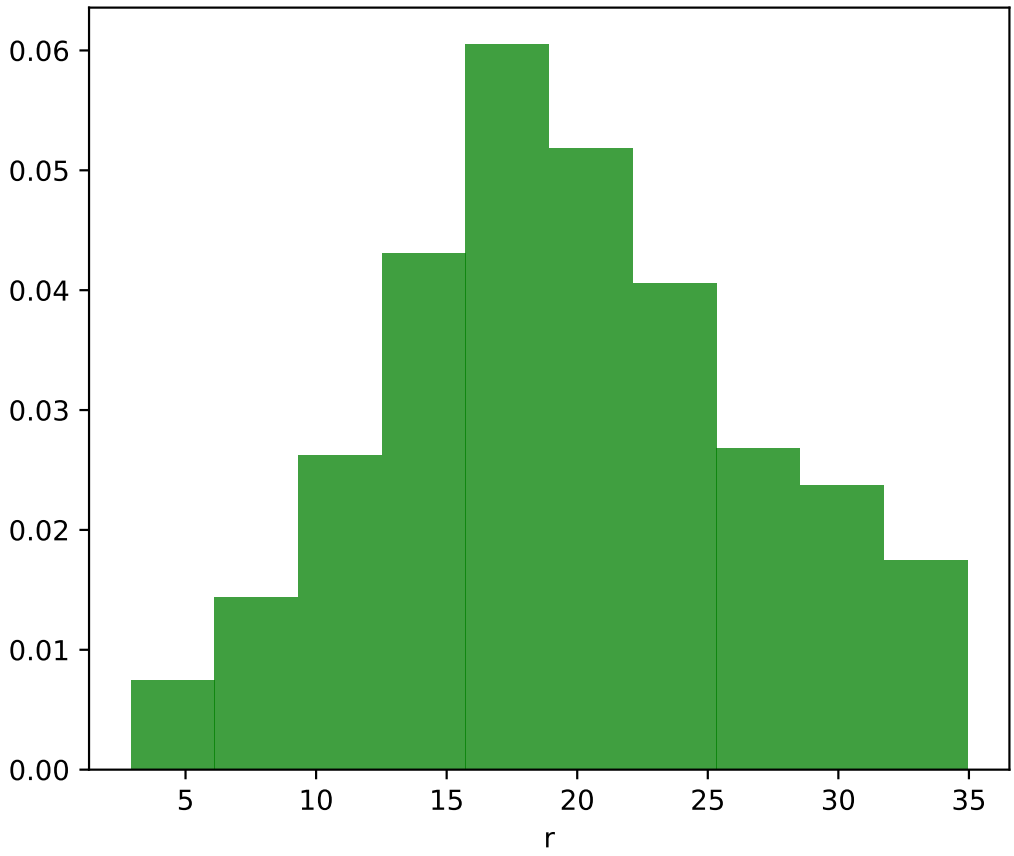

Figure 2.9: Distribution of shifts between void centres in the original distribution and the subgroup particles. Initial particles are assumed to follow ZOBOV void-like density and velocity profiles. Image credit: Massara et al. 2022

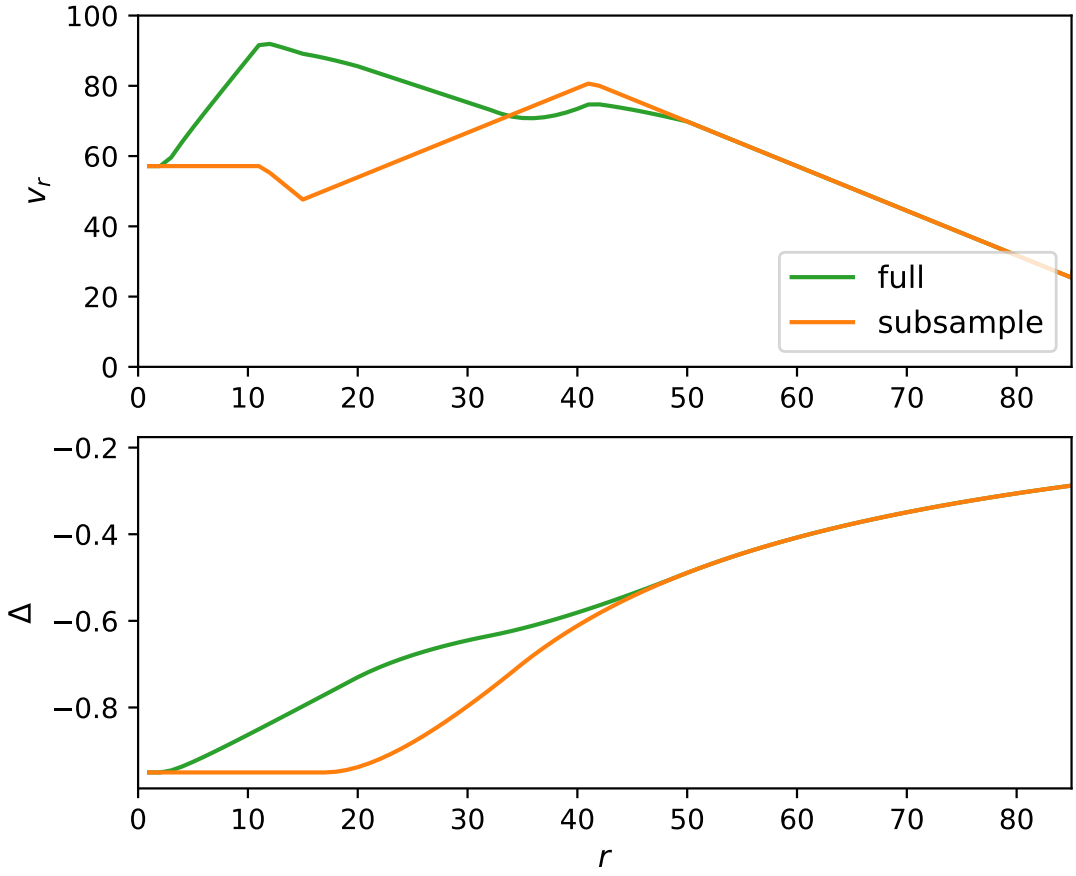

Figure 2.10: Velocity (top) and enclosed density (bottom) profiles of the 1D toy model. The green line shows the profiles of the full matter field and the orange line shows the profiles of the subsampled matter field. Image credit: Massara et al. 2022

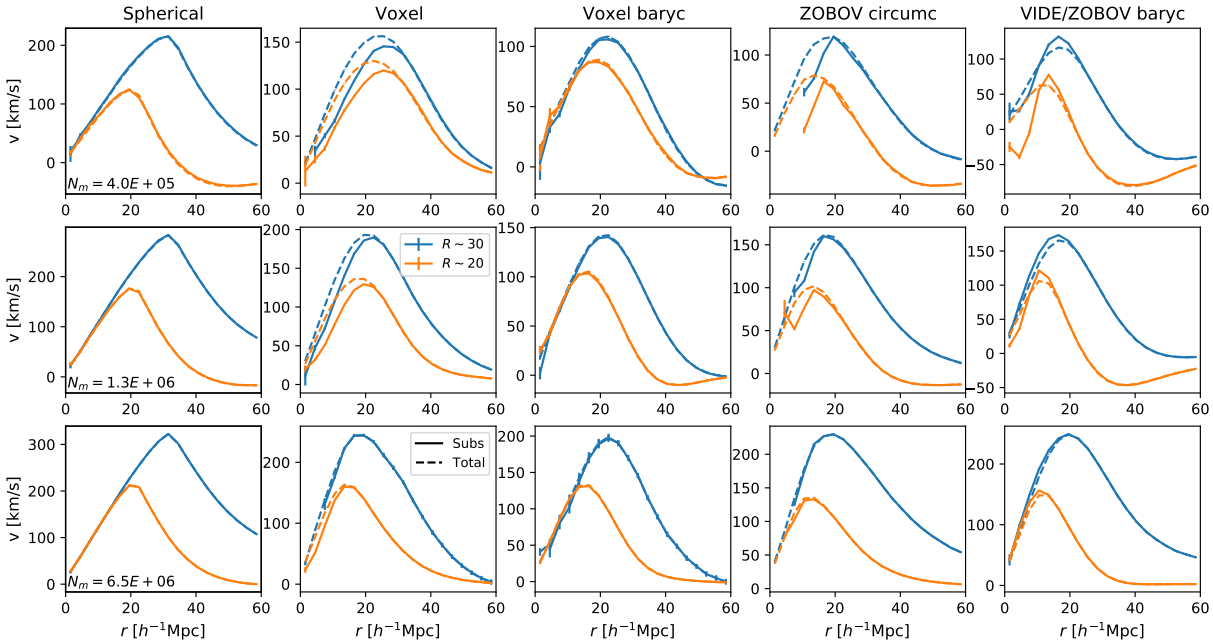

Figure 2.11: Velocity profiles from voids identified using the subsampled matter field. Different rows correspond to different numbers of matter particles in the subsampled field, and columns represent different void finders/centre definitions. Void sizes are shown in different colours, dashed lines are for the measured profile in the total matter field, and solid lines show measured profiles in the subsampled matter field. Image credit: Massara et al. 2022

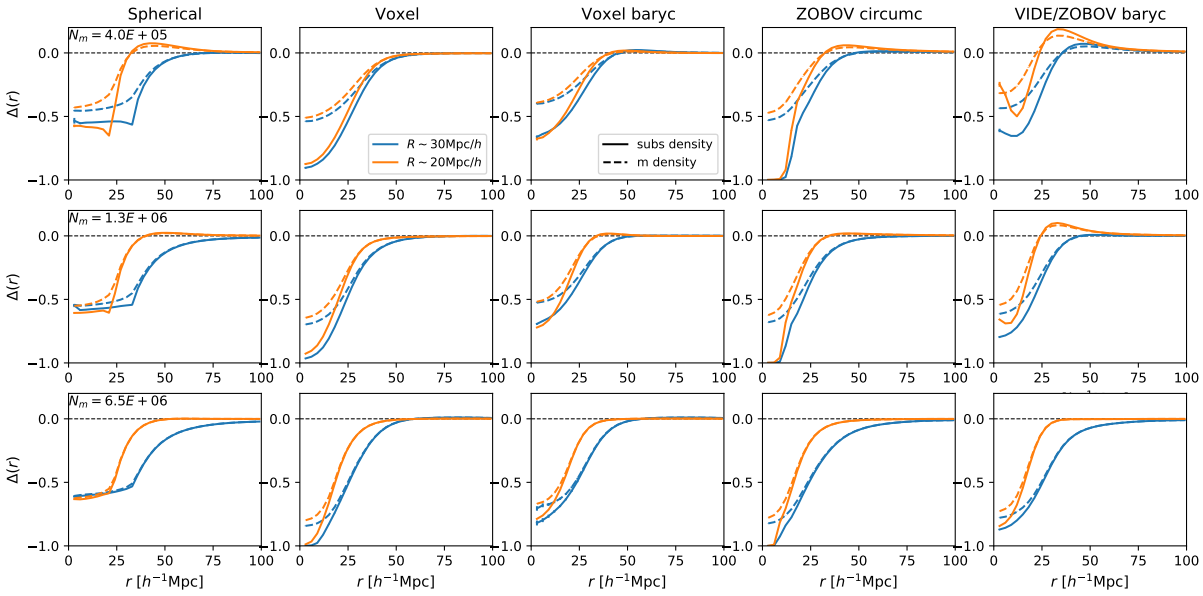

Figure 2.12: Enclosed density profiles for voids found in the subsampled field. The solid line shows voids found in the subsampled matter field and the dashed line shows voids found in the total matter field. The line colour corresponds to the void size. Image credit: Massara et al. 2022

VOXEL void finders. The difference increases as the distances from the centres decrease, reaching 40% in the centre of the voids.

Velocity profiles are used inside the Jacobian of models for the void galaxy correlation function to map from real to redshift space (see equation 2.18). Differences in the matter and halo velocity profiles, seen in simulations data be of the order of $20 - 40\%$, translate to errors of $\sim 5\%$ in the Jacobian. This is of similar magnitude to the systematic errors found in the analysis of Chapter 4 (see Section 4.3.2).

This is of concern to future work (e.g. Hamaus et al., 2022; Radinović et al., 2023) where the forecast statistical uncertainties in $f\sigma_8$ will be much smaller than the current limits. Future RSD analysis using the void-galaxy correlation function will need to take into account the effect of sparsity on the halo/galaxy velocity profiles to avoid a biased estimation of $f\sigma_8$ when using watershed algorithms. Spherical voids appear affected much less by this effect and should be used in future analyses of cosmic voids.

2.10 Previous Analyses Involving the Void-Galaxy Correlation Function

This thesis measures the void-galaxy correlation function. The following section summarises previous analyses that used the void-galaxy correlation function on galaxy spectroscopic survey data. This is not intended to be a complete list but rather to provide an overview of approaches previously used when analyzing the void-galaxy correlation function.

Paz et al. (2013) were the first to measure the void-galaxy correlation function in galaxy spectroscopic data, using data from SDSS Main Galaxy sample (see Section 3.2.1). This work obtained evidence of a two-fold population of voids (with and without a surrounding overdensity) but did not constrain cosmological parameters.

Hamaus et al. (2016) analysed BOSS CMASS DR11 data (see Section 3.2.2) in the redshift range $0.43 < z < 0.7$ using fitting functions to model the matter density around voids. The authors accounted for both RSD around voids as well as AP effect in their results and found $\beta(z = 0.57) = 0.417 \pm 0.089$ and $\epsilon(z = 0.57) = 1.003 \pm 0.012$. Hamaus et al. (2020) reanalyzed BOSS CMASS data from the later data release DR12 and used a deprojection technique instead of fitting functions to model the matter density and found (we quote the best constraints that used mock catalogues to calibrate nuisance parameters) and found $\beta(z = 0.51) = 0.347 \pm 0.023$ and $\epsilon(z = 0.51) = 1.0011 \pm 0.0060$.

Hawken et al. (2017) analysed voids in the VIMOS Public Extragalactic Redshift Survey (VIPERS) to measure the growth rate of structure around cosmic voids but did not account for the AP effect. Using a deprojection technique they found $\beta(z = 0.727) = 0.423^{+0.104}_{-0.108}$. Hawken et al. (2020) applied a similar technique to eBOSS DR14 LRGs and Quasar Stellar Objects (QSOs) and found $\beta(z = 0.703) = 0.58^{+0.33}_{-0.29}$ and $\beta(z = 1.53) = 0.15^{+0.13}_{-0.12}$ respectively; however, they noted that the QSO catalogue may be contaminated by spurious Poisson voids resulting in a systematically low value of β.

Achitouv et al. (2017) analysed voids in the 6dF Galaxy Survey to measure the growth rate of structure around cosmic voids but did not account for the AP effect. They used mock catalogues designed to match this survey and followed a template-based approach (as in this thesis) but did not account for any adverse effects from void finding in redshift space and found $f\sigma_8(z = 0.052) = 0.39\pm, 0.11$. Achitouv (2019) applied a similar technique to BOSS DR12 LOWZ and CMASS samples (see Section 3.2.2) and found $\beta(z = 0.32) = 0.33 \pm 0.06$ and $\beta(z = 0.54) = 0.36 \pm 0.05$ respectively.

Aubert et al. (2022b) analysed voids in the SDSS eBOSS sample (see Section 3.2.3) to measure the growth rate of structure around cosmic voids but did not account for the AP effect. Their model, based on the first-order derivation of linear perturbation theory requires no knowledge of ξ^r nor specific modelling of peculiar velocities, however, it neglects any adverse effects from void finding in redshift space. All three available eBOSS tracers (LRGs, ELGs, and QSOs) were analysed finding $\beta(z = 0.74) = 0.415 \pm 0.087$, $\beta(z = 0.85) = 0.52 \pm 0.10$, and $\beta(z = 1.48) = 0.30 \pm 0.13$ respectively.

Nadathur et al. (2019a) measured voids in the SDSS CMASS sample in the redshift range $0.43 < z < 0.7$ and their modelling accounted for both RSD around voids as well as AP effect. This publication applies a similar analysis method to that used in subsequent chapters of this thesis including the use of reconstruction prior to void finding to account for adverse effects from void finding in redshift space and found $\beta = 0.417 \pm 0.089$ and $\epsilon = 1.003 \pm 0.012$. Nadathur et al. (2020b) applied a similar analysis technique to eBOSS LRGs and found $f\sigma_8 = 0.356 \pm 0.077$ and $\epsilon = 1.005 \pm 0.018$. This later work applied a data analysis pipeline consistent with work in later chapters of this thesis and does not contain any overlap in galaxies considered. These results are present in conjunction with results from Chapters 3, 4, & 5 to present measurement from the full SDSS LRG sample using a consistent data analysis technique.

Chapter 3

The Sloan Digital Sky Survey and Measurements of the Void-Galaxy Correlation Function

3.1 Introduction

Modern galaxy surveys aim to generate large maps of the Universe. The clustering of galaxies in these maps can then be used to pull out useful cosmological information. Their main goal is to improve our understanding of the accelerating expansion of the Universe (i.e. dark energy) but they also contain a wealth of information about the cosmic web, the distribution of dark matter, and the growth rate of large-scale structure. These 3-dimensional maps of the Universe originated when galaxy photographic surveys were first combined with spectroscopic surveys in the 1980s, pioneered by the CfA Redshift survey that surveyed approximately 3000 galaxies out to redshift $z = 0.04$ (Geller and Huchra, 1983).

More recent surveys have measured millions of redshifts thanks to advances in instrumentation. Recent and upcoming spectrographic surveys use instruments that allow for multiple galaxy spectra to be measured simultaneously, increasing survey speeds by factors of hundreds to thousands. Recent surveys include the 2-degree Field Galaxy redshift survey (2dFGRS; Colless et al. 2003), WiggleZ (Drinkwater et al., 2010), and SDSS (York et al., 2000). A section of SDSS galaxies is shown in Figure 3.1. Upcoming surveys include the Dark Energy Spectroscopic Instrument (DESI; DESI Collaboration et al. 2016a) and Euclid (Laureijs et al., 2011). This thesis primarily uses data from SDSS; this survey and

the samples included within it are described in more detail below. This is the first time voids in the full SDSS LRG range have been analysed using a consistent data analysis technique.

There are three main types of tracers available in these surveys: luminous red galaxies (LRGs), emission line galaxies (ELGs), and quasars. LRGs are the most luminous galaxies in clusters and are well known to have a very homogeneous population (Postman and Lauer, 1995) with a narrow colour range and luminosity. As spectroscopic surveys aim to select a uniform sample this makes LRGs excellent targets. As their name implies, they are luminous and can be seen out to high redshifts. ELGs are galaxies that have strong emission lines in their spectra. These are typically low-mass star-forming galaxies that are more luminous than LRGs and can be seen to higher redshifts than LRGs. Quasars are even more luminous galaxies than ELGs that are seen via the accretion onto supermassive black holes at the centres of galaxies. As these objects are extremely bright they can be seen out to much higher redshifts than LRGs and ELGs. In this thesis, we focus on LRGs that have a higher number density in SDSS and have been well studied in previous work involving voids (e.g. Nadathur et al., 2017; Hawken et al., 2017; Nadathur et al., 2019a; Achitouv, 2016, 2019).

The focus of this thesis is the cosmological analysis of voids identified in galaxy samples within the Sloan Digital Sky Survey. We analyse the Main Galaxy Sample (MGS; Howlett et al. 2015b; Ross et al. 2015) of SDSS-II (York et al., 2000), the Baryon Oscillation Spectroscopic Survey (BOSS; Dawson et al., 2013) of SDSS-III (Eisenstein et al., 2011), and the extended BOSS (eBOSS; Dawson et al., 2016) of SDSS-IV (Blanton et al., 2017), covering a wide range in redshift and using a consistent analysis method. These data represent the best public galaxy redshift survey data available to date. BOSS is composed of two data samples, LOWZ and CMASS, both of which are used in this analysis. The analysis method used is consistent with that applied to eBOSS in Nadathur et al. (2020b) which is presented with our results. It has not previously been applied to the MGS or low redshift BOSS samples. By analysing these new data and consolidating previous analyses, we are able to build a picture of the geometrical evolution of the Universe and the evolution of the growth of structure within it from only the analysis of SDSS galaxies around voids.

This thesis does not consider the additional BOSS/eBOSS samples of quasars and emission line galaxies (ELGs) that extend out to higher redshifts ($z < 2.2$). The sparsity of tracers in the quasar sample means that the reconstruction technique our method relies on is not efficient. This can be seen in Figure 3.2. If reconstruction is able to correctly remove redshift space distortions from a sample of tracers then the reconstructed power spectrum multipoles will match those of the real space power spectrum on all scales; this figure shows that this is not the case. This was tested on OuterRim cubic boxes, simulated

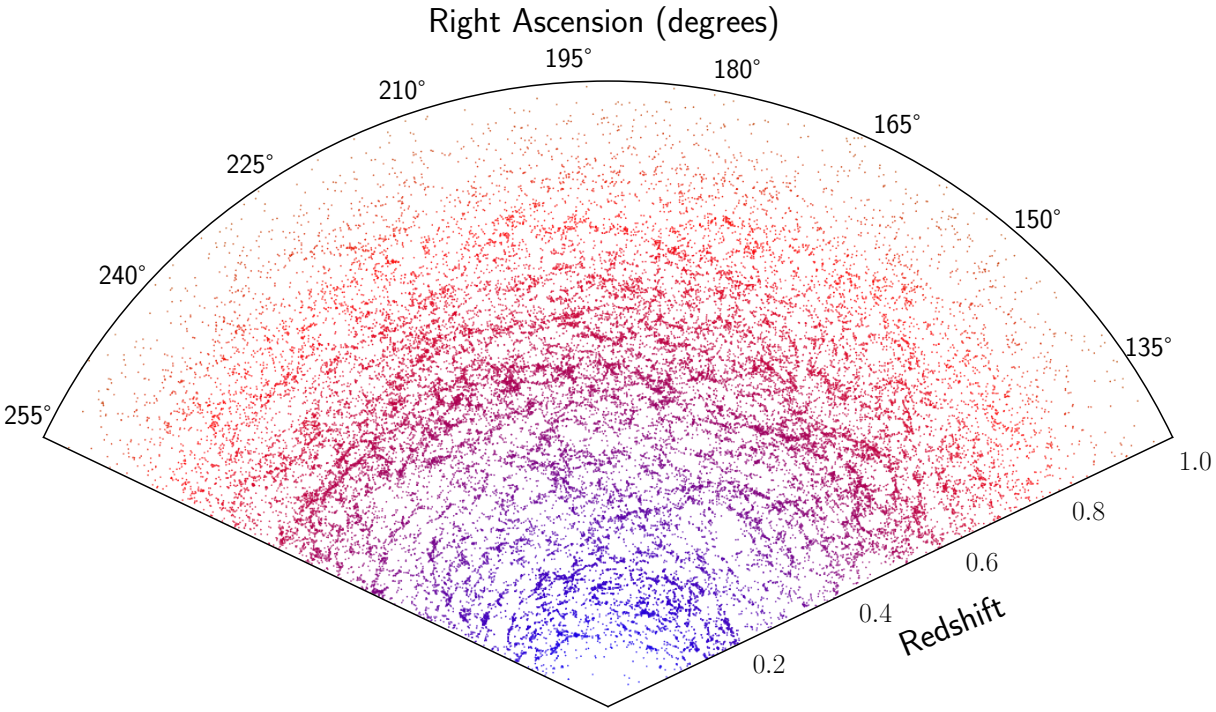

Figure 3.1: A slice of SDSS LRGs shown in redshift space. Galaxies are included from MGS, BOSS, and eBOSS. Only galaxies from BOSS and eBOSS NGC are shown. Galaxies are trimmed to a narrow range (2.3 degrees) in declination to highlight large-scale structure in the survey. The full range in Right Ascension is not shown and has been narrowed to show a section with full sky coverage across all redshift ranges shown (see Figure 3.3).

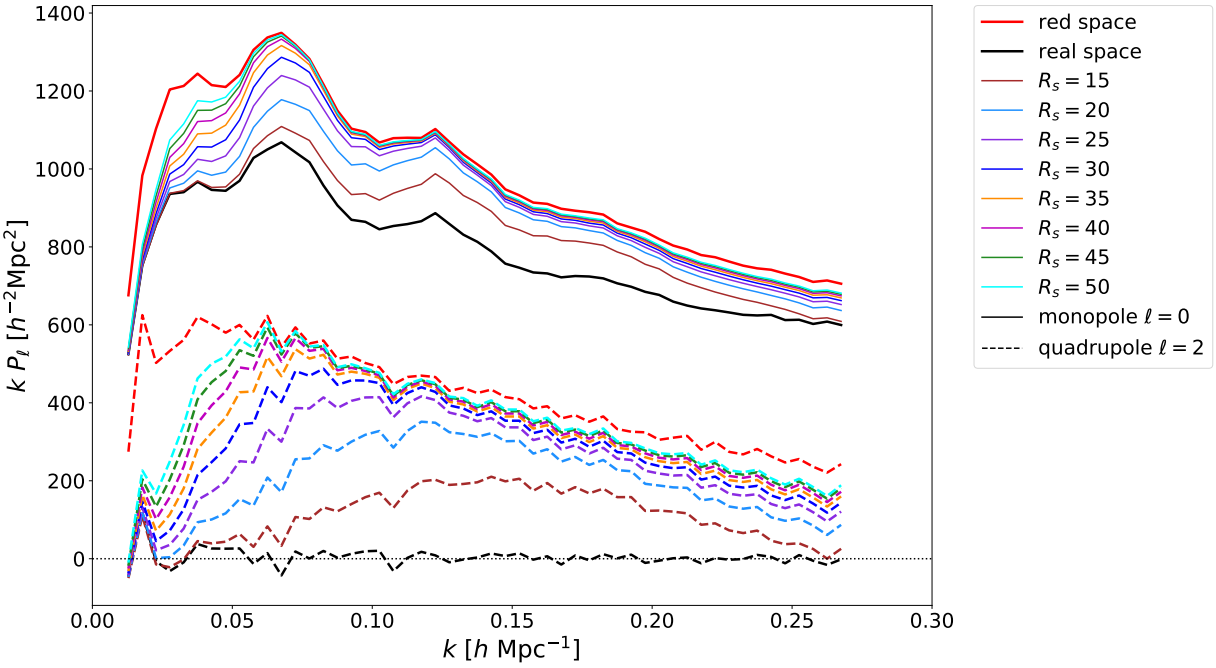

Figure 3.2: Power spectrum multipoles in the OuterRim cubic boxes. OuterRim is a simulated volume of the Universe of side length 3.0 h^{-1}Gpc, with galaxies designed to closely match those of the eBOSS Quasar sample (Smith et al., 2020; Heitmann et al., 2019). It can be seen that for all reasonable values of smoothing parameter R_s the reconstruction technique fails to properly match the power spectrum multipoles in real space, unlike for the LRGs shown in Figure 3.4.

cubic boxes of side length 3.0 h^{-1}Gpc that are designed to closely match the properties of the eBOSS quasar sample (Smith et al., 2020; Heitmann et al., 2019). No value of the smoothing parameter R_s used in the reconstruction technique allows the reconstructed multipoles to match that of the multipoles found in real space closely. On the other hand, the ELG sample was selected from imaging data that had anisotropic properties and suffered from significant angular fluctuations (Raichoor et al., 2021). Tamone et al. (2020); de Mattia et al. (2021) showed that careful corrections for these effects could be made for BAO and RSD analyses of galaxy clustering, but we leave extensions of this work to the void-galaxy correlation to future work.

In this chapter, the data and mock catalogues analysed in Chapter 4 are introduced. This work was originally published in first-author publication Woodfinden et al. (2022). In addition to the MGS and BOSS data, mock galaxy catalogues are used as tests of the

analysis pipeline and to estimate the statistical errors in data measurements (described in Sections 3.2.1 & 3.2.2). A smaller collection of full N-body mocks are used, in addition to the approximate mocks, to quantify the magnitude of the systematic errors (described in Section 3.2.2). Mocks are created from full N-body simulation boxes with dark matter information to calibrate template profiles used in the theoretical modelling (described in Section 3.2.4). We summarise the voids found in SDSS data in Section 3.3 and the void-galaxy correlation functions measured from these in Section 3.4. Finally, we present the template functions needed to model the void-galaxy correlation function in Section 3.5.

3.2 Surveys

3.2.1 MGS

The Main Galaxy Sample (MGS; Strauss et al., 2002) is a selection of galaxies from the SDSS-I and SDSS-II surveys (York et al., 2000) Data Release 7 (DR7; Abazajian et al., 2009), at redshifts $0.07 < z < 0.2$, with spectra taken using spectrographs mounted on the 2.5-meter telescope at Apache Point Observatory in New Mexico. A subsample of this catalogue, created for large-scale structure analyses, is described by Ross et al. (2015) and Howlett et al. (2015b), which used additional colour, magnitude and redshift cuts to obtain a high-bias ($b \sim 1.5$) sample of galaxies occupying dark matter halos with $M_{\rm halo} > 10^{12}\,M_{\odot}$, and with a high galaxy density. This sample, which we refer to as MGS, consists of 62 163 galaxies covering a contiguous footprint of 6813 deg^2 in the Northern Galactic Cap (NGC) region between redshifts $0.07 < z < 0.2$. The MGS footprint is shown in Figure 3.3. Systematic weights are included in the catalogue to correct for angular fluctuations due to target selection effects (Ross et al., 2012). Main results from BAO and RSD are published in Ross et al. (2015); Howlett et al. (2015b) with best fit measurements from the combination of these two finding $f\sigma_8(z = 0.15) = 0.53 \pm 0.16$ and $D_{\rm V}/r_{\rm d}(z = 0.15) = (zD_{\rm M}^2 D_{\rm H})^{1/3}/r_{\rm d} = 4.51 \pm 0.14$.

MGS Mocks

The MGS mocks contain 1000 mock galaxy catalogues matching the footprint, redshift distribution and clustering properties of the MGS data (Howlett et al., 2015b). These mocks were built from 500 independent dark matter simulations at $z = 0.15$ created using the `PICOLA` algorithm (Howlett et al., 2015a), with fiducial cosmology $\Omega_{\rm m} = 0.31$, $\Omega_b =$

0.048, $h = 0.67$, $\sigma_8 = 0.83$ and $n_s = 0.96$. Halos were selected in this field using a friends-of-friends algorithm and populated with mock galaxies using a Halo Occupation Distribution (HOD) prescription with parameters fitted to the MGS data, as described in Ross et al. (2015). From each box two non-overlapping sections were then cut out to match the MGS footprint, and the mocks subsampled to match the redshift-dependence of the mean galaxy density in the data.

In Chapter 4 all 1000 of these mocks were used to obtain an accurate estimate of the covariance matrix for the measurement and a subset of 250 of them were used to test the analysis methods for systematic errors. All 1000 mocks were used in the calculation of ξ^r described in Section 3.5.

3.2.2 BOSS

The Baryon Oscillation Spectroscopic Survey (BOSS; Dawson et al., 2013) of SDSS-III (Eisenstein et al., 2011) measured spectra from more than 1.5 million objects using spectrographs upgraded from those used for MGS, mounted on the 2.5-meter Sloan telescope (Gunn et al., 2006). The target sample covered nearly 10 000 deg^2 of the sky over two hemispheres, the North Galactic Cap (NGC) and the South Galactic Cap (SGC). The final BOSS data were included in Data Release 12 (DR12; Alam et al., 2015). The large-scale structure catalogues were created using two different target selection algorithms, LOWZ and CMASS (Reid et al., 2016). The LOWZ sample was designed to target luminous red galaxies in a narrow mass range over the redshift range $0.2 \lesssim z \lesssim 0.4$, while the CMASS sample was designed to target LRGs in a narrow mass range over the redshift range $0.4 \lesssim z \lesssim 0.75$. The LOWZ footprint is slightly smaller than, and fully encompassed within, the CMASS footprint, as shown in Figure 3.3.

Despite these differences, the LOWZ and CMASS samples show very similar clustering amplitudes across both NGC and SGC. Following Alam et al. (2017) when measuring the void-galaxy correlation function in BOSS data this work analysed the *combined sample*, including a small region of redshift overlap. As described below in Section 3.3, the change in the survey footprint around $z \simeq 0.43$ must be accounted for when identifying voids but allows for more efficient use of the data.

In the recent eBOSS Data Release 16 (DR16; Ahumada et al., 2020) cosmological analyses (Alam et al., 2021), the high-redshift end of the CMASS sample at $z > 0.6$ was combined with the eBOSS LRG sample, which overlaps with it in redshift and footprint. A measurement of the void-galaxy cross-correlation in this combined eBOSS+CMASS sample has already been presented by Nadathur et al. (2020b), using very similar methods to those

we presented here. In analysing the BOSS data the analysis is therefore restricted to the section of the combined BOSS LOWZ and CMASS samples that are below this redshift. In practice, to minimize the loss of voids due to edge effects close to a survey boundary, all galaxies within $0.2 < z < 0.63$ were used for void-finding, but then only those voids with centres that lie at $z < 0.6$ were used for the cross-correlation measurement.

Main results from BAO and RSD are published in Alam et al. (2017) and found $f\sigma_8(z = 0.38) = 0.497 \pm 0.045$, $f\sigma_8(z = 0.51) = 0.459 \pm 0.038$, $D_{\rm M}/r_{\rm d}(z = 0.38) = 10.27 \pm 0.15$, $D_{\rm M}/r_{\rm d}(z = 0.51) = 13.38 \pm 0.18$, $D_{\rm H}/r_{\rm d}(z = 0.38) = 24.89 \pm 0.58$, and $D_{\rm H}/r_{\rm d}(z = 0.51) = 22.43 \pm 0.48$ from a combination of these two measurement techniques. The void-galaxy cross-correlation in a subset of these data, corresponding to the CMASS sample alone in the range $0.43 < z < 0.7$, was analysed by Nadathur et al. (2019b). That work used a single redshift bin and reported precise constraints on $f\sigma_8(z = 0.57) = 0.501 \pm 0.051$ and $D_{\rm M}/D_{\rm H}(z = 0.57) = 0.4367 \pm 0.0045$. However, the CMASS data used partially overlaps (at $z > 0.6$) with the eBOSS+CMASS sample used by Nadathur et al. (2020b) and with the combined LOWZ+CMASS sample used here. The work presented in this thesis aims to provide a coherent analysis of the data superseding that of Nadathur et al. (2019b) over a range of redshift bins that can be combined with the eBOSS results of Nadathur et al. (2020b) without overlap.

Patchy Mocks

The Patchy mocks are a set of 1000 independent mock catalogues on the lightcone created to match the clustering and the survey properties of the BOSS galaxies (Kitaura et al., 2016). They were created using the fast approximate `Patchy` algorithm (Kitaura et al., 2014) based on augmented Lagrangian perturbation theory (Kitaura and Heß, 2013), run with fiducial cosmological parameters $\Omega_{\rm m} = 0.307$, $\Omega_b = 0.0482$, $h = 0.6777$, $\sigma_8 = 0.8225$ and $n_s = 0.96$. Mock galaxies were assigned to halos using halo abundance matching, with parameters chosen to reproduce the monopole and quadrupole moments of the galaxy clustering in the BOSS data. The survey mask and selection function were then also matched to those of BOSS.

All 1000 of the Patchy mocks were used to estimate covariance matrices and a smaller subset of 250 of them to test our analysis method for systematic errors. These are analyzed in the same way as with the BOSS data with the same redshift cuts, i.e. restricting to galaxies with redshift $0.2 < z < 0.63$ and voids with redshift $0.2 < z < 0.6$ to avoid redshift overlap with the section of the data included in the eBOSS analysis. 250 mocks were used in the calculation of ξ^r described in Section 3.5.

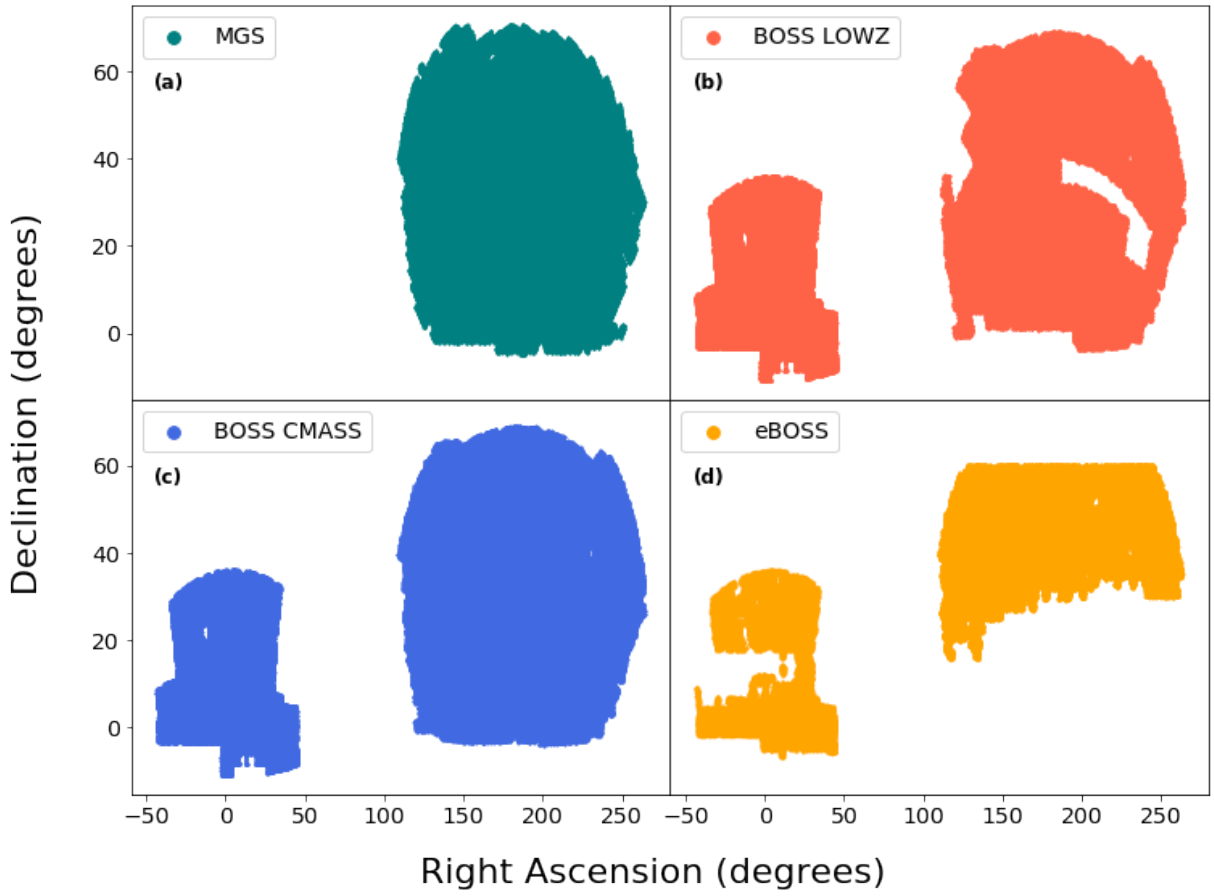

Figure 3.3: Footprints of the different SDSS galaxy catalogues: (a) the MGS from SDSS DR7, covering $0.07 < z < 0.2$; (b) the BOSS LOWZ catalogue from SDSS DR12, covering $0.2 < z \lesssim 0.43$; (c) the BOSS CMASS catalogue from SDSS DR12, covering $0.4 \lesssim z \lesssim 0.75$; (d) the eBOSS LRG catalogue from SDSS DR16, covering $0.6 < z < 1.0$.

NSERIES Mocks

The NSERIES mocks are a collection of 84 cut-sky mocks made from 7 independent full N-body dark matter simulations with 2048^3 particles per box and a mass resolution of $1.5 \times 10^{11} \mathrm{M}_{\odot}/h$, generated using a flat ΛCDM cosmology with $\Omega_{\mathrm{m}} = 0.286$, $\Omega_b = 0.0470$, $h = 0.70$, $\sigma_8 = 0.82$, and $n_s = 0.96$. Halos at redshift $z = 0.55$ were populated with mock galaxies using a halo occupation distribution (HOD) prescription adjusted to match the clustering of the CMASS sample. From each of the 7 simulation boxes, 12 cut-sky mock catalogues were then created, covering the NGC sky region and matching the selection function for the CMASS sample over the redshift range $0.43 < z < 0.7$.

The NSERIES mocks do not match the full volume or redshift distribution of the combined BOSS data used in this work and so cannot be used for estimating covariances. However, unlike the MGS and Patchy mocks, they were created from full N-body simulations without approximation and so contain more accurate RSD information on small scales. This makes them useful for testing the analysis pipeline used in this work for systematic errors; this is shown in Section 4.3.

3.2.3 eBOSS

The extended Baryon Oscillation Spectroscopic Survey (eBOSS Alam et al., 2021) of SDSS-IV (Dawson et al., 2016) measured spectra from more than 975 000 objects, including 300 000 LRGs, using spectrographs mounted on the 2.5-meter Sloan telescope (Gunn et al., 2006). The target sample covered over 6 000 deg^2 of the sky over two hemispheres, the North Galactic Cap (NGC) and the South Galactic Cap (SGC). The redshift extent of the eBOSS LRG sample is $0.6 < z < 1.0$, overlapping the higher redshift range of CMASS data. The final eBOSS data were included in Data Release 16 (DR16 Ahumada et al., 2020). The footprint is smaller than, and fully encompassed within, the CMASS footprint, as is shown in Figure 3.3.

The main results from the measurement of BAO and RSD in this data are published in Alam et al. (2021). Values of $f\sigma_8(z = 0.70) = 0.473 \pm 0.041$, $D_{\mathrm{M}}/r_{\mathrm{d}}(z = 0.70) = 17.65 \pm 0.30$, and $D_{\mathrm{H}}/r_{\mathrm{d}}(z = 0.70) = 19.78 \pm 0.46$ are found from the combination of these two techniques. An analysis of the void-galaxy cross-correlation in the eBOSS DR16 LRG sample combined with a portion of the BOSS CMASS sample in the redshift range $0.6 < z < 1$ was presented by Nadathur et al. (2020b). As noted above. The BOSS galaxy catalogue data is cut to exclude the high-redshift section that was included together with the eBOSS LRGs in that work. The aim of this Chapter and Chapter 4 is to provide

a consistent voids analysis of all the data in the MGS, BOSS and eBOSS samples over $0.07 < z < 1.0$. Since the method used is very similar to that already presented by Nadathur et al. (2020b) we do not repeat it and so do not directly use the eBOSS data here. Nevertheless in Section 4.4 the results of this earlier work are reported alongside the new results from the lower redshift samples, and so for completeness alongside MGS and BOSS the eBOSS LRG survey footprint is presented in Figure 3.3 and the redshift distribution of the eBOSS voids in Figure 3.5.

EZ Mocks

The EZmock catalogues are a set of 1000 independent mock galaxy catalogues created to mimic the clustering properties of the eBOSS+CMASS LRG sample. They are created using the `EZMock` algorithm, a fast approximate Zeldovich algorithm combined with deterministic and stochastic bias relations, a PDF mapping scheme and additional corrections to account for RSD (Chuang et al., 2015; Zhao et al., 2020). The mocks are created on a lightcone combining the output from 4 and 5 different redshift snapshots and are trimmed to match the survey footprint and selection functions. The mocks are constructed using a flat ΛCDM cosmology, with $\Omega_m = 0.307$, $\Omega_b = 0.0482$, $h = 0.6777$, $\sigma_8 = 0.8225$ and $n_s = 0.96$.

3.2.4 Big MultiDark Simulation

The Big MultiDark (BigMD) simulation is a full N-body simulation of 3840^3 dark matter particles evolved in a $2.5h^{-1}$Gpc box using the same cosmology as for the Patchy mocks (Klypin et al., 2016). This simulation used the TreePM N-body code gadget-2 (Springel, 2005). The particle mass resolution of the simulation is $2.359 \times 10^{10}\ M_\odot/h$. This simulation does not contain galaxy catalogues and does not match the footprint of any of the SDSS data like the MGS, Patchy, NSERIES, or EZmock mocks. The primary benefit of this simulation is that dark matter information is readily available. In Chapter 4 this dark matter information is needed in order to calculate the enclosed matter density, $\Delta(r, z)$, and the velocity dispersion, $\sigma_{v_{||}}(r, z)$, around voids (see Section 2.8). To do so this simulation must be cut down to match the sky footprint and selection function of SDSS data. This process is described in Section 3.5.

3.3 Voids in SDSS

The void-galaxy cross-correlation is calculated from SDSS LRGs using the analysis technique described in Chapter 2. This section describes the application of void finding to SDSS using this technique, Section 3.4 described how the void-galaxy cross-correlation is measured, and Section 3.5 describes how the required template functions are measured.

Prior to running void-finding a reconstruction step was first run as described and motivated in Section 2.6. This was done using an RSD removal method and is performed using the `Revolver` code run using a 512^3 grid for all samples. The densities estimated on the grid were first smoothed with a Gaussian kernel of width $R_s = 10\,h^{-1}$Mpc before solving for the displacement. The performance of the reconstruction algorithm depends on the choice of smoothing scale used: see Figure 3.4. The real space power spectrum of a simulation box that closely matches the properties of the galaxy survey was used to determine what smoothing scale to use. We used a NSERIES cubic box, as described in Section 3.2.2, to closely match the survey properties. Reconstruction was run on this simulation at a variety of values of R_s and the value that best matches the real space multipole is used. Figure 3.4 shows that for a BOSS-like survey a value of $R_s = 10\,h^{-1}$Mpc provides a good fit, while $R_s = 15\,h^{-1}$Mpc fails to properly fit the real space multipoles.

Void-finding was performed on the RSD-removed galaxy distribution obtained after reconstruction, using the `Revolver` code. `Revolver` provides several options for the void-finding algorithm; we choose the one based on an adaptation of the `ZOBOV` void-finder (Neyrinck, 2008). As described in Section 2.3, this algorithm first estimates the local density using a Voronoi tessellation of the discrete galaxy distribution, and then identifies voids at the locations of local minima of this density field, using a watershed algorithm to distinguish neighbouring voids.

Instead of running reconstruction and then void-finding on the BOSS LOWZ and CMASS catalogues separately, this was performed directly with the combined BOSS sample composed of both catalogues, including a small redshift range around $z = 0.43$ where they overlap. In the analysis of voids found in eBOSS LRGs in Nadathur et al. (2020b), eBOSS LRGs were combined with high redshift CMASS LRGs at $z \geq 0.6$. To prevent the duplication of information with this work the $z > 0.6$ section of the CMASS data was excluded. Only BOSS data are used below this redshift. However, to minimise the loss of data due to the truncation of voids close to survey boundaries, a slightly larger selection of BOSS galaxies over $0.2 < z < 0.63$ was used in the first instance before restricting the final selection to only those voids with centres in the desired $0.2 < z < 0.6$ redshift range in post-processing. This prevented voids in the CMASS sample close to the redshift boundary

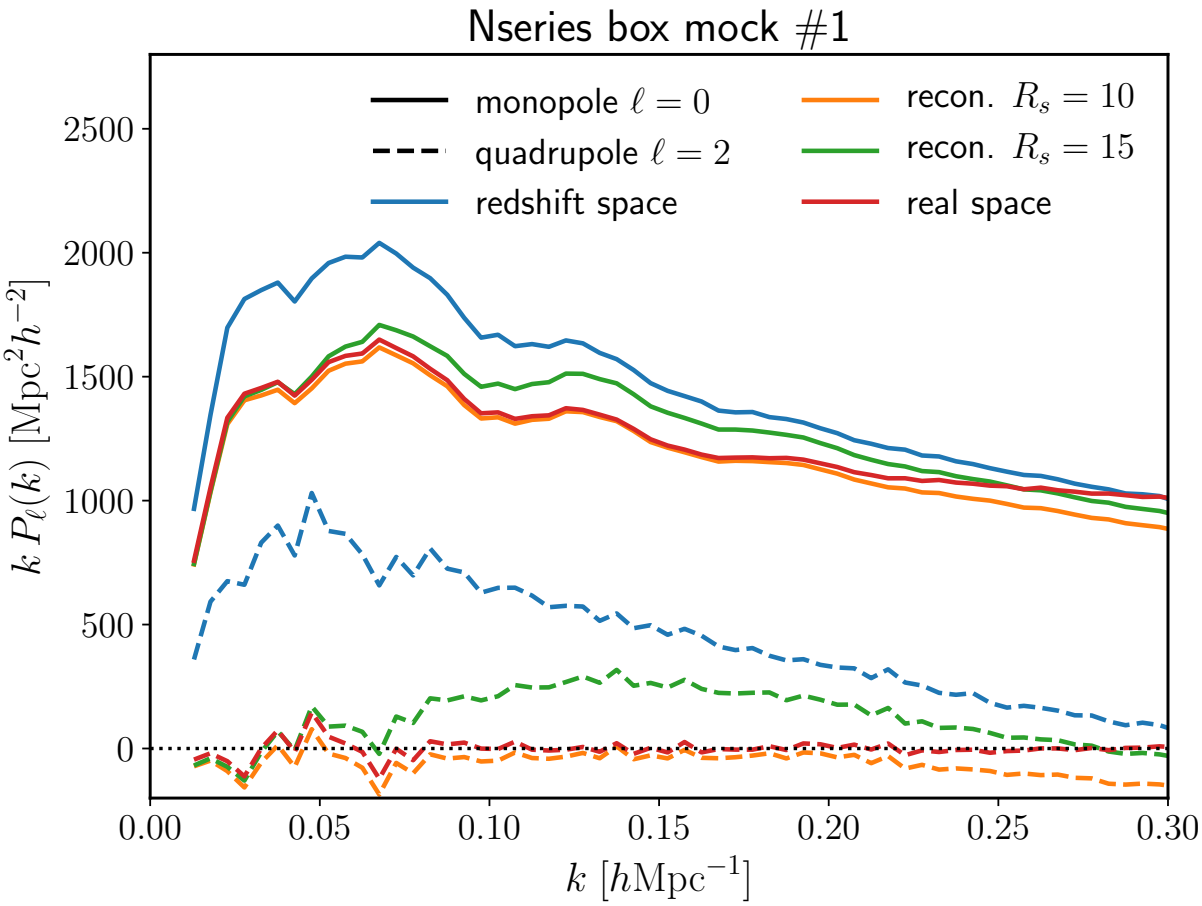

Figure 3.4: Power spectrum multipoles in NSERIES cubic box (one full box of side length 2.6 h^{-1}Gpc, with CMASS-like mock galaxies) showing how well reconstruction recovers the real space power. Note the dependence on smoothing scale R_s. Image Credit: Sesh Nadathur

of $z = 0.6$ (but that can be properly identified and resolved) from being excluded due to edge effects.

Working with the combined BOSS sample means that the change in the survey footprint between LOWZ and CMASS needs to be accounted for (see Figure 3.3 that shows these different footprints and Section 3.2.2 for more details). To do this a modified version of the standard `Revolver` algorithm was used that introduced a layer of boundary particles at $z = 0.43$ around the regions in the CMASS footprint that are not included in LOWZ, in the same way as boundary particles are used around all other survey boundaries, see Section 2.3. This prevents the tessellation from leaking out of the survey volume and thus guards against recovering spuriously low densities near these boundaries. Additional modifications were also needed to `Revolver` to correctly calculate the composite survey volume when estimating the local mean galaxy density used to normalise the measured fluctuations. This procedure is the same as that used by Nadathur et al. (2020b) when analysing the combined eBOSS+CMASS data, which also had a change in survey footprint, see Section 3.2.3. No such modifications were required for the MGS catalogue (see Section 3.2.1) since reconstruction and void-finding were run on this sample separately without combining with BOSS.

After density field estimation, the individual voids obtained from the watershed algorithm are irregularly shaped and lack spherical symmetry, so the definition of the void centre is not unique. The definition introduced by Nadathur and Hotchkiss (2015) was used, which corresponds to the centre of the largest completely empty sphere that can be inscribed within the void and which generally produces a better match to the modelled void-galaxy correlation (Nadathur and Percival, 2019). This is because the validity of the model assumed for the outflow velocity (see equation 2.20 in Section 2.8) can be a less good description of the mean outflow around other centre definitions available, resulting in worse overall predictions for ξ^s. This void centre definition is the circumcentre void centre for a `ZOBOV` void finder, described in more detail in Section 2.3.

A minimum size cut was also applied to the raw void catalogues, keeping only voids larger than the median obtained size in that catalogue for the final analysis. This cut was needed as the RSD modelling of Section 2.8 is not expected to be valid for small voids where galaxy velocities are dominated by environmental effects (i.e. are not undergoing expansion, Nadathur et al. 2017). After this cut was applied no further size-based distinctions were made. Figure 3.5 summarises the redshift distribution of the voids obtained from each of the different datasets after these selection cuts.

All of the above steps were also performed in exactly the same manner on the respective MGS, Patchy and BigMD mock catalogues. For the NSERIES mocks the procedure

was very slightly different since these lie in the CMASS NGC footprint only and so the additional steps above to deal with changes in footprint were not required.

Since void-finding is always performed after reconstruction, the resultant void catalogues inherit a dependence on the parameter β, which is allowed for when fitting to the data. For each catalogue, reconstruction was performed at many values of β over a wide range (see Section 4.2) and the total void numbers obtained are found to vary by up to around $\pm 2\%$ with changes in β. The void numbers shown in Figure 3.5 and recorded in Table 3.1 correspond to the values $\beta = 0.31$ for MGS, $\beta = 0.37$ for BOSS LOWZ and CMASS, and $\beta = 0.35$ for eBOSS.

For completeness, the distribution of voids found in the eBOSS+CMASS LRG sample by Nadathur et al. (2020b) is also shown in both Table 3.1 and Figure 3.5. Chapter 4 presents these results in combination with new work run on MGS and BOSS data. The void-galaxy analysis of Nadathur et al. (2020b) is consistent with that presented in Chapters 2 & 4 and as such is presented together with lower redshift results to build up a ladder of measurements from voids of both $f\sigma_8$ and the AP effect over a wide range in redshift ($0.07 < z < 1.0$).

A total of 14,200 voids ($\pm 2\%$ depending on the value of β used in reconstruction prior to void finding) were found in all SDSS data considered spread over the redshift range $0.07 < z < 1.0$. This was split into 6 total redshift bins (see Section 3.3.1) with a sky area varying from 6813 deg^2 at the lowest redshift to 4242 deg^2 at the highest redshift, and peaking at 9376 deg^2 in the CMASS range of $0.43 < z < 0.75$. Approximately 7100 voids were kept after void size cuts are applied at the median redshift in each redshift bin. The median void size in each redshift bin increases with redshift, starting at $40h^{-1}$Mpc at the lowest redshift bin and up to $49h^{-1}$Mpc at the highest redshift bin. This median void size is largely driven by the tracer density and other survey effects rather than being an intrinsic property of the void redshift evolution. These results are summarised in Table 3.1. Figure 3.6 shows the number of voids as a function of radius for each of the redshift bins used in this thesis, after a void size cut has been applied. Figure 3.7 shows the void size function for the 4 BOSS redshift slices along with the void size function for each of the 250 Patchy mocks used in this analysis in the same redshift range.

3.3.1 Choice of redshift bins

In the work of Chapter 4 the MGS data and mocks are measured in a single self-contained redshift bin, $0.07 < z < 0.2$. However, the BOSS data contain a much larger number of voids extending over a larger range of redshifts, so it was possible to split them into a set

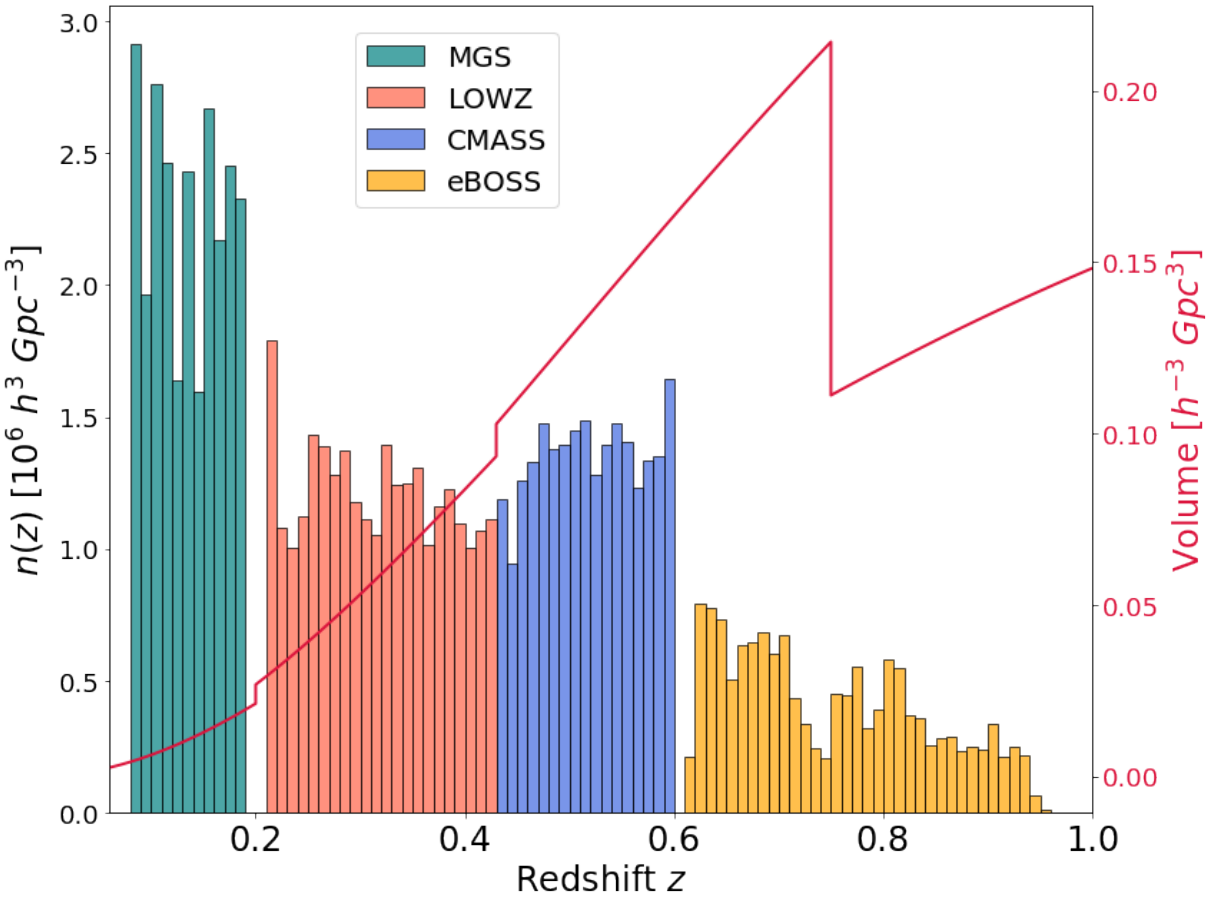

Figure 3.5: The number density of voids obtained after the application of all selection cuts across the redshift range of the data (coloured histograms, left axis). Voids from MGS are shown in teal, and those from the combined BOSS LOWZ and CMASS catalogues at $z < 0.6$ in orange and blue, where we use the change of colour to indicate the dominant contributing sample to the combination. The yellow histogram shows the $n(z)$ for voids from the combination of the eBOSS LRG and BOSS CMASS catalogues at $z > 0.6$ analysed separately by Nadathur et al. (2020b) and labelled as 'eBOSS' for convenience. Voids were obtained after reconstruction using the fiducial values $\beta = 0.31$ (MGS), $\beta = 0.37$ (BOSS LOWZ and CMASS) and $\beta = 0.35$ (eBOSS). The survey volume in $\Delta z = 0.01$ slices is shown as a function of redshift by the red line (right axis), showing the shifts due to changes in the survey mask.

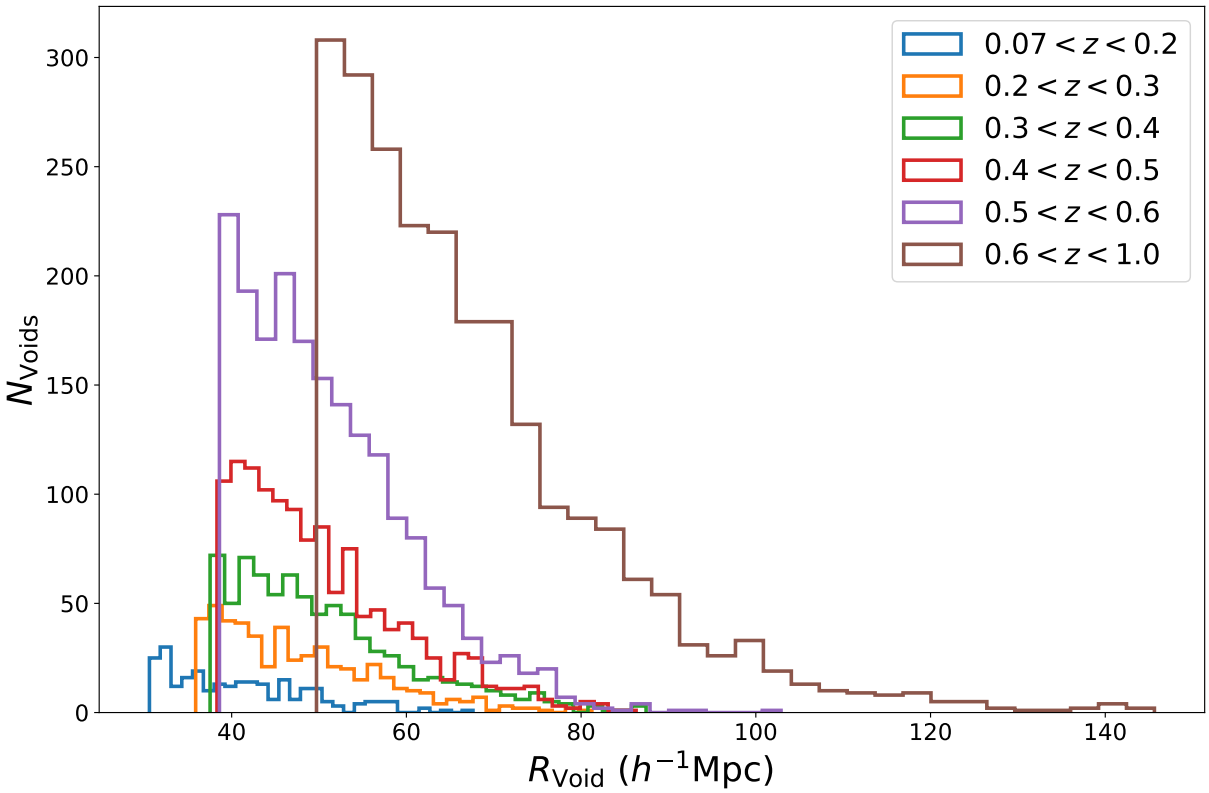

Figure 3.6: The void size function, i.e. the number of voids as a function of the void radius. The data are separated into the same redshift bins as is analysed in this thesis: see Section 3.3.1. A void size cut has been applied to the data with values for this shown in Table 3.1. Voids were obtained after reconstruction using the fiducial values $\beta = 0.31$ ($0.07 < z < 0.2$), $\beta = 0.37$ ($0.2 < z < 0.6$) and $\beta = 0.35$ ($0.6 < z < 1.0$). The number of voids measured varies $\pm 2\%$ depending on the choice of parameter β used in reconstruction prior to void finding.

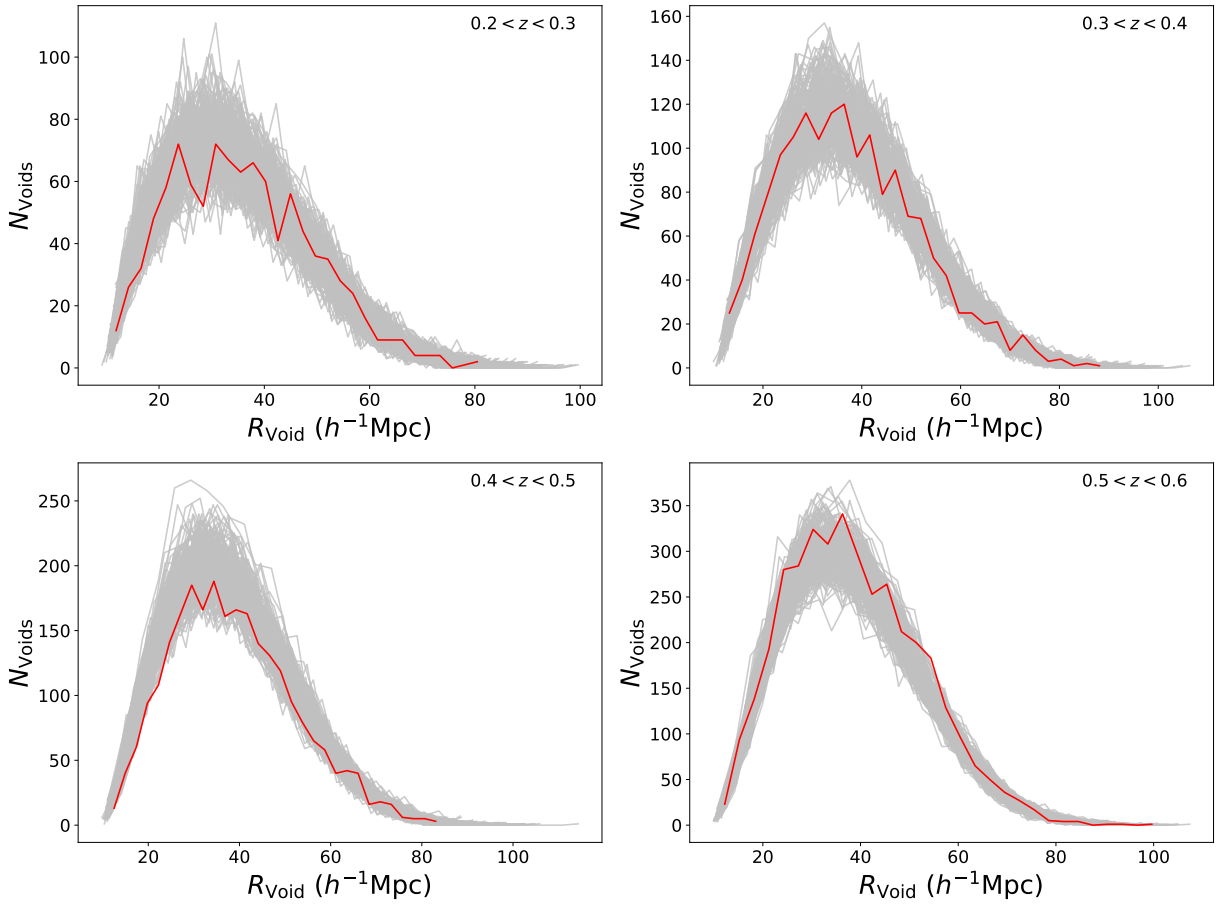

Figure 3.7: The void size function, i.e. the number of voids as a function of their radius of the BOSS redshift bins used in this thesis. Shown in grey is the void size function of voids found in each of the 250 Patchy mocks, and red shows the void size function for the data. Voids are obtained after reconstruction using a fiducial value of $\beta = 0.37$ ($0.2 < z < 0.6$). No void size cut has been applied, unlike Figure 3.6.

Table 3.1: Summary of the redshift bins and survey properties. The redshift range, effective redshift, sky area, the total number of voids $N_{\rm voids}$, the void size cut applied $R_{\rm cut}$, and the number of voids remaining after this cut, $N^{\rm cut}_{\rm voids}$ is presented. The void size cut varies up to $\pm 3\%$ depending on the choice of mock/data galaxy catalogue as well as reconstruction parameter β. Void numbers vary by up to $\pm 2\%$ depending on reconstruction parameter β, numbers reported are for the fiducial choices of β. Where a redshift bin is composed of two overlapping samples, one name is chosen to best represent the composite. Data for the final row, $0.6 < z < 1.0$, are taken from Nadathur et al. (2020b) and shown here for completeness.

Redshift range	Sample name	Sky area (deg^2)	$z_{\rm eff}$	$N_{\rm voids}$	$R_{\rm cut}(h^{-1}{\rm Mpc})$	$N^{\rm cut}_{\rm voids}$
$0.07 < z < 0.2$	MGS	6813	0.15	517	40	258
$0.2 < z < 0.3$	BOSS LOWZ	8337	0.26	1009	47	504
$0.3 < z < 0.4$	BOSS LOWZ	8337	0.35	1596	48	798
$0.4 < z < 0.5$	BOSS CMASS	8337[i]/9376[ii]	0.47	2526	48	1263
$0.5 < z < 0.6$	BOSS CMASS	9376	0.54	3830	49	1915
$0.6 < z < 1.0$	eBOSS LRG	9376[ii]/4242[iii]	0.69	4706	49	2341

[i] for the LOWZ footprint ($0.2 < z < 0.43$) [ii] for the CMASS footprint ($0.43 < z < 0.75$) [iii] for the eBOSS footprint ($z > 0.75$)

of narrower redshift bins to understand the evolution of the void-galaxy cross-correlation with redshift. Doing so also allows for the fact that the growth rate and galaxy bias, and thus the parameter β entering into reconstruction, may evolve with redshift. These considerations led us to split the voids obtained from the combined BOSS sample into 4 non-overlapping redshift bins: $0.2 < z < 0.3$, $0.3 < z < 0.4$, $0.4 < z < 0.5$, and $0.5 < z < 0.6$. Previous work from Nadathur et al. (2020b) used the eBOSS+CMASS LRG sample with $0.6 < z < 1.0$: this data was not reanalysed but their results are presented again together with SDSS MGS and BOSS data. In total, six redshift bins cover the range $0.07 < z < 1.0$, as summarised in Table 3.1.

Within each bin, the effective redshift of the void-galaxy measurement was calculated as a weighted sum

$$z_{\rm eff} = \frac{\Sigma_{ij}\left(\frac{Z_i+z_j}{2}w_j\right)}{\Sigma_{ij}w_j}, \tag{3.1}$$

where Z_i is the redshift of the void centre, z_j is the galaxy redshift, w_j is the associated galaxy systematic weight, and the sum extends over all void-galaxy pairs up to the maximum separation considered, $s = 120\,h^{-1}$Mpc. The effective redshifts for the bins are shown in Table 3.1. Where the data covers both galactic caps there was no difference seen between the $z_{\rm eff}$ values obtained from the NGC and SGC samples in any redshift bin, so the values reported are for both caps taken together.

3.3.2 Void Randoms

As discussed in greater detail in Section 2.7, the distribution of voids in the survey volume differs from the distribution of galaxies. Separate, unclustered void random catalogues were constructed to match the spatial distribution of the voids by running the reconstruction and void-finding steps described above on each of the 1000 mock MGS or 250 Patchy galaxy mocks respectively to create 1000/250 realisations of the void catalogues. Void positions were randomly drawn from the 1000/250 mock catalogues stacked together to make a void random catalogue that has 50 times more objects than obtained in the survey data while containing no clustering that is present in each individual mock. Figure 3.8 shows the number of voids and voids randoms binned as a function of the redshift. The count with redshift can be seen to closely match with differences due to shot noise.

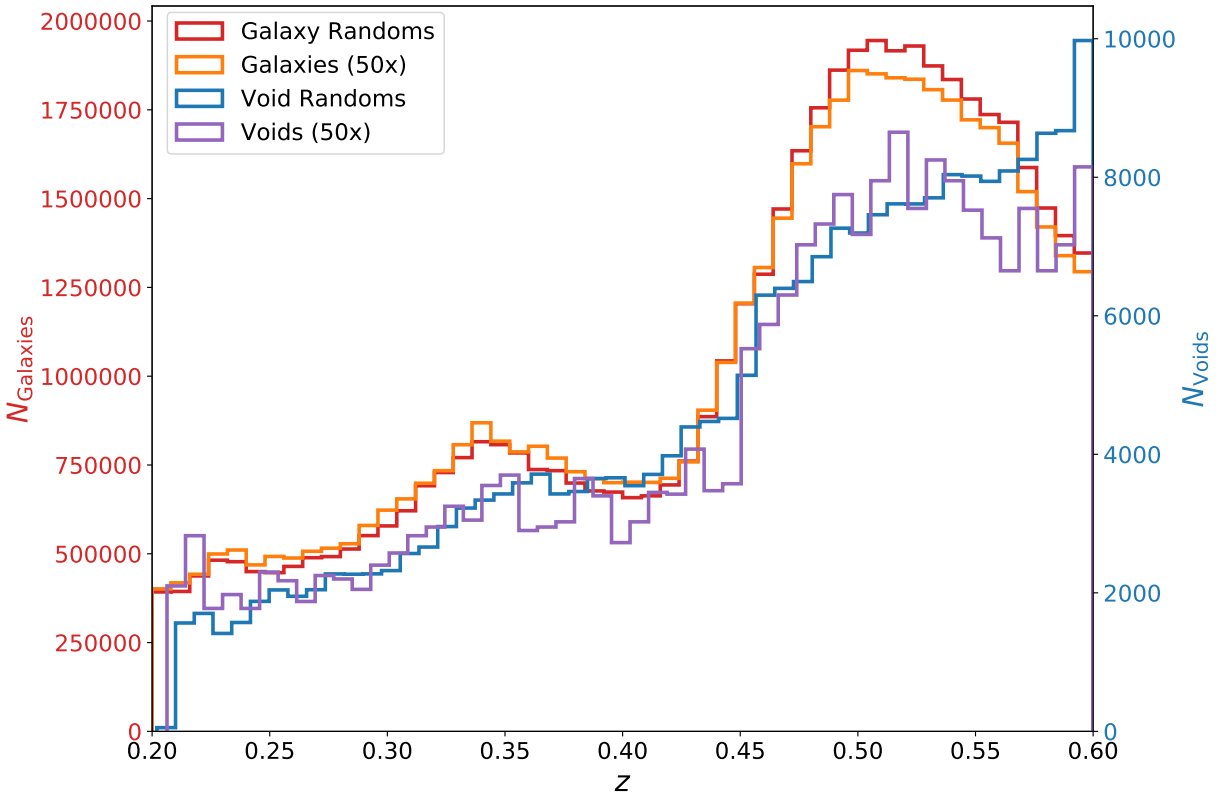

Figure 3.8: The redshift distribution of both voids and galaxies found in SDSS data in the redshift range $0.2 < z < 0.6$. The left axis corresponds to the number of galaxies/galaxy randoms per redshift bin, while the right axis corresponds to the number of voids/void randoms. Both the number of voids and the number of galaxies have been multiplied by a factor of 50 in order to match the scale of the number of randoms. Both the void and void randoms have a dependence on β coming from the reconstruction step being applied prior to void finding. A value of $\beta = 0.40$ is used in this figure, chosen at random. The number of objects per redshift bin has not been normalised by the survey volume.

3.3.3 Fiducial Cosmology

When analysing the BOSS data and the BOSS mocks, unless otherwise specified a reference fiducial cosmological model was adopted with $\Omega_{\rm m} = 0.307$, $\Omega_\Lambda = 0.693$, $h = 0.676$ and zero curvature to convert galaxy redshifts to distances. When analysing the MGS data and the MGS mocks, unless otherwise specified a reference fiducial cosmological model was adopted with $\Omega_{\rm m} = 0.31$, $\Omega_\Lambda = 0.69$, $h = 0.676$ and zero curvature to convert galaxy redshifts to distances. This cosmological model is very close to that indicated by the Planck Collaboration et al. (2020) CMB results and matches the cosmology of the MGS and Patchy mocks. The dependence of the choice of fiducial cosmology on results from analysis of the void-galaxy cross-correlation is shown in Section 4.3.2 and systematic errors due to the need to assume a fiducial cosmology were quantified and incorporated into the total systematic error budget of the measurement.

3.4 Correlation Function Measurement

The binned void-galaxy correlation function ξ^s (or ξ^r) was measured in redshift space (real space) in 30 bins of the observed void galaxy separation distance s (r) and 80 bins of the cosine of the angle μ_s (μ_r) between the separation vector and the line-of-sight direction to the void centre using the Landy-Szalay estimator shown in equation 2.11 (Landy and Szalay, 1993). The galaxy randoms needed for this correlation function estimation were taken from the publicly provided random catalogues for each sample by SDSS. As described above, the void random catalogues were constructed manually.

3.5 Template Functions

The modelling described in Section 2.8 relies on three template functions: the matter density profile, the velocity dispersion profile, and the real space correlation function. The density and velocity dispersion profiles were taken from mock catalogues with available dark matter information, while the real space correlation function was taken from the average of many mocks designed to closely match the survey properties. These are described below.

3.5.1 Density and Velocity Templates

To create the dark matter profile around void and velocity dispersion templates dark matter information from simulations is required. This is not available for the MGS, Patchy or NSERIES mocks described above for the redshift range needed. Instead, halo catalogues were extracted from simulation snapshots of the Big Multidark Simulation (described in Section 3.2.4) at $z = 0.1$, $z = 0.32$, and $z = 0.52$. These dark matter simulation boxes were populated with halos according to a HOD prescription designed to match the clustering of the galaxy data in the different samples. HOD parameters matching those of the 'Main2' mocks of Nadathur and Hotchkiss (2015) are used at $z = 0.1$ to mimic the MGS sample, matching those from Manera et al. (2015) at $z = 0.32$ to mimic the LOWZ sample, and matching those from Manera et al. (2013) at $z = 0.52$ to mimic the CMASS sample. Sections of the box were then cut out to match the survey mask in each case and downsampled to match the survey selection functions. This collection of mock catalogues is referred to as the BigMD mocks.

These newly created BigMD mocks were used to create templates used in the later analysis only. To do this, the reconstruction and void-finding pipeline described in Sections 2.6 and 3.3 were run on these mocks exactly as for the corresponding MGS and BOSS data samples. For the voids obtained, stacked profiles for the enclosed matter density around voids, $\Delta(r, z)$, and the velocity dispersion, $\sigma_{v_{||}}(r, z)$, were measured from the simulations. These functions were used as templates in the modelling as described in Section 2.8. It is worth noting that the steps taken above to match the survey masks in the BigMD mocks are very important since survey edges can have strong effects on the distribution of void sizes obtained using our algorithm and would thus result in changes to these template functions as well. For each redshift slice described in Section 3.3.1 the closest BigMD mock to the mean redshift in said slice was chosen and used to construct the templates. Figure 3.9 shows the matter density and velocity dispersion profiles used in Chapter 4 to model the mapping from redshift space to real space void-galaxy correlation functions.

3.5.2 Real Space Void-Galaxy Correlation Function

Real space void-galaxy correlation functions ξ^r were taken from mock catalogues (described in Sections 3.2.1 & 3.2.2) designed to closely match the footprint, redshift distribution and clustering properties of the surveys. All steps taken to calculate the redshift space multipoles (i.e. reconstruction, void finding, and correlation function measurements) were mirrored with the sole exception being that instead of correlating the post-reconstruction void centre positions with redshift space galaxies we correlated the post-reconstruction void

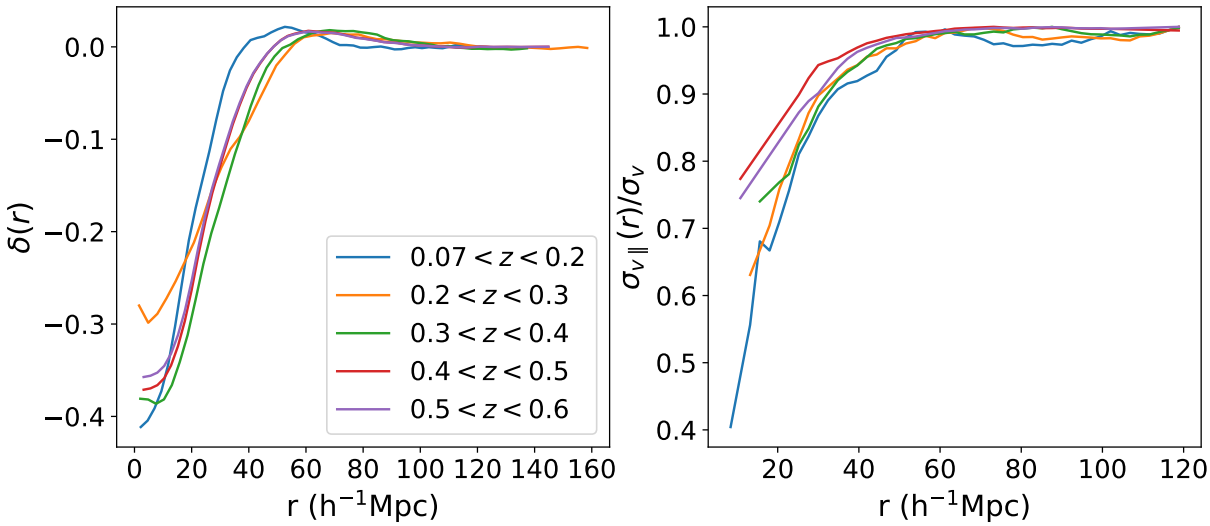

Figure 3.9: The matter density (left) and galaxy velocity dispersion (right) profiles as measured around voids. These are measured from the custom-built mock void and galaxy catalogue in the Big MultiDark simulation at snapshot redshift z = 0.1, 0,32, and 0.52 where the closest snapshot to each redshift slice is used. Both are measured as angle-averaged functions of the real space distance from the void centre, r. The velocity dispersion profile is shown as normalised by its asymptotic value at large radii.

centre positions with the post-reconstruction galaxy position field. Note that voids are only identified in the approximation to the real space galaxy field obtained from RSD removal after reconstruction. All measured void-galaxy cross-correlations use these void centres and thus implicitly depend on the parameter β used in reconstruction. Measurement of $\xi^s(s, \mu_s)$ used the original (redshift space) galaxy positions but still retained the implicit dependence on β from the void identification step. On the other hand, as the true real space positions of galaxies are not known the true real space cross-correlation ξ^r cannot be directly determined, and instead is estimated by measuring the cross-correlation with the post-reconstruction galaxy positions with RSD approximately removed. In the following, where necessary $\hat{\xi}^r$ is used to distinguish this measured estimate of the true real space cross-correlation ξ^r.

The real space void-galaxy correlation functions were taken from 1000 of the MGS mock catalogues when analysing MGS data and mocks, but only 250 Patchy mocks when analysing BOSS data and mocks. The lower number of patchy mocks was chosen to be high enough to eliminate shot noise in the measurement of the $\hat{\xi}^r$ profile while reducing the computational expense of this analysis. Figure 3.10 shows the monopole and quadrupole moments of the real space void-galaxy correlation function used for each of the redshift slices shown in this work.

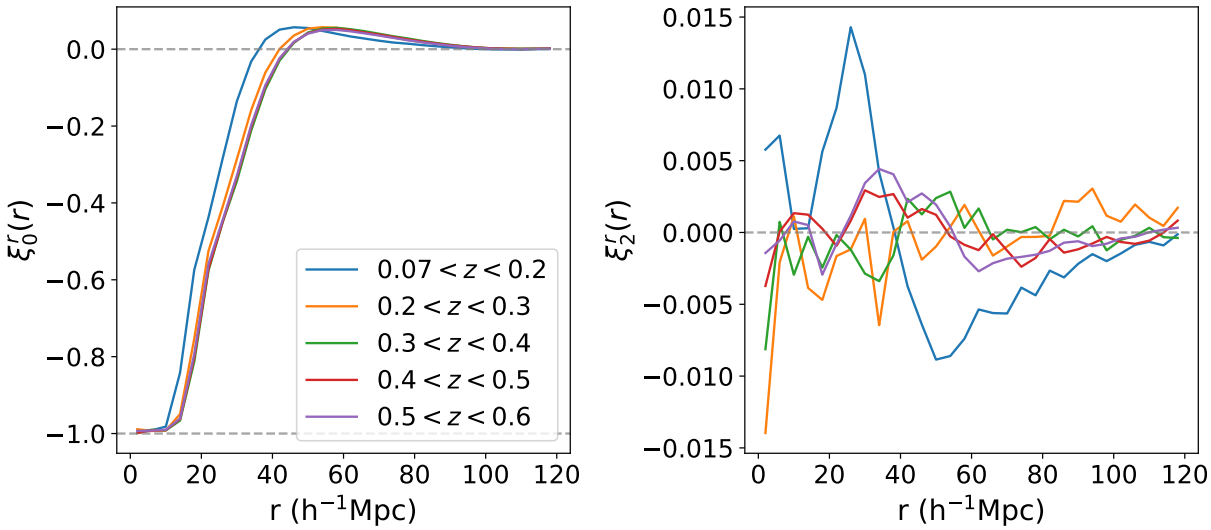

Figure 3.10: The real space void-galaxy correlation function multipole moments as measured by the average of many mocks. Real space is approximated by post-reconstruction void centre and galaxy positions. This causes the correlation functions to inherent a dependence on β from the reconstruction algorithm. Plotted correlation functions are shown at a value of $\beta = 0.30$ for the $0.07 < z < 0.2$ redshift slice and $\beta = 0.35$ for all other redshift slices. These are chosen to be close to the true fiducial value for these mock catalogues.

Chapter 4

Extracting Alcock-Paczynki and Redshift Space Distortion Information from the Void-Galaxy Correlation Function

4.1 Introduction

In this Chapter, we build on previous work developed for the cosmological analysis of voids to analyse galaxy samples within the Sloan Digital Sky Survey (SDSS-II; York et al. 2000). We analyse the Main Galaxy Sample (MGS, see Section 3.2.1), Baryon Oscillation Spectroscopic Survey(BOSS, see Section 3.2.2), and the extended BOSS (eBOSS, see Section 3.2.3) LRG samples covering a wide range in redshift using a single analysis method for the first time. This analysis method is presented in Chapter 2 and applied to SDSS data in Chapter 3. These data represent the best public galaxy redshift survey data available to date. The analysis method used is consistent with that applied to eBOSS in Nadathur et al. (2020b), and is a development of that used for BOSS by Nadathur and Percival (2019). It has not previously been applied to the MGS or low redshift BOSS samples. Data products from voids in these data (i.e. void positions, void-galaxy correlation functions, template density functions, template velocity functions, and template real space void-galaxy correlation functions) are presented in Chapter 3. In this Chapter, we focus on the likelihood measurements to extract our parameter constraints, test for and quantify systematic errors in these measurements, and discuss results from these measurements.

In Chapter 5, cosmological models fits to voids and the combination of voids with other probes are presented.

By analysing these new data and consolidating previous analyses, we are able to build a picture of the geometrical evolution of the Universe and the evolution of the growth of structure within it from only the analysis of SDSS galaxies around voids. For voids, we can distinguish RSD and AP because they affect the apparent shape in different ways (Nadathur et al., 2019b). The measurements of the AP and RSD effects from voids are not strongly correlated with those obtained from analyses of galaxy-galaxy clustering (Nadathur et al., 2020a; Woodfinden et al., 2023), so they represent additional information that can be obtained from existing surveys.

This Chapter is structured as follows: Section 4.2 presents the likelihood estimation used to determine cosmological parameters. In Section 4.3, systematic errors due to limitations in the theoretical model and the choice of the fiducial cosmological model are quantified and added to the total error budget. Section 4.4 presents the results from this analysis and context from similar measurement techniques and galaxy spectroscopic surveys is given. Finally, we conclude in Section 4.5.

4.2 Likelihood

All comparisons of model and data were performed using the `Victor` void-galaxy correlation analysis tool, with data vector $\xi^s = (\xi^s_0(s), \xi^s_2(s))$ formed from the monopole and quadrupole moments of the redshift space correlation function. It is simple to add the hexadecapole and other higher order moments to the analysis in `Victor` but they do not add much information at the measurement precision of current data and are ignored in what follows. The calculation of the theory model $\xi^{s,\mathrm{th}}$ described in Section 2.8 has an explicit dependence on $f\sigma_8$, $\alpha_\perp/\alpha_\parallel$ and σ_v, and an implicit dependence on β, while the measured data vector ξ^s also depends on β. The parameter space we explore is therefore 4-dimensional.

We used mocks to construct an estimate of the covariance matrix,

$$C = \frac{1}{n_s - 1} \sum_{k=1}^{n_s} \left(\xi^{sk} - \overline{\xi^s}^k\right) \left(\xi^{sk} - \overline{\xi^s}^k\right) , \tag{4.1}$$

from $n_s = 1000$ mocks, where ξ^{sk} is the measured data vector in the kth mock realisation, and $\overline{\xi^s}^k$ is the mean over the mocks. At a given point $\left(f\sigma_8, \beta, \alpha_\perp/\alpha_\parallel, \sigma_v\right)$ in parameter

space, we then use this covariance matrix estimate to obtain the χ^2 for the model fit,

$$\chi^2 = \left(\xi^{s,\mathrm{th}} - \xi^s\right) C^{-1} \left(\xi^{s,\mathrm{th}} - \xi^s\right) . \tag{4.2}$$

In doing so we treat the covariance matrix as fixed and do not attempt to account for its dependence on cosmology. A sample covariance matrix is shown in Figure 4.1 for one of the redshift slices used in this analysis ($0.5 < z < 0.6$).

Since the estimate of the covariance matrix in equation 4.1 from the mocks is itself uncertain, it is necessary to propagate this uncertainty through to the likelihood. To do this, we use the procedure outlined by Percival et al. (2021) to calculate the posterior

$$f(\theta|\xi^s) \propto \left[1 + \frac{\chi^2}{(n_s - 1)}\right]^{-\frac{m}{2}} , \tag{4.3}$$

where the power law index m is given by

$$m = n_\theta + 2 + \frac{n_s - 1 + B(n_d - n_\theta)}{1 + B(n_d - n_\theta)} , \tag{4.4}$$

$$B = \frac{(n_s - n_d - 2)}{(n_s - n_d - 1)(n_s - n_d - 4)} , \tag{4.5}$$

and $n_s = 1000$ is the number of mocks, $n_d = 60$ the number of data points fitted and $n_\theta = 4$ the number of model parameters. This procedure adopts flat and uninformative priors on all parameters and a prior on the covariance matrix such that we can match the Bayesian results to frequentist expectations to first order, allowing us to compare credible intervals derived from the posterior to confidence regions derived from the scatter of results from the mocks (Percival et al., 2021).

To explore the model parameter space, we used the MCMC sampling implemented in `Victor` via an interface with the `Cobaya` sampling package (Torrado and Lewis, 2019a, 2021a). Since directly repeating the reconstruction, void-finding and cross-correlation measurements at each value of β would make the MCMC prohibitively expensive, we adopted a time-saving interpolation strategy. Before running the MCMC we computed all the necessary cross-correlations on a closely-spaced grid of β values, β_i.

4.2.1 Likelihood Interpolation

During the MCMC run, for each input β, we evaluated the likelihood twice at the grid points bracketing it $\beta_i \leq \beta \leq \beta_{i+1}$, and then linearly interpolated between these values;

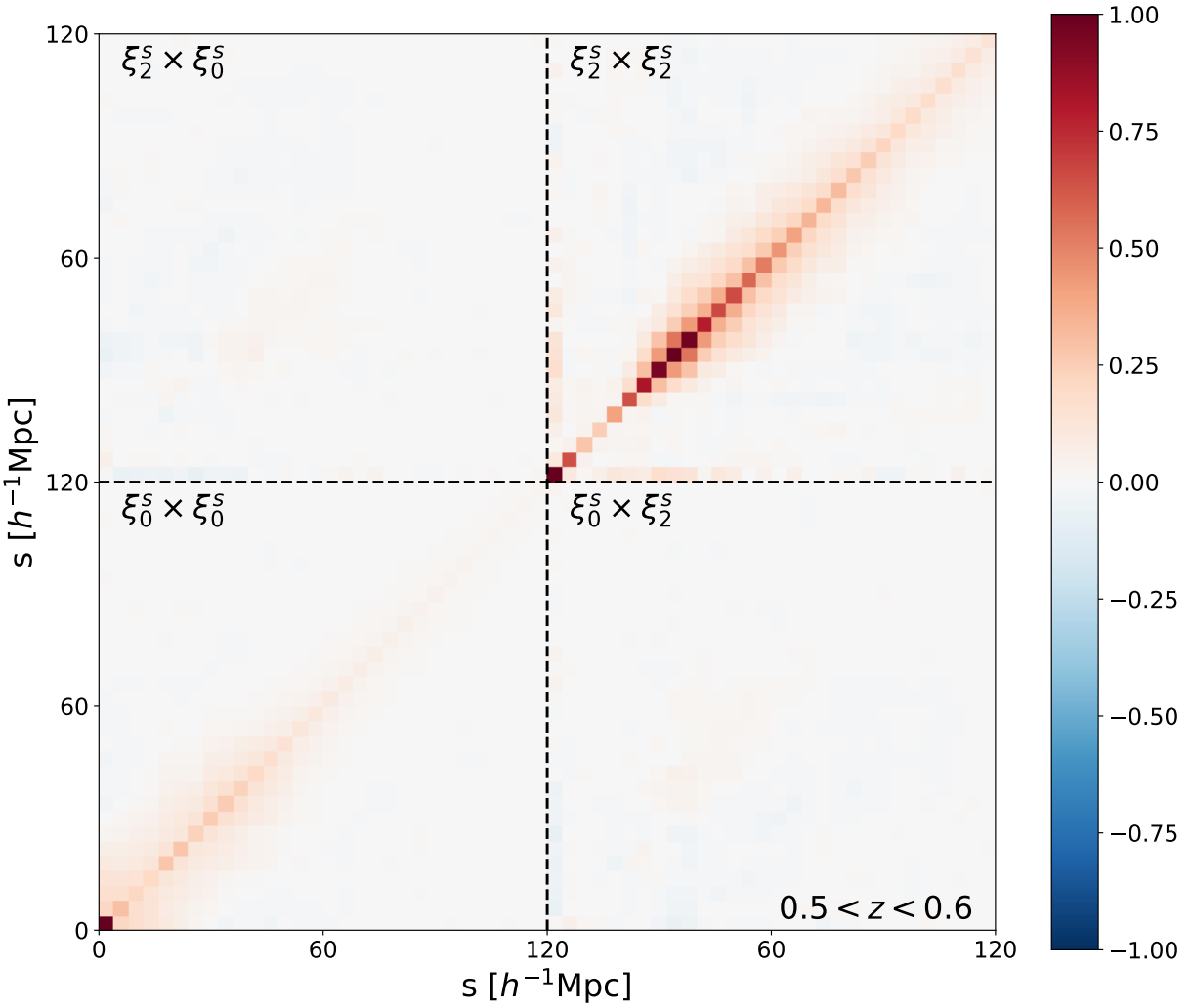

Figure 4.1: The normalised covariance matrix used for the redshift space multipole measurement for the redshift slice $0.5 < z < 0.6$. This matrix is determined from 1000 Patchy mocks at a fiducial value of $\beta = 0.37$. Subscript 0 denotes the monopole, and subscript 2 denotes the monopole of the void galaxy cross-correlation. Superscript ^{s} denotes that this is calculated in redshift space.

we refer to this method as likelihood interpolation. This differs from the method used by Nadathur et al. (2019b, 2020b), who performed the interpolation at the level of the correlation functions; we refer to this method as data vector interpolation. It was found during this analysis that data vector interpolation results in an artificial reduction of noise in the region in between values of β_i and β_{i+1}.

To illustrate this effect Figure 4.2 shows a toy model of two sine waves of amplitude 1 that have been shifted up (shown in blue) and down (shown in red) by a value of 3. The dashed line shows these original sine waves, while the solid line shows these same sine waves where noise has been added following a normal distribution centred at 0 with a standard deviation of 1. The orange line shows the interpolation between these shifted data vectors at their midpoint. The dashed line is the interpolation with no noise added, and the solid line is the interpolation between data vectors with added noise. The standard deviation of the interpolation between noisy data vectors shows a value significantly lower than the standard deviation of the data vectors being interpolated. Repeating this toy model on $10,000$ samples reduces the standard deviation of the interpolated data by 30% on average compared to that of the original noisy data vector.

This effect results in a lower χ^2 between the β grid points when interpolation is performed at the level of the correlation function. The choice was made in the work of this thesis to interpolate between the grid points bracketing the β value to alleviate this artificial reduction in χ^2. As a result, the best-fit value of β will always be found at a β grid point, so a closely spaced grid must be used in the analysis. Figure 4.3 highlights these results for an example likelihood surface from one of the Patchy mocks used in this analysis for a redshift slice of $0.4 < z < 0.5$. Several dips can be seen in between grid points in the interpolation at the level of the correlation function that is due to this artificial reduction in noise. These dips cause the likelihood surface to be at a minimum that does not match the true underlying minimum of the distribution. Figure 4.4 shows the shift in the mean value of the likelihood for cosmologically significant parameters $\alpha_\perp/\alpha_\parallel$ and $f\sigma_8$. As can be seen, these shifts are mostly small albeit non-zero.

The likelihood surface with respect to β can be seen to be noisy in Figure 4.3. Both our data vectors (ξ^s) and model (which has a dependence on ξ^r) are calculated on a grid of β values that are used during reconstruction (see Section 2.6). Noise brought in through reconstruction leads to a noisy comparison, as shown. Different values of β significantly change the noisy model. This differs from other parameters in our fits (e.g. $f\sigma_8$ shown in Figure 4.5) as for these parameters model is allowed to vary smoothly. The interpretation of the posterior surface will still give the correct probability of the model and, on average, will display a Gaussian likelihood, but noise is introduced at the level of an individual realization.

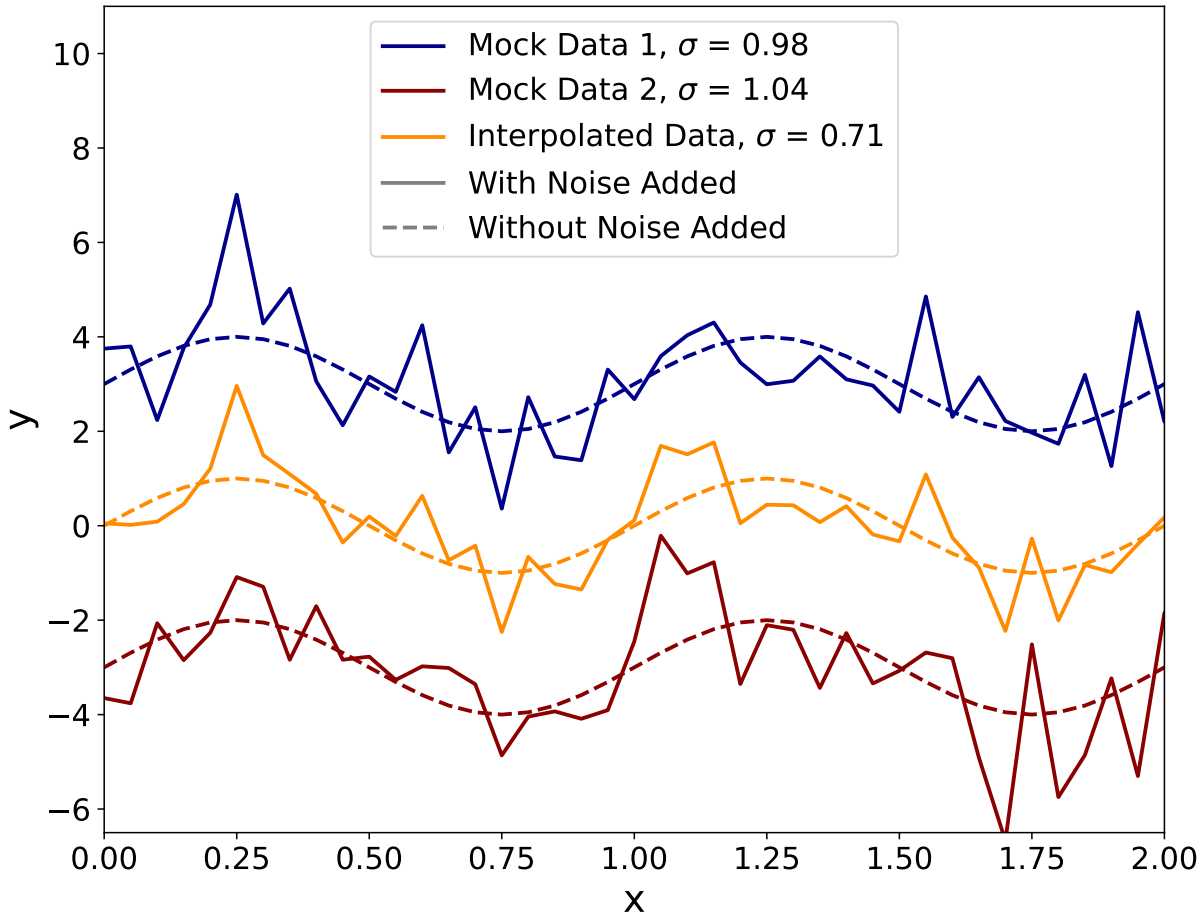

Figure 4.2: Two sine waves of amplitude 1 have been shifted up (blue) and down (red) by a value of 3. The dashed line shows the original sine wave, and the solid line shows this same sine waves when noise has been randomly added following a normal distribution with a standard deviation of 1. The orange line shows the interpolation between the blue and red sine waves with zero offset. The dashed line interpolates the original sine waves and the solid line between those with added noise. As can be seen in the figure legend, the standard deviation of the interpolated data vector with noise has a lower standard deviation than that of either of the two original sine waves being interpolated between.

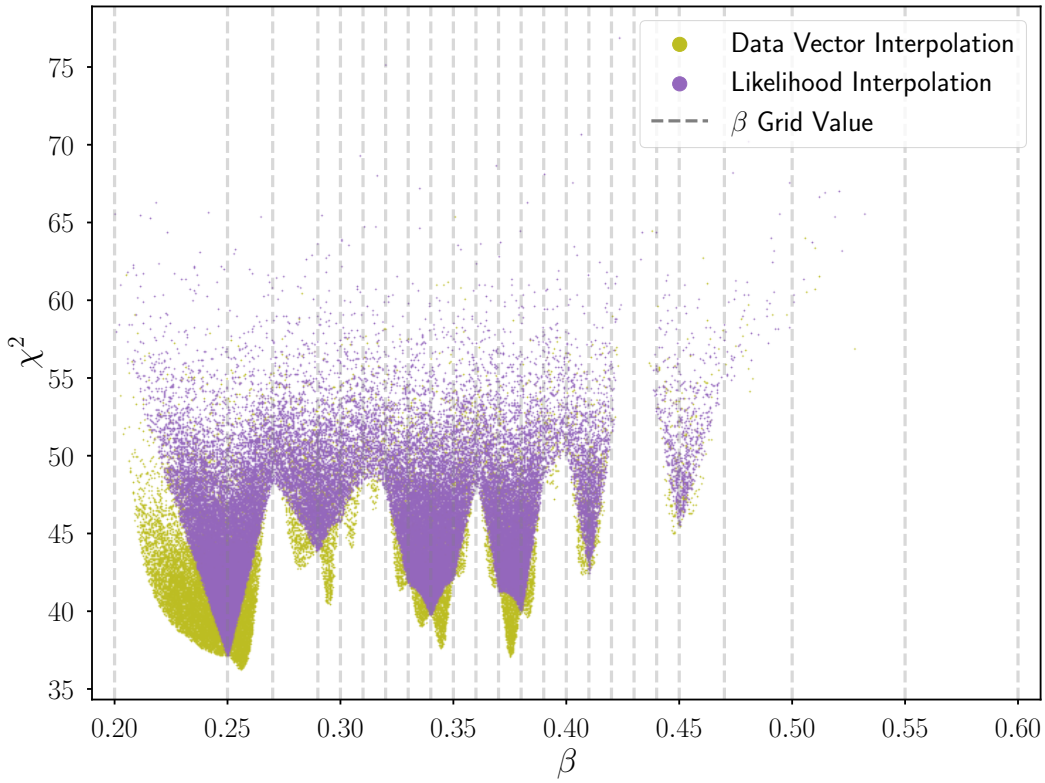

Figure 4.3: A comparison between β likelihood surfaces for one of the Patchy mocks used in this analyses at a randomly chosen redshift slice of $0.4 < z < 0.5$. Data vector interpolation refers to where points not sampled in β space are found by interpolating at the level of the data vector between the closest two neighbouring β grid values; this is the original interpolation method used in prior work. Likelihood interpolation is where this happens at the likelihood stage and not at the data vector stage; this is the new interpolation method used in this work.

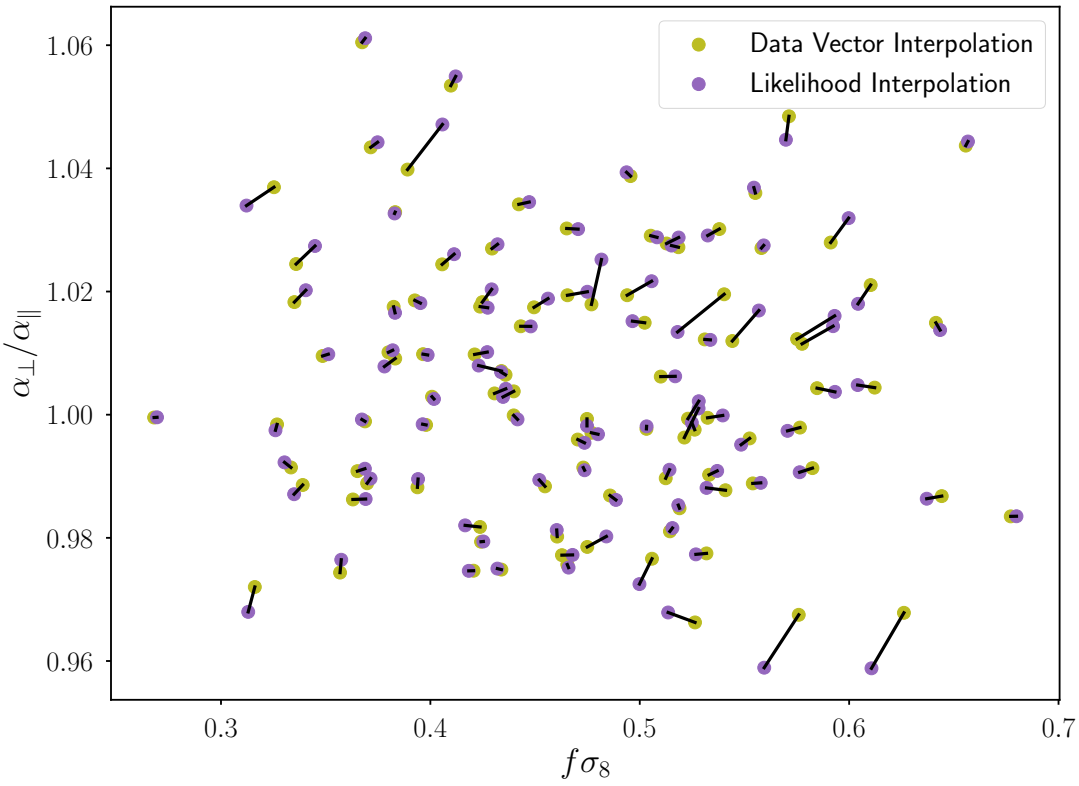

Figure 4.4: The shift between the mean value of the likelihood for 250 Patchy mocks in the redshift slice $0.4 < z < 0.5$. Results are shown for two different methods of interpolating between grid points in the β parameter. Data vector interpolation refers to where points not sampled in β space are found by interpolating at the level of the data vector between the closest two neighbouring β grid values. Likelihood interpolation is where this happens at the likelihood stage and not at the data vector stage.

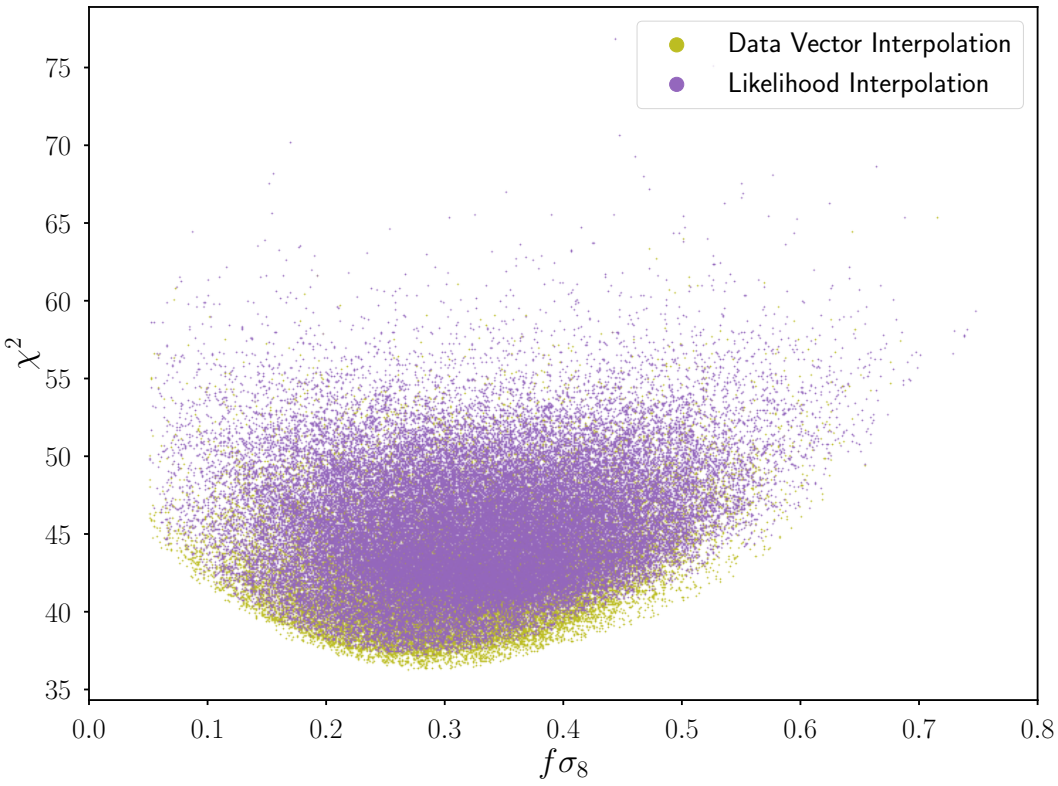

Figure 4.5: A comparison between $f\sigma_8$ likelihood surfaces for one of the Patchy mocks used in this analyses at a randomly chosen redshift slice of $0.4 < z < 0.5$. Data vector interpolation refers to where points not sampled in β space are found by interpolating at the level of the data vector between the closest two neighbouring β grid values. Likelihood interpolation is where this happens at the likelihood stage and not at the data vector stage.

4.3 Tests of systematic errors

This Section describes a series of tests to examine sources of systematic error and quantify their contribution to the total error budget for the two model parameters of cosmological interest, $f\sigma_8$ and $\alpha_\perp/\alpha_\parallel$. These are divided into two categories: errors that may be introduced by limitations in the theoretical model when applied to representative survey data (referred to as 'modelling systematics') and errors associated with the choice of the fiducial cosmological model in which the data analysis is performed. These tests include the effects of the noisy posterior surface described above. We discuss these separately in Sections 4.3.1 and 4.3.2 and combine results into a total systematic error budget in Section 4.3.3.

4.3.1 Modelling Systematics

We used the mock catalogues described in Chapter 3 and ran the full measurement and fitting pipeline on 250 realisations each of the MGS and Patchy mocks. These mocks were treated in exactly the same manner as the corresponding MGS and BOSS data samples. This involved running void finding on the whole sample, splitting the voids found into the same redshift bins as the data, and performing subsequent analysis in these bins. We initially used the true cosmology of the mocks as the fiducial model for converting redshifts to distance. From the fits to each mock, we obtained the mean values of the cosmologically interesting parameters $f\sigma_8$ and $\alpha_\perp/\alpha_{||}$, after marginalising over β and σ_v, and compared the averages over all mocks, $\langle f\sigma_8\rangle$ and $\langle\alpha_\perp/\alpha_{||}\rangle$ to the known values for the mock cosmology in that redshift bin. These results are summarised in Table 4.1, and Figure 4.6 shows the scatter in the recovered values over all 250 mocks in each redshift bin.

Statistically significant systematic errors are defined as being detected when the mean over the mocks for a given parameter differs from its expectation value by more than twice the expected statistical error in the mean, calculated as $1/\sqrt{N_{\rm mocks}}$ times the average marginalised 1D parameter uncertainty for a single mock. Significant offsets are seen in $f\sigma_8$ for two redshift bins ($0.3 < z < 0.4$ and $0.4 < z < 0.5$) and in $\alpha_\perp/\alpha_\parallel$ for two redshift bins ($0.07 < z < 0.2$ and $0.5 < z < 0.6$). These offsets are however always small compared to the statistical precision that can be obtained in the data. Section 4.3.3 describes how these are incorporated into the total systematic error budget.

Table 4.1: Performance of the model when analyzing mock catalogues. The mocks are analyzed in their own cosmology, indicated in bold, as well as perturbations around this at $\Omega_{\rm m} = 0.28$ and $\Omega_{\rm m} = 0.34$ to find the error budget due to analyzing the mocks in the wrong cosmology. The differences are shown between the mean values obtained by the mocks and the expected values. The 2σ uncertainties on these differences are found as twice the mean of the 1D marginalised parameter uncertainties in the individual mocks multiplied by $1/\sqrt{N_{\rm mocks}}$. Values that are more than 2σ deviant from expectation are highlighted in bold font.

Mock	$N_{\rm mock}$	Redshift Range	Ref Cosmology	$\langle f\sigma_8 \rangle$	$\langle \alpha_\perp/\alpha_\parallel \rangle$	$\Delta(f\sigma_8) \pm 2\sigma$	$\Delta(\alpha_\perp/\alpha_\parallel) \pm 2\sigma$
MGS	250	$0.07 < z < 0.2$	$\Omega_{\rm m} = 0.28$	0.4661	0.9968	$\mathbf{0.0464 \pm 0.0334}$	$\mathbf{-0.0098 \pm 0.0053}$
			$\mathbf{\Omega_m = 0.31}$	0.4661	1.0000	0.0112 ± 0.0252	$\mathbf{-0.0167 \pm 0.0055}$
			$\Omega_{\rm m} = 0.34$	0.4661	1.0035	0.0162 ± 0.0297	$\mathbf{-0.0094 \pm 0.0053}$
Patchy	250	$0.2 < z < 0.3$	$\Omega_{\rm m} = 0.28$	0.4733	0.9945	-0.0097 ± 0.0208	0.0044 ± 0.0047
			$\mathbf{\Omega_m = 0.307}$	0.4733	1.0000	-0.0108 ± 0.0210	0.0034 ± 0.0047
			$\Omega_{\rm m} = 0.34$	0.4733	1.0061	0.0111 ± 0.0199	-0.0014 ± 0.0047
Patchy	250	$0.3 < z < 0.4$	$\Omega_{\rm m} = 0.28$	0.4786	0.9928	$\mathbf{-0.0275 \pm 0.0153}$	$\mathbf{0.0065 \pm 0.0038}$
			$\mathbf{\Omega_m = 0.307}$	0.4786	1.0000	$\mathbf{-0.0269 \pm 0.0150}$	0.0038 ± 0.0039
			$\Omega_{\rm m} = 0.34$	0.4786	1.0080	$\mathbf{-0.0190 \pm 0.0164}$	-0.0013 ± 0.0037
Patchy	250	$0.4 < z < 0.5$	$\Omega_{\rm m} = 0.28$	0.4795	0.9907	$\mathbf{-0.0221 \pm 0.0138}$	$\mathbf{0.0094 \pm 0.0029}$
			$\mathbf{\Omega_m = 0.307}$	0.4795	1.0000	$\mathbf{-0.0226 \pm 0.0130}$	0.0018 ± 0.0028
			$\Omega_{\rm m} = 0.34$	0.4795	1.0102	$\mathbf{-0.0271 \pm 0.0116}$	-0.0001 ± 0.0029
Patchy	250	$0.5 < z < 0.6$	$\Omega_{\rm m} = 0.28$	0.4773	0.9896	-0.0112 ± 0.0113	$\mathbf{0.0102 \pm 0.0026}$
			$\mathbf{\Omega_m = 0.307}$	0.4773	1.0000	-0.0047 ± 0.0111	$\mathbf{0.0037 \pm 0.0026}$
			$\Omega_{\rm m} = 0.34$	0.4773	1.0113	-0.0073 ± 0.0103	-0.0001 ± 0.0025
NSERIES	84	$0.43 < z < 0.5$	$\mathbf{\Omega_m = 0.286}$	0.4687	1.0000	-0.0065 ± 0.0246	-0.0053 ± 0.0056
NSERIES	84	$0.5 < z < 0.6$	$\mathbf{\Omega_m = 0.286}$	0.4687	1.0000	-0.0154 ± 0.0173	-0.0008 ± 0.0045

In addition to analysing the MGS and Patchy approximate mocks, Table 4.1 shows the equivalent results obtained from fitting to the 84 NSERIES mocks. These NSERIES mocks cover only a subset of the full redshift range of the BOSS data and only the NGC sky region. We analysed them in modified redshift bins $0.43 < z < 0.5$ and $0.5 < z < 0.6$ and used a covariance matrix appropriate to the reduced sky area but otherwise treated them in the same manner as for the data catalogues. Since they do not match the sky footprint and redshift range of the SDSS data, we do not include offsets determined from the NSERIES mocks in our estimation of the total systematic error budget. Nevertheless, as these mocks are drawn from the full N-body simulations they are expected to reproduce the true RSD signal to higher accuracy and smaller scales than possible with the approximate Patchy mocks. It is therefore reassuring that, within the slightly reduced precision afforded by the smaller number of mock realisations, no systematic offsets are found in the recovered values of either $f\sigma_8$ or $\alpha_\perp/\alpha_{||}$ from NSERIES.

4.3.2 Effect of the fiducial cosmology

To estimate the systematic error introduced by performing the analysis with a fiducial cosmological model that differs from the true cosmology the entire analysis was repeated over the 250 MGS and Patchy mocks using different cosmological models. Perturbations around the true cosmology of the mocks were considered by setting $\Omega_\mathrm{m} = 0.28$ and $\Omega_\mathrm{m} = 0.34$. All other aspects of the analysis remained the same as before. The recovered mean values $\langle f\sigma_8 \rangle$ and $\langle \alpha_\perp/\alpha_{||} \rangle$ over all the mocks are summarised in Table 4.1 for each redshift bin and cosmology tested.

As above, a statistically significant systematic error is defined as detected if the mean value over the mocks differs from the truth by more than twice the expected error in the mean, estimated as $1/\sqrt{N_\mathrm{mocks}}$ times the average marginalised 1D parameter uncertainty for a single mock. Table 4.1 shows that this threshold was exceeded for several redshift bins when $\Omega_\mathrm{m}^\mathrm{fid} = 0.28$, and occasionally when $\Omega_\mathrm{m}^\mathrm{fid} = 0.34$, though the differences are still small compared to the statistical uncertainty in fitting to a single realisation. This increased occurrence of systematic offsets may indicate a deficiency in the modelling used when the fiducial model is far from the truth. Further improvements to the modelling in future work may be able to eliminate this source of error, but for the current work, this was instead incorporated into the total systematic error budget as described below.

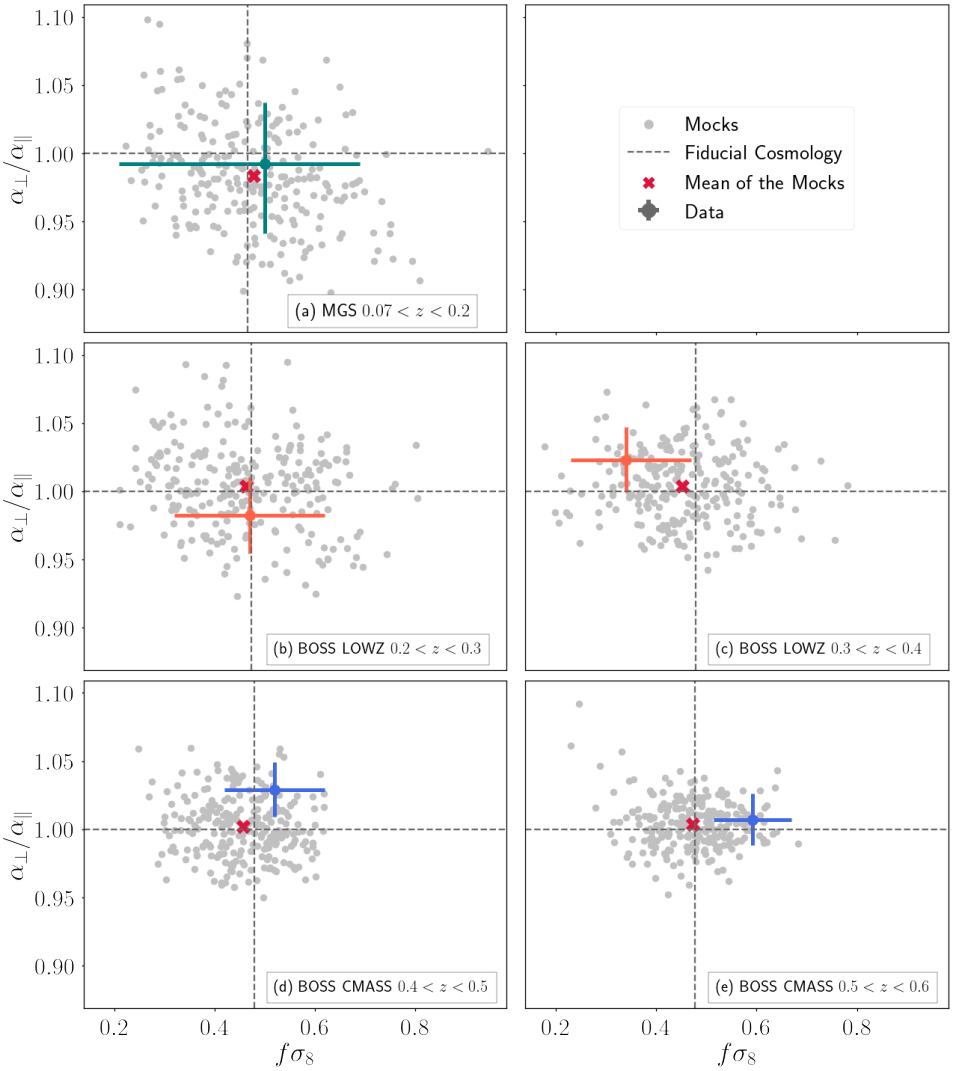

Figure 4.6: Model performance in recovering the fiducial values of $f\sigma_8$ and $\alpha_\perp/\alpha_{||}$ in mocks. Grey points show the results for the mean values of $f\sigma_8$ and $\alpha_\perp/\alpha_{||}$ (after marginalising over other fit parameters) obtained from repeating the analysis on each of 250 MGS mocks ($0.07 < z < 0.2$) and 250 Patchy mocks (all other) when evaluated in their own fiducial cosmology. The means of these individual results are shown by the red crosses, and the expected truth values of the parameters are indicated by the dashed lines. The differences between the means and the expected values are quantified and included in the systematic error budget (Section 4.3). The coloured points with error bars indicate the result and the associated 1σ statistical errors obtained from the MGS (teal), BOSS LOWZ (orange) and BOSS CMASS (blue) data in the same redshift bins. Image Credit: Woodfinden et al. (2022)

4.3.3 Total Systematic Error Budget

To determine the total systematic error in our measurements the results for the differences with respect to the true values, $\Delta(f\sigma_8)$ and $\Delta(\alpha_\perp/\alpha_{||})$, are used for the MGS and Patchy mocks shown in Table 4.1. These reported offsets do not show strong correlations across redshift bins and choices of fiducial cosmology, comparing both positive and negative values, some of which are statistically significant. They were therefore modelled as arising from a draw from an underlying distribution and used the results shown in the table to estimate this distribution's mean and standard deviation. The weighted means and standard deviations for $\Delta(f\sigma_8)$ and $\Delta(\alpha_\perp/\alpha_{||})$ were computed separately using inverse variance weights for each row in Table 4.1, with the variance corresponding to the statistical uncertainty in the measurement of the mean in each redshift bin.

Following this procedure, for $f\sigma_8$ the systematic error in the measurement was estimated to have a mean $\sigma_{\rm sys,offset} = -0.0113$ and a standard deviation $\sigma_{\rm sys,error} = 0.0161$. The corresponding values for $\alpha_\perp/\alpha_\parallel$ are $\sigma_{\rm sys,offset} = 0.0029$ and $\sigma_{\rm sys,error} = 0.0061$. To incorporate these into the total systematic error budget:

1. the corresponding value of $\sigma_{\rm sys,offset}$ was subtracted from the reported mean result for each parameter to correct mean bias, and
2. both systematic error estimates were added in quadrature to the statistical error to determine the total error budget, $\sigma_{\rm total} = \sqrt{\sigma^2_{\rm syst,offset} + \sigma^2_{\rm syst,error} + \sigma^2_{\rm stat}}$ (where $\sigma_{\rm stat}$ was obtained from the fit to the SDSS data).

Table 4.2 summarises the results for each redshift bin. In each redshift bin $\sigma_{\rm sys,offset}$ and $\sigma_{\rm sys,error}$ are both small compared to the statistical error $\sigma_{\rm stat}$ so they resulted in only a modest increase in the total error budget in each case.

4.4 Results

Having quantified the contribution of systematic errors through analysis of the mocks, the SDSS data was examined. The fitting pipeline was run on the data in each redshift bin exactly as described above for the mocks, using a fiducial cosmology with $\Omega_{\rm m} = 0.31$. Figure 4.9 shows the comparisons between the measured void-galaxy correlation in each bin and the corresponding best-fit model obtained from the fit, together with shading indicating the one standard deviation range of the mock data for the same redshift bin.

Table 4.2: Summary of the total error budget for measurement of $f\sigma_8$ and $\alpha_\perp/\alpha_\parallel$ in each redshift bin. Statistical errors $\sigma_{\rm stat}$ are determined from posterior fits to the data. The total systematic error budget is determined by adding in quadrature the individual contributions described in Section 4.3.3, $\sigma_{\rm total} = \sqrt{\sigma^2_{\rm syst,offset} + \sigma^2_{\rm syst,error} + \sigma^2_{\rm stat}}$. Here $\sigma_{\rm syst,offset} = -0.0113$ for $f\sigma_8$ and 0.0029 for $\alpha_\perp/\alpha_\parallel$, and $\sigma_{\rm syst,error} = 0.0161$ for $f\sigma_8$ and 0.0061 for $\alpha_\perp/\alpha_\parallel$.

Redshift Range	Parameter	$\sigma_{\rm stat}$	$\sigma_{\rm total}$
$0.07 < z < 0.2$	$f\sigma_8$	$^{+0.16}_{-0.23}$	$^{+0.16}_{-0.23}$
	$\alpha_\perp/\alpha_\parallel$	$^{+0.044}_{-0.052}$	$^{+0.045}_{-0.053}$
$0.2 < z < 0.3$	$f\sigma_8$	$^{+0.14}_{-0.16}$	$^{+0.14}_{-0.16}$
	$\alpha_\perp/\alpha_\parallel$	$^{+0.028}_{-0.028}$	$^{+0.029}_{-0.029}$
$0.3 < z < 0.4$	$f\sigma_8$	$^{+0.11}_{-0.11}$	$^{+0.11}_{-0.11}$
	$\alpha_\perp/\alpha_\parallel$	$^{+0.024}_{-0.024}$	$^{+0.025}_{-0.025}$
$0.4 < z < 0.5$	$f\sigma_8$	$^{+0.10}_{-0.10}$	$^{+0.10}_{-0.10}$
	$\alpha_\perp/\alpha_\parallel$	$^{+0.020}_{-0.020}$	$^{+0.021}_{-0.021}$
$0.5 < z < 0.6$	$f\sigma_8$	$^{+0.084}_{-0.084}$	$^{+0.086}_{-0.086}$
	$\alpha_\perp/\alpha_\parallel$	$^{+0.019}_{-0.019}$	$^{+0.020}_{-0.020}$

Table 4.3: Marginalised 1D constraints on $f\sigma_8$ and $D_{\rm M}/D_{\rm H}$ at different redshifts, and their correlation coefficient ρ.

$z_{\rm eff}$	$f\sigma_8$	$D_{\rm M}/D_{\rm H}$	ρ
0.15	$0.51^{+0.16}_{-0.23}$	$0.156^{+0.007}_{-0.008}$	-0.351
0.26	$0.44^{+0.14}_{-0.16}$	$0.273^{+0.008}_{-0.008}$	-0.293
0.35	$0.33^{+0.11}_{-0.11}$	$0.397^{+0.009}_{-0.009}$	-0.287
0.47	$0.53^{+0.1}_{-0.1}$	$0.556^{+0.011}_{-0.011}$	-0.158
0.54	$0.64^{+0.077}_{-0.077}$	$0.642^{+0.012}_{-0.012}$	-0.158
0.69[iv]	$0.356^{+0.079}_{-0.079}$	$0.868^{+0.017}_{-0.017}$	-0.154

[iv] From Nadathur et al. (2020b)

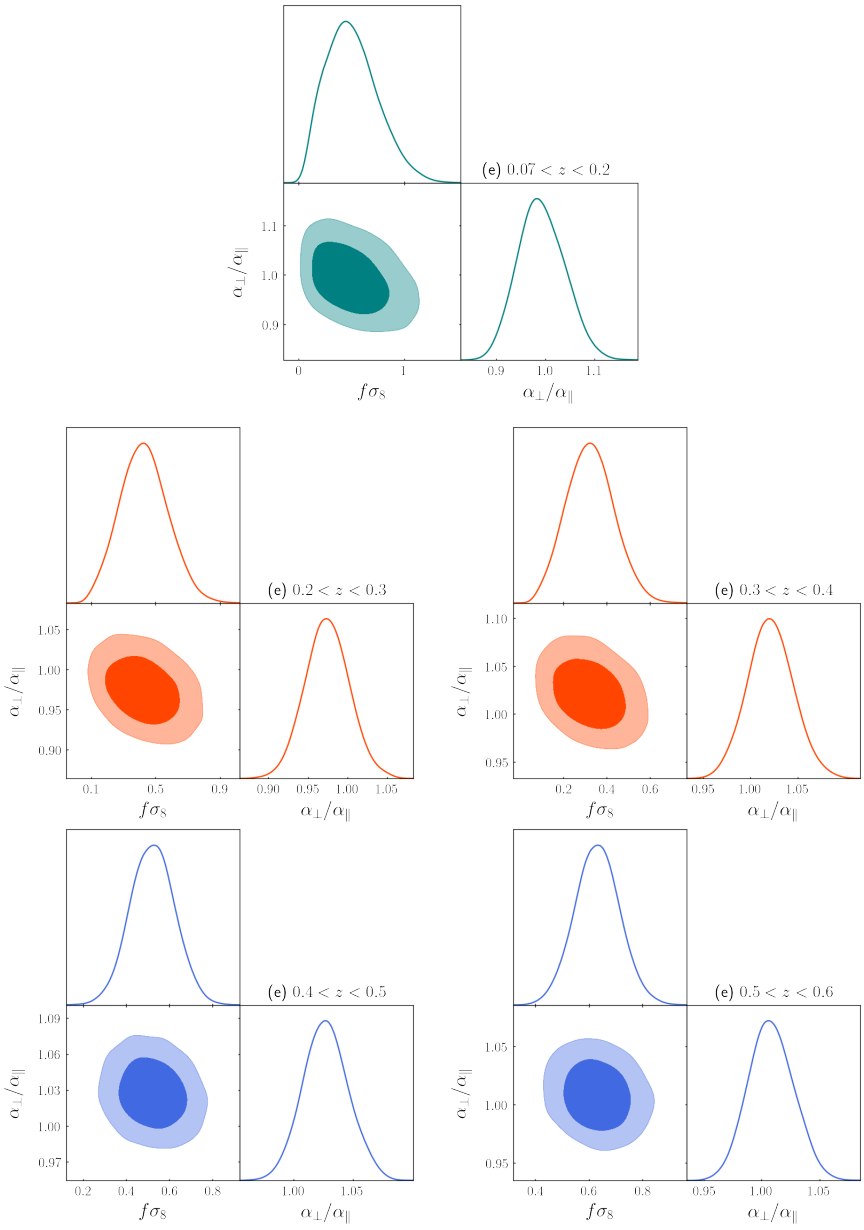

Figure 4.7: Marginalised posterior constraints on the cosmological parameters $f\sigma_8$ and $\alpha_\perp/\alpha_\parallel$ from the fit to MGS and BOSS data in the different redshift bins from Table 3.1. Panel (a) (top row) is for MGS, panels (b) and (c) (middle row) are for the two BOSS LOWZ bins, and panels (d) and (e) (bottom row) are for BOSS CMASS, with the colours for the samples matching those in Figure 3.3. Shaded contours show the 68% and 95% confidence limit regions. These plots include only statistical errors. Image Credit: Woodfinden et al. (2022)

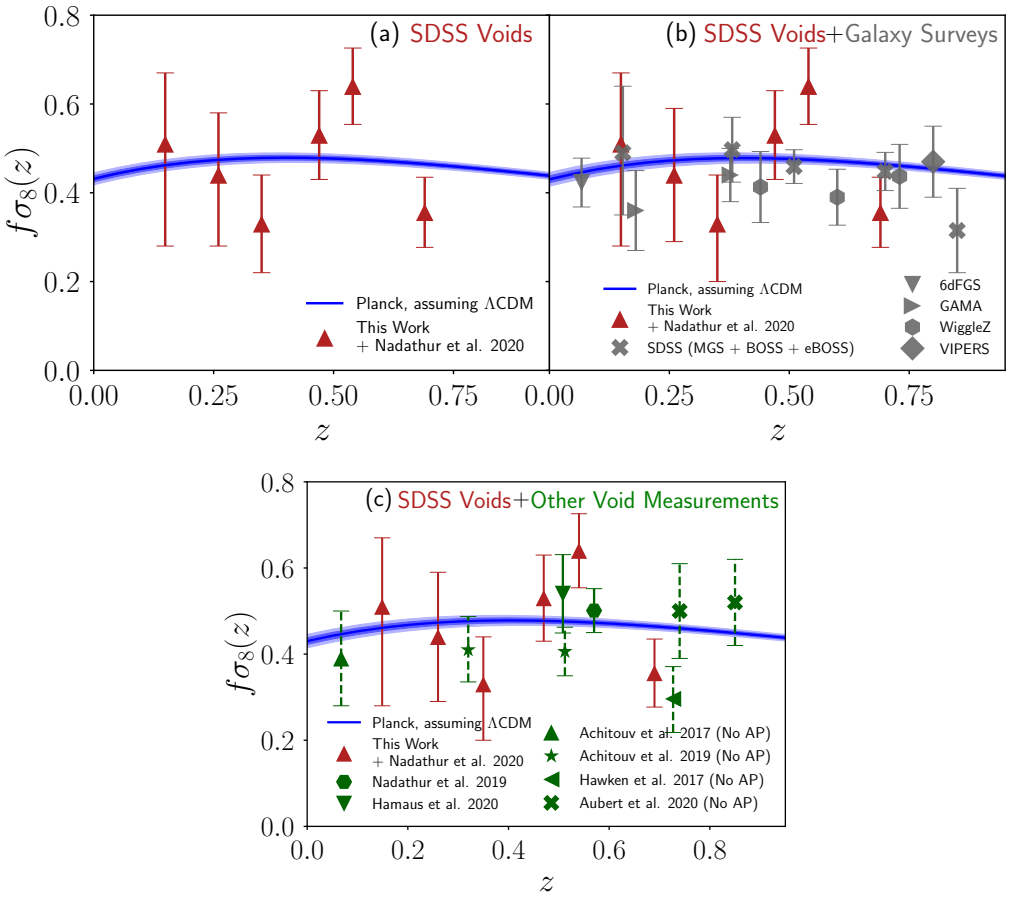

Figure 4.8: (a): Results for the growth rate as a function of redshift, $f(z)\sigma_8(z)$, determined from measurement of the void-galaxy cross-correlation in the MGS and BOSS data presented in this work and in eBOSS from Nadathur et al. (2020b). The blue line (shaded regions) represents the 68% (95%) confidence limits derived from extrapolating CMB measurements from Planck down to these redshift (assuming ΛCDM). (b): As above, but with results from the galaxy clustering and power spectrum from various surveys shown in red. Galaxy survey results are shown from 6dFGS (Beutler et al., 2012), GAMA (Blake et al., 2013), WiggleZ (Blake et al., 2012), VIPERS (de la Torre et al., 2013), MGS (Howlett et al., 2015b), BOSS (Alam et al., 2017), and eBOSS (Alam et al., 2021). (c) As above, but showing results obtained from other analyses of the void-galaxy correlation using alternative analysis techniques in green, from VIPERS (Hawken et al., 2017), 6dFGS (Achitouv et al., 2017), multiple re-analyses of BOSS (Nadathur et al., 2019b; Hamaus et al., 2020; Achitouv, 2019), eBOSS LRG voids (Aubert et al., 2022a), and eBOSS ELG voids (Aubert et al., 2022a). Points shown with dashed error bars are from studies that fix the cosmological model and do not marginalise over the Alcock-Paczynski parameter. Image Credit: Woodfinden et al. (2022)

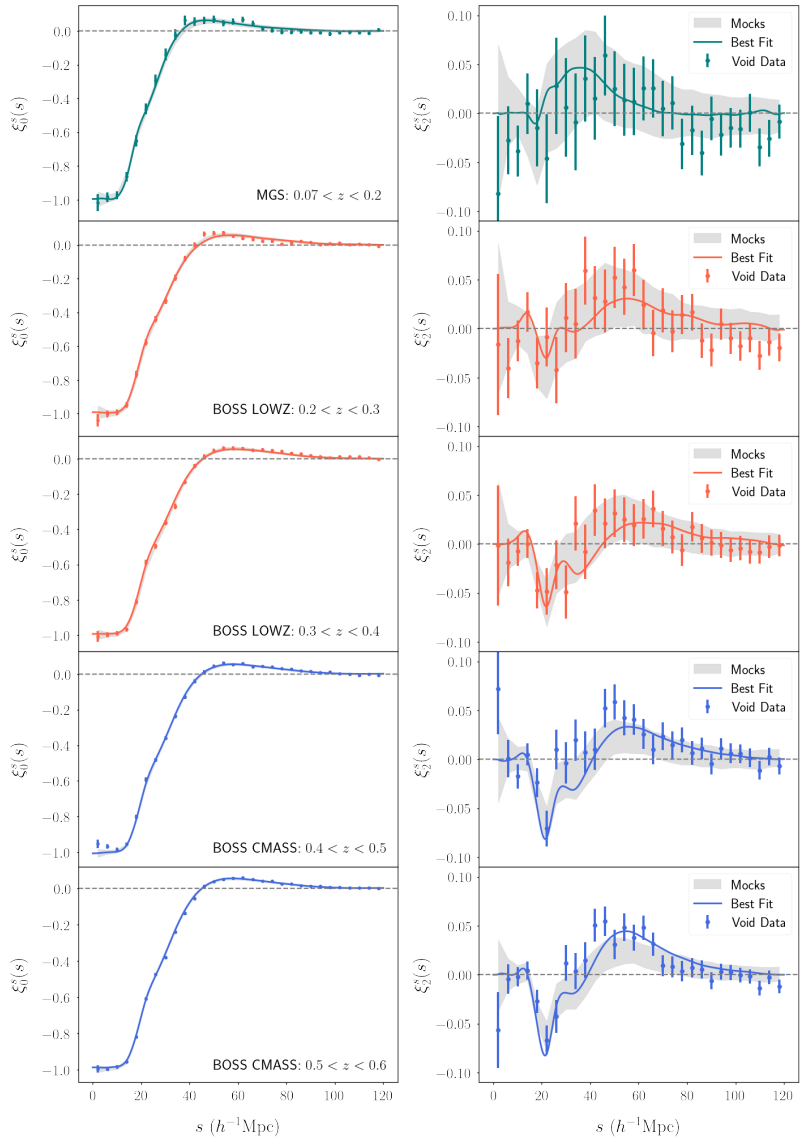

Figure 4.9: Multipole moments of the measured void-galaxy cross-correlation from the MGS and BOSS data across redshift slices (rows). The left column shows the monopole moments and the right column the quadrupole moments. The observed data vector depends on β; results here are shown for the best-fit β values in each redshift bin, $\beta = 0.32, 0.30, 0.41, 0.41, 0.43$ from top to bottom. Error bars are derived from diagonal entries of the covariance matrix obtained from 1000 realisations of the respective MGS or Patchy mocks. The solid black line shows the best-fit model of equation 2.18. The shaded regions show the 68% confidence range for the same multipole moments measured in mocks, evaluated at the same values of β as the observed data vector.

The resultant marginalised constraints (including only statistical errors) on $f\sigma_8$ and $\alpha_\perp/\alpha_\parallel$ are shown in Figure 4.7.

The most likely parameter values from the fit to the data, along with the associated statistical error, are also displayed in Figure 4.6 for comparison with the scatter seen in the fit to the mocks. The scatter in the mock results was found to be consistent with the mean value and statistical error derived from the MCMC analysis of the data. Table 4.2 summarises the statistical and systematic contribution to the total marginalised 1D errors on $f\sigma_8$ and $\alpha_\perp/\alpha_\parallel$ in each redshift bin.

The final results are presented in Table 4.3. Here measurements of $\alpha_\perp/\alpha_\parallel$ were converted to values for the cosmological distance ratio $D_\mathrm{M}/D_\mathrm{H}$ at each redshift using the values of $D_\mathrm{M}^\mathrm{fid}$ and $D_\mathrm{H}^\mathrm{fid}$ in the fiducial cosmology. 1D marginalised mean and uncertainty on $f\sigma_8$ and $D_\mathrm{M}/D_\mathrm{H}$ are presented individually, and also the correlation coefficient for their uncertainties, estimated from the statistical errors in the MCMC fit only (as the systematic errors are assumed uncorrelated, Section 4.3). It is apparent that the fit values of $f\sigma_8$ and $D_\mathrm{M}/D_\mathrm{H}$ are negatively correlated, decreasing correlation with increasing redshift.

Figure 4.8 displays the measurements of the growth rate $f\sigma_8$ obtained here in comparison to other observational results in the same range of redshifts. Panel (a) compares results from the void-galaxy measurements in this work and Nadathur et al. (2020b) to those extrapolated to low redshifts from a fit to the Planck CMB data, assuming a flat ΛCDM cosmology.

Panel (b) compares our results to those measured from standard galaxy clustering techniques without voids obtained from SDSS as well as other surveys in the same range of redshifts. The precision obtained on $f\sigma_8$ from voids alone is comparable to that from galaxy clustering, and Nadathur et al. (2019b, 2020b); Woodfinden et al. (2023) have shown how these two approaches can be consistently combined to obtain more precise measurements than for either alone.

Finally in panel (c) of Figure 4.8, growth rate measurements are compared to those obtained from a number of other void-galaxy analyses in the literature. Where these literature results have been reported only in terms of constraints on $\beta = f/b$ (Achitouv, 2019) for the purposes of comparison these values are translated to equivalent constraints on $f\sigma_8$ assuming perfect knowledge of the fiducial galaxy bias b (taking $b = 1.85$ for LRGs Alam et al., 2017), and with $\sigma_8(z)$ obtained from extrapolating the central value from Planck Collaboration et al. (2020). Several previous void-galaxy analyses (e.g. Achitouv et al., 2017; Hawken et al., 2017; Achitouv, 2019; Aubert et al., 2022a) performed fits for the RSD contributions only, with the value of $D_\mathrm{M}/D_\mathrm{H}$ being fixed to that in the fiducial cosmology. Given the correlation between these two parameters (Table 4.3), fixing the

cosmology in this way will lead to an underestimate of the marginalised uncertainty in $f\sigma_8$, so the published uncertainties should be treated as lower bounds only. The error bars for these studies are shown with dashed lines in the figure to highlight this caveat.

Figure 4.10 summarises results on the background expansion, showing our measurements and marginalised uncertainties for the distance ratio $D_{\rm M}/D_{\rm H}$ divided by redshift z for visual clarity, as a function of z. Also shown for context are the expectations for two example flat models, with $\Omega_{\rm m} = 1$, $\Omega_\Lambda = 0$ and $\Omega_{\rm m} = 0$, $\Omega_\Lambda = 1$ respectively. For comparison, the grey points show the equivalent constraints obtained on this quantity from the measurement of the BAO signal in the BOSS and eBOSS LRG samples (Alam et al., 2021). The ratio $D_{\rm M}/D_{\rm H}$ can only be measured by anisotropic fits to the BAO, which were not possible for the SDSS MGS sample at low redshift (Ross et al., 2015) or the emission line galaxy sample at $z = 0.85$ (Raichoor et al., 2021; de Mattia et al., 2021). The blue band indicates the 68% confidence region obtained from a flat ΛCDM model fit to the Planck CMB data extrapolated down to low redshifts. The green band shows the same thing for the ww_aCDM extended dark energy model but where the fit now includes Planck CMB temperature, polarization and lensing, and Pantheon type Ia supernova data. This differs quite markedly from the blue band because of the known slight preference of the Planck data for a dark energy equation of state $w \neq -1$. Figure 4.10 makes clear the role that the geometrical void-galaxy correlation measurements of $D_{\rm M}/D_{\rm H}$ at low redshifts can have in distinguishing models of late-time acceleration.

Figure 5.5 shows marginalised posterior constraints for a non-flat model with free $\Omega_{\rm m}$ and Ω_Λ but fixed dark energy equation of state $w = -1$, commonly referred to as the oCDM model. The constraint from voids appears as a narrow band in the $\Omega_{\rm m}$-Ω_Λ plane. Assuming only that $\Omega_{\rm m}$ cannot be negative, we find that our void measurements alone show very strong evidence for dark energy and accelerated expansion, requiring that $\Omega_\Lambda > 0$ at approximately the 8.7σ level (determined from the posterior for Ω_Λ at fixed $\Omega_{\rm m} = 0$).

A similar band-like degeneracy in the $\Omega_{\rm m}$-Ω_Λ plane was obtained by Nadathur et al. (2020a) when using only one measurement of $D_{\rm M}/D_{\rm H}$ from voids at $z = 0.57$. From equation 1.20 it follows that the Alcock-Paczysnki parameter $D_{\rm M}/D_{\rm H}$ that is measured here depends on the curvature $\Omega_{\rm K} = 1 - \Omega_{\rm m} - \Omega_\Lambda$ and the normalised expansion rate $H(z)/H_0$. For models with a constant dark energy equation of state $w = -1$, this gives rise to a locus of models in the $\Omega_{\rm m}$-Ω_Λ plane which have constant $D_{\rm M}/D_{\rm H}$ at a given redshift. Thus measurement of $D_{\rm M}/D_{\rm H}$ at a single redshift corresponds to a perfect degeneracy between $\Omega_{\rm m}$ and Ω_Λ. With $\Omega_\Lambda = a + b\Omega_{\rm m}$ for arbitrary a and b, requiring a constant value of $D_{\rm M}/D_{\rm H}$ at redshift $z = 0.15$ sets the local gradient $b = 0.58$, while for example at redshift $z = 0.69$ this translates to $b = 0.81$. This indicates that in principle, measurements of $D_{\rm M}/D_{\rm H}$ made at sufficiently many widely separated redshifts can break the $\Omega_{\rm m}$-Ω_Λ degeneracy in

this class of models. The precision obtained in our current results covering the redshift range $0.15 \leq z \leq 0.69$ is not sufficient to fully break this degeneracy and close the void-only contours shown, but the inclusion of more data at higher redshifts (such as those expected from the upcoming DESI and Euclid surveys) will help to achieve this. See Section 5.4.3 and Figure 5.8 for more details. Along with presenting cosmological measurements from the void-galaxy cross-correlation on previously unanalysed datasets (see Section 3.1), the consistent analyses method applied to datasets over a wide range in redshift is novel in that it allows for information to be extracted from the behaviour of cosmological parameters (i.e. $D_{\rm M}/D_{\rm H}$ and $f\sigma_8$) at different redshifts.

Since the degeneracy direction is different to that obtained from BAO or type Ia supernovae data, one can combine void measurements with these complementary probes to obtain significantly tighter constraints on dark energy, as done by Nadathur et al. (2020a); Woodfinden et al. (2023). Chapter 5 delves more into the combination of void information with alternative probes.

4.5 Conclusions

This work presents a cosmological analysis of the anisotropic void-galaxy cross-correlation measured over a wide redshift range in the SDSS DR7 (MGS) and SDSS DR12 (BOSS LOWZ and BOSS CMASS) galaxy surveys. Voids were extracted after running reconstruction-based RSD removal on the galaxy field to remove systematic void selection bias effects. This was implemented using the `Revolver` code along with `ZOBOV`, a watershed-based void-finder. A joint fit was performed to the multipoles of the measured correlation to determine the growth rate of structure $f\sigma_8$ and the Alcock-Paczynski distance ratio $D_{\rm M}/D_{\rm H}$ in five redshift bins. These methods are consistent with those used in previous analyses by Nadathur et al. (2019b, 2020b), with only minor differences in the treatment of uncertainties in the estimated covariance in the likelihood and in the interpolation in between measured points in the parameter β. Therefore, the measurements performed in this work are combined with the results presented by Nadathur et al. (2020b) using the eBOSS DR16 data at redshift $z > 0.6$ to build a consistent picture of the growth of structure and geometrical evolution of the Universe using voids alone in six independent redshift bins jointly covering the range $0.15 \leq z \leq 0.69$. Our final results for $f\sigma_8$ and $D_{\rm M}/D_{\rm H}$ are summarised in Table 4.3 and are in excellent agreement with the standard flat ΛCDM cosmological model.

A large suite of mock galaxy surveys—constructed using both full N-body simulations and approximate gravity solvers—were used to perform multiple tests of possible systematic

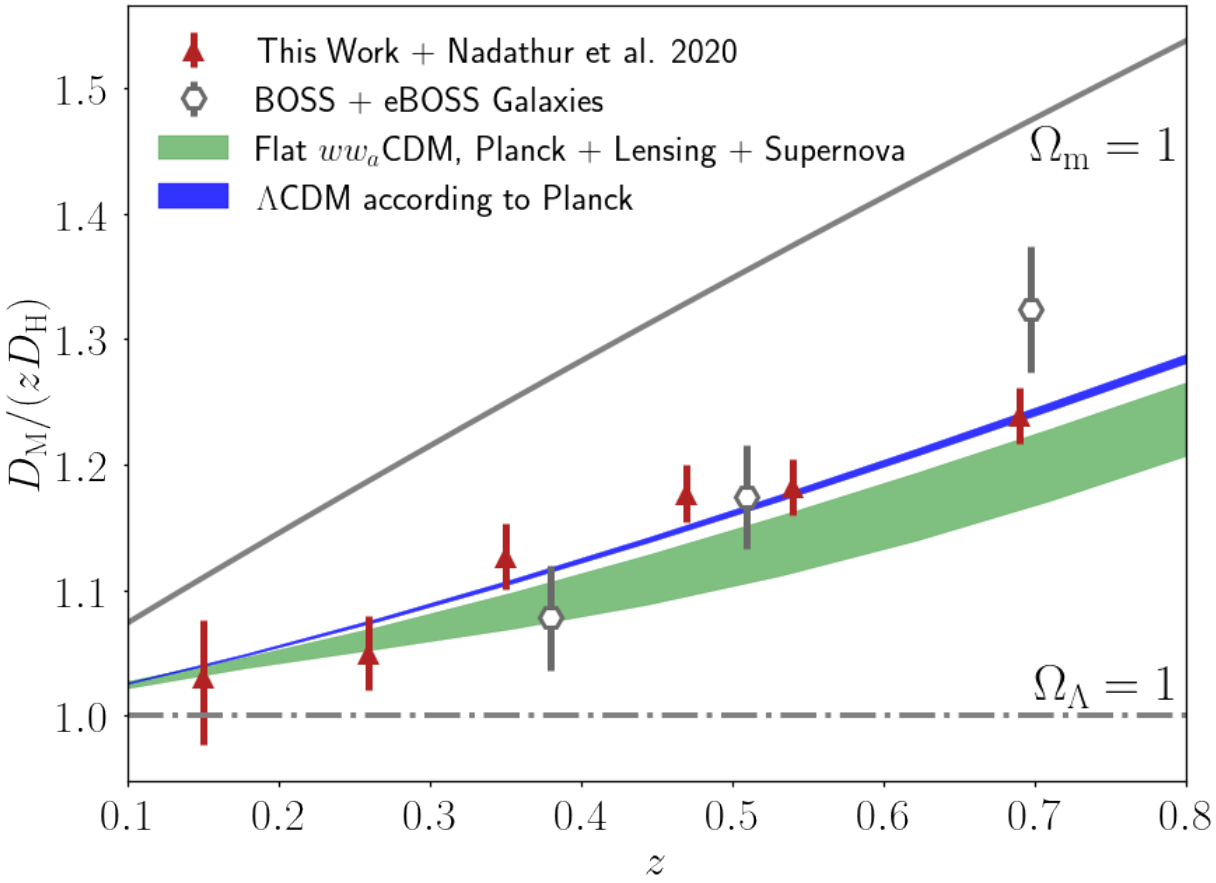

Figure 4.10: Measurements of D_M/D_H, divided by the redshift z, from voids in this work are shown as the red triangles with associated error bars. Open grey points show the corresponding results from Alam et al. (2017, 2021) obtained using BAO measured in the same galaxy samples where applicable (transverse and perpendicular BAO were not separately constrained for MGS at $z = 0.15$). The blue shaded band is the 68% C.L. region obtained from extrapolating the Planck CMB constraints to low redshifts assuming ΛCDM. The green shaded band shows the 68% C.L. region from fits to Planck CMB and CMB lensing and Pantheon supernovae in the ww_aCDM model with varying DE equation of state. The grey solid and dot-dashed lines show the expectation for a flat pure matter Universe ($\Omega_m = 1, \Omega_\Lambda = 0$, $w = -1$) and a flat pure dark energy Universe ($\Omega_m = 0, \Omega_\Lambda = 1$, $w = -1$) respectively. Image Credit: Woodfinden et al. (2022)

errors in our analysis in Section 4.3. These were quantified as part of the total error budget reported for our results. The systematic errors were always small compared to the statistical uncertainties from the data, ensuring that the method and results presented here are robust. Nevertheless, further improvements on the method presented here will be required to make full use of the much greater statistical precision that is expected from the much larger datasets that will be available from the DESI and Euclid surveys in the near future.

It should be noted that mock catalogues used in this work rely on a HOD to place galaxies in dark matter halos. This HOD is consistent across all environments in the mock and was not adjusted based on whether a galaxy is placed in a high-density or low-density region (such as a void). Tinker et al. (2006, 2008); Tinker and Conroy (2009) show that galaxy-halo connection displays no strong changes in low-density environments such as voids. In contrast, Verza et al. (2022) find a scale dependence for halo bias inside voids. Effects of other prescriptions for HODs will be tested in future work.

Our work shows the importance of voids as cosmological probes and motivates the inclusion of voids as standard tools in the analysis of galaxy survey data due to the information gain available from void-galaxy correlations. This is particularly relevant to low-redshift geometrical tests of cosmological expansion and discriminating between alternative models of dark energy that change the expansion history at late times. The voids presented in this chapter from the analyses of the void-galaxy correlation function are used (both on their own and in combination with other cosmological probes such as BAO, RSD, CMB, SN, etc.) to test a variety of plausible cosmological models in Chapter 5.

Chapter 5

Cosmological Models Fits to Voids and the Combination of Voids with Other Probes

5.1 Introduction

In this chapter, we investigate the resulting constraints from applying measurements from Chapter 4 to a range of cosmological models. The large-scale structure of the Universe contains a wealth of information about the expansion history of the Universe as well as the growth of structure within it. Measurements of these from spectroscopic galaxy surveys within the low-redshift Universe, in combination with Cosmic Microwave Background observations from Planck Collaboration et al. (2020), provide the best evidence currently available for the standard Λ Cold Dark Matter (ΛCDM) cosmological model. Modern spectroscopic galaxy surveys are focused on observing the baryon acoustic oscillation (BAO) feature, a relic of primordial sound waves, which can be used as a standard ruler (e.g. Alam et al., 2015, 2021). In addition to the BAO feature, cosmological information can be extracted using various other techniques including redshift space distortions (RSD, Kaiser, 1987) and the galaxy distribution around voids (Lavaux and Wandelt, 2012).

We used all available SDSS data for luminous red galaxies (LRG). Measurements of the growth rate of structure and Alcock-Paczynski measurements were taken from the distribution of galaxies around voids (hereon referred to as voids) (Woodfinden et al., 2022; Nadathur et al., 2020b) presented in Chapter 4, as well as information from BAO and RSD from the same galaxy sample (hereon referred to as galaxies). We aimed to combine this

information to provide the most accurate cosmological constraints available from SDSS. These cosmological constraints were provided for a selection of realistic cosmological models (ex. ΛCDM, wCDM). In addition to the information from available SDSS data, we used data from the CMB (Planck Collaboration et al., 2020) and Pantheon SN Ia (Scolnic et al., 2018) in combination with SDSS to provide very accurate cosmological constraints from the best currently accessible data.

This Chapter is structured as follows: in Section 5.2 we very briefly summarise the data and mock catalogues presented in Chapter 3 & 4 and used in this work including the determination of their cross-covariance. In Section 5.3 we review the theoretical background allowing consensus results between the void-galaxy and galaxy-galaxy clustering techniques using the same data set. In Section 5.4 we present the results of our analysis for a wide range of varying cosmologies and discuss the implications of this. Finally, we conclude in Section 5.5.

5.2 Data and Mocks

Previous analysis of the void-galaxy correlation function is published in Nadathur et al. (2020b), Woodfinden et al. (2022) and presented in Chapter 4. These results are presented in combination with BAO and RSD results from galaxy clustering made from the SDSS-II (Howlett et al., 2015b), SDSS-III (Alam et al., 2015), and SDSS-IV (Bautista et al., 2021; Gil-Marín et al., 2020). Previous Measurements are shown in Table 5.1. Information from the void-galaxy clustering is shown in Table 4.3 while information from galaxy-galaxy clustering is shown in Table 5.1.

Howlett et al. (2015b) analysed galaxies in the MGS sample (see Section 3.2.1) including measurements of RSD from the two-point correlation function as well as Alcock-Paczynsi measurements from BAO. This paper did not split Alcock-Paczynski measurements into $D_{\rm M}/r_{\rm d}$ and $D_{\rm H}/r_{\rm d}$ as was done for BOSS and eBOSS analysis. Instead, measurements are available for the volume-averaged distance $D_{\rm V}/r_{\rm d} = (zD_{\rm M}^2 D_{\rm H})^{1/3}/r_{\rm d}$. Along with the MGS data, we made use of mock catalogues from Section 3.2.1 to calculate the cross-covariance between information available from Voids, BAO, and RSD (Howlett et al., 2015b).

Alam et al. (2017) analysed BOSS galaxies from Section 3.2.2 measuring $D_{\rm M}/r_{\rm d}$ and $D_{\rm H}/r_{\rm d}$ from the BAO method and $f\sigma_8$ from RSD. Measurements were analysed in 3 partially overlapping redshift shells, $0.2 < z < 0.5$, $0.4 < z < 0.6$, and $0.5 < z < 0.75$. The highest redshift shell overlaps entirely with a combination of the $0.4 < z < 0.6$ and $0.5 < z < 0.75$ shells in the redshift range $0.6 < z < 1.0$ and so was not included in

this work. Measurements are summarised in Table 5.1. $D_{\rm M}/r_{\rm d}$ and $D_{\rm H}/r_{\rm d}$ information has been converted into $D_{\rm M}/D_{\rm H}$ and $D_{\rm V}/r_{\rm d}$ using the published correlation coefficients between them. Along with the BOSS data, we made use of the Patchy mocks from Section 3.2.2 to create our cross-covariance matrix described in Section 5.3.

Bautista et al. (2021) and Gil-Marín et al. (2020) analysed eBOSS galaxies from Section 3.2.3 using BAO and RSD features from the galaxy two-point correlation function and power spectrum to infer geometrical and dynamical cosmological constraints shown in Table 5.1. Along with eBOSS data, we made use of the EZmocks described in Zhao et al. (2020) to create our cross-covariance matrix described in Section 5.3. Void finding was run on these mock catalogues in Nadathur et al. (2020b) and resultant parameter constraints on each mock were used.

Figures 4.8 & 4.10 shows the measurements from both voids and galaxies on $f\sigma_8$ and $D_{\rm M}/D_{\rm H}$ on SDSS LRG. The best-fit model for ΛCDM measured by Planck Collaboration et al. (2020) is shown for comparison in both these figures.

Joint fits to both RSD and AP for voids and galaxies combined lead to increased precision in measurements of both the AP effect and $f\sigma_8$ compared to that from voids or galaxies alone. This can be seen in Figure 5.1. The combination of these two measurements, described in more detail in Section 5.3, therefore results in a large gain of information than using either of these techniques individually due to the perpendicularity of the likelihood contours. To obtain this combination we have taken information available across a wide range in redshift (see Tables 4.4 & 5.1) and compressed this, under the assumption of a flat ΛCDM cosmology, into a single redshift at $z = 0.52$ (the mean redshift of voids).

5.3 Combination of Results and Likelihoods

We combined void-galaxy and galaxy-galaxy clustering measurements to take advantage of the significant gain of information from the complementary directions of parameter contours. As both methods were applied to the same data, the large-scale structure could conceivably affect both measurements. We accounted for any covariance between the two using the method from Alam et al. (2017) and Sánchez et al. (2017a) and previously applied to the void-galaxy correlation function in combination with galaxy clustering in Nadathur and Percival (2019) and Nadathur et al. (2020b). A cross-covariance matrix, Ψ was constructed for all observables using measurements made on mock catalogues described in Chapter 3. The covariance between measurements made on different mock catalogues (ex. between MGS mocks in the redshift range $0.07 < z < 0.2$ and eBOSS mocks in the

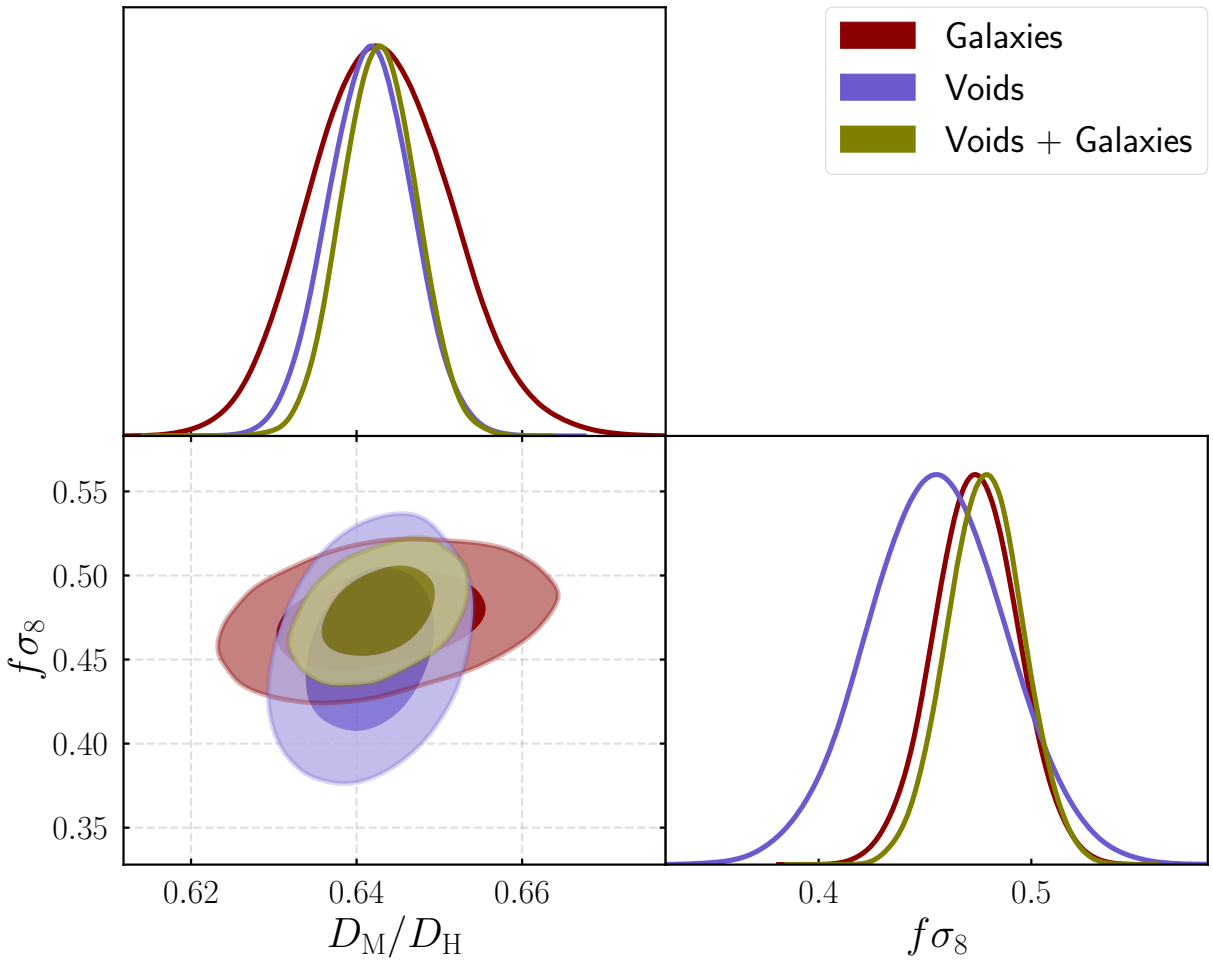

Figure 5.1: Marginalised compressed constraints on $f\sigma_8$ and $D_{\rm M}/D_{\rm H}$ at a single redshift $z_{\rm eff} = 0.52$ (the mean redshift of voids used) obtained from the combination of data shown in Table 5.1 under the assumption of a flat ΛCDM cosmological model. Shaded contours show the 68% and 95% confidence limit regions and corresponding mean values and marginalised 68% credible intervals are shown in Tables 5.3 & 5.4. Image Credit: (Woodfinden et al., 2023).

Table 5.1: Galaxy measurements from SDSS are from Howlett et al. (2015b); Ross et al. (2015); Alam et al. (2015); Bautista et al. (2021) and Gil-Marín et al. (2020). Here 'Galaxies' refers to BAO+RSD results from galaxy clustering. $z_{\rm eff}$ is the effective redshift at which the measurement was taken. Note that galaxy clustering can provide separate measurements of $D_{\rm M}$ and $D_{\rm H}$ using the BAO scale as a standard ruler while the void-galaxy correlation provides a measurement of their ratio $D_{\rm M}/D_{\rm H}$ by using a standard shape (i.e. a stack of voids). $D_{\rm M}/r_{\rm d}$ and $D_{\rm H}/r_{\rm d}$ information from galaxies has been converted into $D_{\rm M}/D_{\rm H}$ and $D_{\rm V}/r_{\rm d}$ using the published correlation coefficients between them. Similar results for voids are presented in Table 5.2.

Method	Redshift Range	$z_{\rm eff}$	$D_{\rm M}/D_{\rm H}$	$D_{\rm V}/r_{\rm d}$	$f\sigma_8$
Galaxies	$0.07 < z < 0.2$	0.15	———	4.51 ± 0.14	0.53 ± 0.16
Galaxies	$0.2 < z < 0.5$	0.38	0.410 ± 0.016	9.98 ± 0.11	0.497 ± 0.045
Galaxies	$0.4 < z < 0.6$	0.51	0.599 ± 0.021	12.67 ± 0.13	0.459 ± 0.038
Galaxies	$0.6 < z < 1.0$	0.70	0.924 ± 0.035	16.26 ± 0.21	0.473 ± 0.041

redshift range $0.6 < z < 1.0$) will only be non-zero due to random noise and are set equal to 0. This is typical of combined analyses and the correlations for non-overlapping galaxy samples (this is *not* the case for the BOSS galaxy samples) are close to zero (Sánchez et al., 2017b). Figure 5.2 shows that the cross-correlation between different void redshift slices is small. It is not possible to measure the cross-correlation directly between SDSS samples as this would require mock catalogues with a combination of volume and resolution which is not currently possible for our samples.

We combined all observables into one data vector $\vec{D}$, and at each point in theory space being sampled we calculated the χ^2 value as

$$\chi^2 = (\vec{D} - \vec{T})^t \Psi (\vec{D} - \vec{T}) \tag{5.1}$$

where $\vec{T}$ is a vector containing the value of all observables at a particular point in the theory space being sampled.

The data vectors used have already included a prior designed to match the Bayesian results to frequentist expectations to first order allowing for errors in the covariance matrix used when fitting to the correlation functions. From these fits, we only used the covariant parameter measurements: hence only needing a smaller number of mocks, which are only used to estimate the covariance between measurements in the same redshift bins. As such we can assume these measurements as a Gaussian fit and so use an appropriate likelihood function (Woodfinden et al., 2022; Percival et al., 2021). To explore the model

parameter space we used MCMC sampling implemented using the `Cobaya` sampling package (Torrado and Lewis, 2019b, 2021b) and use a mixture of `CAMB`[1] and `CLASS`[2] as the underlying cosmological codes (Lewis et al., 2000; Lesgourgues, 2011). This involved writing numerical calculation code capable of returning values of $f\sigma_8$ and $D_{\rm M}/D_{\rm H}$ for a variety of redshifts and incorporating this into existing `CAMB` and `CLASS` code. Chains were run for all combinations of datasets of interest (e.g. just voids, just galaxies, galaxies and voids) as well as all cosmologies tested in Section 5.4 below.

Figure 5.2 shows the cross-correlation matrix corresponding to the cross-covariance matrix. Only a weak correlation can be seen between measurements of $f\sigma_8$ and $D_{\rm M}/D_{\rm H}$ as measured by voids. While results are reported for galaxy clustering in the parameters $f\sigma_8$, $D_{\rm M}$, and $D_{\rm H}$ we performed a change of basis to $f\sigma_8$, $D_{\rm M}/D_{\rm H}$, and $D_{\rm V}$ using the published correlation coefficients between them.

Results from BAO+RSD for galaxies showed a strong correlation in measured parameters. We see that for all redshift bins considered, there is a strong positive correlation between $f\sigma_8$ and $D_{\rm M}/D_{\rm H}$, and little correlation elsewhere. We also saw similar trends when looking at the correlations between redshift bins $0.2 < z < 0.5$ and $0.4 < z < 0.6$. This significant correlation between these bins was expected as these come from the same mock catalogues which are later split into redshift shells as well as overlap in the $0.4 < z < 0.5$ range.

No significant correlation could be seen between results from voids and galaxies when looking at data measured from the same mock catalogues. We also did not see a correlation between redshift shells measured in the same mock catalogues for voids as we do for galaxies. A combination of measurements from voids and galaxies therefore should result in a significant gain in information compared to each measurement individually. The results from combining information from void-galaxy and galaxy-galaxy correlations on measured parameters $f\sigma_8$, $D_{\rm M}$, $D_{\rm H}$, and $D_{\rm M}/D_{\rm H}$ are shown in Table 5.2. These were found assuming a ΛCDM cosmological model.

Parameter contours plotted in Figure 5.1 demonstrate the significant gain of information from the combination of these results; this gain of information is due to the orthogonality of degeneracy directions between void-galaxy and galaxy-galaxy correlations as well as the weak correlation between these two methods.

[1] https://camb.info/
[2] https://lesgourg.github.io/class_public/class.html

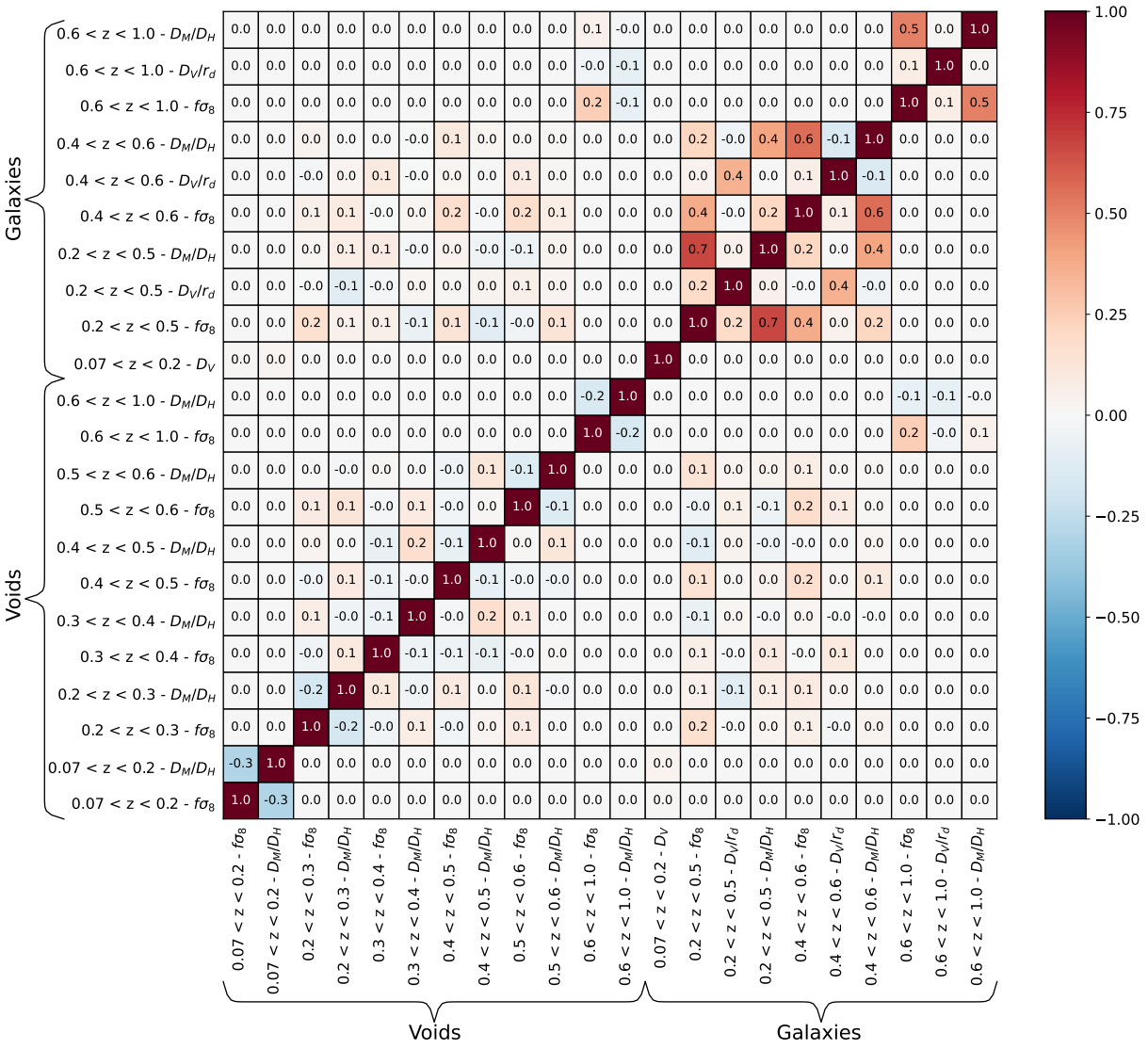

Figure 5.2: Correlation coefficients between measured values of $f\sigma_8$, $D_\mathrm{M}/D_\mathrm{H}$, and D_V obtained from voids and galaxies in various redshift bins from SDSS LRGs. The cross correlation between measurements taken from different mock catalogues is set to 0 to reduce noise in unrelated measurements. Image Credit: (Woodfinden et al., 2023)

Table 5.2: Final results for the combination of void-galaxy and galaxy-galaxy clustering. We report results at the effective redshift of voids $z_{\rm eff}$ The combination of measurements shown is made by assuming a ΛCDM cosmological model. Galaxies refer to constraints found through measurement of the BAO+RSD and void refers to constraints found through void-galaxy cross-correlation. Reported errors are the 68% credible intervals.

Tracer	Redshift range	$z_{\rm eff}$	$f\sigma_8$	$D_{\rm M}/r_{\rm d}$	$D_{\rm H}/r_{\rm d}$	$D_{\rm M}/D_{\rm H}$
Voids + Galaxies	$0.07 < z < 1.0$	0.52	0.464 ± 0.017	17.36 ± 0.13	19.70 ± 0.21	0.8655 ± 0.0071
Voids + Galaxies	$0.4 < z < 0.6$	0.51	0.479 ± 0.028	13.40 ± 0.15	22.36 ± 0.30	0.6410 ± 0.0075
Voids + Galaxies	$0.2 < z < 0.5$	0.39	0.513 ± 0.028	10.35 ± 0.13	24.18 ± 0.34	0.4282 ± 0.0051

5.4 Results

We split the discussion of our results by the cosmological model assumed when MCMC fits to the data were ran. Relevant cosmological parameters are shown in each section.

5.4.1 ΛCDM

For a base ΛCDM model the AP information constrains $\Omega_{\rm m}$, as shown in Tables 5.3 & 5.4. If we do not know $r_{\rm d}$, then the BAO measurements reduce to only the relative constraints from the AP effect, while without an independent constraint on σ_8, the RSD measurement also becomes a relative measure, and only depends on the matter density.

Of note in Tables 5.3 & 5.4, the uncertainty on $\Omega_{\rm m}$ from voids+galaxies is 43% lower than that from galaxies alone due to the increase in precision in measurements of $D_{\rm M}/D_{\rm H}$. The measured value of $\Omega_{\rm m}$ from the full SDSS results is consistent with results from Planck Collaboration et al. (2020) within 1.6σ; however, this is in increased tension as that from galaxies alone agrees with Planck within 1σ due to a larger uncertainty.

The combination of Planck and SN only measured $\Omega_m = 0.3143 \pm 0.0079$ and $H_0 = 67.43 \pm 0.57$. The additional information from SDSS (voids+galaxies) resulted in a 30% reduction in the measured error on $\Omega_{\rm m}$ and a 28% reduction in the measured error on H_0.

Table 5.3: Final parameter constraints from a combination of different probes. V refers to measurements made through the void-galaxy correlation function. G refers to constraints found through measurement of the BAO peak position and peculiar velocities of galaxies. V + G are both measurements from SDSS. C refers to measurements of the cosmic microwave background from Planck Collaboration et al. (2020). S refers to measurements from the Pantheon SN Ia sample (Scolnic et al., 2018). Reported errors are the 68% credible intervals. Voids provide constraints in a narrow band in the $\Omega_m - \Omega_\Lambda$ plane in open cosmologies, shown in Figure 5.5 however are not able to constrain Ω_m or Ω_Λ and are not shown. Void, Galaxies, and Voids + Galaxies without additional CMB +SN data were unable to provide constraints on $w(z)CDM$ and $ow(z)CDM$ models within a reasonable prior volume, and so are excluded from this table.

Measurement	Ω_m	Ω_Λ	Ω_k	w_0	w_a	H_0
ΛCDM						
V	0.354 ± 0.029	———	———	———	———	———
G	$0.360^{+0.038}_{-0.045}$	———	———	———	———	———
V+G	0.356 ± 0.024	———	———	———	———	———
V+C+S	0.3170 ± 0.0069	———	———	———	———	67.24 ± 0.50
G+C+S	0.3117 ± 0.0056	———	———	———	———	67.62 ± 0.42
V+G+C+S	0.3127 ± 0.0055	———	———	———	———	67.55 ± 0.41
wCDM						
V	$0.330^{+0.11}_{-0.033}$	———	———	$-1.17^{+0.64}_{-0.31}$	———	———
G	0.359 ± 0.044	———	———	$-1.91^{+0.45}_{-0.85}$	———	———
V+G	$0.391^{+0.028}_{-0.021}$	———	———	$-1.50^{+0.43}_{-0.28}$	———	———
V+C+S	0.3148 ± 0.00715	———	———	$-0.906^{+0.10}_{-0.071}$	———	67.39 ± 0.52
G+C+S	0.3149 ± 0.0066	———	———	-0.960 ± 0.045	———	67.39 ± 0.49
V+G+C+S	0.3172 ± 0.0061	———	———	-0.930 ± 0.039	———	67.22 ± 0.45
w(z)CDM						
V+C+S	0.3152 ± 0.0072	———	———	-1.02 ± 0.34	> -0.54	67.37 ± 0.52
G+C+S	0.3139 ± 0.0070	———	———	$-0.998^{+0.097}_{-0.11}$	$0.16^{+0.51}_{-0.36}$	67.46 ± 0.51
V+G+C+S	0.3152 ± 0.0067	———	———	-0.995 ± 0.094	$0.27^{+0.40}_{-0.33}$	67.37 ± 0.49

Table 5.4: Continuation of Table 5.3.

Measurement	Ω_m	Ω_Λ	Ω_k	w_0	w_a	H_0
oCDM						
V	———-	———-	———-	———	———	———
G	$0.358^{+0.045}_{-0.058}$	$0.641^{+0.083}_{-0.069}$	$0.001^{+0.094}_{-0.11}$	———	———	———
V+G	$0.354^{+0.045}_{-0.055}$	0.638 ± 0.049	$0.008^{+0.098}_{-0.083}$	———	———	———
V+C+S	0.335 ± 0.015	0.671 ± 0.011	-0.0061 ± 0.0045	———	———	65.1 ± 1.6
G+C+S	0.3114 ± 0.0063	0.6881 ± 0.0058	0.0004 ± 0.0020	———	———	67.72 ± 0.66
V+G+C+S	0.3120 ± 0.0060	0.6873 ± 0.0055	$0.0007^{+0.0019}_{-0.0018}$	———	———	67.71 ± 0.63
owCDM						
V	$0.385^{+0.082}_{-0.13}$	$0.657^{+0.077}_{-0.14}$	$-0.04^{+0.22}_{-0.15}$	$-1.29^{+0.58}_{-0.32}$	———	———
G	$0.326^{+0.046}_{-0.064}$	$0.582^{+0.063}_{-0.077}$	$0.093^{+0.11}_{-0.083}$	$-1.98^{+0.46}_{-0.86}$	———	———
V+G	$0.331^{+0.067}_{-0.094}$	$0.607^{+0.078}_{-0.12}$	$0.06^{+0.18}_{-0.13}$	$-1.41^{+0.70}_{-0.31}$	———	———
V+C+S	0.332 ± 0.017	0.674 ± 0.013	-0.0052 ± 0.0048	$-0.954^{+0.14}_{-0.075}$	———	$65.5^{+1.7}_{-1.9}$
G+C+S	0.323 ± 0.011	0.6800 ± 0.0088	$-0.0029^{+0.0036}_{-0.0032}$	$-0.910^{+0.078}_{-0.069}$	———	66.4 ± 1.2
V+G+C+S	0.3239 ± 0.0085	0.6791 ± 0.0069	-0.0031 ± 0.0028	-0.889 ± 0.052	———	66.29 ± 0.93
ow(z)CDM						
V+C+S	$0.360^{+0.021}_{-0.026}$	$0.652^{+0.019}_{-0.016}$	$-0.0126^{+0.0074}_{-0.0057}$	-1.22 ± 0.43	> -0.48	62.8 ± 2.1
G+C+S	0.322 ± 0.014	0.680 ± 0.011	$-0.0027^{+0.0042}_{-0.0038}$	-0.91 ± 0.17	$-0.02^{+0.56}_{-0.48}$	66.5 ± 1.6
V+G+C+S	0.323 ± 0.011	0.6795 ± 0.0087	-0.0030 ± 0.0034	-0.90 ± 0.14	$0.02^{+0.49}_{-0.42}$	66.3 ± 1.2

5.4.2 wCDM

We now consider a wCDM model, where we expand the ΛCDM model to consider a dark energy component with equation of state $w_0 \equiv p/\rho$, where p is the dark energy pressure and ρ is the dark energy density. In the standard ΛCDM model, $w_0 = -1$, describing dark energy as a cosmological constant. A value of $w_0 < -1/3$ is required for an accelerating expansion of the Universe while a value of $w_0 < -1$ means that dark energy density increases as the Universe expands.

An uninformative, flat prior of $-3 < w < -1/3$ was imposed. Figure 5.3 shows results for this cosmology and Tables 5.3 & 5.4 lists the mean values and marginalised 68% credible intervals obtained for various combinations of measurement techniques. Results show reasonable agreement with standard ΛCDM cosmology where $w = -1$.

The combination of Planck and SN only measured $\Omega_m = 0.307 \pm 0.011$, $w = -1.036 \pm 0.037$ and $H_0 = 68.3 \pm 1.1$. The additional information from SDSS (voids+galaxies) resulted in a 5% reduction in the measured error on Ω_m, a 5% increase in the measured error on w and a 59% reduction in the measured error on H_0.

5.4.3 w(z)CDM

We now consider adding more flexibility to the equations of state of dark energy. If dark energy is a generic dynamical fluid then the equation of state parameter w should be allowed to vary over time. We adopted an equation of state parameter for dark energy with the functional form $w(a) = w_0 + (1 - a)w_\mathrm{a}$. Here w_0 and w_a are fitting parameters and a is the scale factor. In a ΛCDM model $w_0 = -1$ and $w_\mathrm{a} = 0$.

Uninformative, flat priors of $-3 < w < -1/3$ and $-3 < w_\mathrm{a} < 2$ were imposed. Figure 5.4 shows results for this cosmology and Tables 5.3 & 5.4 lists the mean values and marginalised 68% credible intervals obtained for various combinations of measurement techniques. Only the combination of SDSS data with CMB and SN results from Planck Collaboration et al. (2020) and Scolnic et al. (2018) are shown, as SDSS alone did not have enough constraining power within a reasonable prior volume. All results showed agreement with $w_0 = -1$ and $w_\mathrm{a} = 0$, demonstrating consistency with a ΛCDM model. For the combination of voids with CMB and SN data, the constraints on w_a were seen to be hitting the upper bound of the prior, as such only lower limits are given in Tables 5.3 & 5.4.

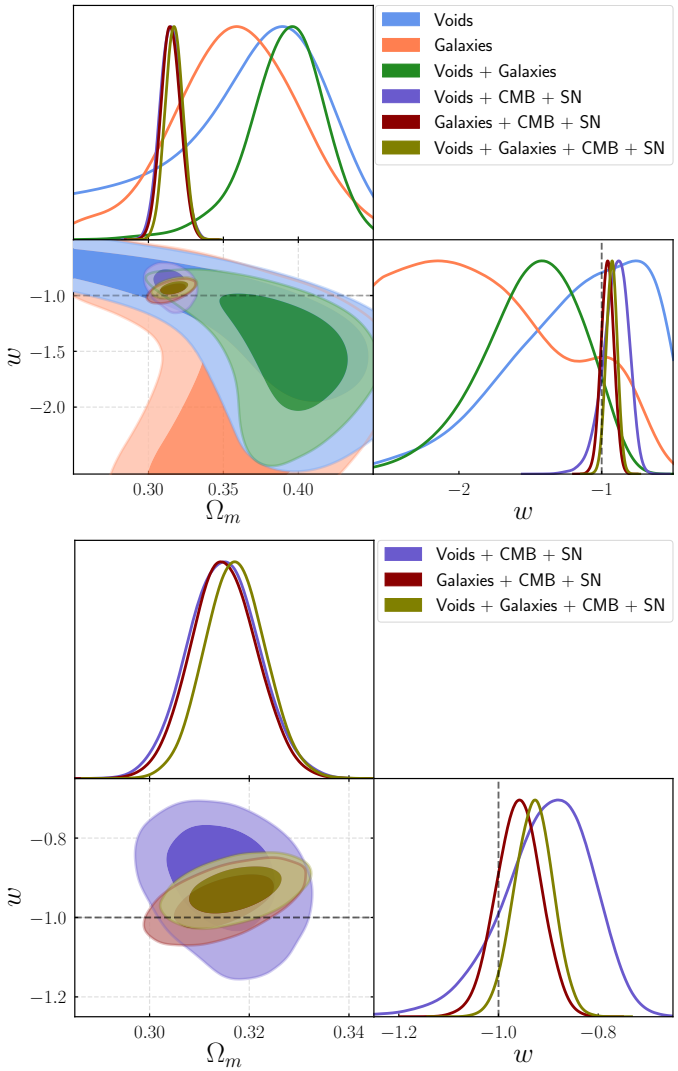

Figure 5.3: Marginalised posterior constraints on cosmological parameters under the assumption of a wCDM cosmology. Shaded contours show the 68% and 95% confidence limit regions and corresponding mean values and marginalised 68% credible intervals are shown in Table 5.2. Top shows results from SDSS Voids and Galaxies alone as well as the combination of these two datasets. These three combinations with the addition of CMB measurements from Planck TT,TE,EE+lowE+lensing and SN measurements from the Pantheon SN Ia sample. Bottom shows only the combination of SDSS data with Planck and Pantheon. The addition of void information results in a significant gain of information both with and without the inclusion of CMB + SN data. The dashed line corresponds to the ΛCDM prediction of $w = -1$. Image Credit: (Woodfinden et al., 2023)

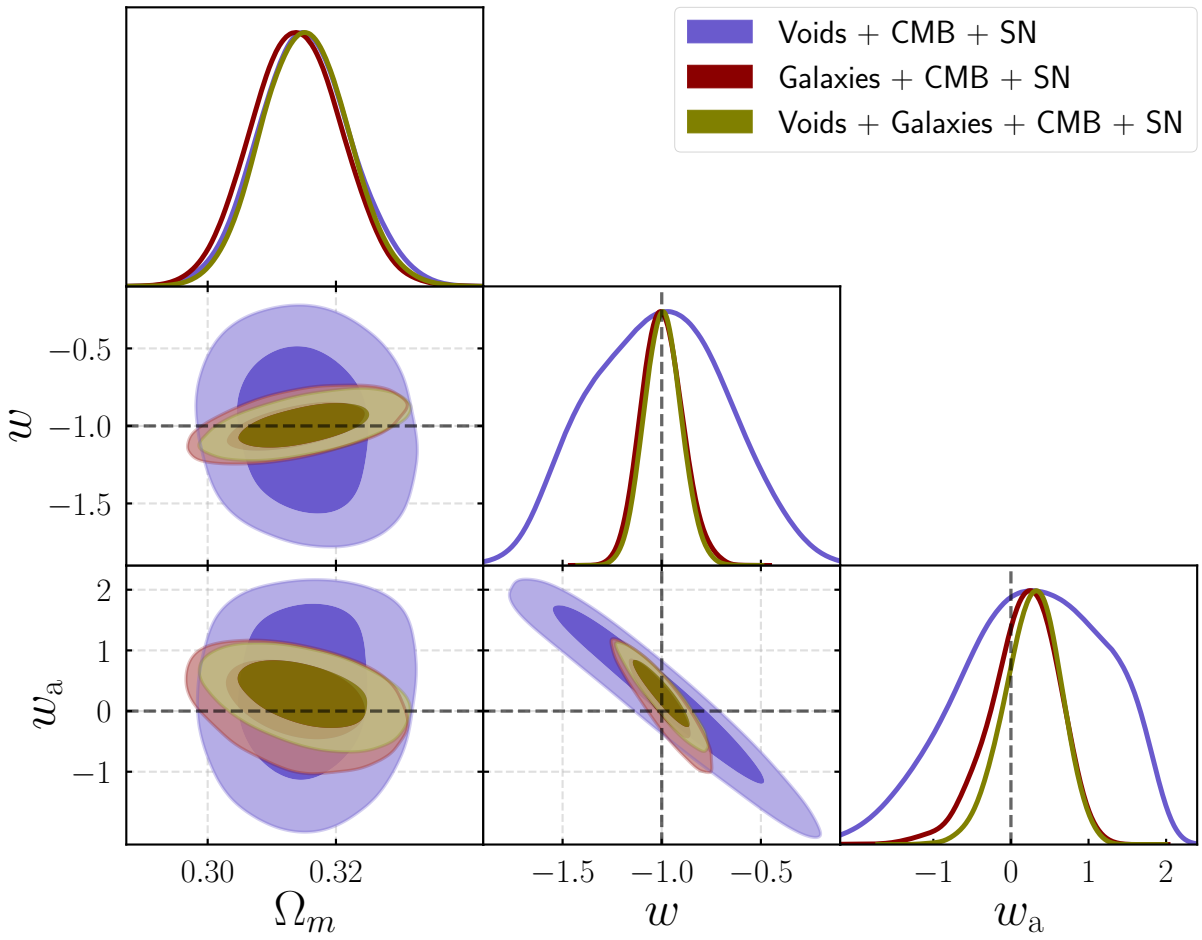

Figure 5.4: Marginalised posterior constraints on cosmological parameters under the assumption of a ww_aCDM cosmology. Shaded contours show the 68% and 95% confidence limit regions and corresponding mean values and marginalised 68% credible intervals are shown in Table 5.2. Results are for combinations of SDSS probes (Voids and Galaxies) in combination with CMB measurements from Planck TT,TE,EE+lowE+lensing and SN measurements from the Pantheon SN Ia sample. The Void + CMB + SN constraints can be seen to be hitting the upper boundary of the prior on w_a so only lower limits are reported. The dashed line corresponds to the ΛCDM prediction of $w = -1$ and $w_a = 0$. Image Credit: (Woodfinden et al., 2023)

5.4.4 oCDM

We now apply an *o*CDM model, where $\Omega_{\rm k} \equiv \Omega_{\rm m} + \Omega_\Lambda - 1$ is left as a free parameter. In ΛCDM spatial curvature is considered to be flat (i.e. $\Omega_{\rm k} = 0$). A value of $\Omega_{\rm k} < 0$ indicates a closed Universe while $\Omega_{\rm k} > 0$ indicates an open Universe.

An uninformative, flat prior of $-1 < \Omega_{\rm k} < 1$ was imposed. Figure 5.5 shows constraints for this cosmology and Tables 5.3 & 5.4 lists the mean values and marginalised 68% credible intervals obtained for various combinations of measurement techniques. All models showed a reasonable agreement with a ΛCDM prediction for a flat Universe.

Void constraints at a single redshift are unable to close contours in the $\Omega_{\rm m} - \Omega_\Lambda$ plane (Woodfinden et al., 2022; Nadathur et al., 2020a). This is because measurement of $D_{\rm M}/D_{\rm H}$ at a single redshift leads to a perfect degeneracy between these two parameters. As described in Section 5.4.7, over a wide range in redshift the variation in loci of models in the $\Omega_{\rm m} - \Omega_\Lambda$ plane that result in the same measurement of $D_{\rm M}/D_{\rm H}$ breaks this degeneracy (see Figure 5.8). There is still a strong degeneracy between these parameters that is not broken enough to close the contours in the $\Omega_{\rm m} - \Omega_\Lambda$ plane; however, a narrowing can be observed.

The combination of Planck and SN only measured $\Omega_m = 0.336 \pm 0.022$, $\Omega_{\rm k} = -0.0062^{+0.0062}_{-0.0054}$ and $H_0 = 65.1 \pm 2.2$. The additional information from SDSS (voids+galaxies) resulted in a 32% reduction in the measured error on $\Omega_{\rm m}$, a 68% reduction in the measured error on $\Omega_{\rm k}$ and a 71% reduction in the measured error on H_0.

5.4.5 owCDM

We next consider an *ow*CDM model, where $\Omega_{\rm k}$ is allowed to vary so that we are not imposing a flat curvature and allow the constant equation of state parameter for dark energy w_0 to vary. In a ΛCDM model $\Omega_{\rm k} = 0$ and $w_0 = -1$.

Uninformative, flat priors of $-3 < w < -1/3$ and $-1.0 < \Omega_{\rm k} < 1.0$ are imposed. Figure 5.6 shows results for this cosmology and Table 5.2 lists the mean values and marginalised 68% credible intervals for a variety of combinations of different measurement techniques. We find reasonable agreement with flat spatial curvature with all values of $\Omega_{\rm k}$ consistent with 0 and w_0 consistent with -1 within 2σ.

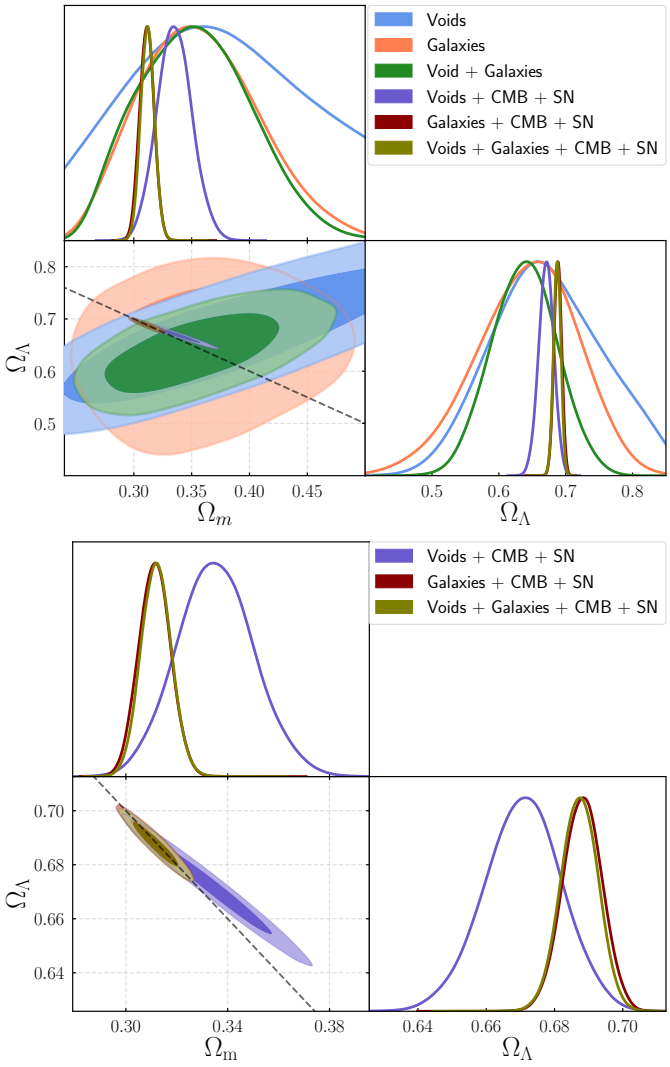

Figure 5.5: Marginalised posterior constraints on cosmological parameters under the assumption of an *o*CDM cosmology. Shaded contours show the 68% and 95% confidence limit regions and corresponding mean values and marginalised 68% credible intervals are shown in Table 5.2. On the top, we show results from SDSS Voids and Galaxies alone and the combination of these two datasets. CMB measurements from Planck TT,TE,EE+lowE+lensing and SN measurements from Pantheon SN Ia sample are combined with these three combinations to provide tighter constraints. The bottom plot shows only the combination of SDSS data with Planck. The addition of void information results in a significant gain of information both with and without the inclusion of CMB + SN data. The dashed line corresponds to the ΛCDM prediction of a spatially flat Universe with $\Omega_\mathrm{k} = 0$. Image Credit: (Woodfinden et al., 2023)

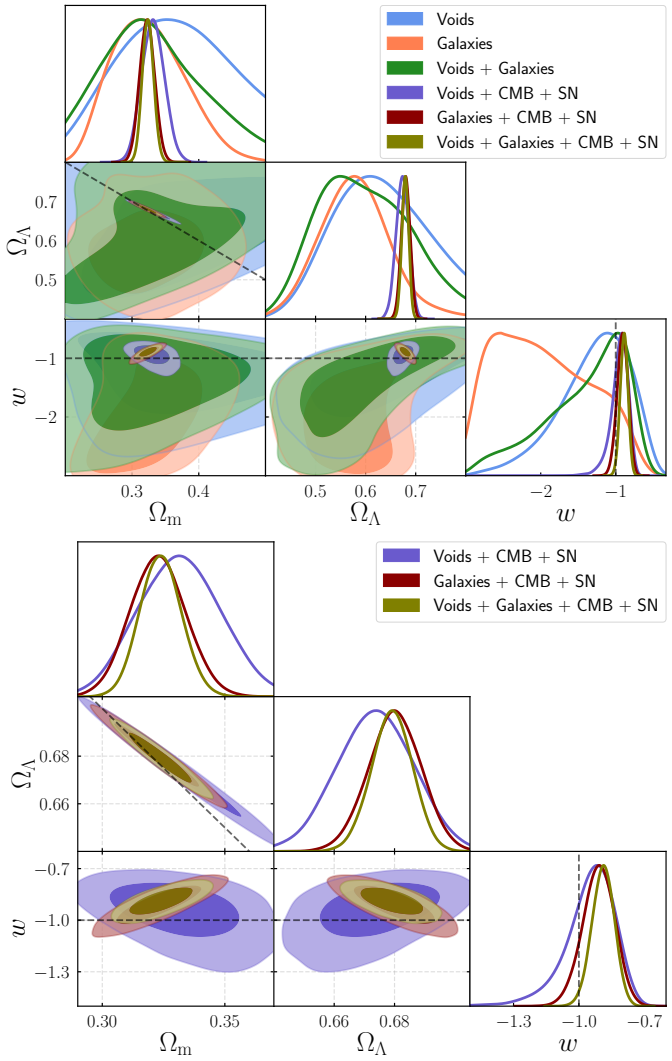

Figure 5.6: Marginalised posterior constraints on cosmological parameters under the assumption of an *ow*CDM cosmology. Shaded contours show the 68% and 95% confidence limit regions and corresponding mean values and marginalised 68% credible intervals are shown in Table 5.2. On the top, we show results from SDSS Voids and Galaxies alone and their combination. Additionally, we show these three combinations with the addition of CMB measurements from Planck TT,TE,EE+lowE+lensing and SN measurements from the Pantheon SN Ia sample. The bottom plot shows only the combination of SDSS data with Planck. The addition of void information results in a significant gain of information both with and without the inclusion of CMB + SN data. The dashed line corresponds to the ΛCDM prediction of $w = -1$ and a spatially flat Universe with $\Omega_k = 0$. Image Credit: (Woodfinden et al., 2023)

5.4.6 ow(z)CDM

We now consider a $ow(z)$CDM model. We did not impose spatial flatness, allowing Ω_k to be a free parameter. We also allowed for a time-varying equation of state parameter w as in Section 5.4.3. In a ΛCDM model $\Omega_k = 0$, $w = -1$, and $w_a = 0$.

Uninformative, flat priors of $-3 < w < -1/3$, $-3 < w_a < 2$, and $-1 < \Omega_k < 1$ were imposed. Figure 5.7 shows results for this cosmology and Table 5.2 lists the mean values and marginalised 68% credible intervals. Only the combination of SDSS data with CMB and SN results from Planck Collaboration et al. (2020) and Scolnic et al. (2018) are shown, as SDSS alone did not have enough constraining power within a reasonable prior volume. Once again we see reasonable agreement with flat spatial curvature, $w_0 = -1$, and $w_a = 0$ across all measurement techniques. For the combination of voids with CMB and SN data, the constraints on w_a were be seen to be hitting the upper bound of the prior, as such only lower limits are given in Tables 5.3 & 5.4.

5.4.7 Information Gain Through Measurements Taken at Multiple Redshift

For a given cosmology and redshift, the constraints on D_M/D_H have a strong degeneracy following the locus of models that predict the same theoretical value of D_M/D_H. The direction of this locus changes with redshift as shown in Figure 5.8 for models where w and Ω_m are varied, as well as models where Ω_m and Ω_Λ are varied. The change in locus depends on Equation 1.20.

The change in locus means that we significantly improve our constraints by having measurements at multiple redshifts compared with a measurement with an equivalent total error at a single redshift. Thus having void measurements at a series of redshifts is an important resource and significantly improves the cosmological constraints presented here. Measurements from upcoming surveys at high redshift will provide additional constraints on wCDM and oCDM beyond constraints due to the increased volume that these surveys measure.

This demonstrates that the novelty of this work goes beyond the application of the void-galaxy cross-correlation to new datasets (see Chapter 3), applying these results to a set of cosmological models to find resultant constraints and combining this information with that from other cosmological probes. The use of measurements over a wide range of redshift is an improvement to previous void analyses that present measurements at a single redshift (e.g. Nadathur et al., 2019b; Hamaus et al., 2020; Aubert et al., 2022b).

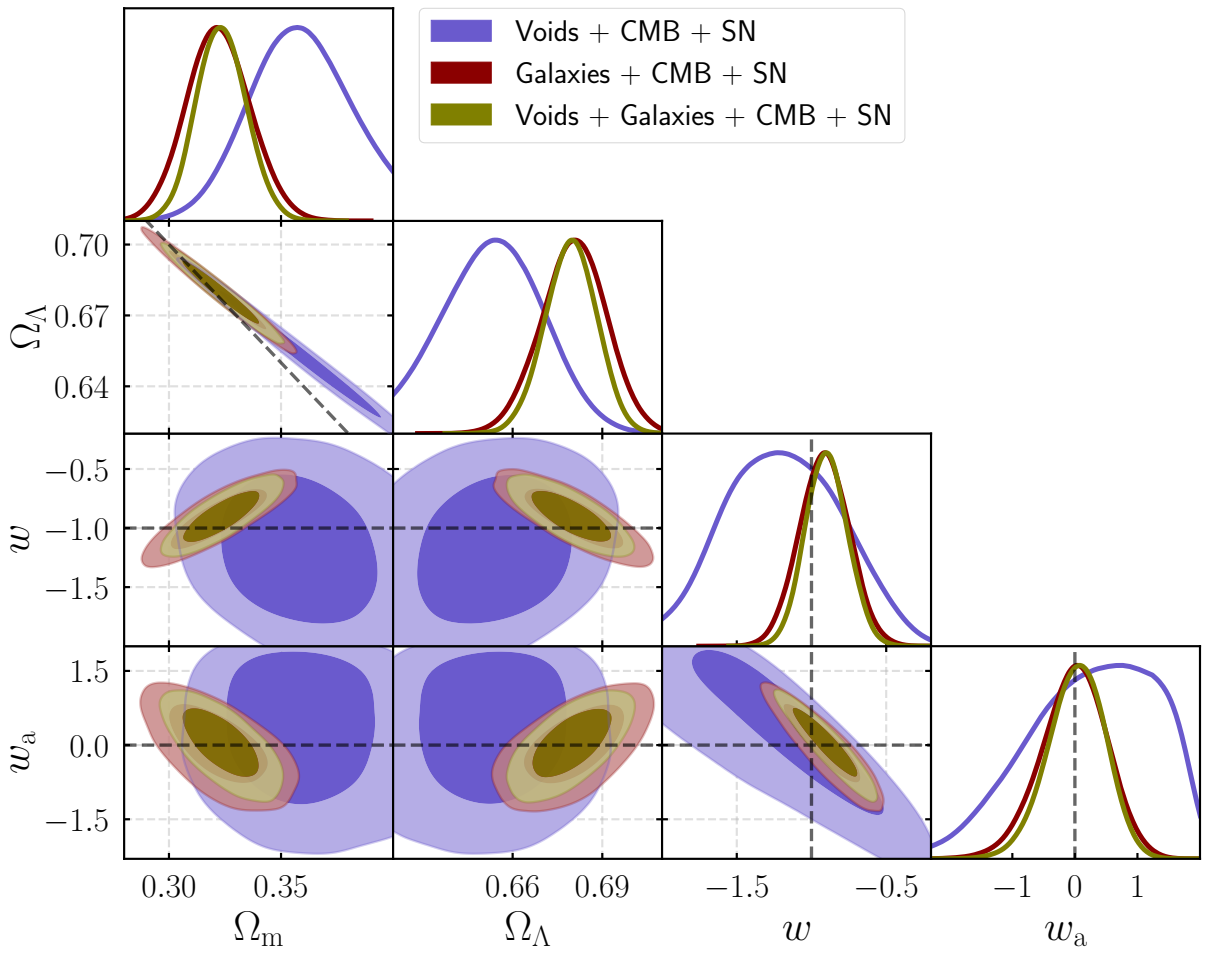

Figure 5.7: Marginalised posterior constraints on cosmological parameters under the assumption of a $ow(z)$CDM cosmology. Shaded contours show the 68% and 95% confidence limit regions and corresponding mean values and marginalised 68% credible intervals are shown in Table 5.2. The w_a constraint for the Void + CMB + SN result can be seen to be hitting the upper prior boundary of $w_a = 2$ and as such is not reported in our results. The dashed line corresponds to the ΛCDM prediction of $w = -1$, $w_a = 0$, and a spatially flat Universe with $\Omega_k = 0$. Image Credit: (Woodfinden et al., 2023)

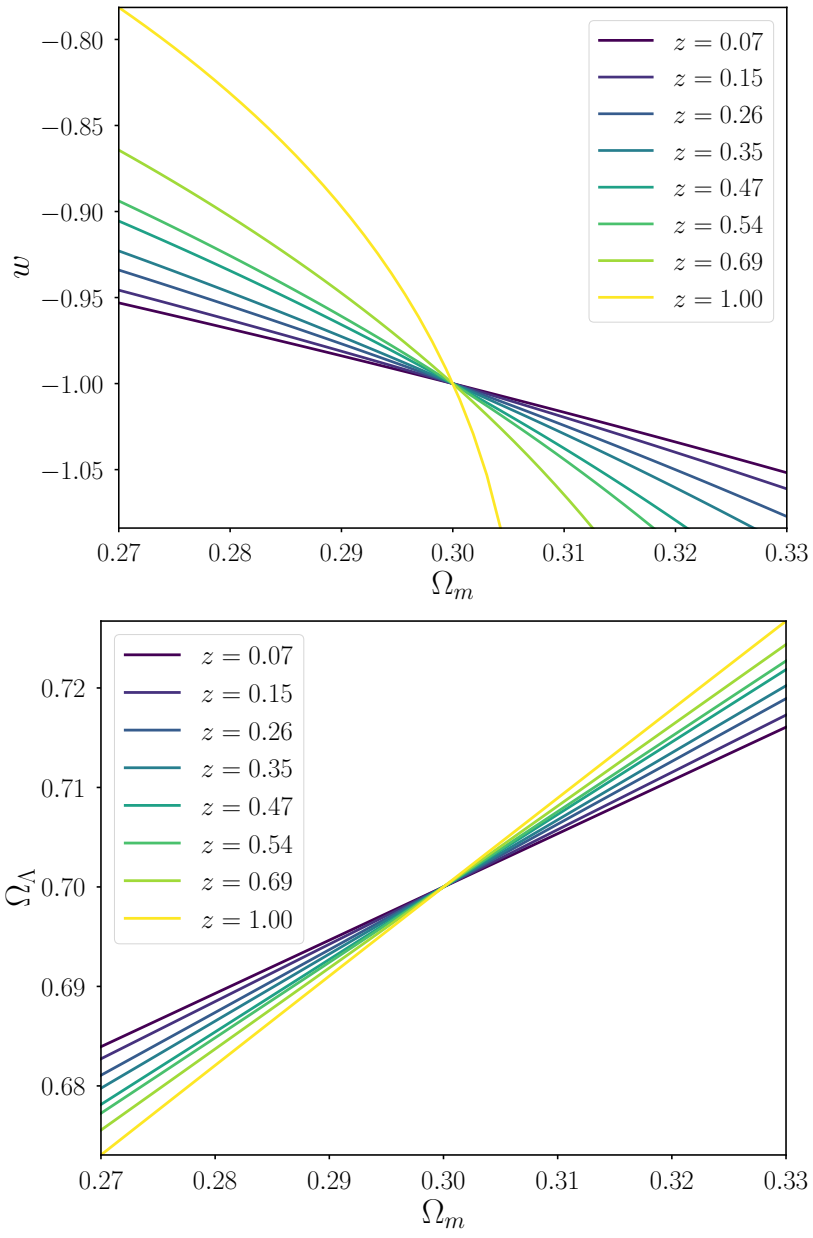

Figure 5.8: The loci of models with $D_{\rm M}/D_{\rm H}$ matching that of a cosmological model with $\Omega_{\rm m} = 0.3$, $\Omega_\Lambda = 0.7$, and $w = -1$, for a wide range in redshift. The top panel shows loci for a wCDM cosmology while the bottom panel shows loci for an oCDM cosmology. Redshifts from $z = 0.07$ up to $z = 1.0$ are chosen to match the average redshift of the slices described in Table 5.1 as well as the minimum and maximum redshifts of the data used. Image Credit: (Woodfinden et al., 2023)

5.5 Conclusions

We have presented the cosmological implications of void-galaxy and galaxy-galaxy clustering over a wide redshift range in the SDSS DR7 (MGS), SDSS DR12 (BOSS), and SDSS DR16 (eBOSS) galaxy surveys. Void-galaxy and galaxy-galaxy clustering results are combined, taking into account cross-correlations between different measurement techniques and redshift bins. We saw a significant gain of information from the combination of these measurement techniques, as well as from the inclusion of data from a wide range in redshift. The constraints on $D_{\rm M}/D_{\rm H}$ have a strong degeneracy following a locus of models that predict the same value (see Figure 5.8). The direction of this locus changes with redshift meaning that void measurements over a wide redshift range improve the cosmological constraints presented in this work beyond increased precision solely due to an increased volume measured.

We performed a Bayesian analysis, comparing these measurements to various cosmological models including base ΛCDM, a constant dark energy equation of state allowed to vary from $w = -1$ (wCDM), a time-varying dark energy equation of state ($w(z)$CDM), allowing for spatial curvature (oCDM), allowing for spatial curvature with a constant dark energy equation of state allowed to vary from $w = -1$ (owCDM), allowing for spatial curvature with a time-varying dark energy equation of state ($ow(z)$CDM). Final constraints on these cosmologies are shown in Tables 5.3 & 5.4. Results from SDSS were also combined with CMB results from Planck Collaboration et al. (2020) and Pantheon SN Ia sample from Scolnic et al. (2018) to provide extremely tight constraints on these cosmological models. With currently available data, parameter estimations and associated errors are heavily influenced by the already stringent CMB constraints. The inclusion of void information did improve the CMB constraints and is of increasing importance for models with more freedom in the low-redshift behaviour. This is true for many low-redshift cosmological constraints. However, a clear improvement was seen in many parameter constraints from the inclusion of void data in addition to bringing in BAO & RSD and SN measurements. In the near future, upcoming data from next-generation surveys will offer comparable uncertainty to Planck CMB results using void-galaxy and galaxy-galaxy clustering alone (e.g. DESI Collaboration et al., 2016a; Radinović et al., 2023).

The combination of void-galaxy and galaxy-galaxy clustering results in SDSS provided a large gain of information compared to that from galaxy-galaxy clustering alone. Results for ΛCDM provided a 43% reduction in the size of the error on $\Omega_{\rm m}$ compared to galaxy clustering alone. Results for wCDM provided a 44% and 45% reduction in the size of the error on $\Omega_{\rm m}$ and w. Results for $w(z)$CDM provided a 4% and 9%, and 16% reduction in the size of the error on $\Omega_{\rm m}$, w, and $w(z)$ when used in combination with CMB measurements

from Planck and SN measurements from Pantheon. Results for oCDM provided a 35% and 11% reduction in the size of the error on Ω_Λ and Ω_k compared to galaxy clustering alone. Results for owCDM provided a 31%, and 38% reduction in the size of the error on Ω_m, and w when used in combination with CMB measurements from Planck and SN from Pantheon. Finally, results for $ow(z)$CDM provided a 21%, 15%, 18%, and 13% reduction in the size of the error on Ω_m, Ω_k, w_0, and w_a when used in combination with CMB + SN measurements.

Void-galaxy and galaxy-galaxy clustering results were also combined with CMB + SN results as shown in Tables 5.3 & 5.4. The addition of void-galaxy and galaxy-galaxy data can further increase the precision of cosmological parameters shown in various models. All results shown are in agreement with a base ΛCDM cosmological model.

Our work shows the importance of including voids as a cosmological probe and motivates the inclusion of voids as standard in the analysis of galaxy surveys due to the large information gain provided, especially when used in combination with measurements from other techniques. This is particularly important for low-redshift geometrical tests of cosmic expansion and discriminating between alternative cosmological models. Results expected shortly from DESI and Euclid will probe larger volumes over a wider redshift range. Void-galaxy and galaxy-galaxy clustering results in these surveys will provide powerful tests of the behaviour of cosmological models at low redshift.

Chapter 6

Summary and Future

We now summarise the work presented in this thesis. We then consider the possible future directions for precision cosmology with voids.

Chapter 1 presents an overview of the current state of cosmology. The field of cosmology is briefly presented, and density fields in the Universe are discussed. The FRW framework fundamental to the analysis of galaxy-spectrographic surveys is presented, and the geometry of the Universe in this framework is discussed, as well as distortions to these geometries. Finally, observational probes of the Universe are summarised, and tensions in current cosmological measurements are discussed to motivate the need for increasingly precise observations to confirm these tensions and provide hints at their solutions.

Chapter 2 then delves into the use of voids as cosmological probes. This chapter focuses on the theory behind the void-galaxy correlation function and how it can be used to extract information. Void-finders are first presented with a focus on the void-centre definitions. These definitions are used to summarise void densities and different factors affecting these profiles. The void-galaxy correlation function is then discussed including what this aims to measure and correlation function estimators. The need for reconstruction prior to void-finding is motivated and an efficient way to calculate this is shown. The expected density of voids differs from that of galaxies and is needed in the calculation of the void-galaxy correlation function, so modelling of the expected void density in surveys is presented. A section dedicated to previous void analyses is then shown. Modelling of the void-galaxy correlation function is presented including how this is used to extract cosmological information. The velocity field in voids is then discussed, showing how void-centre definitions can lead to incorrect void centres being found due to shot noise which then affects the velocity profile of voids. Finally, the relevance of voids to cosmology is

presented.

Chapter 3 describes the data used in this thesis, starting with a summary of galaxy spectroscopic surveys and the tracers used to understand large-scale structure. The galaxy surveys used in this work are described (MGS, BOSS, and eBOSS). The remaining sections discuss details of how to generate the data products in this work, i.e. void-galaxy correlation functions. This includes reconstruction, void-finding, correlation function estimation, data measurements (as opposed to measurements from mocks), and template function calculation (density and velocity dispersion). These latter sections describing the calculation of correlation functions from SDSS data are from work initially published in the first-author paper Woodfinden et al. (2022).

Chapter 4 represent the remainder of first-author publication Woodfinden et al. (2022) not discussed in Chapter 3. This chapter constitutes the likelihood estimation of cosmological parameters measured as described in Chapters 2 & 3. The determination of systematic errors from these measurements is detailed including those due to errors in the modelling of the void-galaxy correlation function as well as this due to the need to assume a fiducial cosmology when converting redshifts to distances. Results are then presented that include these systematic uncertainties and context for these results with regard to other similar works (from both void-based measurements as well as from BAO/RSD). Finally, the conclusions from this paper are discussed.

Chapter 5 constitutes work from a separate first-author publication Woodfinden et al. (2023). This paper discusses the cosmological model fits to the void-galaxy correlation function presented in Chapters 3 & 4 as well as in combination with other probes, namely BAO/RSD, the CMB, and SN. The cross-covariance needed to properly combine these measurements is introduced and shown and the gain of information from having multiple measurements at different redshifts is explained. Various plausible cosmological models are fit to the data to show constraints on parameters, including ΛCDM, wCDM, oCDM, $w(z)$CDM, owCDM, and $ow(z)$CDM. Finally, the conclusions of this work are presented.

This thesis presents the measurements of voids from the SDSS LRGs. This covers a wide range in redshift using a single analysis method for the first time. These data represent the best public galaxy redshift survey data available to date and will only be exceeded when DESI (DESI Collaboration et al., 2016a,b) & Euclid (Laureijs et al., 2011) results are released in the next few years. By analysing these new data and consolidating previous analyses, we are able to build a picture of the geometrical evolution of the Universe and the evolution of the growth of structure within it from only the analysis of SDSS galaxies around voids.

The DESI survey is a next-generation galaxy redshift survey with an order of magnitude

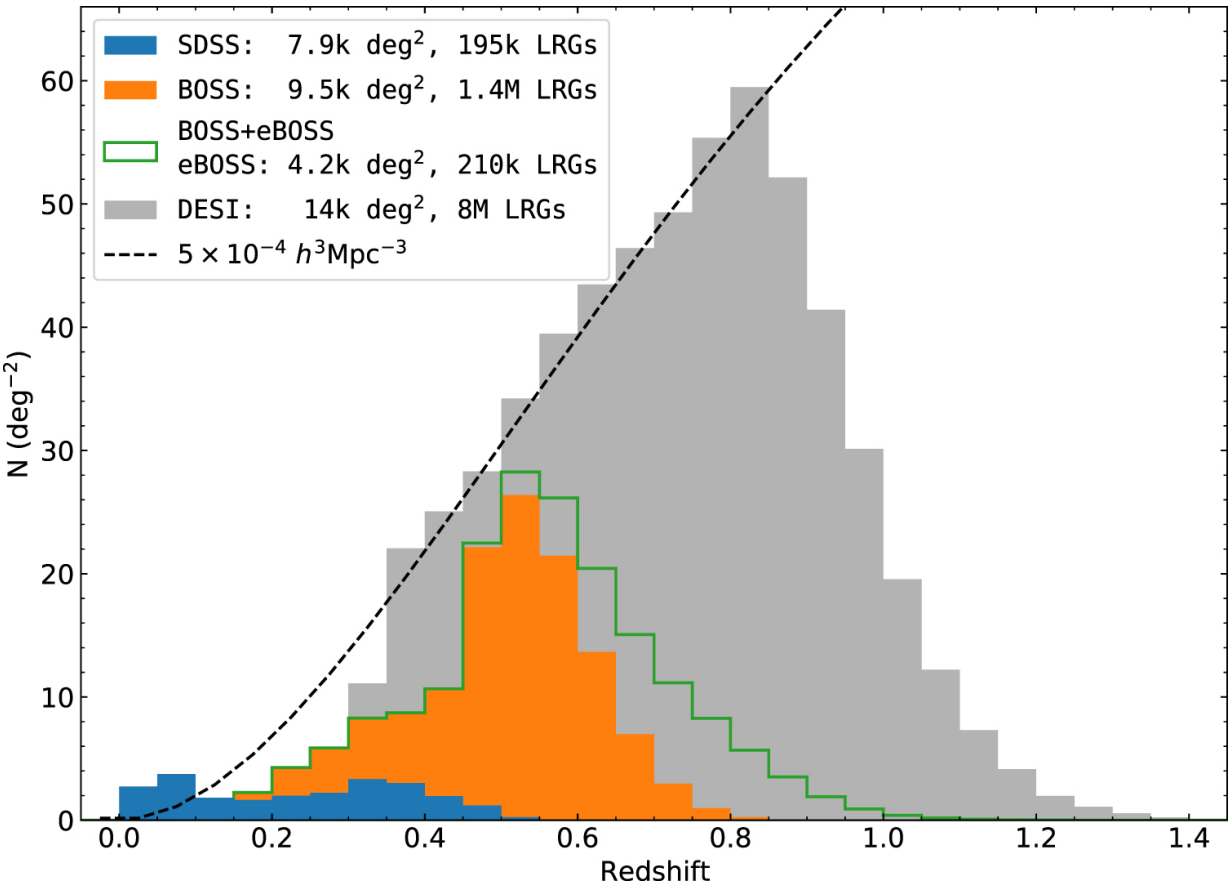

Figure 6.1: The redshift distribution of the DESI LRG sample, as well as LRGs from SDSS MGS, BOSS, and eBOSS. The y-axis shows the number of objects in each redshift bin of width 0.05 per deg^2. Image Credit (Zhou et al., 2023).

larger volume than eBOSS. DESI is a state-of-the-art spectroscopic instrument mounted on the ground-based Mayall telescope. It uses a focal plane with 5000 individual optical fibres enabling it to capture the spectra of 5000 different objects simultaneously with the aim of measuring the spectra of more than 40 million galaxies, a factor of 20 more than current surveys leading to a factor of $\sim$5 improvement in the precision of parameters measured in SDSS data (DESI Collaboration et al., 2016a). This includes 8M LRGs that will be surveyed up to redshift $\sim$1.2. Figure 6.1 shows the expected number density and redshift distribution of DESI LRGs compared to those from SDSS MGS, BOSS, and eBOSS. I am a member of the DESI collaboration through which I have attended several collaboration meetings, participated in an observing shift over four nights in March 2023, and am providing guidance on a project that aims to use voids to extract information from DESI data. In particular, the tests of systematic errors shown in Chapter 4, while small in relation to SDSS data, will become significant with the reduced statistical error bars from next-generation surveys. This necessitates the use of new techniques to optimally extract information from voids, such as using an emulator to measure the void-galaxy correlation function from a Latin hypercube of varying cosmological models.

Euclid (Laureijs et al., 2011) is an upcoming space-based mission that will observe galaxy clustering and weak lensing. Clustering statistics will be extracted from spectroscopic data of the redshift of tens of millions of galaxies over the wide redshift range $0.9 \leq z < 1.8$. This will provide complementary measurements to those expected from DESI as well as existing measurements up to $z = 1.0$ presented in this thesis. Forecast results using a similar method to that presented in this work are published in Radinović et al. (2023). I am a member of the Euclid collaboration and a co-author on this paper where I provided guidance and helped develop the theoretical modelling; this was done concurrently with modelling developed for Woodfinden et al. (2022).

The methods applied to make forecasts for Euclid differ in a variety of ways from previous publications using a similar analysis method (Nadathur et al., 2019b, 2020b; Woodfinden et al., 2022). This includes the choice to use a `VOXEL` void finder used. `VOXEL` is less memory intensive and significantly faster than the `ZOBOV` void finder used in Chapter 3, see Section 2.3 for more detail on these two void finding algorithms. In addition to being significantly faster and requiring less memory to run, the `VOXEL` method of estimating the galaxy density field more easily accounts for complex survey masks and systematic effects than popular tessellation-based density estimation methods used in other void finders such as `ZOBOV`. As noted in Section 2.3.4, at the time of work of Woodfinden et al. (2022) the `VOXEL` algorithm implementation in the `Revolver` code used contained several bugs and produced worse systematic errors than `ZOBOV` (this led to the `ZOBOV` algorithm being used in Chapter 3). After significant work from both myself and several co-authors of Radinović

et al. (2023), these bugs have since been resolved and `VOXEL` was able to be shown to be effective.

Only a single mock currently exists that matches the expected selection function, window function, and clustering of Euclid. This thesis along with similar previous work made use of many (typically 1000) mock catalogues to estimate the real space void-galaxy correlation function ξ^r (see Section 2.5), as well as in the calculation of the covariance matrix (see Section 4.2). For Euclid forecast results this single mock catalogue was also used as the data in which measurements are made.

To be able to make forecast results Radinović et al. (2023) calculated the real space void-galaxy correlation function ξ^r from the single mock realization. The use of a single mock will be noisier than one taken from the average of many mocks and the redshift space void-galaxy correlation function ξ^s will be correlated with ξ^r. This correlation can be accounted for in the covariance matrix used which reduces the statistical uncertainty; however, systematic errors were then seen to produce poor results. Instead, this was not accounted for and so the forecast estimates should be considered to be conservative estimates.

As the use of many mock catalogues to calculate the covariance matrix is not possible, Radinović et al. (2023) calculated the covariances matrix using a jackknife technique. In a jackknife calculation subsets of the data are systematically excluded and the variance is evaluated between those subsets (Mohammad and Percival, 2022).

Another complication of the single mock catalogue available was that dark matter information was not available. These are used in the calculation of the dark matter density profile template seen in Section 3.5 and required in the modelling of the void-galaxy correlation function presented in Section 2.8. Instead, as the dark matter density profile and the void velocity profile of equation 2.20 are directly related, the void velocity profile was measured directly from the single mock realization available and used in its place.

Included in this forecast paper were expected measurements of cosmological parameters, as well as cosmological model fits to a wCDM cosmology. Measurements of the geometrical distance ratio $D_\mathrm{m}/D_\mathrm{H}$ were forecast to achieve a statistical precision of 0.3% from measurements of the void-galaxy correlation function in the redshift range $0.9 < z < 1.8$ as well as a $5\% - 8\%$ measurement of the growth rate parameter $f\sigma_8$. These parameter estimations for the four redshift bins considered are shown in Figure 6.2 where perfect reconstruction refers to the ξ^r vector being measured in real space while realistic reconstruction refers to this being measured from a reconstruction algorithm being applied to the redshift space galaxy field. Similar to Figures 4.8, & 4.10 these measurements can be plotted against the effective redshift to determine the evolution of these parameters; this is

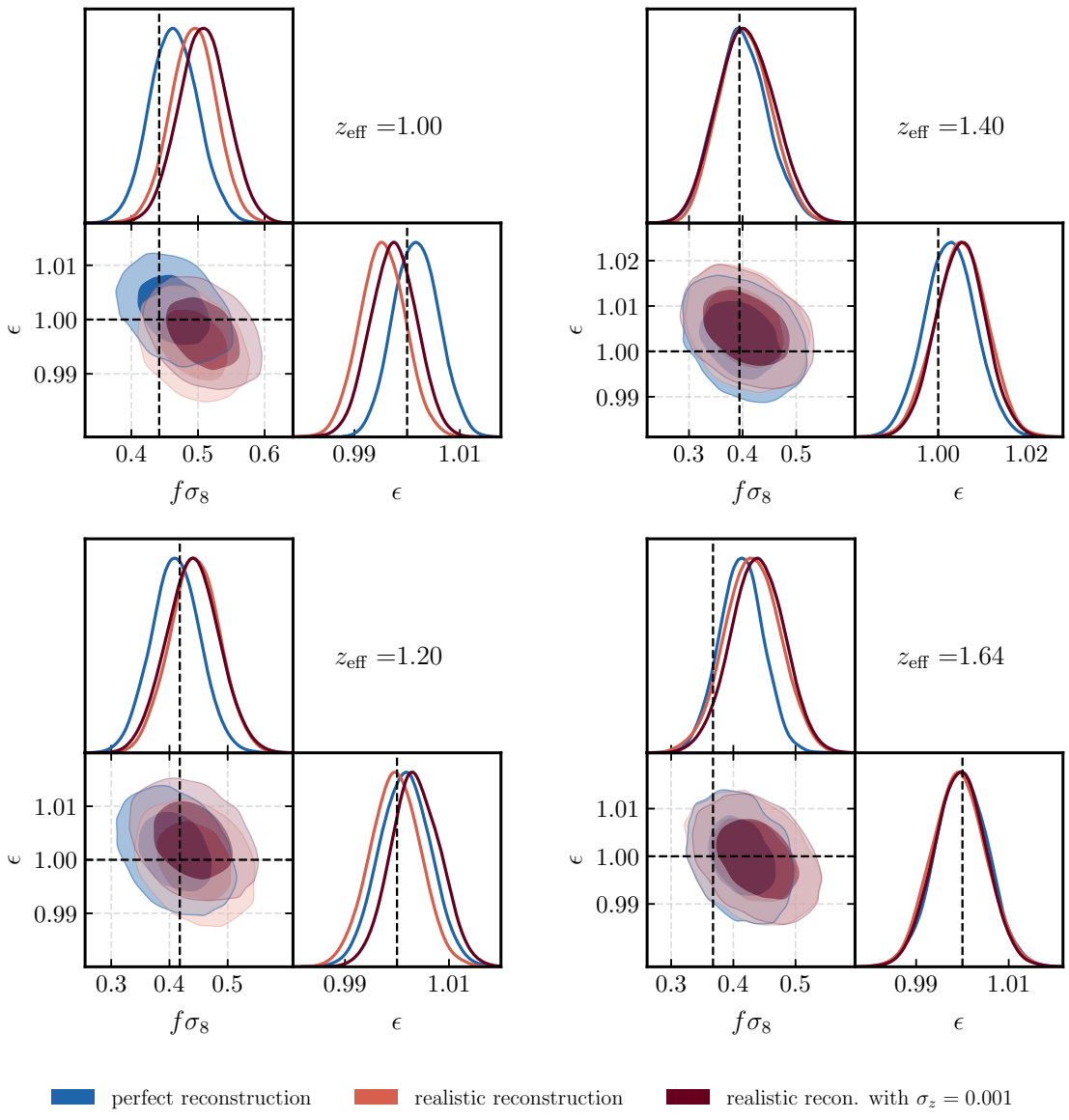

Figure 6.2: Marginalised 1D and 2D posterior constraints for parameters $f\sigma_8$ and ϵ from fits to the Flagship (i.e. Euclid) void-galaxy CCF measurements in four redshift bins. Contours show the 68.3% (1σ) and 95.5% (2σ) confidence intervals obtained in the case of perfect reconstruction (blue), realistic reconstruction (light red), and realistic reconstruction with added redshift error (dark red). Dashed cross-hairs indicate the true values of the Flagship cosmology. Image Credit: Radinović et al. (2023).

shown in Figure 6.3 and compared to the predicted contours for a ΛCDM cosmology using best-fit values from Planck Collaboration et al. (2020). Geometrical and growth rate constraints provide a powerful test of cosmological models, forecast constraints of parameters $\Omega_{\rm m}$ and w for a wCDM cosmology are plotted in Figure 6.5 where a statistical precision of 3% was expected to be achieved for $\Omega_{\rm m}$ and 6% precision is expected for w. These represent significant improvements to the parameters shown from this work in Table 5.2 and demonstrate the powerful test of cosmology that next-generation surveys will be.

Within the last 10-15 years the study of cosmic voids as tracers of the large-scale structure of the Universe has developed from a novel technique to a field quickly gaining traction as providing competitive constraints on cosmological parameters. Various techniques have emerged to extract information from voids, including the void size function, gravitational lensing around voids, void clustering, and the void-galaxy correlation function. This thesis focuses on the latter and provides, for the first time, measurements of the geometry and growth rate of the Universe across the full redshift range of the Sloan Digital Sky Survey Luminous Red Galaxy sample. One of the remarkable aspects of utilizing cosmic voids is that no new observations are needed. Leveraging existing galaxy spectroscopic surveys voids can be used to extract more information from the same data. This is done by combining information from the void-galaxy correlation function with information readily available from techniques such as BAO and RSD that have already been applied to these surveys.

The best current cosmological model, Lambda Cold Dark Matter (ΛCDM), has had remarkable success explaining a wide range of observations. Despite this success, tensions have developed and grown, demonstrating the potential for new physics. More precise cosmological measurements and more independent probes are needed to confirm these tensions and measure deviations predicted by extension to this model. The analysis of cosmic voids provides another method to measure cosmology and allows for more precise measurements from existing surveys. This thesis used voids to provide independent cosmological constraints, as well as combined with BAO/RSD to increase the precision of information extracted from galaxy spectroscopic surveys. Looking ahead, future surveys will need to continue to build on this work to reduce systematic errors and provide valuable hints towards resolving these tensions and illuminating the fundamental nature of our Universe.

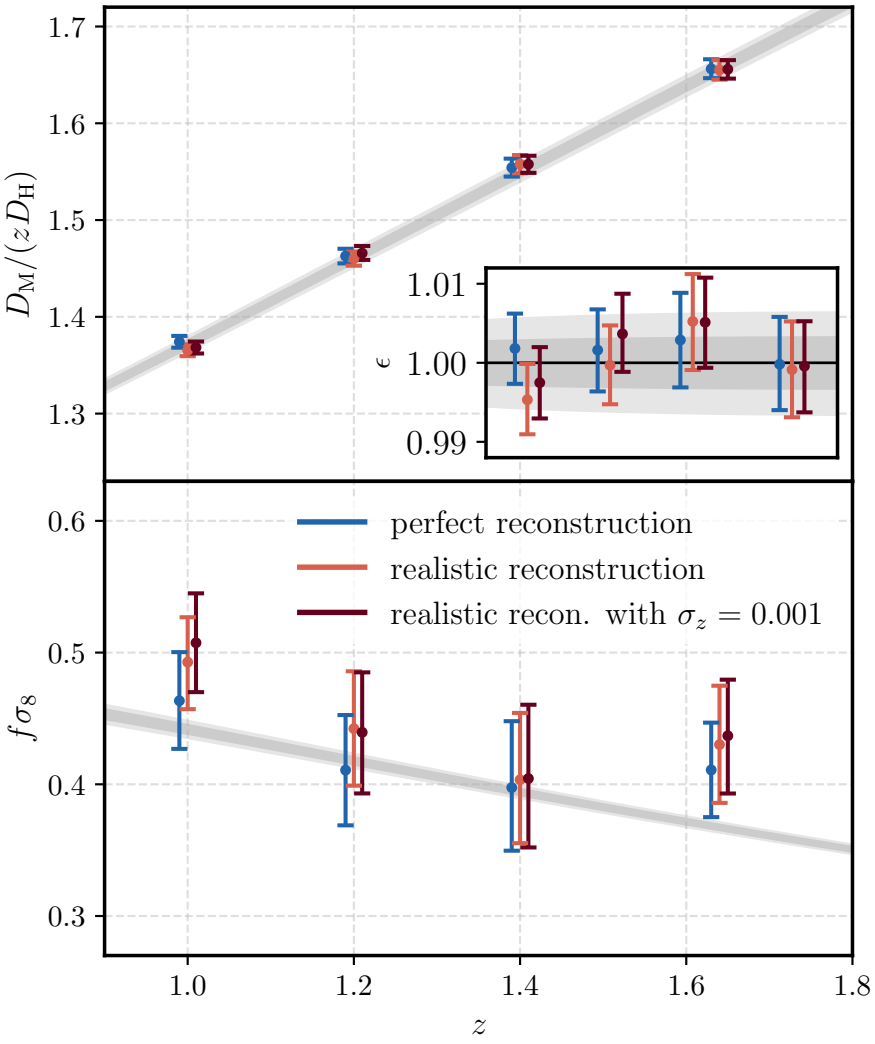

Figure 6.3: Redshift dependence of the measured cosmological parameters obtained from fits to Flagship simulation data. The top panel shows constraints on the ratio of comoving transverse and Hubble distances divided by redshift z, $D_M/(zD_H)$, which is derived from ϵ (inset). The bottom panel shows measurements of the growth rate $f\sigma_8$. Coloured data points indicate the different reconstruction scenarios considered, plotted at slightly shifted redshift locations for clarity. The grey shaded bands represent the 68.3% (1σ) and 95.5% (2σ) confidence intervals from fits to Planck Collaboration et al. (2020), extrapolated down to these redshifts assuming ΛCDM, and centred on the Flagship cosmology. Image Credit: Radinović et al. (2023).

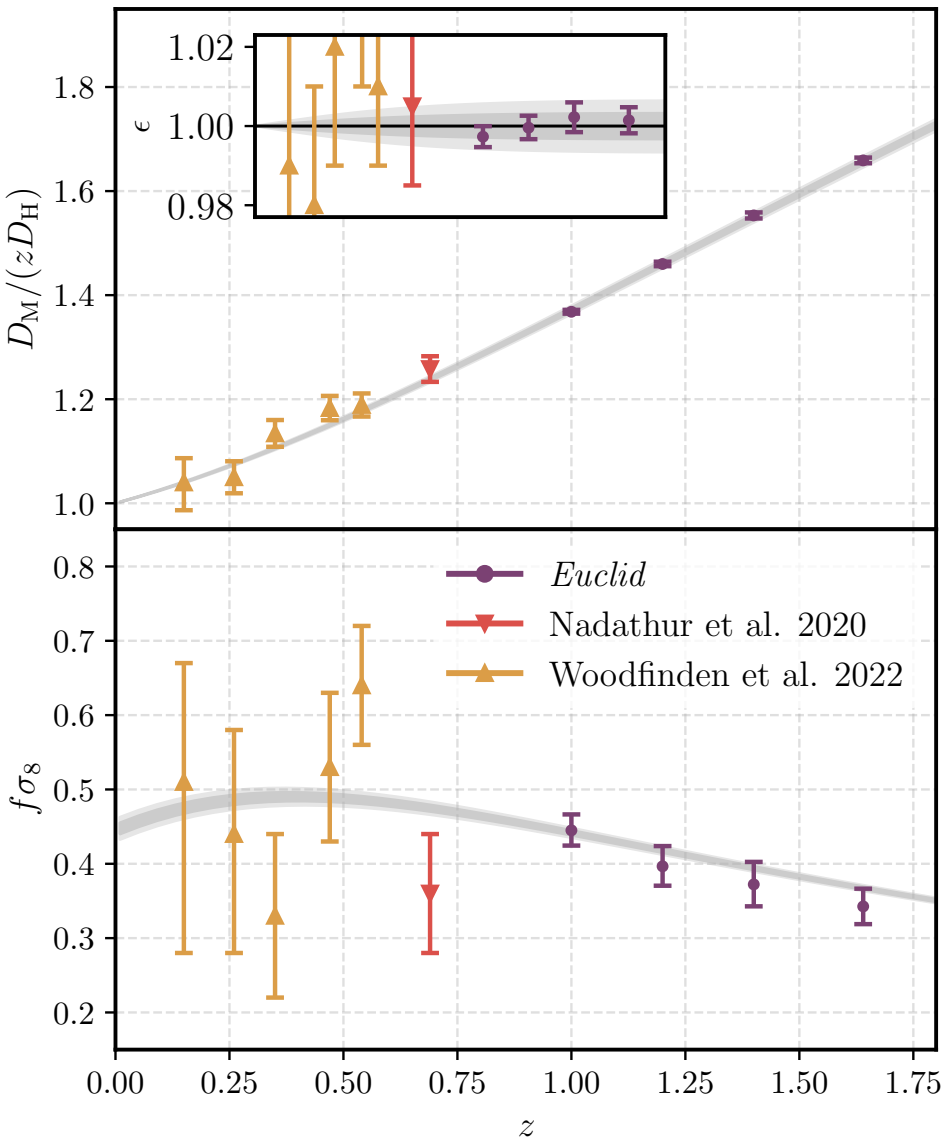

Figure 6.4: Forecast measurements that could be obtained from the 15 000 deg^2 Euclid survey (purple data points). Low redshift measurements from current SDSS data obtained using the same analysis method by Nadathur et al. (2020b) and Woodfinden et al. (2022) are included for comparison. Image Credit: Radinović et al. (2023).

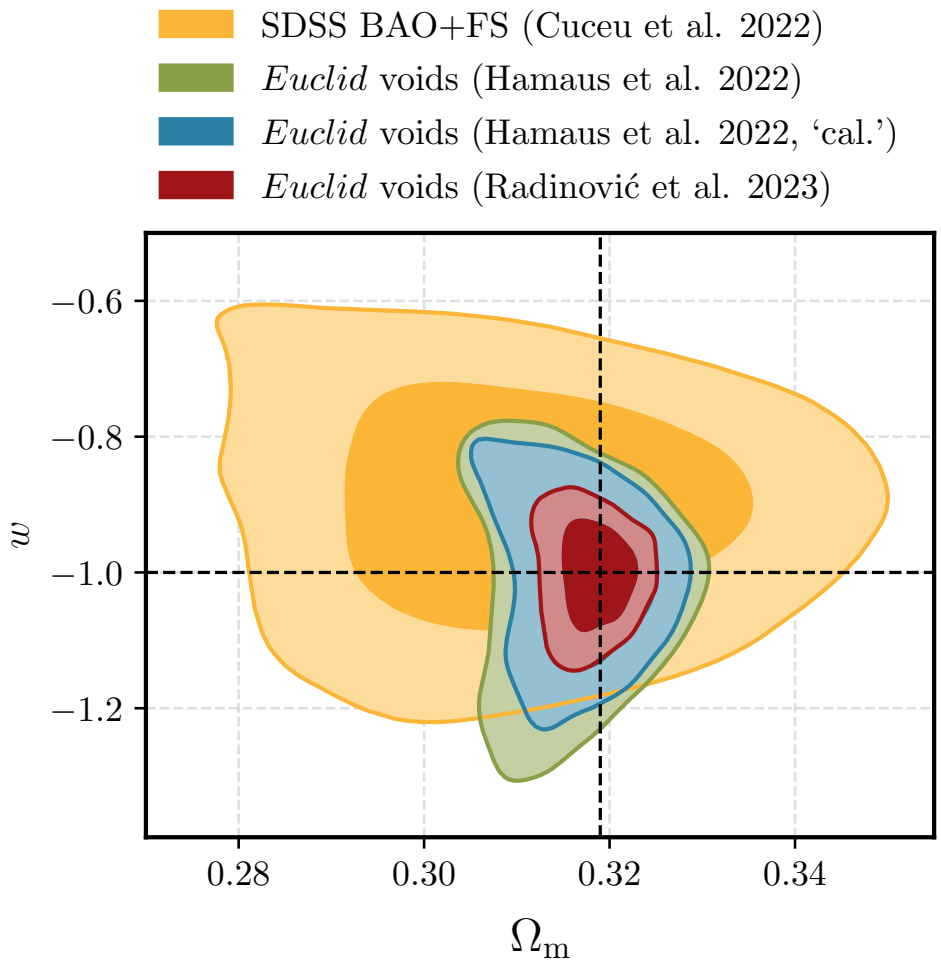

Figure 6.5: Forecast constraints on the matter density parameter $\Omega_{\rm m}$ and the dark energy equation of state w in a wCDM cosmological model from a measurement of the void-galaxy CCF with Euclid (red contours), corresponding to $w = -1.00^{+0.06}_{-0.05}$. Also shown are previous forecasts for the Euclid void-galaxy correlation function – obtained using a different model and measurement method – by Hamaus et al. (2022), for the 'independent' (green contours) and 'calibrated' (blue, labelled 'cal.' here) cases in that paper, corresponding to whether nuisance parameters are marginalised over or fixed. For context, current measurements are shown from current BAO and 'full-shape' measurements in the SDSS galaxy, quasar and Lyman-α datasets from the MGS, BOSS and eBOSS surveys (yellow) presented by Cuceu et al. (2022). Image Credit: Radinović et al. (2023).

References

Abazajian, K. N., Adelman-McCarthy, J. K., Agüeros, M. A., Allam, S. S., Allende Prieto, C., An, D., Anderson, K. S. J., Anderson, S. F., Annis, J., Bahcall, N. A., and et al. (2009). The Seventh Data Release of the Sloan Digital Sky Survey. *ApJS*, 182(2):543–558.

Abbott, T. M. C., Aguena, M., Alarcon, A., Allam, S., Allen, S., Annis, J., Avila, S., Bacon, D., Bechtol, K., Bermeo, A., Bernstein, G. M., Bertin, E., Bhargava, S., Bocquet, S., Brooks, D., Brout, D., Buckley-Geer, E., Burke, D. L., Carnero Rosell, A., Carrasco Kind, M., Carretero, J., Castander, F. J., Cawthon, R., Chang, C., Chen, X., Choi, A., Costanzi, M., Crocce, M., da Costa, L. N., Davis, T. M., De Vicente, J., DeRose, J., Desai, S., Diehl, H. T., Dietrich, J. P., Dodelson, S., Doel, P., Drlica-Wagner, A., Eckert, K., Eifler, T. F., Elvin-Poole, J., Estrada, J., Everett, S., Evrard, A. E., Farahi, A., Ferrero, I., Flaugher, B., Fosalba, P., Frieman, J., García-Bellido, J., Gatti, M., Gaztanaga, E., Gerdes, D. W., Giannantonio, T., Giles, P., Grandis, S., Gruen, D., Gruendl, R. A., Gschwend, J., Gutierrez, G., Hartley, W. G., Hinton, S. R., Hollowood, D. L., Honscheid, K., Hoyle, B., Huterer, D., James, D. J., Jarvis, M., Jeltema, T., Johnson, M. W. G., Johnson, M. D., Kent, S., Krause, E., Kron, R., Kuehn, K., Kuropatkin, N., Lahav, O., Li, T. S., Lidman, C., Lima, M., Lin, H., MacCrann, N., Maia, M. A. G., Mantz, A., Marshall, J. L., Martini, P., Mayers, J., Melchior, P., Mena-Fernández, J., Menanteau, F., Miquel, R., Mohr, J. J., Nichol, R. C., Nord, B., Ogando, R. L. C., Palmese, A., Paz-Chinchón, F., Plazas, A. A., Prat, J., Rau, M. M., Romer, A. K., Roodman, A., Rooney, P., Rozo, E., Rykoff, E. S., Sako, M., Samuroff, S., Sánchez, C., Sanchez, E., Saro, A., Scarpine, V., Schubnell, M., Scolnic, D., Serrano, S., Sevilla-Noarbe, I., Sheldon, E., Smith, J. A., Smith, M., Suchyta, E., Swanson, M. E. C., Tarle, G., Thomas, D., To, C., Troxel, M. A., Tucker, D. L., Varga, T. N., von der Linden, A., Walker, A. R., Wechsler, R. H., Weller, J., Wilkinson, R. D., Wu, H., Yanny, B., Zhang, Y., Zhang, Z., Zuntz, J., and DES Collaboration (2020). Dark Energy Survey Year 1 Results: Cosmological constraints from cluster abundances and weak lensing. *Phys. Ref. D*, 102(2):023509.

Abbott, T. M. C., Aguena, M., Alarcon, A., Allam, S., Alves, O., Amon, A., Andrade-Oliveira, F., Annis, J., Avila, S., Bacon, D., Baxter, E., Bechtol, K., Becker, M. R., Bernstein, G. M., Bhargava, S., Birrer, S., Blazek, J., Brandao-Souza, A., Bridle, S. L., Brooks, D., Buckley-Geer, E., Burke, D. L., Camacho, H., Campos, A., Carnero Rosell, A., Carrasco Kind, M., Carretero, J., Castander, F. J., Cawthon, R., Chang, C., Chen, A., Chen, R., Choi, A., Conselice, C., Cordero, J., Costanzi, M., Crocce, M., da Costa, L. N., da Silva Pereira, M. E., Davis, C., Davis, T. M., De Vicente, J., DeRose, J., Desai, S., Di Valentino, E., Diehl, H. T., Dietrich, J. P., Dodelson, S., Doel, P., Doux, C., Drlica-Wagner, A., Eckert, K., Eifler, T. F., Elsner, F., Elvin-Poole, J., Everett, S., Evrard, A. E., Fang, X., Farahi, A., Fernandez, E., Ferrero, I., Ferté, A., Fosalba, P., Friedrich, O., Frieman, J., García-Bellido, J., Gatti, M., Gaztanaga, E., Gerdes, D. W., Giannantonio, T., Giannini, G., Gruen, D., Gruendl, R. A., Gschwend, J., Gutierrez, G., Harrison, I., Hartley, W. G., Herner, K., Hinton, S. R., Hollowood, D. L., Honscheid, K., Hoyle, B., Huff, E. M., Huterer, D., Jain, B., James, D. J., Jarvis, M., Jeffrey, N., Jeltema, T., Kovacs, A., Krause, E., Kron, R., Kuehn, K., Kuropatkin, N., Lahav, O., Leget, P. F., Lemos, P., Liddle, A. R., Lidman, C., Lima, M., Lin, H., MacCrann, N., Maia, M. A. G., Marshall, J. L., Martini, P., McCullough, J., Melchior, P., Mena-Fernández, J., Menanteau, F., Miquel, R., Mohr, J. J., Morgan, R., Muir, J., Myles, J., Nadathur, S., Navarro-Alsina, A., Nichol, R. C., Ogando, R. L. C., Omori, Y., Palmese, A., Pandey, S., Park, Y., Paz-Chinchón, F., Petravick, D., Pieres, A., Plazas Malagón, A. A., Porredon, A., Prat, J., Raveri, M., Rodriguez-Monroy, M., Rollins, R. P., Romer, A. K., Roodman, A., Rosenfeld, R., Ross, A. J., Rykoff, E. S., Samuroff, S., Sánchez, C., Sanchez, E., Sanchez, J., Sanchez Cid, D., Scarpine, V., Schubnell, M., Scolnic, D., Secco, L. F., Serrano, S., Sevilla-Noarbe, I., Sheldon, E., Shin, T., Smith, M., Soares-Santos, M., Suchyta, E., Swanson, M. E. C., Tabbutt, M., Tarle, G., Thomas, D., To, C., Troja, A., Troxel, M. A., Tucker, D. L., Tutusaus, I., Varga, T. N., Walker, A. R., Weaverdyck, N., Wechsler, R., Weller, J., Yanny, B., Yin, B., Zhang, Y., Zuntz, J., and DES Collaboration (2022). Dark Energy Survey Year 3 results: Cosmological constraints from galaxy clustering and weak lensing. *Phys. Ref. D*, 105(2):023520.

Abrahamsen, P. (1997). A review of gaussian random fields and correlation functions.

Achitouv, I. (2016). Testing the imprint of nonstandard cosmologies on void profiles using monte carlo random walks. *Phys. Rev. D*, 94:103524.

Achitouv, I. (2019). New constraints on the linear growth rate using cosmic voids in the SDSS DR12 datasets. *Phys. Ref. D*, 100(12):123513.

Achitouv, I., Blake, C., Carter, P., Koda, J., and Beutler, F. (2017). Consistency of the

growth rate in different environments with the 6-degree field galaxy survey: Measurement of the void-galaxy and galaxy-galaxy correlation functions. *Physical Review D*, 95(8).

Ahumada, R., Prieto, C. A., Almeida, A., Anders, F., Anderson, S. F., Andrews, B. H., Anguiano, B., Arcodia, R., Armengaud, E., Aubert, M., Avila, S., Avila-Reese, V., Badenes, C., Balland, C., Barger, K., Barrera-Ballesteros, J. K., Basu, S., Bautista, J., Beaton, R. L., Beers, T. C., Benavides, B. I. T., Bender, C. F., Bernardi, M., Bershady, M., Beutler, F., Bidin, C. M., Bird, J., Bizyaev, D., Blanc, G. A., Blanton, M. R., Boquien, M., Borissova, J., Bovy, J., Brandt, W. N., Brinkmann, J., Brownstein, J. R., Bundy, K., Bureau, M., Burgasser, A., Burtin, E., Cano-Díaz, M., Capasso, R., Cappellari, M., Carrera, R., Chabanier, S., Chaplin, W., Chapman, M., Cherinka, B., Chiappini, C., Doohyun Choi, P., Chojnowski, S. D., Chung, H., Clerc, N., Coffey, D., Comerford, J. M., Comparat, J., da Costa, L., Cousinou, M.-C., Covey, K., Crane, J. D., Cunha, K., Ilha, G. d. S., Dai, Y. S., Damsted, S. B., Darling, J., Davidson, James W., J., Davies, R., Dawson, K., De, N., de la Macorra, A., De Lee, N., Queiroz, A. B. d. A., Deconto Machado, A., de la Torre, S., Dell'Agli, F., du Mas des Bourboux, H., Diamond-Stanic, A. M., Dillon, S., Donor, J., Drory, N., Duckworth, C., Dwelly, T., Ebelke, G., Eftekharzadeh, S., Davis Eigenbrot, A., Elsworth, Y. P., Eracleous, M., Erfanianfar, G., Escoffier, S., Fan, X., Farr, E., Fernández-Trincado, J. G., Feuillet, D., Finoguenov, A., Fofie, P., Fraser-McKelvie, A., Frinchaboy, P. M., Fromenteau, S., Fu, H., Galbany, L., Garcia, R. A., García-Hernández, D. A., Oehmichen, L. A. G., Ge, J., Maia, M. A. G., Geisler, D., Gelfand, J., Goddy, J., Gonzalez-Perez, V., Grabowski, K., Green, P., Grier, C. J., Guo, H., Guy, J., Harding, P., Hasselquist, S., Hawken, A. J., Hayes, C. R., Hearty, F., Hekker, S., Hogg, D. W., Holtzman, J. A., Horta, D., Hou, J., Hsieh, B.-C., Huber, D., Hunt, J. A. S., Chitham, J. I., Imig, J., Jaber, M., Angel, C. E. J., Johnson, J. A., Jones, A. M., Jönsson, H., Jullo, E., Kim, Y., Kinemuchi, K., Kirkpatrick, Charles C., I., Kite, G. W., Klaene, M., Kneib, J.-P., Kollmeier, J. A., Kong, H., Kounkel, M., Krishnarao, D., Lacerna, I., Lan, T.-W., Lane, R. R., Law, D. R., Le Goff, J.-M., Leung, H. W., Lewis, H., Li, C., Lian, J., Lin, L., Long, D., Longa-Peña, P., Lundgren, B., Lyke, B. W., Ted Mackereth, J., MacLeod, C. L., Majewski, S. R., Manchado, A., Maraston, C., Martini, P., Masseron, T., Masters, K. L., Mathur, S., McDermid, R. M., Merloni, A., Merrifield, M., Mészáros, S., Miglio, A., Minniti, D., Minsley, R., Miyaji, T., Mohammad, F. G., Mosser, B., Mueller, E.-M., Muna, D., Muñoz-Gutiérrez, A., Myers, A. D., Nadathur, S., Nair, P., Nandra, K., do Nascimento, J. C., Nevin, R. J., Newman, J. A., Nidever, D. L., Nitschelm, C., Noterdaeme, P., O'Connell, J. E., Olmstead, M. D., Oravetz, D., Oravetz, A., Osorio, Y., Pace, Z. J., Padilla, N., Palanque-Delabrouille, N., Palicio, P. A., Pan, H.-A., Pan, K., Parker, J., Paviot, R., Peirani, S., Ramŕez, K. P., Penny, S., Percival, W. J., Perez-Fournon, I.,

Pérez-Ràfols, I., Petitjean, P., Pieri, M. M., Pinsonneault, M., Poovelil, V. J., Povick, J. T., Prakash, A., Price-Whelan, A. M., Raddick, M. J., Raichoor, A., Ray, A., Rembold, S. B., Rezaie, M., Riffel, R. A., Riffel, R., Rix, H.-W., Robin, A. C., Roman-Lopes, A., Román-Zúñiga, C., Rose, B., Ross, A. J., Rossi, G., Rowlands, K., Rubin, K. H. R., Salvato, M., Sánchez, A. G., Sánchez-Menguiano, L., Sánchez-Gallego, J. R., Sayres, C., Schaefer, A., Schiavon, R. P., Schimoia, J. S., Schlafly, E., Schlegel, D., Schneider, D. P., Schultheis, M., Schwope, A., Seo, H.-J., Serenelli, A., Shafieloo, A., Shamsi, S. J., Shao, Z., Shen, S., Shetrone, M., Shirley, R., Aguirre, V. S., Simon, J. D., Skrutskie, M. F., Slosar, A., Smethurst, R., Sobeck, J., Sodi, B. C., Souto, D., Stark, D. V., Stassun, K. G., Steinmetz, M., Stello, D., Stermer, J., Storchi-Bergmann, T., Streblyanska, A., Stringfellow, G. S., Stutz, A., Suárez, G., Sun, J., Taghizadeh-Popp, M., Talbot, M. S., Tayar, J., Thakar, A. R., Theriault, R., Thomas, D., Thomas, Z. C., Tinker, J., Tojeiro, R., Toledo, H. H., Tremonti, C. A., Troup, N. W., Tuttle, S., Unda-Sanzana, E., Valentini, M., Vargas-González, J., Vargas-Magaña, M., Vázquez-Mata, J. A., Vivek, M., Wake, D., Wang, Y., Weaver, B. A., Weijmans, A.-M., Wild, V., Wilson, J. C., Wilson, R. F., Wolthuis, N., Wood-Vasey, W. M., Yan, R., Yang, M., Yèche, C., Zamora, O., Zarrouk, P., Zasowski, G., Zhang, K., Zhao, C., Zhao, G., Zheng, Z., Zheng, Z., Zhu, G., and Zou, H. (2020). The 16th Data Release of the Sloan Digital Sky Surveys: First Release from the APOGEE-2 Southern Survey and Full Release of eBOSS Spectra. *ApJS*, 249(1):3.

Alam, S., Albareti, F. D., Allende Prieto, C., Anders, F., Anderson, S. F., Anderton, T., Andrews, B. H., Armengaud, E., Aubourg, É., Bailey, S., and et al. (2015). The Eleventh and Twelfth Data Releases of the Sloan Digital Sky Survey: Final Data from SDSS-III. *ApJS*, 219:12.

Alam, S., Ata, M., Bailey, S., Beutler, F., Bizyaev, D., Blazek, J. A., Bolton, A. S., Brownstein, J. R., Burden, A., Chuang, C.-H., Comparat, J., Cuesta, A. J., Dawson, K. S., Eisenstein, D. J., Escoffier, S., Gil-Marín, H., Grieb, J. N., Hand, N., Ho, S., Kinemuchi, K., Kirkby, D., Kitaura, F., Malanushenko, E., Malanushenko, V., Maraston, C., McBride, C. K., Nichol, R. C., Olmstead, M. D., Oravetz, D., Padmanabhan, N., Palanque-Delabrouille, N., Pan, K., Pellejero-Ibanez, M., Percival, W. J., Petitjean, P., Prada, F., Price-Whelan, A. M., Reid, B. A., Rodríguez-Torres, S. A., Roe, N. A., Ross, A. J., Ross, N. P., Rossi, G., Rubiño-Martín, J. A., Saito, S., Salazar-Albornoz, S., Samushia, L., Sánchez, A. G., Satpathy, S., Schlegel, D. J., Schneider, D. P., Scóccola, C. G., Seo, H.-J., Sheldon, E. S., Simmons, A., Slosar, A., Strauss, M. A., Swanson, M. E. C., Thomas, D., Tinker, J. L., Tojeiro, R., Magaña, M. V., Vazquez, J. A., Verde, L., Wake, D. A., Wang, Y., Weinberg, D. H., White, M., Wood-Vasey, W. M., Yèche, C.,

Zehavi, I., Zhai, Z., and Zhao, G.-B. (2017). The clustering of galaxies in the completed SDSS-III Baryon Oscillation Spectroscopic Survey: cosmological analysis of the DR12 galaxy sample. *MNRAS*, 470(3):2617–2652.

Alam, S., Aubert, M., Avila, S., Balland, C., Bautista, J. E., Bershady, M. A., Bizyaev, D., Blanton, M. R., Bolton, A. S., Bovy, J., Brinkmann, J., Brownstein, J. R., Burtin, E., Chabanier, S., Chapman, M. J., Choi, P. D., Chuang, C.-H., Comparat, J., Cousinou, M.-C., Cuceu, A., Dawson, K. S., de la Torre, S., de Mattia, A., Agathe, V. d. S., des Bourboux, H. d. M., Escoffier, S., Etourneau, T., Farr, J., Font-Ribera, A., Frinchaboy, P. M., Fromenteau, S., Gil-Marín, H., Le Goff, J.-M., Gonzalez-Morales, A. X., Gonzalez-Perez, V., Grabowski, K., Guy, J., Hawken, A. J., Hou, J., Kong, H., Parker, J., Klaene, M., Kneib, J.-P., Lin, S., Long, D., Lyke, B. W., de la Macorra, A., Martini, P., Masters, K., Mohammad, F. G., Moon, J., Mueller, E.-M., Muñoz-Gutiérrez, A., Myers, A. D., Nadathur, S., Neveux, R., Newman, J. A., Noterdaeme, P., Oravetz, A., Oravetz, D., Palanque-Delabrouille, N., Pan, K., Paviot, R., Percival, W. J., Pérez-Ràfols, I., Petitjean, P., Pieri, M. M., Prakash, A., Raichoor, A., Ravoux, C., Rezaie, M., Rich, J., Ross, A. J., Rossi, G., Ruggeri, R., Ruhlmann-Kleider, V., Sánchez, A. G., Sánchez, F. J., Sánchez-Gallego, J. R., Sayres, C., Schneider, D. P., Seo, H.-J., Shafieloo, A., Slosar, A., Smith, A., Stermer, J., Tamone, A., Tinker, J. L., Tojeiro, R., Vargas-Magaña, M., Variu, A., Wang, Y., Weaver, B. A., Weijmans, A.-M., Yèche, C., Zarrouk, P., Zhao, C., Zhao, G.-B., and Zheng, Z. (2021). Completed SDSS-IV extended Baryon Oscillation Spectroscopic Survey: Cosmological implications from two decades of spectroscopic surveys at the Apache Point Observatory. *Phys. Ref. D*, 103(8):083533.

Alcock, C. and Paczynski, B. (1979). An evolution free test for non-zero cosmological constant. *Nature*, 281:358.

Anderson, L., Aubourg, É., Bailey, S., Beutler, F., Bhardwaj, V., Blanton, M., Bolton, A. S., Brinkmann, J., Brownstein, J. R., Burden, A., Chuang, C.-H., Cuesta, A. J., Dawson, K. S., Eisenstein, D. J., Escoffier, S., Gunn, J. E., Guo, H., Ho, S., Honscheid, K., Howlett, C., Kirkby, D., Lupton, R. H., Manera, M., Maraston, C., McBride, C. K., Mena, O., Montesano, F., Nichol, R. C., Nuza, S. E., Olmstead, M. D., Padmanabhan, N., Palanque-Delabrouille, N., Parejko, J., Percival, W. J., Petitjean, P., Prada, F., Price-Whelan, A. M., Reid, B., Roe, N. A., Ross, A. J., Ross, N. P., Sabiu, C. G., Saito, S., Samushia, L., Sánchez, A. G., Schlegel, D. J., Schneider, D. P., Scoccola, C. G., Seo, H.-J., Skibba, R. A., Strauss, M. A., Swanson, M. E. C., Thomas, D., Tinker, J. L., Tojeiro, R., Magaña, M. V., Verde, L., Wake, D. A., Weaver, B. A., Weinberg, D. H., White, M., Xu, X., Yèche, C., Zehavi, I., and Zhao, G.-B. (2014). The clustering

of galaxies in the SDSS-III Baryon Oscillation Spectroscopic Survey: baryon acoustic oscillations in the Data Releases 10 and 11 Galaxy samples. *MNRAS*, 441(1):24–62.

Asgari, M., Lin, C.-A., Joachimi, B., Giblin, B., Heymans, C., Hildebrandt, H., Kannawadi, A., Stölzner, B., Tröster, T., van den Busch, J. L., Wright, A. H., Bilicki, M., Blake, C., de Jong, J., Dvornik, A., Erben, T., Getman, F., Hoekstra, H., Köhlinger, F., Kuijken, K., Miller, L., Radovich, M., Schneider, P., Shan, H., and Valentijn, E. (2021). KiDS-1000 cosmology: Cosmic shear constraints and comparison between two point statistics. *A&A*, 645:A104.

Aubert, M., Cousinou, M.-C., Escoffier, S., Hawken, A. J., Nadathur, S., Alam, S., Bautista, J., Burtin, E., Chuang, C.-H., de la Macorra, A., de Mattia, A., Gil-Marín, H., Hou, J., Jullo, E., Kneib, J.-P., Neveux, R., Rossi, G., Schneider, D., Smith, A., Tamone, A., Vargas Magaña, M., and Zhao, C. (2022a). The completed SDSS-IV extended Baryon Oscillation Spectroscopic Survey: growth rate of structure measurement from cosmic voids. *MNRAS*, 513(1):186–203.

Aubert, M., Cousinou, M.-C., Escoffier, S., Hawken, A. J., Nadathur, S., Alam, S., Bautista, J., Burtin, E., Chuang, C.-H., de la Macorra, A., de Mattia, A., Gil-Marín, H., Hou, J., Jullo, E., Kneib, J.-P., Neveux, R., Rossi, G., Schneider, D., Smith, A., Tamone, A., Vargas Magaña, M., and Zhao, C. (2022b). The completed SDSS-IV extended Baryon Oscillation Spectroscopic Survey: growth rate of structure measurement from cosmic voids. *MNRAS*, 513(1):186–203.

Ballinger, W., Peacock, J., and Heavens, A. (1996). Measuring the cosmological constant with redshift surveys. *MNRAS*, 282(3):877–888.

Bardeen, J. M., Bond, J. R., Kaiser, N., and Szalay, A. S. (1986). The Statistics of Peaks of Gaussian Random Fields. *ApJ*, 304:15.

Barrow, J. D. and Turner, M. S. (1981). Baryosynthesis and the origin of galaxies. *Nature*, 291(5815):469–472.

Bautista, J. E., Paviot, R., Vargas Magaña, M., de la Torre, S., Fromenteau, S., Gil-Marín, H., Ross, A. J., Burtin, E., Dawson, K. S., Hou, J., Kneib, J.-P., de Mattia, A., Percival, W. J., Rossi, G., Tojeiro, R., Zhao, C., Zhao, G.-B., Alam, S., Brownstein, J., Chapman, M. J., Choi, P. D., Chuang, C.-H., Escoffier, S., de la Macorra, A., du Mas des Bourboux, H., Mohammad, F. G., Moon, J., Müller, E.-M., Nadathur, S., Newman, J. A., Schneider, D., Seo, H.-J., and Wang, Y. (2021). The completed SDSS-IV extended Baryon Oscillation Spectroscopic Survey: measurement of the BAO and growth rate of

structure of the luminous red galaxy sample from the anisotropic correlation function between redshifts 0.6 and 1. *MNRAS*, 500(1):736–762.

Bernardeau, F. (1994). The effects of smoothing on the statistical properties of large-scale cosmic fields. *A&A*, 291:697–712.

Beutler, F., Blake, C., Colless, M., Jones, D. H., Staveley-Smith, L., Poole, G. B., Campbell, L., Parker, Q., Saunders, W., and Watson, F. (2012). The 6dF Galaxy Survey: z≈ 0 measurements of the growth rate and σ_8. *MNRAS*, 423(4):3430–3444.

Blake, C., Baldry, I. K., Bland-Hawthorn, J., Christodoulou, L., Colless, M., Conselice, C., Driver, S. P., Hopkins, A. M., Liske, J., Loveday, J., and et al. (2013). Galaxy and mass assembly (gama): improved cosmic growth measurements using multiple tracers of large-scale structure. *Monthly Notices of the Royal Astronomical Society*, 436(4):3089–3105.

Blake, C., Brough, S., Colless, M., Contreras, C., Couch, W., Croom, S., Croton, D., Davis, T. M., Drinkwater, M. J., Forster, K., and et al. (2012). The wigglez dark energy survey: joint measurements of the expansion and growth history atz$<$ 1. *Monthly Notices of the Royal Astronomical Society*, 425(1):405–414.

Blanton, M. R., Bershady, M. A., Abolfathi, B., Albareti, F. D., Allende Prieto, C., Almeida, A., Alonso-García, J., Anders, F., Anderson, S. F., Andrews, B., Aquino-Ortíz, E., Aragón-Salamanca, A., Argudo-Fernández, M., Armengaud, E., Aubourg, E., Avila-Reese, V., Badenes, C., Bailey, S., Barger, K. A., Barrera-Ballesteros, J., Bartosz, C., Bates, D., Baumgarten, F., Bautista, J., Beaton, R., Beers, T. C., Belfiore, F., Bender, C. F., Berlind, A. A., Bernardi, M., Beutler, F., Bird, J. C., Bizyaev, D., Blanc, G. A., Blomqvist, M., Bolton, A. S., Boquien, M., Borissova, J., van den Bosch, R., Bovy, J., Brandt, W. N., Brinkmann, J., Brownstein, J. R., Bundy, K., Burgasser, A. J., Burtin, E., Busca, N. G., Cappellari, M., Delgado Carigi, M. L., Carlberg, J. K., Carnero Rosell, A., Carrera, R., Chanover, N. J., Cherinka, B., Cheung, E., Gómez Maqueo Chew, Y., Chiappini, C., Choi, P. D., Chojnowski, D., Chuang, C.-H., Chung, H., Cirolini, R. F., Clerc, N., Cohen, R. E., Comparat, J., da Costa, L., Cousinou, M.-C., Covey, K., Crane, J. D., Croft, R. A. C., Cruz-Gonzalez, I., Garrido Cuadra, D., Cunha, K., Damke, G. J., Darling, J., Davies, R., Dawson, K., de la Macorra, A., Dell'Agli, F., De Lee, N., Delubac, T., Di Mille, F., Diamond-Stanic, A., Cano-Díaz, M., Donor, J., Downes, J. J., Drory, N., du Mas des Bourboux, H., Duckworth, C. J., Dwelly, T., Dyer, J., Ebelke, G., Eigenbrot, A. D., Eisenstein, D. J., Emsellem, E., Eracleous, M., Escoffier, S., Evans, M. L., Fan, X., Fernández-Alvar, E., Fernandez-Trincado, J. G., Feuillet, D. K., Finoguenov, A., Fleming, S. W., Font-Ribera, A., Fredrickson, A., Freischlad, G., Frinchaboy, P. M.,

Fuentes, C. E., Galbany, L., Garcia-Dias, R., García-Hernández, D. A., Gaulme, P., Geisler, D., Gelfand, J. D., Gil-Marín, H., Gillespie, B. A., Goddard, D., Gonzalez-Perez, V., Grabowski, K., Green, P. J., Grier, C. J., Gunn, J. E., Guo, H., Guy, J., Hagen, A., Hahn, C., Hall, M., Harding, P., Hasselquist, S., Hawley, S. L., Hearty, F., Gonzalez Hernández, J. I., Ho, S., Hogg, D. W., Holley-Bockelmann, K., Holtzman, J. A., Holzer, P. H., Huehnerhoff, J., Hutchinson, T. A., Hwang, H. S., Ibarra-Medel, H. J., da Silva Ilha, G., Ivans, I. I., Ivory, K., Jackson, K., Jensen, T. W., Johnson, J. A., Jones, A., Jönsson, H., Jullo, E., Kamble, V., Kinemuchi, K., Kirkby, D., Kitaura, F.-S., Klaene, M., Knapp, G. R., Kneib, J.-P., Kollmeier, J. A., Lacerna, I., Lane, R. R., Lang, D., Law, D. R., Lazarz, D., Lee, Y., Le Goff, J.-M., Liang, F.-H., Li, C., Li, H., Lian, J., Lima, M., Lin, L., Lin, Y.-T., Bertran de Lis, S., Liu, C., de Icaza Lizaola, M. A. C., Long, D., Lucatello, S., Lundgren, B., MacDonald, N. K., Deconto Machado, A., MacLeod, C. L., Mahadevan, S., Geimba Maia, M. A., Maiolino, R., Majewski, S. R., Malanushenko, E., Malanushenko, V., Manchado, A., Mao, S., Maraston, C., Marques-Chaves, R., Masseron, T., Masters, K. L., McBride, C. K., McDermid, R. M., McGrath, B., McGreer, I. D., Medina Peña, N., Melendez, M., Merloni, A., Merrifield, M. R., Meszaros, S., Meza, A., Minchev, I., Minniti, D., Miyaji, T., More, S., Mulchaey, J., Müller-Sánchez, F., Muna, D., Munoz, R. R., Myers, A. D., Nair, P., Nandra, K., Correa do Nascimento, J., Negrete, A., Ness, M., Newman, J. A., Nichol, R. C., Nidever, D. L., Nitschelm, C., Ntelis, P., O'Connell, J. E., Oelkers, R. J., Oravetz, A., Oravetz, D., Pace, Z., Padilla, N., Palanque-Delabrouille, N., Alonso Palicio, P., Pan, K., Parejko, J. K., Parikh, T., Pâris, I., Park, C., Patten, A. Y., Peirani, S., Pellejero-Ibanez, M., Penny, S., Percival, W. J., Perez-Fournon, I., Petitjean, P., Pieri, M. M., Pinsonneault, M., Pisani, A., Poleski, R., Prada, F., Prakash, A., Queiroz, A. B. d. A., Raddick, M. J., Raichoor, A., Barboza Rembold, S., Richstein, H., Riffel, R. A., Riffel, R., Rix, H.-W., Robin, A. C., Rockosi, C. M., Rodríguez-Torres, S., Roman-Lopes, A., Román-Zúñiga, C., Rosado, M., Ross, A. J., Rossi, G., Ruan, J., Ruggeri, R., Rykoff, E. S., Salazar-Albornoz, S., Salvato, M., Sánchez, A. G., Aguado, D. S., Sánchez-Gallego, J. R., Santana, F. A., Santiago, B. X., Sayres, C., Schiavon, R. P., da Silva Schimoia, J., Schlafly, E. F., Schlegel, D. J., Schneider, D. P., Schultheis, M., Schuster, W. J., Schwope, A., Seo, H.-J., Shao, Z., Shen, S., Shetrone, M., Shull, M., Simon, J. D., Skinner, D., Skrutskie, M. F., Slosar, A., Smith, V. V., Sobeck, J. S., Sobreira, F., Somers, G., Souto, D., Stark, D. V., Stassun, K., Stauffer, F., Steinmetz, M., Storchi-Bergmann, T., Streblyanska, A., Stringfellow, G. S., Suárez, G., Sun, J., Suzuki, N., Szigeti, L., Taghizadeh-Popp, M., Tang, B., Tao, C., Tayar, J., Tembe, M., Teske, J., Thakar, A. R., Thomas, D., Thompson, B. A., Tinker, J. L., Tissera, P., Tojeiro, R., Hernandez Toledo, H., de la Torre, S., Tremonti, C., Troup, N. W., Valenzuela, O., Martinez Valpuesta, I., Vargas-González, J., Vargas-Magaña, M., Vazquez, J. A.,

Villanova, S., Vivek, M., Vogt, N., Wake, D., Walterbos, R., Wang, Y., Weaver, B. A., Weijmans, A.-M., Weinberg, D. H., Westfall, K. B., Whelan, D. G., Wild, V., Wilson, J., Wood-Vasey, W. M., Wylezalek, D., Xiao, T., Yan, R., Yang, M., Ybarra, J. E., Yèche, C., Zakamska, N., Zamora, O., Zarrouk, P., Zasowski, G., Zhang, K., Zhao, G.-B., Zheng, Z., Zheng, Z., Zhou, X., Zhou, Z.-M., Zhu, G. B., Zoccali, M., and Zou, H. (2017). Sloan Digital Sky Survey IV: Mapping the Milky Way, Nearby Galaxies, and the Distant Universe. *AJ*, 154(1):28.

Brout, D., Scolnic, D., Popovic, B., Riess, A. G., Carr, A., Zuntz, J., Kessler, R., Davis, T. M., Hinton, S., Jones, D., Kenworthy, W. D., Peterson, E. R., Said, K., Taylor, G., Ali, N., Armstrong, P., Charvu, P., Dwomoh, A., Meldorf, C., Palmese, A., Qu, H., Rose, B. M., Sanchez, B., Stubbs, C. W., Vincenzi, M., Wood, C. M., Brown, P. J., Chen, R., Chambers, K., Coulter, D. A., Dai, M., Dimitriadis, G., Filippenko, A. V., Foley, R. J., Jha, S. W., Kelsey, L., Kirshner, R. P., Möller, A., Muir, J., Nadathur, S., Pan, Y.-C., Rest, A., Rojas-Bravo, C., Sako, M., Siebert, M. R., Smith, M., Stahl, B. E., and Wiseman, P. (2022). The Pantheon+ Analysis: Cosmological Constraints. *ApJ*, 938(2):110.

Burden, A., Percival, W. J., and Howlett, C. (2015). Reconstruction in Fourier space. *MNRAS*, 453:456–468.

Cai, Y.-C., Padilla, N., and Li, B. (2015). Testing gravity using cosmic voids. *Monthly Notices of the Royal Astronomical Society*, 451(1):1036–1055.

Cai, Y.-C., Taylor, A., Peacock, J. A., and Padilla, N. (2016). Redshift-space distortions around voids. *MNRAS*, 462:2465–2477.

Cautun, M., Paillas, E., Cai, Y.-C., Bose, S., Armijo, J., Li, B., and Padilla, N. (2018). The Santiago–Harvard–Edinburgh–Durham void comparison – I. SHEDding light on chameleon gravity tests. *Monthly Notices of the Royal Astronomical Society*, 476(3):3195–3217.

Cautun, M., van de Weygaert, R., Jones, B. J. T., and Frenk, C. S. (2014). Evolution of the cosmic web. *MNRAS*, 441(4):2923–2973.

Ceccarelli, L., Paz, D., Lares, M., Padilla, N., and Lambas, D. G. (2013). Clues on void evolution - I. Large-scale galaxy distributions around voids. *MNRAS*, 434(2):1435–1442.

Chapman, M. J., Mohammad, F. G., Zhai, Z., Percival, W. J., Tinker, J. L., Bautista, J. E., Brownstein, J. R., Burtin, E., Dawson, K. S., Gil-Marín, H., de la Macorra, A.,

Ross, A. J., Rossi, G., Schneider, D. P., and Zhao, G.-B. (2022). The completed SDSS-IV extended Baryon Oscillation Spectroscopic Survey: measurement of the growth rate of structure from the small-scale clustering of the luminous red galaxy sample. *MNRAS*, 516(1):617–635.

Chuang, C.-H., Kitaura, F.-S., Liang, Y., Font-Ribera, A., Zhao, C., McDonald, P., and Tao, C. (2017). Linear redshift space distortions for cosmic voids based on galaxies in redshift space. *Phys. Ref. D*, 95(6):063528.

Chuang, C.-H., Kitaura, F.-S., Liang, Y., Font-Ribera, A., Zhao, C., McDonald, P., and Tao, C. (2017). Linear redshift space distortions for cosmic voids based on galaxies in redshift space. *Physical Review D*, 95(6).

Chuang, C.-H., Zhao, C., Prada, F., Munari, E., Avila, S., Izard, A., Kitaura, F.-S., Manera, M., Monaco, P., Murray, S., Knebe, A., Scóccola, C. G., Yepes, G., Garcia-Bellido, J., Marín, F. A., Müller, V., Skibba, R., Crocce, M., Fosalba, P., Gottlöber, S., Klypin, A. A., Power, C., Tao, C., and Turchaninov, V. (2015). nIFTy cosmology: Galaxy/halo mock catalogue comparison project on clustering statistics. *MNRAS*, 452:686–700.

Clampitt, J., Cai, Y.-C., and Li, B. (2013). Voids in modified gravity: excursion set predictions. *Monthly Notices of the Royal Astronomical Society*, 431(1):749–766.

Colless, M., Peterson, B. A., Jackson, C., Peacock, J. A., Cole, S., Norberg, P., Baldry, I. K., Baugh, C. M., Bland-Hawthorn, J., Bridges, T., Cannon, R., Collins, C., Couch, W., Cross, N., Dalton, G., De Propris, R., Driver, S. P., Efstathiou, G., Ellis, R. S., Frenk, C. S., Glazebrook, K., Lahav, O., Lewis, I., Lumsden, S., Maddox, S., Madgwick, D., Sutherland, W., and Taylor, K. (2003). The 2dF Galaxy Redshift Survey: Final Data Release. *arXiv e-prints*, pages astro–ph/0306581.

Cooke, R. J., Pettini, M., Nollett, K. M., and Jorgenson, R. (2016). The Primordial Deuterium Abundance of the Most Metal-poor Damped Lyman-α System. *ApJ*, 830(2):148.

Correa, C. M. (2022). Cosmic voids as cosmological laboratories. *arXiv e-prints*, page arXiv:2210.17459.

Correa, C. M., Paz, D. J., Padilla, N. D., Ruiz, A. N., Angulo, R. E., and Sánchez, A. G. (2019). Non-fiducial cosmological test from geometrical and dynamical distortions around voids. *MNRAS*, 485(4):5761–5772.

Correa, C. M., Paz, D. J., Padilla, N. D., Sánchez, A. G., Ruiz, A. N., and Angulo, R. E. (2022). Redshift-space effects in voids and their impact on cosmological tests - II. The void-galaxy cross-correlation function. *MNRAS*, 509(2):1871–1884.

Correa, C. M., Paz, D. J., Sánchez, A. G., Ruiz, A. N., Padilla, N. D., and Angulo, R. E. (2021). Redshift-space effects in voids and their impact on cosmological tests. Part I: the void size function. *MNRAS*, 500(1):911–925.

Cuceu, A., Font-Ribera, A., Nadathur, S., Joachimi, B., and Martini, P. (2022). New constraints on the expansion rate at redshift 2.3 from the Lyman-α forest. *Phys. Review Letter*, page arXiv:2209.13942.

Davies, C. T., Paillas, E., Cautun, M., and Li, B. (2021). Optimal void finders in weak lensing maps. *MNRAS*, 500(2):2417–2439.

Davis, M. and Peebles, P. J. E. (1983). A survey of galaxy redshifts. V. The two-point position and velocity correlations. *ApJ*, 267:465–482.

Dawson, K. S., Kneib, J.-P., Percival, W. J., Alam, S., Albareti, F. D., Anderson, S. F., Armengaud, E., Aubourg, É., Bailey, S., Bautista, J. E., Berlind, A. A., Bershady, M. A., Beutler, F., Bizyaev, D., Blanton, M. R., Blomqvist, M., Bolton, A. S., Bovy, J., Brandt, W. N., Brinkmann, J., Brownstein, J. R., Burtin, E., Busca, N. G., Cai, Z., Chuang, C.-H., Clerc, N., Comparat, J., Cope, F., Croft, R. A. C., Cruz-Gonzalez, I., da Costa, L. N., Cousinou, M.-C., Darling, J., de la Macorra, A., de la Torre, S., Delubac, T., du Mas des Bourboux, H., Dwelly, T., Ealet, A., Eisenstein, D. J., Eracleous, M., Escoffier, S., Fan, X., Finoguenov, A., Font-Ribera, A., Frinchaboy, P., Gaulme, P., Georgakakis, A., Green, P., Guo, H., Guy, J., Ho, S., Holder, D., Huehnerhoff, J., Hutchinson, T., Jing, Y., Jullo, E., Kamble, V., Kinemuchi, K., Kirkby, D., Kitaura, F.-S., Klaene, M. A., Laher, R. R., Lang, D., Laurent, P., Le Goff, J.-M., Li, C., Liang, Y., Lima, M., Lin, Q., Lin, W., Lin, Y.-T., Long, D. C., Lundgren, B., MacDonald, N., Geimba Maia, M. A., Malanushenko, E., Malanushenko, V., Mariappan, V., McBride, C. K., McGreer, I. D., Ménard, B., Merloni, A., Meza, A., Montero-Dorta, A. D., Muna, D., Myers, A. D., Nandra, K., Naugle, T., Newman, J. A., Noterdaeme, P., Nugent, P., Ogando, R., Olmstead, M. D., Oravetz, A., Oravetz, D. J., Padmanabhan, N., Palanque-Delabrouille, N., Pan, K., Parejko, J. K., Pâris, I., Peacock, J. A., Petitjean, P., Pieri, M. M., Pisani, A., Prada, F., Prakash, A., Raichoor, A., Reid, B., Rich, J., Ridl, J., Rodriguez-Torres, S., Carnero Rosell, A., Ross, A. J., Rossi, G., Ruan, J., Salvato, M., Sayres, C., Schneider, D. P., Schlegel, D. J., Seljak, U., Seo, H.-J., Sesar, B., Shandera, S., Shu, Y., Slosar, A., Sobreira, F., Streblyanska, A., Suzuki, N., Taylor, D., Tao, C.,

Tinker, J. L., Tojeiro, R., Vargas-Magaña, M., Wang, Y., Weaver, B. A., Weinberg, D. H., White, M., Wood-Vasey, W. M., Yeche, C., Zhai, Z., Zhao, C., Zhao, G.-b., Zheng, Z., Ben Zhu, G., and Zou, H. (2016). The SDSS-IV Extended Baryon Oscillation Spectroscopic Survey: Overview and Early Data. *AJ*, 151(2):44.

Dawson, K. S., Schlegel, D. J., Ahn, C. P., Anderson, S. F., Aubourg, É., Bailey, S., Barkhouser, R. H., Bautista, J. E., Beifiori, A., Berlind, A. A., Bhardwaj, V., Bizyaev, D., Blake, C. H., Blanton, M. R., Blomqvist, M., Bolton, A. S., Borde, A., Bovy, J., Brandt, W. N., Brewington, H., Brinkmann, J., Brown, P. J., Brownstein, J. R., Bundy, K., Busca, N. G., Carithers, W., Carnero, A. R., Carr, M. A., Chen, Y., Comparat, J., Connolly, N., Cope, F., Croft, R. A. C., Cuesta, A. J., da Costa, L. N., Davenport, J. R. A., Delubac, T., de Putter, R., Dhital, S., Ealet, A., Ebelke, G. L., Eisenstein, D. J., Escoffier, S., Fan, X., Filiz Ak, N., Finley, H., Font-Ribera, A., Génova-Santos, R., Gunn, J. E., Guo, H., Haggard, D., Hall, P. B., Hamilton, J.-C., Harris, B., Harris, D. W., Ho, S., Hogg, D. W., Holder, D., Honscheid, K., Huehnerhoff, J., Jordan, B., Jordan, W. P., Kauffmann, G., Kazin, E. A., Kirkby, D., Klaene, M. A., Kneib, J.-P., Le Goff, J.-M., Lee, K.-G., Long, D. C., Loomis, C. P., Lundgren, B., Lupton, R. H., Maia, M. A. G., Makler, M., Malanushenko, E., Malanushenko, V., Mandelbaum, R., Manera, M., Maraston, C., Margala, D., Masters, K. L., McBride, C. K., McDonald, P., McGreer, I. D., McMahon, R. G., Mena, O., Miralda-Escudé, J., Montero-Dorta, A. D., Montesano, F., Muna, D., Myers, A. D., Naugle, T., Nichol, R. C., Noterdaeme, P., Nuza, S. E., Olmstead, M. D., Oravetz, A., Oravetz, D. J., Owen, R., Padmanabhan, N., Palanque-Delabrouille, N., Pan, K., Parejko, J. K., Pâris, I., Percival, W. J., Pérez-Fournon, I., Pérez-Ràfols, I., Petitjean, P., Pfaffenberger, R., Pforr, J., Pieri, M. M., Prada, F., Price-Whelan, A. M., Raddick, M. J., Rebolo, R., Rich, J., Richards, G. T., Rockosi, C. M., Roe, N. A., Ross, A. J., Ross, N. P., Rossi, G., Rubiño-Martin, J. A., Samushia, L., Sánchez, A. G., Sayres, C., Schmidt, S. J., Schneider, D. P., Scóccola, C. G., Seo, H.-J., Shelden, A., Sheldon, E., Shen, Y., Shu, Y., Slosar, A., Smee, S. A., Snedden, S. A., Stauffer, F., Steele, O., Strauss, M. A., Streblyanska, A., Suzuki, N., Swanson, M. E. C., Tal, T., Tanaka, M., Thomas, D., Tinker, J. L., Tojeiro, R., Tremonti, C. A., Vargas Magaña, M., Verde, L., Viel, M., Wake, D. A., Watson, M., Weaver, B. A., Weinberg, D. H., Weiner, B. J., West, A. A., White, M., Wood-Vasey, W. M., Yeche, C., Zehavi, I., Zhao, G.-B., and Zheng, Z. (2013). The Baryon Oscillation Spectroscopic Survey of SDSS-III. *AJ*, 145:10.

de la Torre, S., Guzzo, L., Peacock, J. A., Branchini, E., Iovino, A., Granett, B. R., Abbas, U., Adami, C., Arnouts, S., Bel, J., and et al. (2013). The vimos public extragalactic redshift survey (vipers). *Astronomy & Astrophysics*, 557:A54.

de Mattia, A., Ruhlmann-Kleider, V., Raichoor, A., Ross, A. J., Tamone, A., Zhao, C., Alam, S., Avila, S., Burtin, E., Bautista, J., Beutler, F., Brinkmann, J., Brownstein, J. R., Chapman, M. J., Chuang, C.-H., Comparat, J., du Mas des Bourboux, H., Dawson, K. S., de la Macorra, A., Gil-Marín, H., Gonzalez-Perez, V., Gorgoni, C., Hou, J., Kong, H., Lin, S., Nadathur, S., Newman, J. A., Mueller, E.-M., Percival, W. J., Rezaie, M., Rossi, G., Schneider, D. P., Tiwari, P., Vivek, M., Wang, Y., and Zhao, G.-B. (2021). The completed SDSS-IV extended Baryon Oscillation Spectroscopic Survey: measurement of the BAO and growth rate of structure of the emission line galaxy sample from the anisotropic power spectrum between redshift 0.6 and 1.1. *MNRAS*, 501(4):5616–5645.

DESI Collaboration, Aghamousa, A., Aguilar, J., Ahlen, S., Alam, S., Allen, L. E., Allende Prieto, C., Annis, J., Bailey, S., Balland, C., Ballester, O., Baltay, C., Beaufore, L., Bebek, C., Beers, T. C., Bell, E. F., Bernal, J. L., Besuner, R., Beutler, F., Blake, C., Bleuler, H., Blomqvist, M., Blum, R., Bolton, A. S., Briceno, C., Brooks, D., Brownstein, J. R., Buckley-Geer, E., Burden, A., Burtin, E., Busca, N. G., Cahn, R. N., Cai, Y.-C., Cardiel-Sas, L., Carlberg, R. G., Carton, P.-H., Casas, R., Castander, F. J., Cervantes-Cota, J. L., Claybaugh, T. M., Close, M., Coker, C. T., Cole, S., Comparat, J., Cooper, A. P., Cousinou, M. C., Crocce, M., Cuby, J.-G., Cunningham, D. P., Davis, T. M., Dawson, K. S., de la Macorra, A., De Vicente, J., Delubac, T., Derwent, M., Dey, A., Dhungana, G., Ding, Z., Doel, P., Duan, Y. T., Ealet, A., Edelstein, J., Eftekharzadeh, S., Eisenstein, D. J., Elliott, A., Escoffier, S., Evatt, M., Fagrelius, P., Fan, X., Fanning, K., Farahi, A., Farihi, J., Favole, G., Feng, Y., Fernandez, E., Findlay, J. R., Finkbeiner, D. P., Fitzpatrick, M. J., Flaugher, B., Flender, S., Font-Ribera, A., Forero-Romero, J. E., Fosalba, P., Frenk, C. S., Fumagalli, M., Gaensicke, B. T., Gallo, G., Garcia-Bellido, J., Gaztanaga, E., Pietro Gentile Fusillo, N., Gerard, T., Gershkovich, I., Giannantonio, T., Gillet, D., Gonzalez-de-Rivera, G., Gonzalez-Perez, V., Gott, S., Graur, O., Gutierrez, G., Guy, J., Habib, S., Heetderks, H., Heetderks, I., Heitmann, K., Hellwing, W. A., Herrera, D. A., Ho, S., Holland, S., Honscheid, K., Huff, E., Hutchinson, T. A., Huterer, D., Hwang, H. S., Illa Laguna, J. M., Ishikawa, Y., Jacobs, D., Jeffrey, N., Jelinsky, P., Jennings, E., Jiang, L., Jimenez, J., Johnson, J., Joyce, R., Jullo, E., Juneau, S., Kama, S., Karcher, A., Karkar, S., Kehoe, R., Kennamer, N., Kent, S., Kilbinger, M., Kim, A. G., Kirkby, D., Kisner, T., Kitanidis, E., Kneib, J.-P., Koposov, S., Kovacs, E., Koyama, K., Kremin, A., Kron, R., Kronig, L., Kueter-Young, A., Lacey, C. G., Lafever, R., Lahav, O., Lambert, A., Lampton, M., Landriau, M., Lang, D., Lauer, T. R., Le Goff, J.-M., Le Guillou, L., Le Van Suu, A., Lee, J. H., Lee, S.-J., Leitner, D., Lesser, M., Levi, M. E., L'Huillier, B., Li, B., Liang, M., Lin, H., Linder, E., Loebman, S. R., Lukić, Z., Ma, J., MacCrann, N., Magneville, C., Makarem, L., Manera, M., Manser, C. J., Marshall, R., Martini, P., Massey, R., Matheson, T.,

McCauley, J., McDonald, P., McGreer, I. D., Meisner, A., Metcalfe, N., Miller, T. N., Miquel, R., Moustakas, J., Myers, A., Naik, M., Newman, J. A., Nichol, R. C., Nicola, A., Nicolati da Costa, L., Nie, J., Niz, G., Norberg, P., Nord, B., Norman, D., Nugent, P., O'Brien, T., Oh, M., Olsen, K. A. G., Padilla, C., Padmanabhan, H., Padmanabhan, N., Palanque-Delabrouille, N., Palmese, A., Pappalardo, D., Pâris, I., Park, C., Patej, A., Peacock, J. A., Peiris, H. V., Peng, X., Percival, W. J., Perruchot, S., Pieri, M. M., Pogge, R., Pollack, J. E., Poppett, C., Prada, F., Prakash, A., Probst, R. G., Rabinowitz, D., Raichoor, A., Ree, C. H., Refregier, A., Regal, X., Reid, B., Reil, K., Rezaie, M., Rockosi, C. M., Roe, N., Ronayette, S., Roodman, A., Ross, A. J., Ross, N. P., Rossi, G., Rozo, E., Ruhlmann-Kleider, V., Rykoff, E. S., Sabiu, C., Samushia, L., Sanchez, E., Sanchez, J., Schlegel, D. J., Schneider, M., Schubnell, M., Secroun, A., Seljak, U., Seo, H.-J., Serrano, S., Shafieloo, A., Shan, H., Sharples, R., Sholl, M. J., Shourt, W. V., Silber, J. H., Silva, D. R., Sirk, M. M., Slosar, A., Smith, A., Smoot, G. F., Som, D., Song, Y.-S., Sprayberry, D., Staten, R., Stefanik, A., Tarle, G., Sien Tie, S., Tinker, J. L., Tojeiro, R., Valdes, F., Valenzuela, O., Valluri, M., Vargas-Magana, M., Verde, L., Walker, A. R., Wang, J., Wang, Y., Weaver, B. A., Weaverdyck, C., Wechsler, R. H., Weinberg, D. H., White, M., Yang, Q., Yeche, C., Zhang, T., Zhao, G.-B., Zheng, Y., Zhou, X., Zhou, Z., Zhu, Y., Zou, H., and Zu, Y. (2016a). The DESI Experiment Part I: Science,Targeting, and Survey Design. *arXiv e-prints*, page arXiv:1611.00036.

DESI Collaboration, Aghamousa, A., Aguilar, J., Ahlen, S., Alam, S., Allen, L. E., Allende Prieto, C., Annis, J., Bailey, S., Balland, C., Ballester, O., Baltay, C., Beaufore, L., Bebek, C., Beers, T. C., Bell, E. F., Bernal, J. L., Besuner, R., Beutler, F., Blake, C., Bleuler, H., Blomqvist, M., Blum, R., Bolton, A. S., Briceno, C., Brooks, D., Brownstein, J. R., Buckley-Geer, E., Burden, A., Burtin, E., Busca, N. G., Cahn, R. N., Cai, Y.-C., Cardiel-Sas, L., Carlberg, R. G., Carton, P.-H., Casas, R., Castander, F. J., Cervantes-Cota, J. L., Claybaugh, T. M., Close, M., Coker, C. T., Cole, S., Comparat, J., Cooper, A. P., Cousinou, M. C., Crocce, M., Cuby, J.-G., Cunningham, D. P., Davis, T. M., Dawson, K. S., de la Macorra, A., De Vicente, J., Delubac, T., Derwent, M., Dey, A., Dhungana, G., Ding, Z., Doel, P., Duan, Y. T., Ealet, A., Edelstein, J., Eftekharzadeh, S., Eisenstein, D. J., Elliott, A., Escoffier, S., Evatt, M., Fagrelius, P., Fan, X., Fanning, K., Farahi, A., Farihi, J., Favole, G., Feng, Y., Fernandez, E., Findlay, J. R., Finkbeiner, D. P., Fitzpatrick, M. J., Flaugher, B., Flender, S., Font-Ribera, A., Forero-Romero, J. E., Fosalba, P., Frenk, C. S., Fumagalli, M., Gaensicke, B. T., Gallo, G., Garcia-Bellido, J., Gaztanaga, E., Pietro Gentile Fusillo, N., Gerard, T., Gershkovich, I., Giannantonio, T., Gillet, D., Gonzalez-de-Rivera, G., Gonzalez-Perez, V., Gott, S., Graur, O., Gutierrez, G., Guy, J., Habib, S., Heetderks, H., Heetderks, I., Heitmann, K., Hellwing, W. A., Herrera, D. A., Ho, S., Holland, S., Honscheid, K., Huff, E., Hutchin-

son, T. A., Huterer, D., Hwang, H. S., Illa Laguna, J. M., Ishikawa, Y., Jacobs, D., Jeffrey, N., Jelinsky, P., Jennings, E., Jiang, L., Jimenez, J., Johnson, J., Joyce, R., Jullo, E., Juneau, S., Kama, S., Karcher, A., Karkar, S., Kehoe, R., Kennamer, N., Kent, S., Kilbinger, M., Kim, A. G., Kirkby, D., Kisner, T., Kitanidis, E., Kneib, J.-P., Koposov, S., Kovacs, E., Koyama, K., Kremin, A., Kron, R., Kronig, L., Kueter-Young, A., Lacey, C. G., Lafever, R., Lahav, O., Lambert, A., Lampton, M., Landriau, M., Lang, D., Lauer, T. R., Le Goff, J.-M., Le Guillou, L., Le Van Suu, A., Lee, J. H., Lee, S.-J., Leitner, D., Lesser, M., Levi, M. E., L'Huillier, B., Li, B., Liang, M., Lin, H., Linder, E., Loebman, S. R., Lukić, Z., Ma, J., MacCrann, N., Magneville, C., Makarem, L., Manera, M., Manser, C. J., Marshall, R., Martini, P., Massey, R., Matheson, T., McCauley, J., McDonald, P., McGreer, I. D., Meisner, A., Metcalfe, N., Miller, T. N., Miquel, R., Moustakas, J., Myers, A., Naik, M., Newman, J. A., Nichol, R. C., Nicola, A., Nicolati da Costa, L., Nie, J., Niz, G., Norberg, P., Nord, B., Norman, D., Nugent, P., O'Brien, T., Oh, M., Olsen, K. A. G., Padilla, C., Padmanabhan, H., Padmanabhan, N., Palanque-Delabrouille, N., Palmese, A., Pappalardo, D., Pâris, I., Park, C., Patej, A., Peacock, J. A., Peiris, H. V., Peng, X., Percival, W. J., Perruchot, S., Pieri, M. M., Pogge, R., Pollack, J. E., Poppett, C., Prada, F., Prakash, A., Probst, R. G., Rabinowitz, D., Raichoor, A., Ree, C. H., Refregier, A., Regal, X., Reid, B., Reil, K., Rezaie, M., Rockosi, C. M., Roe, N., Ronayette, S., Roodman, A., Ross, A. J., Ross, N. P., Rossi, G., Rozo, E., Ruhlmann-Kleider, V., Rykoff, E. S., Sabiu, C., Samushia, L., Sanchez, E., Sanchez, J., Schlegel, D. J., Schneider, M., Schubnell, M., Secroun, A., Seljak, U., Seo, H.-J., Serrano, S., Shafieloo, A., Shan, H., Sharples, R., Sholl, M. J., Shourt, W. V., Silber, J. H., Silva, D. R., Sirk, M. M., Slosar, A., Smith, A., Smoot, G. F., Som, D., Song, Y.-S., Sprayberry, D., Staten, R., Stefanik, A., Tarle, G., Sien Tie, S., Tinker, J. L., Tojeiro, R., Valdes, F., Valenzuela, O., Valluri, M., Vargas-Magana, M., Verde, L., Walker, A. R., Wang, J., Wang, Y., Weaver, B. A., Weaverdyck, C., Wechsler, R. H., Weinberg, D. H., White, M., Yang, Q., Yeche, C., Zhang, T., Zhao, G.-B., Zheng, Y., Zhou, X., Zhou, Z., Zhu, Y., Zou, H., and Zu, Y. (2016b). The DESI Experiment Part II: Instrument Design. *arXiv e-prints*, page arXiv:1611.00037.

Di Valentino, E., Mena, O., Pan, S., Visinelli, L., Yang, W., Melchiorri, A., Mota, D. F., Riess, A. G., and Silk, J. (2021). In the Realm of the Hubble tension − a Review of Solutions. *arXiv e-prints*, page arXiv:2103.01183.

Dodelson, S. (2003). *Modern Cosmology*.

Drinkwater, M. J., Jurek, R. J., Blake, C., Woods, D., Pimbblet, K. A., Glazebrook, K., Sharp, R., Pracy, M. B., Brough, S., Colless, M., Couch, W. J., Croom, S. M., Davis, T. M., Forbes, D., Forster, K., Gilbank, D. G., Gladders, M., Jelliffe, B., Jones, N., Li,

I. H., Madore, B., Martin, D. C., Poole, G. B., Small, T., Wisnioski, E., Wyder, T., and Yee, H. K. C. (2010). The WiggleZ Dark Energy Survey: survey design and first data release. *MNRAS*, 401(3):1429–1452.

Einasto, J., Kaasik, A., and Saar, E. (1974). Dynamic evidence on massive coronas of galaxies. *Nature*, 250(5464):309–310.

Einstein, A. (1916). Die Grundlage der allgemeinen Relativitätstheorie. *Annalen der Physik*, 354(7):769–822.

Eisenstein, D. J., Seo, H.-J., Sirko, E., and Spergel, D. N. (2007). Improving Cosmological Distance Measurements by Reconstruction of the Baryon Acoustic Peak. *ApJ*, 664(2):675–679.

Eisenstein, D. J., Weinberg, D. H., Agol, E., Aihara, H., Allende Prieto, C., Anderson, S. F., Arns, J. A., Aubourg, É., Bailey, S., Balbinot, E., Barkhouser, R., Beers, T. C., Berlind, A. A., Bickerton, S. J., Bizyaev, D., Blanton, M. R., Bochanski, J. J., Bolton, A. S., Bosman, C. T., Bovy, J., Brandt, W. N., Breslauer, B., Brewington, H. J., Brinkmann, J., Brown, P. J., Brownstein, J. R., Burger, D., Busca, N. G., Campbell, H., Cargile, P. A., Carithers, W. C., Carlberg, J. K., Carr, M. A., Chang, L., Chen, Y., Chiappini, C., Comparat, J., Connolly, N., Cortes, M., Croft, R. A. C., Cunha, K., da Costa, L. N., Davenport, J. R. A., Dawson, K., De Lee, N., Porto de Mello, G. F., de Simoni, F., Dean, J., Dhital, S., Ealet, A., Ebelke, G. L., Edmondson, E. M., Eiting, J. M., Escoffier, S., Esposito, M., Evans, M. L., Fan, X., Femenía Castellá, B., Dutra Ferreira, L., Fitzgerald, G., Fleming, S. W., Font-Ribera, A., Ford, E. B., Frinchaboy, P. M., García Pérez, A. E., Gaudi, B. S., Ge, J., Ghezzi, L., Gillespie, B. A., Gilmore, G., Girardi, L., Gott, J. R., Gould, A., Grebel, E. K., Gunn, J. E., Hamilton, J.-C., Harding, P., Harris, D. W., Hawley, S. L., Hearty, F. R., Hennawi, J. F., González Hernández, J. I., Ho, S., Hogg, D. W., Holtzman, J. A., Honscheid, K., Inada, N., Ivans, I. I., Jiang, L., Jiang, P., Johnson, J. A., Jordan, C., Jordan, W. P., Kauffmann, G., Kazin, E., Kirkby, D., Klaene, M. A., Knapp, G. R., Kneib, J.-P., Kochanek, C. S., Koesterke, L., Kollmeier, J. A., Kron, R. G., Lampeitl, H., Lang, D., Lawler, J. E., Le Goff, J.-M., Lee, B. L., Lee, Y. S., Leisenring, J. M., Lin, Y.-T., Liu, J., Long, D. C., Loomis, C. P., Lucatello, S., Lundgren, B., Lupton, R. H., Ma, B., Ma, Z., MacDonald, N., Mack, C., Mahadevan, S., Maia, M. A. G., Majewski, S. R., Makler, M., Malanushenko, E., Malanushenko, V., Mandelbaum, R., Maraston, C., Margala, D., Maseman, P., Masters, K. L., McBride, C. K., McDonald, P., McGreer, I. D., McMahon, R. G., Mena Requejo, O., Ménard, B., Miralda-Escudé, J., Morrison, H. L., Mullally, F., Muna, D., Murayama, H., Myers, A. D., Naugle, T., Neto, A. F., Nguyen, D. C., Nichol, R. C., Nidever, D. L.,

O'Connell, R. W., Ogando, R. L. C., Olmstead, M. D., Oravetz, D. J., Padmanabhan, N., Paegert, M., Palanque-Delabrouille, N., Pan, K., Pandey, P., Parejko, J. K., Pâris, I., Pellegrini, P., Pepper, J., Percival, W. J., Petitjean, P., Pfaffenberger, R., Pforr, J., Phleps, S., Pichon, C., Pieri, M. M., Prada, F., Price-Whelan, A. M., Raddick, M. J., Ramos, B. H. F., Reid, I. N., Reyle, C., Rich, J., Richards, G. T., Rieke, G. H., Rieke, M. J., Rix, H.-W., Robin, A. C., Rocha-Pinto, H. J., Rockosi, C. M., Roe, N. A., Rollinde, E., Ross, A. J., Ross, N. P., Rossetto, B., Sánchez, A. G., Santiago, B., Sayres, C., Schiavon, R., Schlegel, D. J., Schlesinger, K. J., Schmidt, S. J., Schneider, D. P., Sellgren, K., Shelden, A., Sheldon, E., Shetrone, M., Shu, Y., Silverman, J. D., Simmerer, J., Simmons, A. E., Sivarani, T., Skrutskie, M. F., Slosar, A., Smee, S., Smith, V. V., Snedden, S. A., Stassun, K. G., Steele, O., Steinmetz, M., Stockett, M. H., Stollberg, T., Strauss, M. A., Szalay, A. S., Tanaka, M., Thakar, A. R., Thomas, D., Tinker, J. L., Tofflemire, B. M., Tojeiro, R., Tremonti, C. A., Vargas Magaña, M., Verde, L., Vogt, N. P., Wake, D. A., Wan, X., Wang, J., Weaver, B. A., White, M., White, S. D. M., Wilson, J. C., Wisniewski, J. P., Wood-Vasey, W. M., Yanny, B., Yasuda, N., Yèche, C., York, D. G., Young, E., Zasowski, G., Zehavi, I., and Zhao, B. (2011). SDSS-III: Massive Spectroscopic Surveys of the Distant Universe, the Milky Way, and Extra-Solar Planetary Systems. *AJ*, 142(3):72.

Eisenstein, D. J., Zehavi, I., Hogg, D. W., Scoccimarro, R., Blanton, M. R., Nichol, R. C., Scranton, R., Seo, H.-J., Tegmark, M., Zheng, Z., Anderson, S. F., Annis, J., Bahcall, N., Brinkmann, J., Burles, S., Castander, F. J., Connolly, A., Csabai, I., Doi, M., Fukugita, M., Frieman, J. A., Glazebrook, K., Gunn, J. E., Hendry, J. S., Hennessy, G., Ivezić, Z., Kent, S., Knapp, G. R., Lin, H., Loh, Y.-S., Lupton, R. H., Margon, B., McKay, T. A., Meiksin, A., Munn, J. A., Pope, A., Richmond, M. W., Schlegel, D., Schneider, D. P., Shimasaku, K., Stoughton, C., Strauss, M. A., SubbaRao, M., Szalay, A. S., Szapudi, I., Tucker, D. L., Yanny, B., and York, D. G. (2005). Detection of the Baryon Acoustic Peak in the Large-Scale Correlation Function of SDSS Luminous Red Galaxies. *ApJ*, 633(2):560–574.

El-Ad, H. and Piran, T. (1997). Voids in the Large-Scale Structure. *ApJ*, 491(2):421–435.

Falck, B., Koyama, K., Zhao, G.-B., and Cautun, M. (2017). Using voids to unscreen modified gravity. *Monthly Notices of the Royal Astronomical Society*, 475(3):3262–3272.

Friedmann, A. (1922). Über die Krümmung des Raumes. *Zeitschrift fur Physik*, 10:377–386.

Geller, M. J. and Huchra, J. P. (1983). Groups of galaxies. III. THe CfA survey. *ApJS*, 52:61–87.

Gil-Marín, H., Bautista, J. E., Paviot, R., Vargas-Magaña, M., de la Torre, S., Fromenteau, S., Alam, S., Ávila, S., Burtin, E., Chuang, C.-H., Dawson, K. S., Hou, J., de Mattia, A., Mohammad, F. G., Müller, E.-M., Nadathur, S., Neveux, R., Percival, W. J., Raichoor, A., Rezaie, M., Ross, A. J., Rossi, G., Ruhlmann-Kleider, V., Smith, A., Tamone, A., Tinker, J. L., Tojeiro, R., Wang, Y., Zhao, G.-B., Zhao, C., Brinkmann, J., Brownstein, J. R., Choi, P. D., Escoffier, S., de la Macorra, A., Moon, J., Newman, J. A., Schneider, D. P., Seo, H.-J., and Vivek, M. (2020). The Completed SDSS-IV extended Baryon Oscillation Spectroscopic Survey: measurement of the BAO and growth rate of structure of the luminous red galaxy sample from the anisotropic power spectrum between redshifts 0.6 and 1.0. *MNRAS*, 498(2):2492–2531.

Gunn, J. E., Siegmund, W. A., Mannery, E. J., Owen, R. E., Hull, C. L., Leger, R. F., Carey, L. N., Knapp, G. R., York, D. G., Boroski, W. N., Kent, S. M., Lupton, R. H., Rockosi, C. M., Evans, M. L., Waddell, P., Anderson, J. E., Annis, J., Barentine, J. C., Bartoszek, L. M., Bastian, S., Bracker, S. B., Brewington, H. J., Briegel, C. I., Brinkmann, J., Brown, Y. J., Carr, M. A., Czarapata, P. C., Drennan, C. C., Dombeck, T., Federwitz, G. R., Gillespie, B. A., Gonzales, C., Hansen, S. U., Harvanek, M., Hayes, J., Jordan, W., Kinney, E., Klaene, M., Kleinman, S. J., Kron, R. G., Kresinski, J., Lee, G., Limmongkol, S., Lindenmeyer, C. W., Long, D. C., Loomis, C. L., McGehee, P. M., Mantsch, P. M., Neilsen, Eric H., J., Neswold, R. M., Newman, P. R., Nitta, A., Peoples, John, J., Pier, J. R., Prieto, P. S., Prosapio, A., Rivetta, C., Schneider, D. P., Snedden, S., and Wang, S.-i. (2006). The 2.5 m Telescope of the Sloan Digital Sky Survey. *AJ*, 131(4):2332–2359.

Guth, A. H. (1981). Inflationary universe: A possible solution to the horizon and flatness problems. *Phys. Ref. D*, 23(2):347–356.

Hamana, T., Shirasaki, M., Miyazaki, S., Hikage, C., Oguri, M., More, S., Armstrong, R., Leauthaud, A., Mandelbaum, R., Miyatake, H., Nishizawa, A. J., Simet, M., Takada, M., Aihara, H., Bosch, J., Komiyama, Y., Lupton, R., Murayama, H., Strauss, M. A., and Tanaka, M. (2020). Cosmological constraints from cosmic shear two-point correlation functions with HSC survey first-year data. *PASJ*, 72(1):16.

Hamaus, N., Aubert, M., Pisani, A., Contarini, S., Verza, G., Cousinou, M. C., Escoffier, S., Hawken, A., Lavaux, G., Pollina, G., Wandelt, B. D., Weller, J., Bonici, M., Carbone, C., Guzzo, L., Kovacs, A., Marulli, F., Massara, E., Moscardini, L., Ntelis, P., Percival, W. J., Radinović, S., Sahlén, M., Sakr, Z., Sánchez, A. G., Winther, H. A., Auricchio, N., Awan, S., Bender, R., Bodendorf, C., Bonino, D., Branchini, E., Brescia, M., Brinchmann, J., Capobianco, V., Carretero, J., Castander, F. J., Castellano, M., Cavuoti, S.,

Cimatti, A., Cledassou, R., Congedo, G., Conversi, L., Copin, Y., Corcione, L., Cropper, M., Da Silva, A., Degaudenzi, H., Douspis, M., Dubath, F., Duncan, C. A. J., Dupac, X., Dusini, S., Ealet, A., Ferriol, S., Fosalba, P., Frailis, M., Franceschi, E., Franzetti, P., Fumana, M., Garilli, B., Gillis, B., Giocoli, C., Grazian, A., Grupp, F., Haugan, S. V. H., Holmes, W., Hormuth, F., Jahnke, K., Kermiche, S., Kiessling, A., Kilbinger, M., Kitching, T., Kümmel, M., Kunz, M., Kurki-Suonio, H., Ligori, S., Lilje, P. B., Lloro, I., Maiorano, E., Marggraf, O., Markovic, K., Massey, R., Maurogordato, S., Melchior, M., Meneghetti, M., Meylan, G., Moresco, M., Munari, E., Niemi, S. M., Padilla, C., Paltani, S., Pasian, F., Pedersen, K., Pettorino, V., Pires, S., Poncet, M., Popa, L., Pozzetti, L., Rebolo, R., Rhodes, J., Rix, H., Roncarelli, M., Rossetti, E., Saglia, R., Schneider, P., Secroun, A., Seidel, G., Serrano, S., Sirignano, C., Sirri, G., Starck, J. L., Tallada-Crespí, P., Tavagnacco, D., Taylor, A. N., Tereno, I., Toledo-Moreo, R., Torradeflot, F., Valentijn, E. A., Valenziano, L., Wang, Y., Welikala, N., Zamorani, G., Zoubian, J., Andreon, S., Baldi, M., Camera, S., Mei, S., Neissner, C., and Romelli, E. (2022). Euclid: Forecasts from redshift-space distortions and the Alcock-Paczynski test with cosmic voids. *A&A*, 658:A20.

Hamaus, N., Cousinou, M.-C., Pisani, A., Aubert, M., Escoffier, S., and Weller, J. (2017). Multipole analysis of redshift-space distortions around cosmic voids. *J. Cosmology Astropart. Phys.*, 7:014.

Hamaus, N., Pisani, A., Choi, J.-A., Lavaux, G., Wandelt, B. D., and Weller, J. (2020). Precision cosmology with voids in the final boss data. *Journal of Cosmology and Astroparticle Physics*, 2020(12):023–023.

Hamaus, N., Pisani, A., Sutter, P. M., Lavaux, G., Escoffier, S., Wandelt, B. D., and Weller, J. (2016). Constraints on Cosmology and Gravity from the Dynamics of Voids. *Physical Review Letters*, 117(9):091302.

Hamaus, N., Sutter, P. M., Lavaux, G., and Wandelt, B. D. (2015). Probing cosmology and gravity with redshift-space distortions around voids. *J. Cosmology Astropart. Phys.*, 2015(11):036–036.

Hamaus, N., Sutter, P. M., and Wandelt, B. D. (2014). Universal Density Profile for Cosmic Voids. *Phys. Review Letter*, 112(25):251302.

Hamilton, A. J. S. (1993). Toward Better Ways to Measure the Galaxy Correlation Function. *ApJ*, 417:19.

Hamilton, A. J. S. (2005). Power Spectrum Estimation I. Basics. *arXiv e-prints*, pages astro–ph/0503603.

Hawken, A. J., Aubert, M., Pisani, A., Cousinou, M.-C., Escoffier, S., Nadathur, S., Rossi, G., and Schneider, D. P. (2020). Constraints on the growth of structure around cosmic voids in eBOSS DR14. *J. Cosmology Astropart. Phys.*, 2020(6):012.

Hawken, A. J., Granett, B. R., Iovino, A., Guzzo, L., Peacock, J. A., de la Torre, S., Garilli, B., Bolzonella, M., Scodeggio, M., Abbas, U., Adami, C., Bottini, D., Cappi, A., Cucciati, O., Davidzon, I., Fritz, A., Franzetti, P., Krywult, J., Le Brun, V., Le Fèvre, O., Maccagni, D., Małek, K., Marulli, F., Polletta, M., Pollo, A., Tasca, L. A. M., Tojeiro, R., Vergani, D., Zanichelli, A., Arnouts, S., Bel, J., Branchini, E., De Lucia, G., Ilbert, O., Moscardini, L., and Percival, W. J. (2017). The VIMOS Public Extragalactic Redshift Survey. Measuring the growth rate of structure around cosmic voids. *A&A*, 607:A54.

Heitmann, K., Finkel, H., Pope, A., Morozov, V., Frontiere, N., Habib, S., Rangel, E., Uram, T., Korytov, D., Child, H., Flender, S., Insley, J., and Rizzi, S. (2019). The Outer Rim Simulation: A Path to Many-core Supercomputers. *ApJS*, 245(1):16.

Heymans, C., Tröster, T., Asgari, M., Blake, C., Hildebrandt, H., Joachimi, B., Kuijken, K., Lin, C.-A., Sánchez, A. G., van den Busch, J. L., Wright, A. H., Amon, A., Bilicki, M., de Jong, J., Crocce, M., Dvornik, A., Erben, T., Fortuna, M. C., Getman, F., Giblin, B., Glazebrook, K., Hoekstra, H., Joudaki, S., Kannawadi, A., Köhlinger, F., Lidman, C., Miller, L., Napolitano, N. R., Parkinson, D., Schneider, P., Shan, H., Valentijn, E. A., Verdoes Kleijn, G., and Wolf, C. (2021). KiDS-1000 Cosmology: Multi-probe weak gravitational lensing and spectroscopic galaxy clustering constraints. *A&A*, 646:A140.

Howlett, C., Manera, M., and Percival, W. J. (2015a). L-PICOLA: A parallel code for fast dark matter simulation. *Astronomy and Computing*, 12:109–126.

Howlett, C., Ross, A. J., Samushia, L., Percival, W. J., and Manera, M. (2015b). The clustering of the SDSS main galaxy sample - II. Mock galaxy catalogues and a measurement of the growth of structure from redshift space distortions at z = 0.15. *MNRAS*, 449(1):848–866.

Hoyle, F. and Vogeley, M. S. (2002). Voids in the Point Source Catalogue Survey and the Updated Zwicky Catalog. *ApJ*, 566(2):641–651.

Hubble, E. (1929). A Relation between Distance and Radial Velocity among Extra-Galactic Nebulae. *Proceedings of the National Academy of Science*, 15(3):168–173.

Huterer, D. and Turner, M. S. (2001). Probing dark energy: Methods and strategies. *Physical Review D*, 64(12):123527.

Jones, A. and Lasenby, A. (1998). The Cosmic Microwave Background. *Living Reviews in Relativity*, 1(1):11.

Kaiser, N. (1987). Clustering in real space and in redshift space. *MNRAS*, 227:1–21.

Kerscher, M., Szapudi, I., and Szalay, A. S. (2000). A Comparison of Estimators for the Two-Point Correlation Function. *ApJ*, 535(1):L13–L16.

Kitaura, F.-S. and Heß, S. (2013). Cosmological structure formation with augmented Lagrangian perturbation theory. *MNRAS*, 435:L78–L82.

Kitaura, F.-S., Rodríguez-Torres, S., Chuang, C.-H., Zhao, C., Prada, F., Gil-Marín, H., Guo, H., Yepes, G., Klypin, A., Scóccola, C. G., Tinker, J., McBride, C., Reid, B., Sánchez, A. G., Salazar-Albornoz, S., Grieb, J. N., Vargas-Magana, M., Cuesta, A. J., Neyrinck, M., Beutler, F., Comparat, J., Percival, W. J., and Ross, A. (2016). The clustering of galaxies in the SDSS-III Baryon Oscillation Spectroscopic Survey: mock galaxy catalogues for the BOSS Final Data Release. *MNRAS*, 456(4):4156–4173.

Kitaura, F. S., Yepes, G., and Prada, F. (2014). Modelling baryon acoustic oscillations with perturbation theory and stochastic halo biasing. *MNRAS*, 439:L21–L25.

Klypin, A., Yepes, G., Gottlöber, S., Prada, F., and Heß, S. (2016). MultiDark simulations: the story of dark matter halo concentrations and density profiles. *MNRAS*, 457(4):4340–4359.

Knox, L. and Millea, M. (2020). Hubble constant hunter's guide. *Phys. Ref. D*, 101(4):043533.

Kobayashi, Y., Nishimichi, T., Takada, M., and Miyatake, H. (2022). Full-shape cosmology analysis of the SDSS-III BOSS galaxy power spectrum using an emulator-based halo model: A 5% determination of σ_8. *Phys. Ref. D*, 105(8):083517.

Kreisch, C. D., Pisani, A., Villaescusa-Navarro, F., Spergel, D. N., Wandelt, B. D., Hamaus, N., and Bayer, A. E. (2022). The GIGANTES Data Set: Precision Cosmology from Voids in the Machine-learning Era. *ApJ*, 935(2):100.

Landy, S. D. and Szalay, A. S. (1993). Bias and variance of angular correlation functions. *ApJ*, 412:64–71.

Laureijs, R., Amiaux, J., Arduini, S., Augueres, J. L., Brinchmann, J., Cole, R., Cropper, M., Dabin, C., Duvet, L., Ealet, A., Garilli, B., Gondoin, P., Guzzo, L., Hoar, J.,

Hoekstra, H., Holmes, R., Kitching, T., Maciaszek, T., Mellier, Y., Pasian, F., Percival, W., Rhodes, J., Saavedra Criado, G., Sauvage, M., Scaramella, R., Valenziano, L., Warren, S., Bender, R., Castander, F., Cimatti, A., Le Fèvre, O., Kurki-Suonio, H., Levi, M., Lilje, P., Meylan, G., Nichol, R., Pedersen, K., Popa, V., Rebolo Lopez, R., Rix, H. W., Rottgering, H., Zeilinger, W., Grupp, F., Hudelot, P., Massey, R., Meneghetti, M., Miller, L., Paltani, S., Paulin-Henriksson, S., Pires, S., Saxton, C., Schrabback, T., Seidel, G., Walsh, J., Aghanim, N., Amendola, L., Bartlett, J., Baccigalupi, C., Beaulieu, J. P., Benabed, K., Cuby, J. G., Elbaz, D., Fosalba, P., Gavazzi, G., Helmi, A., Hook, I., Irwin, M., Kneib, J. P., Kunz, M., Mannucci, F., Moscardini, L., Tao, C., Teyssier, R., Weller, J., Zamorani, G., Zapatero Osorio, M. R., Boulade, O., Foumond, J. J., Di Giorgio, A., Guttridge, P., James, A., Kemp, M., Martignac, J., Spencer, A., Walton, D., Blümchen, T., Bonoli, C., Bortoletto, F., Cerna, C., Corcione, L., Fabron, C., Jahnke, K., Ligori, S., Madrid, F., Martin, L., Morgante, G., Pamplona, T., Prieto, E., Riva, M., Toledo, R., Trifoglio, M., Zerbi, F., Abdalla, F., Douspis, M., Grenet, C., Borgani, S., Bouwens, R., Courbin, F., Delouis, J. M., Dubath, P., Fontana, A., Frailis, M., Grazian, A., Koppenhöfer, J., Mansutti, O., Melchior, M., Mignoli, M., Mohr, J., Neissner, C., Noddle, K., Poncet, M., Scodeggio, M., Serrano, S., Shane, N., Starck, J. L., Surace, C., Taylor, A., Verdoes-Kleijn, G., Vuerli, C., Williams, O. R., Zacchei, A., Altieri, B., Escudero Sanz, I., Kohley, R., Oosterbroek, T., Astier, P., Bacon, D., Bardelli, S., Baugh, C., Bellagamba, F., Benoist, C., Bianchi, D., Biviano, A., Branchini, E., Carbone, C., Cardone, V., Clements, D., Colombi, S., Conselice, C., Cresci, G., Deacon, N., Dunlop, J., Fedeli, C., Fontanot, F., Franzetti, P., Giocoli, C., Garcia-Bellido, J., Gow, J., Heavens, A., Hewett, P., Heymans, C., Holland, A., Huang, Z., Ilbert, O., Joachimi, B., Jennins, E., Kerins, E., Kiessling, A., Kirk, D., Kotak, R., Krause, O., Lahav, O., van Leeuwen, F., Lesgourgues, J., Lombardi, M., Magliocchetti, M., Maguire, K., Majerotto, E., Maoli, R., Marulli, F., Maurogordato, S., McCracken, H., McLure, R., Melchiorri, A., Merson, A., Moresco, M., Nonino, M., Norberg, P., Peacock, J., Pello, R., Penny, M., Pettorino, V., Di Porto, C., Pozzetti, L., Quercellini, C., Radovich, M., Rassat, A., Roche, N., Ronayette, S., Rossetti, E., Sartoris, B., Schneider, P., Semboloni, E., Serjeant, S., Simpson, F., Skordis, C., Smadja, G., Smartt, S., Spano, P., Spiro, S., Sullivan, M., Tilquin, A., Trotta, R., Verde, L., Wang, Y., Williger, G., Zhao, G., Zoubian, J., and Zucca, E. (2011). Euclid Definition Study Report. *arXiv e-prints*, page arXiv:1110.3193.

Lavaux, G. and Wandelt, B. D. (2012). Precision cosmography with stacked voids. *ApJ*, 754:109.

Lemaître, G. (1931). The expanding universe. *MNRAS*, 91:490–501.

Lesgourgues, J. (2011). The Cosmic Linear Anisotropy Solving System (CLASS) I: Overview. *arXiv:1104.2932*.

Lewis, A., Challinor, A., and Lasenby, A. (2000). Efficient Computation of Cosmic Microwave Background Anisotropies in Closed Friedmann-Robertson-Walker Models. *ApJ*, 538(2):473–476.

Li, B., Zhao, G., and Koyama, K. (2012). Haloes and voids in f(R) gravity. *Monthly Notices of the Royal Astronomical Society*, 421(4):3481–3487.

Malaney, R. A. and Mathews, G. J. (1993). Probing the early universe: a review of primordial nucleosynthesis beyond the standard big bang. *Phys. Reports*, 229(4):145–219.

Manera, M., Samushia, L., Tojeiro, R., Howlett, C., Ross, A. J., Percival, W. J., Gil-Marín, H., Brownstein, J. R., Burden, A., and Montesano, F. (2015). The clustering of galaxies in the SDSS-III Baryon Oscillation Spectroscopic Survey: mock galaxy catalogues for the low-redshift sample. *MNRAS*, 447(1):437–445.

Manera, M., Scoccimarro, R., Percival, W. J., Samushia, L., McBride, C. K., Ross, A. J., Sheth, R. K., White, M., Reid, B. A., Sánchez, A. G., de Putter, R., Xu, X., Berlind, A. A., Brinkmann, J., Maraston, C., Nichol, B., Montesano, F., Padmanabhan, N., Skibba, R. A., Tojeiro, R., and Weaver, B. A. (2013). The clustering of galaxies in the SDSS-III Baryon Oscillation Spectroscopic Survey: a large sample of mock galaxy catalogues. *MNRAS*, 428(2):1036–1054.

Massara, E., Percival, W. J., Dalal, N., Nadathur, S., Radinović, S., Winther, H. A., and Woodfinden, A. (2022). Velocity profiles of matter and biased tracers around voids. *MNRAS*, 517(3):4458.

Massara, E. and Sheth, R. K. (2018). Density and velocity profiles around cosmic voids. *arXiv e-prints*, page arXiv:1811.03132.

Mo, H., van den Bosch, F. C., and White, S. (2010). *Galaxy Formation and Evolution*.

Mo, H. J. and White, S. D. M. (1996). An analytic model for the spatial clustering of dark matter haloes. *MNRAS*, 282(2):347–361.

Mohammad, F. G. and Percival, W. J. (2022). Creating jackknife and bootstrap estimates of the covariance matrix for the two-point correlation function. *MNRAS*, 514(1):1289–1301.

Nadathur, S. (2016). Testing cosmology with a catalogue of voids in the BOSS galaxy surveys. *MNRAS*, 461:358–370.

Nadathur, S., Carter, P., and Percival, W. J. (2019a). A Zeldovich reconstruction method for measuring redshift space distortions using cosmic voids. *MNRAS*, 482:2459–2470.

Nadathur, S., Carter, P. M., Percival, W. J., Winther, H. A., and Bautista, J. E. (2019b). Beyond BAO: Improving cosmological constraints from BOSS data with measurement of the void-galaxy cross-correlation. *Phys. Ref. D*, 100(2):023504.

Nadathur, S. and Hotchkiss, S. (2014). A robust public catalogue of voids and superclusters in the SDSS Data Release 7 galaxy surveys. *MNRAS*, 440:1248–1262.

Nadathur, S. and Hotchkiss, S. (2015). The nature of voids - II. Tracing underdensities with biased galaxies. *MNRAS*, 454(1):889–901.

Nadathur, S., Hotchkiss, S., and Crittenden, R. (2017). Tracing the gravitational potential using cosmic voids. *MNRAS*, 467:4067–4079.

Nadathur, S. and Percival, W. J. (2019). An accurate linear model for redshift space distortions in the void-galaxy correlation function. *MNRAS*, 483:3472–3487.

Nadathur, S., Percival, W. J., Beutler, F., and Winther, H. A. (2020a). Testing Low-Redshift Cosmic Acceleration with Large-Scale Structure. *Phys. Review Letter*, 124(22):221301.

Nadathur, S., Woodfinden, A., Percival, W. J., Aubert, M., Bautista, J., Dawson, K., Escoffier, S., Fromenteau, S., Gil-Marín, H., Rich, J., Ross, A. J., Rossi, G., Magaña, M. V., Brownstein, J. R., and Schneider, D. P. (2020b). The completed SDSS-IV extended baryon oscillation spectroscopic survey: geometry and growth from the anisotropic void-galaxy correlation function in the luminous red galaxy sample. *MNRAS*, 499(3):4140–4157.

Neyrinck, M. C. (2008). ZOBOV: a parameter-free void-finding algorithm. *MNRAS*, 386:2101–2109.

Nusser, A. and Davis, M. (1994). On the prediction of velocity fields from redshift space galaxy samples. *ApJ*, 421:L1–L4.

Ostriker, J. P., Peebles, P. J. E., and Yahil, A. (1974). The Size and Mass of Galaxies, and the Mass of the Universe. *ApJ*, 193:L1.

Padilla, N. D., Ceccarelli, L., and Lambas, D. G. (2005). Spatial and dynamical properties of voids in a Λ cold dark matter universe. *MNRAS*, 363(3):977–990.

Padmanabhan, N. (2019). Dark Energy Faces Multiple Probes. *Physics Online Journal*, 12:48.

Paillas, E., Cai, Y.-C., Padilla, N., and Sánchez, A. G. (2021). Redshift-space distortions with split densities. *MNRAS*, 505(4):5731–5752.

Paillas, E., Cautun, M., Li, B., Cai, Y.-C., Padilla, N., Armijo, J., and Bose, S. (2019). The Santiago-Harvard-Edinburgh-Durham void comparison II: unveiling the Vainshtein screening using weak lensing. *MNRAS*, 484(1):1149–1165.

Paz, D., Lares, M., Ceccarelli, L., Padilla, N., and Lambas, D. G. (2013). Clues on void evolution-II. Measuring density and velocity profiles on SDSS galaxy redshift space distortions. *MNRAS*, 436:3480–3491.

Paz, D. J., Correa, C. M., Gualpa, S. R., Ruiz, A. N., Bederián, C. S., Graña, R. D., and Padilla, N. D. (2023). Guess the cheese flavour by the size of its holes: a cosmological test using the abundance of popcorn voids. *MNRAS*, 522(2):2553–2569.

Peebles, P. J. (1966). Primeval Helium Abundance and the Primeval Fireball. *Phys. Review Letter*, 16(10):410–413.

Peebles, P. J. E. (1968). Recombination of the Primeval Plasma. *ApJ*, 153:1.

Peebles, P. J. E. (1993). *Principles of physical cosmology*. Princeton University Press.

Percival, W. J., Friedrich, O., Sellentin, E., and Heavens, A. (2021). Matching Bayesian and frequentist coverage probabilities when using an approximate data covariance matrix. *MNRAS*.

Percival, W. J., Samushia, L., Ross, A. J., Shapiro, C., and Raccanelli, A. (2011). Redshift-space distortions. *Philosophical Transactions of the Royal Society of London Series A*, 369(1957):5058–5067.

Percival, W. J. and White, M. (2009). Testing cosmological structure formation using redshift-space distortions. *MNRAS*, 393(1):297–308.

Perlmutter, S., Aldering, G., Goldhaber, G., Knop, R. A., Nugent, P., Castro, P. G., Deustua, S., Fabbro, S., Goobar, A., Groom, D. E., Hook, I. M., Kim, A. G., Kim, M. Y., Lee, J. C., Nunes, N. J., Pain, R., Pennypacker, C. R., Quimby, R., Lidman, C.,

Ellis, R. S., Irwin, M., McMahon, R. G., Ruiz-Lapuente, P., Walton, N., Schaefer, B., Boyle, B. J., Filippenko, A. V., Matheson, T., Fruchter, A. S., Panagia, N., Newberg, H. J. M., Couch, W. J., and Project, T. S. C. (1999). Measurements of Ω and Λ from 42 High-Redshift Supernovae. *ApJ*, 517(2):565–586.

Pisani, A., Lavaux, G., Sutter, P. M., and Wandelt, B. D. (2014). Real-space density profile reconstruction of stacked voids. *MNRAS*, 443(4):3238–3250.

Pisani, A., Massara, E., Spergel, D. N., Alonso, D., Baker, T., Cai, Y.-C., Cautun, M., Davies, C., Demchenko, V., Doré, O., Goulding, A., Habouzit, M., Hamaus, N., Hawken, A., Hirata, C. M., Ho, S., Jain, B., Kreisch, C. D., Marulli, F., Padilla, N., Pollina, G., Sahlén, M., Sheth, R. K., Somerville, R., Szapudi, I., van de Weygaert, R., Villaescusa-Navarro, F., Wandelt, B. D., and Wang, Y. (2019). Cosmic voids: a novel probe to shed light on our Universe. *Bulletin of the AAS*, 51(3):40.

Pisani, A., Sutter, P. M., Hamaus, N., Alizadeh, E., Biswas, R., Wandelt, B. D., and Hirata, C. M. (2015). Counting voids to probe dark energy. *Phys. Ref. D*, 92(8):083531.

Planck Collaboration, Aghanim, N., Akrami, Y., Ashdown, M., Aumont, J., Baccigalupi, C., Ballardini, M., Banday, A. J., Barreiro, R. B., Bartolo, N., Basak, S., Battye, R., Benabed, K., Bernard, J. P., Bersanelli, M., Bielewicz, P., Bock, J. J., Bond, J. R., Borrill, J., Bouchet, F. R., Boulanger, F., Bucher, M., Burigana, C., Butler, R. C., Calabrese, E., Cardoso, J. F., Carron, J., Challinor, A., Chiang, H. C., Chluba, J., Colombo, L. P. L., Combet, C., Contreras, D., Crill, B. P., Cuttaia, F., de Bernardis, P., de Zotti, G., Delabrouille, J., Delouis, J. M., Di Valentino, E., Diego, J. M., Doré, O., Douspis, M., Ducout, A., Dupac, X., Dusini, S., Efstathiou, G., Elsner, F., Enßlin, T. A., Eriksen, H. K., Fantaye, Y., Farhang, M., Fergusson, J., Fernandez-Cobos, R., Finelli, F., Forastieri, F., Frailis, M., Fraisse, A. A., Franceschi, E., Frolov, A., Galeotta, S., Galli, S., Ganga, K., Génova-Santos, R. T., Gerbino, M., Ghosh, T., González-Nuevo, J., Górski, K. M., Gratton, S., Gruppuso, A., Gudmundsson, J. E., Hamann, J., Handley, W., Hansen, F. K., Herranz, D., Hildebrandt, S. R., Hivon, E., Huang, Z., Jaffe, A. H., Jones, W. C., Karakci, A., Keihänen, E., Keskitalo, R., Kiiveri, K., Kim, J., Kisner, T. S., Knox, L., Krachmalnicoff, N., Kunz, M., Kurki-Suonio, H., Lagache, G., Lamarre, J. M., Lasenby, A., Lattanzi, M., Lawrence, C. R., Le Jeune, M., Lemos, P., Lesgourgues, J., Levrier, F., Lewis, A., Liguori, M., Lilje, P. B., Lilley, M., Lindholm, V., López-Caniego, M., Lubin, P. M., Ma, Y. Z., Macías-Pérez, J. F., Maggio, G., Maino, D., Mandolesi, N., Mangilli, A., Marcos-Caballero, A., Maris, M., Martin, P. G., Martinelli, M., Martínez-González, E., Matarrese, S., Mauri, N., McEwen, J. D., Meinhold, P. R., Melchiorri, A., Mennella, A., Migliaccio, M., Millea, M., Mitra, S., Miville-Deschênes,

M. A., Molinari, D., Montier, L., Morgante, G., Moss, A., Natoli, P., Nørgaard-Nielsen, H. U., Pagano, L., Paoletti, D., Partridge, B., Patanchon, G., Peiris, H. V., Perrotta, F., Pettorino, V., Piacentini, F., Polastri, L., Polenta, G., Puget, J. L., Rachen, J. P., Reinecke, M., Remazeilles, M., Renzi, A., Rocha, G., Rosset, C., Roudier, G., Rubiño-Martín, J. A., Ruiz-Granados, B., Salvati, L., Sandri, M., Savelainen, M., Scott, D., Shellard, E. P. S., Sirignano, C., Sirri, G., Spencer, L. D., Sunyaev, R., Suur-Uski, A. S., Tauber, J. A., Tavagnacco, D., Tenti, M., Toffolatti, L., Tomasi, M., Trombetti, T., Valenziano, L., Valiviita, J., Van Tent, B., Vibert, L., Vielva, P., Villa, F., Vittorio, N., Wandelt, B. D., Wehus, I. K., White, M., White, S. D. M., Zacchei, A., and Zonca, A. (2020). Planck 2018 results. VI. Cosmological parameters. *A&A*, 641:A6.

Platen, E., van de Weygaert, R., and Jones, B. J. T. (2007). A cosmic watershed: the WVF void detection technique. *MNRAS*, 380(2):551–570.

Postman, M. and Lauer, T. R. (1995). Brightest Cluster Galaxies as Standard Candles. *ApJ*, 440:28.

Raccanelli, A., Bertacca, D., Pietrobon, D., Schmidt, F., Samushia, L., Bartolo, N., Doré, O., Matarrese, S., and Percival, W. J. (2013). Testing gravity using large-scale redshift-space distortions. *MNRAS*, 436(1):89–100.

Radinović, S., Nadathur, S., Winther, H. A., Percival, W. J., Woodfinden, A., Massara, E., Paillas, E., Contarini, S., Hamaus, N., Kovacs, A., Pisani, A., Verza, G., Aubert, M., Amara, A., Auricchio, N., Baldi, M., Bonino, D., Branchini, E., Brescia, M., Camera, S., Capobianco, V., Carbone, C., Cardone, V. F., Carretero, J., Castellano, M., Cavuoti, S., Cimatti, A., Cledassou, R., Congedo, G., Conversi, L., Copin, Y., Corcione, L., Courbin, F., Da Silva, A., Douspis, M., Dubath, F., Dupac, X., Farrens, S., Ferriol, S., Fosalba, P., Frailis, M., Franceschi, E., Fumana, M., Galeotta, S., Garilli, B., Gillard, W., Gillis, B., Giocoli, C., Grazian, A., Grupp, F., Haugan, S. V. H., Holmes, W., Hornstrup, A., Jahnke, K., Kümmel, M., Kiessling, A., Kilbinger, M., Kitching, T., Kurki-Suonio, H., Ligori, S., Lilje, P. B., Lloro, I., Maiorano, E., Mansutti, O., Marggraf, O., Markovic, K., Marulli, F., Massey, R., Mei, S., Melchior, M., Mellier, Y., Meneghetti, M., Merlin, E., Meylan, G., Moresco, M., Moscardini, L., Niemi, S. M., Nightingale, J. W., Nutma, T., Padilla, C., Paltani, S., Pasian, F., Pedersen, K., Pettorino, V., Pires, S., Polenta, G., Poncet, M., Popa, L. A., Pozzetti, L., Raison, F., Renzi, A., Rhodes, J., Riccio, G., Romelli, E., Roncarelli, M., Rosset, C., Saglia, R., Sapone, D., Sartoris, B., Schneider, P., Secroun, A., Seidel, G., Serrano, S., Sirignano, C., Sirri, G., Stanco, L., Starck, J. L., Surace, C., Tallada-Crespí, P., Tereno, I., Toledo-Moreo, R., Torradeflot, F., Tutusaus, I., Valentijn, E. A., Valenziano, L., Vassallo, T., Wang, Y., Weller, J., Zamorani, G.,

Zoubian, J., and Scottez, V. (2023). Euclid: Cosmology forecasts from the void-galaxy cross-correlation function with reconstruction. *arXiv e-prints*, page arXiv:2302.05302.

Raghunathan, S., Nadathur, S., Sherwin, B. D., and Whitehorn, N. (2020). The Gravitational Lensing Signatures of BOSS Voids in the Cosmic Microwave Background. *ApJ*, 890:168.

Raichoor, A., de Mattia, A., Ross, A. J., Zhao, C., Alam, S., Avila, S., Bautista, J., Brinkmann, J., Brownstein, J. R., Burtin, E., Chapman, M. J., Chuang, C.-H., Comparat, J., Dawson, K. S., Dey, A., du Mas des Bourboux, H., Elvin-Poole, J., Gonzalez-Perez, V., Gorgoni, C., Kneib, J.-P., Kong, H., Lang, D., Moustakas, J., Myers, A. D., Müller, E.-M., Nadathur, S., Newman, J. A., Percival, W. J., Rezaie, M., Rossi, G., Ruhlmann-Kleider, V., Schlegel, D. J., Schneider, D. P., Seo, H.-J., Tamone, A., Tinker, J. L., Tojeiro, R., Vivek, M., Yèche, C., and Zhao, G.-B. (2021). The completed SDSS-IV extended Baryon Oscillation Spectroscopic Survey: large-scale structure catalogues and measurement of the isotropic BAO between redshift 0.6 and 1.1 for the Emission Line Galaxy Sample. *MNRAS*, 500(3):3254–3274.

Reid, B., Ho, S., Padmanabhan, N., Percival, W. J., Tinker, J., Tojeiro, R., White, M., Eisenstein, D. J., Maraston, C., Ross, A. J., Sánchez, A. G., Schlegel, D., Sheldon, E., Strauss, M. A., Thomas, D., Wake, D., Beutler, F., Bizyaev, D., Bolton, A. S., Brownstein, J. R., Chuang, C.-H., Dawson, K., Harding, P., Kitaura, F.-S., Leauthaud, A., Masters, K., McBride, C. K., More, S., Olmstead, M. D., Oravetz, D., Nuza, S. E., Pan, K., Parejko, J., Pforr, J., Prada, F., Rodríguez-Torres, S., Salazar-Albornoz, S., Samushia, L., Schneider, D. P., Scóccola, C. G., Simmons, A., and Vargas-Magana, M. (2016). SDSS-III Baryon Oscillation Spectroscopic Survey Data Release 12: galaxy target selection and large-scale structure catalogues. *MNRAS*, 455(2):1553–1573.

Reid, B. A., Percival, W. J., Eisenstein, D. J., Verde, L., Spergel, D. N., Skibba, R. A., Bahcall, N. A., Budavari, T., Frieman, J. A., Fukugita, M., Gott, J. R., Gunn, J. E., Ivezić, Ž., Knapp, G. R., Kron, R. G., Lupton, R. H., McKay, T. A., Meiksin, A., Nichol, R. C., Pope, A. C., Schlegel, D. J., Schneider, D. P., Stoughton, C., Strauss, M. A., Szalay, A. S., Tegmark, M., Vogeley, M. S., Weinberg, D. H., York, D. G., and Zehavi, I. (2010). Cosmological constraints from the clustering of the Sloan Digital Sky Survey DR7 luminous red galaxies. *MNRAS*, 404(1):60–85.

Riess, A. G., Casertano, S., Yuan, W., Bowers, J. B., Macri, L., Zinn, J. C., and Scolnic, D. (2021). Cosmic Distances Calibrated to 1% Precision with Gaia EDR3 Parallaxes and Hubble Space Telescope Photometry of 75 Milky Way Cepheids Confirm Tension with ΛCDM. *ApJ*, 908(1):L6.

Riess, A. G., Filippenko, A. V., Challis, P., Clocchiatti, A., Diercks, A., Garnavich, P. M., Gilliland, R. L., Hogan, C. J., Jha, S., Kirshner, R. P., Leibundgut, B., Phillips, M. M., Reiss, D., Schmidt, B. P., Schommer, R. A., Smith, R. C., Spyromilio, J., Stubbs, C., Suntzeff, N. B., and Tonry, J. (1998). Observational Evidence from Supernovae for an Accelerating Universe and a Cosmological Constant. *AJ*, 116(3):1009–1038.

Roberts, M. S. and Rots, A. H. (1973). Comparison of Rotation Curves of Different Galaxy Types. *A&A*, 26:483–485.

Robertson, H. P. (1935). Kinematics and World-Structure. *ApJ*, 82:284.

Ross, A. J., Percival, W. J., Sánchez, A. G., Samushia, L., Ho, S., Kazin, E., Manera, M., Reid, B., White, M., Tojeiro, R., and et al. (2012). The clustering of galaxies in the sdss-iii baryon oscillation spectroscopic survey: analysis of potential systematics. *Monthly Notices of the Royal Astronomical Society*, 424(1):564–590.

Ross, A. J., Samushia, L., Howlett, C., Percival, W. J., Burden, A., and Manera, M. (2015). The clustering of the SDSS DR7 main Galaxy sample - I. A 4 per cent distance measure at z = 0.15. *MNRAS*, 449(1):835–847.

Rubin, V. C., Ford, W. K., J., and Thonnard, N. (1978). Extended rotation curves of high-luminosity spiral galaxies. IV. Systematic dynamical properties, Sa -> Sc. *ApJ*, 225:L107–L111.

Rubin, V. C., Ford, W. K., J., and Thonnard, N. (1980). Rotational properties of 21 SC galaxies with a large range of luminosities and radii, from NGC 4605 (R=4kpc) to UGC 2885 (R=122kpc). *ApJ*, 238:471–487.

Ruiz, A. N., Paz, D. J., Lares, M., Luparello, H. E., Ceccarelli, L., and Lambas, D. G. (2015). Clues on void evolution - III. Structure and dynamics in void shells. *MNRAS*, 448(2):1471–1482.

Sánchez, A. G., Grieb, J. N., Salazar-Albornoz, S., Alam, S., Beutler, F., Ross, A. J., Brownstein, J. R., Chuang, C.-H., Cuesta, A. J., Eisenstein, D. J., Kitaura, F.-S., Percival, W. J., Prada, F., Rodríguez-Torres, S., Seo, H.-J., Tinker, J., Tojeiro, R., Vargas-Magaña, M., Vazquez, J. A., and Zhao, G.-B. (2017a). The clustering of galaxies in the completed SDSS-III Baryon Oscillation Spectroscopic Survey: combining correlated Gaussian posterior distributions. *MNRAS*, 464(2):1493–1501.

Sánchez, C., Clampitt, J., Kovacs, A., Jain, B., García-Bellido, J., Nadathur, S., Gruen, D., Hamaus, N., Huterer, D., Vielzeuf, P., Amara, A., Bonnett, C., DeRose, J., Hartley,

W. G., Jarvis, M., Lahav, O., Miquel, R., Rozo, E., Rykoff, E. S., Sheldon, E., Wechsler, R. H., Zuntz, J., Abbott, T. M. C., Abdalla, F. B., Annis, J., Benoit-Lévy, A., Bernstein, G. M., Bernstein, R. A., Bertin, E., Brooks, D., Buckley-Geer, E., Carnero Rosell, A., Carrasco Kind, M., Carretero, J., Crocce, M., Cunha, C. E., D'Andrea, C. B., da Costa, L. N., Desai, S., Diehl, H. T., Dietrich, J. P., Doel, P., Evrard, A. E., Fausti Neto, A., Flaugher, B., Fosalba, P., Frieman, J., Gaztanaga, E., Gruendl, R. A., Gutierrez, G., Honscheid, K., James, D. J., Krause, E., Kuehn, K., Lima, M., Maia, M. A. G., Marshall, J. L., Melchior, P., Plazas, A. A., Reil, K., Romer, A. K., Sanchez, E., Schubnell, M., Sevilla-Noarbe, I., Smith, R. C., Soares-Santos, M., Sobreira, F., Suchyta, E., Tarle, G., Thomas, D., Walker, A. R., Weller, J., and DES Collaboration (2017b). Cosmic voids and void lensing in the Dark Energy Survey Science Verification data. *MNRAS*, 465:746–759.

Scolnic, D., Brout, D., Carr, A., Riess, A. G., Davis, T. M., Dwomoh, A., Jones, D. O., Ali, N., Charvu, P., Chen, R., Peterson, E. R., Popovic, B., Rose, B. M., Wood, C. M., Brown, P. J., Chambers, K., Coulter, D. A., Dettman, K. G., Dimitriadis, G., Filippenko, A. V., Foley, R. J., Jha, S. W., Kilpatrick, C. D., Kirshner, R. P., Pan, Y.-C., Rest, A., Rojas-Bravo, C., Siebert, M. R., Stahl, B. E., and Zheng, W. (2022). The Pantheon+ Analysis: The Full Data Set and Light-curve Release. *ApJ*, 938(2):113.

Scolnic, D. M., Jones, D. O., Rest, A., Pan, Y. C., Chornock, R., Foley, R. J., Huber, M. E., Kessler, R., Narayan, G., Riess, A. G., and et al. (2018). The complete light-curve sample of spectroscopically confirmed sne ia from pan-starrs1 and cosmological constraints from the combined pantheon sample. *The Astrophysical Journal*, 859(2):101.

Sheth, R. K. (1998). An excursion set model for the distribution of dark matter and dark matter haloes. *MNRAS*, 300(4):1057–1070.

Sheth, R. K. and van de Weygaert, R. (2004). A hierarchy of voids: much ado about nothing. *MNRAS*, 350(2):517–538.

Smith, A., Burtin, E., Hou, J., Neveux, R., Ross, A. J., Alam, S., Brinkmann, J., Dawson, K. S., Habib, S., Heitmann, K., Kneib, J.-P., Lyke, B. W., du Mas des Bourboux, H., Mueller, E.-M., Myers, A. D., Percival, W. J., Rossi, G., Schneider, D. P., Zarrouk, P., and Zhao, G.-B. (2020). The completed SDSS-IV extended Baryon Oscillation Spectroscopic Survey: N-body mock challenge for the quasar sample. *MNRAS*, 499(1):269–291.

Springel, V. (2005). The cosmological simulation code GADGET-2. *MNRAS*, 364(4):1105–1134.

Steigman, G. (2004). Big Bang Nucleosynthesis: Probing the First 20 Minutes. In Freedman, W. L., editor, *Measuring and Modeling the Universe*, page 169.

Strauss, M. A., Weinberg, D. H., Lupton, R. H., Narayanan, V. K., Annis, J., Bernardi, M., Blanton, M., Burles, S., Connolly, A. J., Dalcanton, J., Doi, M., Eisenstein, D., Frieman, J. A., Fukugita, M., Gunn, J. E., Ivezić, Ž., Kent, S., Kim, R. S. J., Knapp, G. R., Kron, R. G., Munn, J. A., Newberg, H. J., Nichol, R. C., Okamura, S., Quinn, T. R., Richmond, M. W., Schlegel, D. J., Shimasaku, K., SubbaRao, M., Szalay, A. S., Vanden Berk, D., Vogeley, M. S., Yanny, B., Yasuda, N., York, D. G., and Zehavi, I. (2002). Spectroscopic Target Selection in the Sloan Digital Sky Survey: The Main Galaxy Sample. *AJ*, 124(3):1810–1824.

Sunyaev, R. A. (1974). The thermal history of the universe and the spectrum of relic radiation. In Longair, M. S., editor, *Confrontation of Cosmological Theories with Observational Data*, volume 63, pages 167–173.

Sutter, P. M., Lavaux, G., Hamaus, N., Pisani, A., Wandelt, B. D., Warren, M., Villaescusa-Navarro, F., Zivick, P., Mao, Q., and Thompson, B. B. (2015). VIDE: The Void IDentification and Examination toolkit. *Astronomy and Computing*, 9:1–9.

Tamone, A., Raichoor, A., Zhao, C., de Mattia, A., Gorgoni, C., Burtin, E., Ruhlmann-Kleider, V., Ross, A. J., Alam, S., Percival, W. J., Avila, S., Chapman, M. J., Chuang, C.-H., Comparat, J., Dawson, K. S., de la Torre, S., du Mas des Bourboux, H., Escoffier, S., Gonzalez-Perez, V., Hou, J., Kneib, J.-P., Mohammad, F. G., Mueller, E.-M., Paviot, R., Rossi, G., Schneider, D. P., Wang, Y., and Zhao, G.-B. (2020). The completed SDSS-IV extended baryon oscillation spectroscopic survey: growth rate of structure measurement from anisotropic clustering analysis in configuration space between redshift 0.6 and 1.1 for the emission-line galaxy sample. *MNRAS*, 499(4):5527–5546.

Tinker, J. L. and Conroy, C. (2009). The Void Phenomenon Explained. *ApJ*, 691(1):633–639.

Tinker, J. L., Conroy, C., Norberg, P., Patiri, S. G., Weinberg, D. H., and Warren, M. S. (2008). Void Statistics in Large Galaxy Redshift Surveys: Does Halo Occupation of Field Galaxies Depend on Environment? *ApJ*, 686(1):53–71.

Tinker, J. L., Weinberg, D. H., and Warren, M. S. (2006). Cosmic Voids and Galaxy Bias in the Halo Occupation Framework. *ApJ*, 647(2):737–752.

Torrado, J. and Lewis, A. (2019a). Cobaya: Bayesian analysis in cosmology.

Torrado, J. and Lewis, A. (2019b). Cobaya: Bayesian analysis in cosmology.

Torrado, J. and Lewis, A. (2021a). Cobaya: code for Bayesian analysis of hierarchical physical models. *J. Cosmology Astropart. Phys.*, 2021(5):057.

Torrado, J. and Lewis, A. (2021b). Cobaya: code for Bayesian analysis of hierarchical physical models. *J. Cosmology Astropart. Phys.*, 2021(5):057.

Tröster, T., Sánchez, A. G., Asgari, M., Blake, C., Crocce, M., Heymans, C., Hildebrandt, H., Joachimi, B., Joudaki, S., Kannawadi, A., Lin, C.-A., and Wright, A. (2020). Cosmology from large-scale structure. Constraining ΛCDM with BOSS. *A&A*, 633:L10.

Verza, G., Carbone, C., and Renzi, A. (2022). The halo bias inside cosmic voids. *arXiv e-prints*, page arXiv:2207.04039.

Villaescusa-Navarro, F., Hahn, C., Massara, E., Banerjee, A., Delgado, A. M., Ramanah, D. K., Charnock, T., Giusarma, E., Li, Y., Allys, E., Brochard, A., Uhlemann, C., Chiang, C.-T., He, S., Pisani, A., Obuljen, A., Feng, Y., Castorina, E., Contardo, G., Kreisch, C. D., Nicola, A., Alsing, J., Scoccimarro, R., Verde, L., Viel, M., Ho, S., Mallat, S., Wandelt, B., and Spergel, D. N. (2020). The Quijote Simulations. *ApJS*, 250(1):2.

Walker, A. G. (1937). On Milne's Theory of World-Structure. *Proceedings of the London Mathematical Society*, 42:90–127.

Wang, B. Y., Pisani, A., Villaescusa-Navarro, F., and Wandelt, B. D. (2022). Machine learning cosmology from void properties. *arXiv e-prints*, page arXiv:2212.06860.

Weinberg, D. H., Mortonson, M. J., Eisenstein, D. J., Hirata, C., Riess, A. G., and Rozo, E. (2013). Observational probes of cosmic acceleration. *Phys. Reports*, 530(2):87–255.

White, M. and Hu, W. (1997). The Sachs-Wolfe effect. *A&A*, 321:8–9.

Woodfinden, A., Nadathur, S., Percival, W. J., Radinovic, S., Massara, E., and Winther, H. A. (2022). Measurements of cosmic expansion and growth rate of structure from voids in the sloan digital sky survey between redshift 0.07 and 1.0. *MNRAS*, 516(3):4307–4323.

Woodfinden, A., Percival, W. J., Nadathur, S., Winther, H. A., Fraser, T. S., Massara, E., Paillas, E., and Radinović, S. (2023). Cosmological measurements from void-galaxy and galaxy-galaxy clustering in the Sloan Digital Sky Survey. *arXiv e-prints*, page arXiv:2303.06143.

Wright, E. L., Mather, J. C., Fixsen, D. J., Kogut, A., Shafer, R. A., Bennett, C. L., Boggess, N. W., Cheng, E. S., Silverberg, R. F., Smoot, G. F., and Weiss, R. (1994). Interpretation of the COBE FIRAS CMBR Spectrum. *ApJ*, 420:450.

York, D. G., Adelman, J., Anderson, John E., J., Anderson, S. F., Annis, J., Bahcall, N. A., Bakken, J. A., Barkhouser, R., Bastian, S., Berman, E., Boroski, W. N., Bracker, S., Briegel, C., Briggs, J. W., Brinkmann, J., Brunner, R., Burles, S., Carey, L., Carr, M. A., Castander, F. J., Chen, B., Colestock, P. L., Connolly, A. J., Crocker, J. H., Csabai, I., Czarapata, P. C., Davis, J. E., Doi, M., Dombeck, T., Eisenstein, D., Ellman, N., Elms, B. R., Evans, M. L., Fan, X., Federwitz, G. R., Fiscelli, L., Friedman, S., Frieman, J. A., Fukugita, M., Gillespie, B., Gunn, J. E., Gurbani, V. K., de Haas, E., Haldeman, M., Harris, F. H., Hayes, J., Heckman, T. M., Hennessy, G. S., Hindsley, R. B., Holm, S., Holmgren, D. J., Huang, C.-h., Hull, C., Husby, D., Ichikawa, S.-I., Ichikawa, T., Ivezić, Ž., Kent, S., Kim, R. S. J., Kinney, E., Klaene, M., Kleinman, A. N., Kleinman, S., Knapp, G. R., Korienek, J., Kron, R. G., Kunszt, P. Z., Lamb, D. Q., Lee, B., Leger, R. F., Limmongkol, S., Lindenmeyer, C., Long, D. C., Loomis, C., Loveday, J., Lucinio, R., Lupton, R. H., MacKinnon, B., Mannery, E. J., Mantsch, P. M., Margon, B., McGehee, P., McKay, T. A., Meiksin, A., Merelli, A., Monet, D. G., Munn, J. A., Narayanan, V. K., Nash, T., Neilsen, E., Neswold, R., Newberg, H. J., Nichol, R. C., Nicinski, T., Nonino, M., Okada, N., Okamura, S., Ostriker, J. P., Owen, R., Pauls, A. G., Peoples, J., Peterson, R. L., Petravick, D., Pier, J. R., Pope, A., Pordes, R., Prosapio, A., Rechenmacher, R., Quinn, T. R., Richards, G. T., Richmond, M. W., Rivetta, C. H., Rockosi, C. M., Ruthmansdorfer, K., Sandford, D., Schlegel, D. J., Schneider, D. P., Sekiguchi, M., Sergey, G., Shimasaku, K., Siegmund, W. A., Smee, S., Smith, J. A., Snedden, S., Stone, R., Stoughton, C., Strauss, M. A., Stubbs, C., SubbaRao, M., Szalay, A. S., Szapudi, I., Szokoly, G. P., Thakar, A. R., Tremonti, C., Tucker, D. L., Uomoto, A., Vanden Berk, D., Vogeley, M. S., Waddell, P., Wang, S.-i., Watanabe, M., Weinberg, D. H., Yanny, B., Yasuda, N., and SDSS Collaboration (2000). The Sloan Digital Sky Survey: Technical Summary. *AJ*, 120(3):1579–1587.

Yuan, S., Garrison, L. H., Eisenstein, D. J., and Wechsler, R. H. (2022). Stringent σ_8 constraints from small-scale galaxy clustering using a hybrid MCMC + emulator framework. *MNRAS*, 515(1):871–896.

Zel'dovich, Y. B. (1970). Gravitational instability: An approximate theory for large density perturbations. *A&A*, 5:84–89.

Zhao, C., Chuang, C.-H., Bautista, J., de Mattia, A., Raichoor, A., Ross, A. J., Hou, J., Neveux, R., Tao, C., Burtin, E., Dawson, K. S., de la Torre, S., Gil-Marín, H.,

Kneib, J.-P., Percival, W. J., Rossi, G., Tamone, A., Tinker, J. L., Zhao, G.-B., Alam, S., and Mueller, E.-M. (2020). The Completed SDSS-IV extended Baryon Oscillation Spectroscopic Survey: one thousand multi-tracer mock catalogues with redshift evolution and systematics for galaxies and quasars of the final data release. *arXiv e-prints*, page arXiv:2007.08997.

Zhao, C., Tao, C., Liang, Y., Kitaura, F.-S., and Chuang, C.-H. (2016). DIVE in the cosmic web: voids with Delaunay triangulation from discrete matter tracer distributions. *MNRAS*, 459(3):2670–2680.

Zhao, C., Variu, A., He, M., Forero-Sánchez, D., Tamone, A., Chuang, C.-H., Kitaura, F.-S., Tao, C., Yu, J., Kneib, J.-P., Percival, W. J., Shan, H., Zhao, G.-B., Burtin, E., Dawson, K. S., Rossi, G., Schneider, D. P., and de la Macorra, A. (2022). The completed SDSS-IV extended Baryon Oscillation Spectroscopic Survey: cosmological implications from multitracer BAO analysis with galaxies and voids. *MNRAS*, 511(4):5492–5524.

Zhou, R., Dey, B., Newman, J. A., Eisenstein, D. J., Dawson, K., Bailey, S., Berti, A., Guy, J., Lan, T.-W., Zou, H., Aguilar, J., Ahlen, S., Alam, S., Brooks, D., de la Macorra, A., Dey, A., Dhungana, G., Fanning, K., Font-Ribera, A., Gontcho, S. G. A., Honscheid, K., Ishak, M., Kisner, T., Kovács, A., Kremin, A., Landriau, M., Levi, M. E., Magneville, C., Manera, M., Martini, P., Meisner, A. M., Miquel, R., Moustakas, J., Myers, A. D., Nie, J., Palanque-Delabrouille, N., Percival, W. J., Poppett, C., Prada, F., Raichoor, A., Ross, A. J., Schlafly, E., Schlegel, D., Schubnell, M., Tarlé, G., Weaver, B. A., Wechsler, R. H., Yéche, C., and Zhou, Z. (2023). Target Selection and Validation of DESI Luminous Red Galaxies. *AJ*, 165(2):58.

Zivick, P., Sutter, P. M., Wandelt, B. D., Li, B., and Lam, T. Y. (2015). Using cosmic voids to distinguish f(R) gravity in future galaxy surveys. *Monthly Notices of the Royal Astronomical Society*, 451(4):4215–4222.

Zwicky, F. (1933). Die Rotverschiebung von extragalaktischen Nebeln. *Helvetica Physica Acta*, 6:110–127.